2016

Autonomous optimal trajectory design employing convex optimization for powered descent on an asteroid

Robin Marie Pinson
Iowa State University

Recommended Citation

Pinson, Robin Marie, "Autonomous optimal trajectory design employing convex optimization for powered descent on an asteroid" (2016). *Graduate Theses and Dissertations*. 15791.
http://lib.dr.iastate.edu/etd/15791

Autonomous optimal trajectory design employing convex optimization for powered descent on an asteroid

by

Robin Marie Pinson

A dissertation submitted to the graduate faculty
in partial fulfillment of the requirements for the degree of
DOCTOR OF PHILOSOPHY

Major: Aerospace Engineering

Program of Study Committee:
Ping Lu, Major Professor
Ran Dai
Ganesh Rajagopalan
Peter Sherman
Zhijun Wu

Iowa State University
Ames, Iowa
2016

TABLE OF CONTENTS

LIST OF TABLES

LIST OF FIGURES

NOMENCLATURE

A1	1000 x 500 x 250 m triaxial ellipsoidal asteroid
A2	750 x 500 x 250 m triaxial ellipsoidal asteroid
A3	500 x 500 x 250 m triaxial ellipsoidal asteroid
CVX	Matlab based convex optimization solver.
EQ	Equatorial landing site on the triaxial ellipsoidal asteroid with out of plane and uprange initial conditions.
EQ_hov	Equatorial landing site on the triaxial ellipsoidal asteroid with hovering initial conditions.
EQ_LT	Equatorial landing site on the triaxial ellipsoidal asteroid with out of plane and uprange initial conditions for the lower thrust vehicle.
GN&C	Guidance, Navigation, and Control
hr	Abbreviation for hour.
ISU	Iowa State University
JPL	Jet Propulsion Laboratory
LS1	Landing Site 1 on Castalia with out of plane and uprange initial conditions.
LS2	Landing Site 2 on Castalia with out of plane and uprange initial conditions.
LS3	Landing Site 3 on Castalia with out of plane and uprange initial conditions.
LS1_hov	Landing Site 1 on Castalia with hovering initial conditions.
LS2_hov	Landing Site 2 on Castalia with hovering initial conditions.
LS3_hov	Landing Site 3 on Castalia with hovering initial conditions.
LS1_LT	Landing Site 1 on Castalia with out of plane and uprange initial conditions for the lower thrust vehicle.
LS2_LT	Landing Site 2 on Castalia with out of plane and uprange initial conditions for the lower thrust vehicle.

LS3_LT	Landing Site 3 on Castalia with out of plane and uprange initial conditions for the lower thrust vehicle.
NEAR	Near Earth Asteroid Rendezvous
NP	North Pole landing site on the triaxial ellipsoidal asteroid with out of plane and uprange initial conditions.
NP_hov	North Pole landing site on the triaxial ellipsoidal asteroid with hovering initial conditions.
NP_LT	North Pole landing site on the triaxial ellipsoidal asteroid with out of plane and uprange initial conditions for the lower thrust vehicle.
P1	Original nonlinear propellant optimal problem.
P2	Relaxed propellant optimal problem.
P3	Relaxed propellant optimal problem in convex form after variable changes.
s, sec	Abbreviation for seconds.
SOCP	Second order cone program
2x2	2x2 spherical harmonics gravity model with maximum order and degree of 2.
3-D	Three dimensional space
3-DOF	Three degrees of freedom
4x4	4x4 spherical harmonics gravity model with maximum order and degree of 4.
4x4 Bessel	4x4 spherical harmonics gravity model combined with the interior spherical Bessel gravity model.

ABSTRACT

Mission proposals that land spacecraft on asteroids are becoming increasingly popular. However, in order to have a successful mission the spacecraft must reliably and softly land at the intended landing site with pinpoint precision. The problem under investigation is how to design a propellant (fuel) optimal powered descent trajectory that can be quickly computed onboard the spacecraft, without interaction from ground control. The goal is to autonomously design the optimal powered descent trajectory onboard the spacecraft immediately prior to the descent burn for use during the burn. Compared to a planetary powered landing problem, the challenges that arise from designing an asteroid powered descent trajectory include complicated nonlinear gravity fields, small rotating bodies, and low thrust vehicles. The nonlinear gravity fields cannot be represented by a constant gravity model nor a Newtonian model. The trajectory design algorithm needs to be robust and efficient to guarantee a designed trajectory and complete the calculations in a reasonable time frame.

This research investigates the following questions: Can convex optimization be used to design the minimum propellant powered descent trajectory for a soft landing on an asteroid? Is this method robust and reliable to allow autonomy onboard the spacecraft without interaction from ground control? This research designed a convex optimization based method that rapidly generates the propellant optimal asteroid powered descent trajectory. The solution to the convex optimization problem is the thrust magnitude and direction, which designs and determines the trajectory. The propellant optimal problem was formulated as a second order cone program, a subset of convex optimization, through relaxation techniques by including a slack variable, change of variables, and incorporation of the successive solution method. Convex optimization solvers, especially second order cone programs, are robust, reliable, and are guaranteed to find the global minimum provided one exists. In addition, an outer optimization loop using Brent's method determines the optimal flight time corresponding to the minimum propellant usage

over all flight times. Inclusion of additional trajectory constraints, solely vertical motion near the landing site and glide slope, were evaluated.

Through a theoretical proof involving the Minimum Principle from Optimal Control Theory and the Karush-Kuhn-Tucker conditions it was shown that the relaxed problem is identical to the original problem at the minimum point. Therefore, the optimal solution of the relaxed problem is an optimal solution of the original problem, referred to as lossless convexification. A key finding is that this holds for all levels of gravity model fidelity. The designed thrust magnitude profiles were the bang-bang predicted by Optimal Control Theory.

The first high fidelity gravity model employed was the 2x2 spherical harmonics model assuming a perfect triaxial ellipsoid and placement of the coordinate frame at the asteroid's center of mass and aligned with the semi-major axes. The spherical harmonics model is not valid inside the Brillouin sphere and this becomes relevant for irregularly shaped asteroids. Then, a higher fidelity model was implemented combining the 4x4 spherical harmonics gravity model with the interior spherical Bessel gravity model. All gravitational terms in the equations of motion are evaluated with the position vector from the previous iteration, creating the successive solution method. Methodology success was shown by applying the algorithm to three triaxial ellipsoidal asteroids with four different rotation speeds using the 2x2 gravity model. Finally, the algorithm was tested using the irregularly shaped asteroid, Castalia.

CHAPTER 1. INTRODUCTION AND BACKGROUND

This research investigates a convex optimization based method that can rapidly generate the propellant (fuel) optimal asteroid powered descent trajectory. The goal is to autonomously design the optimal powered descent trajectory onboard the spacecraft immediately prior to the descent burn which will be used in flight by the guidance algorithm to fly the vehicle. Compared to a planetary powered landing problem, the major difficulty is the complex gravity field near the surface of an asteroid that cannot be approximated by a constant gravity field. This research uses relaxation techniques and a successive solution process that seeks the solution to the original nonlinear, nonconvex problem through the solutions to a sequence of convex optimal control problems.

The main questions under investigation are: Can convex optimization be used to design the minimum propellant powered descent trajectory for a soft landing on an asteroid? Is this method robust and reliable to allow autonomy onboard the spacecraft without interaction from ground control?

1.1 Introduction

Mission proposals that land spacecraft on asteroids are becoming increasingly popular. However, in order to have a successful mission the spacecraft must reliably and softly land at the intended landing site with pinpoint precision. The problem under investigation is how to design a propellant optimal powered descent trajectory that can be quickly computed onboard the spacecraft without interaction from ground control.

An optimal trajectory designed immediately prior to the powered descent burn has many advantages. These advantages include using the actual vehicle starting state as the initial condition in the trajectory design and the ease of updating the target landing site. This will prevent the need to upload different trajectories and hope one of the trajectories is close enough to the vehicle's starting and ending locations. Due to the distance of the asteroid from Earth, communication with the spacecraft may be infrequent and contain significant lag times. These lag times are easily 20 minutes each direction. This drives the need for autonomy as ground control will not be able to make last minute changes. For long trajectories, the trajectory can be updated periodically by a redesign of the optimal trajectory based on current vehicle conditions to improve guidance performance and landing accuracy. The error at the landing site will be minimal if the true vehicle characteristics with the actual initial and final conditions are used to design the trajectory. The goal for a pinpoint soft landing is to touch down at the landing site with zero velocity relative to the landing site upon arrival.

Challenges that arise from designing an asteroid powered descent trajectory include complicated nonlinear gravity fields, small rotating bodies and low thrust vehicles. The nonlinear gravity fields cannot be represented by a constant gravity model nor a Newtonian model. These are the prevalent models incorporated in traditional planetary landing problems. A higher fidelity model is necessary to achieve an adequate approximation of the asteroid gravity field. Low thrust vehicles are typical as the magnitude of the asteroid's gravitational force is a small fraction of Earth's. The majority of asteroids complete a revolution on the order of hours making their spin rate faster than Earth's.

There are many factors that will not be understood until the spacecraft reaches the asteroid, which is why many missions spend long periods of time near the asteroid characterizing it and choosing the landing site. It is imperative to make the trajectory design algorithm as flexible as possible to account for this updated information. The algorithm would also need to be robust and efficient to complete the calculations and guarantee a successfully designed trajectory in a reasonable time frame.

Asteroids, the focus of this research, are included in the class of bodies referred to as small body. Comets are also included in the small body class. The main difference between a comet and an asteroid is the forces due to out-gassing on the comet (comet's tail). This research can be applied to a comet by including those additional forces.

This research focuses on trajectory design. However, it will be used as an input to the vehicle's guidance system and closely tied to the discipline of Guidance, Navigation, and Control (GN&C). Guidance determines the path the vehicle should follow and commands the direction and thrust magnitude, while navigation determines the vehicle's current state (position and velocity) and acceleration. Control implements the guidance commands. For the purposes of this research it is assumed that: a guidance algorithm can be designed that tracks the trajectory given disturbances, that there is a navigation system that can determine the spacecraft state relative to the asteroid, and that the control system implements the guidance commands perfectly. When final mission planning occurs, GN&C would need to be included in the analysis to determine their effects on following the designed trajectory. During the trajectory design phase, the vehicle is considered a point mass that can achieve the trajectory exactly as designed within the constraints levied on the trajectory.

1.2 Convex Optimization and Second Order Cone Program

Convex optimization is a class of optimization problems that includes many subclasses. It has been studied for the last hundred years; however, it became popular in industry during the last 25 years achieving great success in a wide variety of disciplines. Applications of convex optimization in industry include: estimation and signal processing, modeling statistics, finance, and automatic control systems. It is just starting to make an appearance in aerospace engineering. Given its wide range of applications and advantages, it is a good candidate for solving the propellant optimal powered descent problem.

A convex optimization problem can be solved reliably and efficiently. If the problem is feasible, then the global optimal can be found in a finite number of steps. Depending on the problem formulation the upper bound on the number of steps can be determined a priori. If the problem is infeasible, then no solution is possible. Convex optimization includes the subclasses of linear program, second order cone program (SOCP), quadratic program and least-squares.

The definition of a convex function is located in Equation 1.1 and depicted in Figure 1.1.

$$f\left(\lambda x_1 + (1-\lambda)\, x_2\right) \leq \lambda f\left(x_1\right) + (1-\lambda)\, f\left(x_2\right), \quad 0 \leq \lambda \leq 1 \tag{1.1}$$

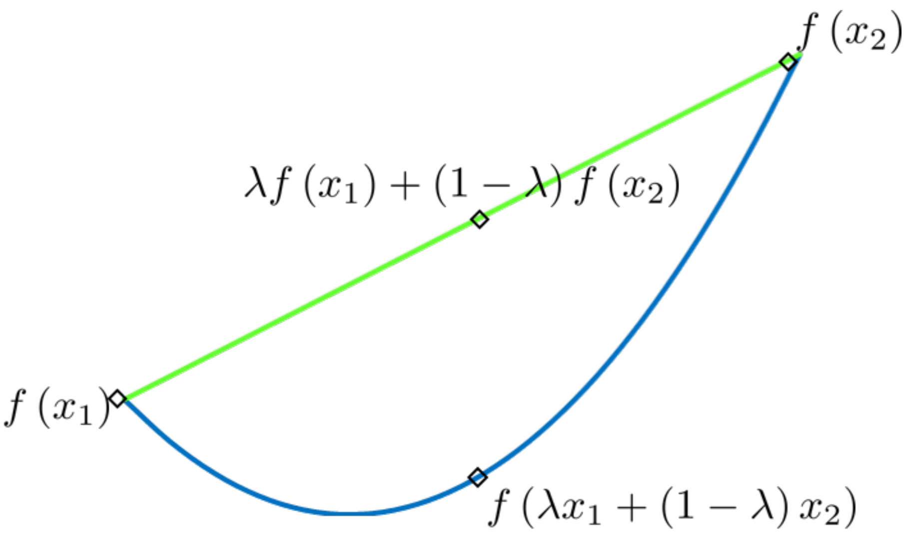

Figure 1.1: Depiction of a convex function. If the function (blue line) is below the line connecting two points on the function (green), then the function is convex.

Connect any two points (x_1 and x_2) on a function (f) with a line, if all values remain below or on that line, then the function is convex. When the equation is a strict equality, the function is the standard linear function, also called affine. Thus, linear functions are convex functions. Another function that is included in the class of convex functions is the second order cone defined in Equation 1.2.

$$\|Ax+b\|_2 \leq c^T x + d \tag{1.2}$$

The matrix A and vectors b, c, and d are sized appropriately to match x. An example of a second order cone is found in Figure 1.2. A second order cone inequality constraint would require all the values to lie inside or on the cone.

The standard form of an optimization problem is located in Equation 1.3.

$$\begin{aligned} &min\ g(x) \\ &s.t.\ f_i(x) \leq 0\ \ i = 1, ..., m \\ &\quad h_j(x) = 0\ \ j = 1, ..., p \end{aligned} \tag{1.3}$$

This minimizes a cost function, $g(x)$, subject to m inequality constraints in the form of $f(x) \leq 0$ and p equality constraints in the form of $h(x) = 0$. For the general optimization problem, these functions and constraints can be any form including numerous nonlinear terms.

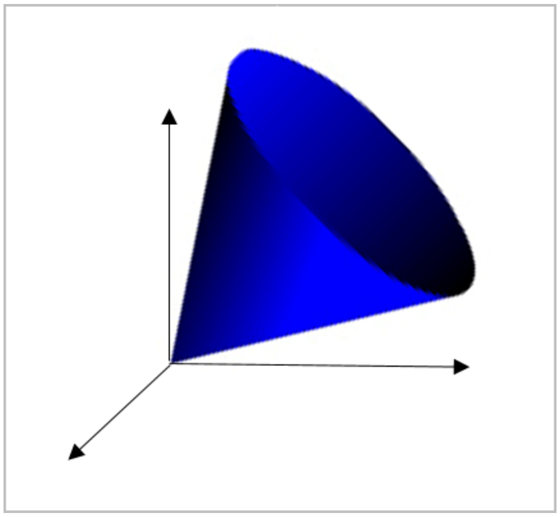

Figure 1.2: Depiction of a second order cone.

A convex optimization problem requires the cost function and the inequality constraints to be convex functions, while the equality constraints are linear or affine. This changes the optimization problem to the following form, Equation 1.4.

$$\begin{aligned} &min\ f_0(x) \\ &s.t.\ f_i(x) \leq 0 \qquad i = 1, ..., m \\ &h_j^T x - k_j = 0\ j = 1, ..., p \end{aligned} \tag{1.4}$$

In Equation 1.4, the functions $f\,(x)$ must be convex, which is defined in Equation 1.1. The vectors h and k are sized to match x.

A special subclass of convex optimization is the second order cone program (SOCP). For this class of optimization problems, the cost function and equality constraints are affine functions (linear). The inequality constraints are second order cone constraints (Equation 1.2). The SOCP standard problem formulation is listed in Equation 1.5.

$$\begin{aligned} &min\ f^T x \\ &s.t.\ \|A_i x + b_i\|_2 \leq c_i^T x + d_i\ i = 1, ..., m \\ &h_j^T x - k_j = 0 \qquad\qquad j = 1, ..., p \end{aligned} \tag{1.5}$$

There are publicly and commercially available solvers for convex optimization problems along with numerous published methods. The subclass SOCP has solvers devoted for that particular problem or it can use any convex solver. If an optimization problem can be formulated as a convex optimization problem, it can be easily solved. The challenge is to turn a nonlinear optimization problem into a convex optimization problem. The propellant optimal asteroid powered descent problem is highly nonlinear.

1.3 Research Contributions

The main contribution of this research is the formulation of and then the solution methodology for the convex optimization landing problem for use with asteroids. This includes adding the rotating small body effects for any rotational axis. Asteroids rotate faster than Mars, the focus of the original work, and not necessarily on the +Z axis. One of the main efforts has been exploring high fidelity gravity models for inclusion in the problem. This started with a 2x2 spherical harmonics gravity model assuming a perfect triaxial ellipsoid. The 2x2 spherical harmonics gravity model includes the terms in the summation through order and degree of 2. For the perfect triaxial ellipsoid, this includes two higher order terms in addition to the Newtonian gravity term. The gravity model was then extended to a 4x4 spherical harmonics model removing the perfect triaxial ellipsoid assumption, (summation through degree and order of 4). Finally, a combination of the 4x4 spherical harmonics gravity model and an interior spherical Bessel model near the asteroid surface was examined. The interior spherical Bessel gravity model is a recently published model, 2014, which makes this one of the early researches to adopt it. The published mathematical equations required subtle changes in order to truly work in the optimization algorithm and equations. Previous bodies of research investigating the propellant optimal powered descent problem used a constant gravity model and the Newtonian gravity model. While working with the higher fidelity gravity models, the proof that the solution to the relaxed convex optimization problem is indeed the solution to the original nonlinear optimization problem was given. It was shown that this equivalence holds for any gravity model that is solely a function of the vehicle position relative to the asteroid and the asteroid shape. Previous perfect relaxation results were limited to the Newtonian or constant gravity models.

The successive solution method was originally demonstrated with a rendezvous and proximity operations trajectory design. This research successfully incorporates this methodology into a landing problem, while increasing the gravity model fidelity and problem complexity. In addition, a second optimization problem was introduced to solve for the optimal flight time via Brent's method. This second optimization problem forms an outer loop around the convex optimization problem. The outer loop methodology had been proposed in literature using a line search method; however, results on its success or lack thereof was not documented.

In addition, the newly developed algorithm for designing the trajectory was used to examine the effects of asteroid size and rotation speed on the designed trajectory. Furthermore, important path constraints were formulated to render the problem more meaningful, realistic, and challenging. This included a glide slope constraint that ensures ground clearance and a landing direction constraint to align the final trajectory with the normal direction of the landing site. The glide slope constraint was formulated in previous research for Mars; however, this applied it to an asteroid and fleshed out physical limitations to the application.

1.4 Coordinate System

An asteroid centered fixed Cartesian coordinate system is the main coordinate system used in the optimization problem derivation and subsequent analysis. This coordinate system, depicted in Figure 1.3, is fixed at the asteroid's center of mass. The X axis is aligned with the largest semi-major axis, the Z axis is aligned with the smallest semi-major axis and the Y axis is aligned with the intermediate semi-major axis. For asteroids that are not perfect ellipsoids, the axes are as closely aligned to the semi-major axes as possible, while still keeping an orthogonal coordinate system.

Some models are originally derived in spherical coordinates and then transformed into Cartesian coordinates. For the spherical coordinates, the r is the radius from the center of the asteroid to the spacecraft. The two angles are latitude (δ) measured from the +Z axis to the radius vector and longitude (λ) measured from the +X axis to the projection of the radius in the X-Y plane, as shown in Figure 1.3.

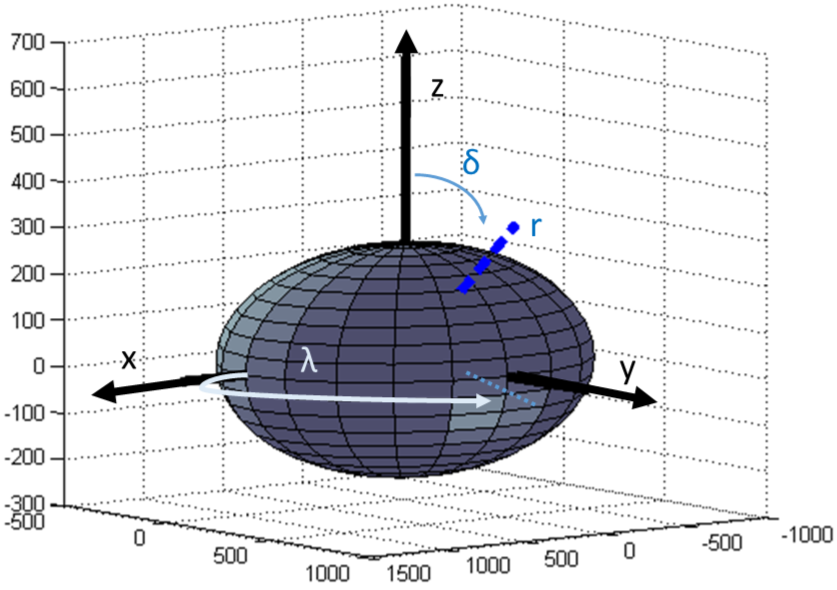

Figure 1.3: Asteroid centered fixed coordinate system used throughout the research.

CHAPTER 2. REVIEW OF LITERATURE

Missions to asteroids and the subsequent descent and landing is a newly studied field. This is seen in the wide range of analysis and available literature, where each author offers a new idea. There are two types of landings commonly analyzed, a full powered descent to the surface and touch-and-go. Touch-and-go is popular for sample return missions, where the vehicle touches down on the surface for a few seconds to retrieve a sample and immediately lifts off. These missions do not use thrusters near the asteroid surface for fear of sample contamination. The full powered descent lands softly on the asteroid after thrusting the entire way to the surface.

There are three missions that have successfully landed on a small body, two on asteroids and one on a comet. In addition, future mission candidates have been analyzed with hopes of selection and flight over the next decade. A brief description of the actual landings and proposed landings is given in Section 2.1. Section 2.2 focuses on the various descent theories that are found in literature in the areas of trajectory design and guidance. All of the approaches have their weaknesses and strengths, with none clearly standing out or being favored. Section 2.3 focuses on the two research sets whose techniques form the background of this research and algorithm development. Neither set was designed for asteroid powered descent trajectories.

2.1 Asteroid Missions

2.1.1 Completed Missions

2.1.1.1 NEAR

The first successful asteroid landing occurred on February 12, 2001 when the Near Earth Asteroid Rendezvous (NEAR) spacecraft descended to the surface of asteroid 433 Eros. NEAR was not designed for descent and landing. After debating options for the spacecraft upon primary mission objectives completion, NASA decided to attempt a controlled descent. The primary goal was to take high resolution pictures during the descent and the secondary was to achieve a soft landing. The ultimate hope was that the vehicle would survive and be able to transmit from the surface. Four braking maneuvers were designed to take place over fifty minutes aimed to slow the vehicle descent to 1.3 m/s upon impact. Each braking burn was designed to achieve a specified change in velocity as measured by the accelerometers. Backup timers were included in case of off-nominal performance. The first braking burn began at a 5 km altitude and slowed the descent rate 6 m/s. Overall, the four burns slowed the vehicle 16 m/s. When NEAR impacted the surface, the change in velocity target had not been reached, causing it to keep burning thus pushing the spacecraft into Eros. The spacecraft came to rest leaning on two of its solar panels. The estimated impact speed was 1.5 - 1.8 m/s. Data was received from the spacecraft from the low gain antenna for two weeks after the descent, proving that the spacecraft did indeed survive the landing. One challenge facing the descent was a 17.5 minute one-way communication delay. (Ref. Dunham et al. (2002))

NEAR spent one year mapping and characterizing the surface of Eros in exquisite detail. The information from this allowed development of high fidelity gravity models, along with answering numerous scientific questions. A large number of analyses use Eros models as they are readily available. Eros is the second largest near-Earth asteroid with a size of 34.4 x 11.2 x 11.2 km, a 5.3 hour rotation period and essentially uniform density. (Ref. Cheng (2002))

2.1.1.2 Hayabusa

The Hayabusa spacecraft (originally named MUSES-C) traveled to the asteroid Itokawa. The plan was to stay at a home point 20 km above the surface performing global mapping and characterization of the entire asteroid for six months. The spacecraft would then descend to 500 m altitude by controlling the vertical velocity. At the 500 m point the final descent phase would begin after a go-nogo poll. Upon reaching 150 m altitude, target markers (reflective surfaces) would be released from the vehicle. The target markers would help the spacecraft determine horizontal errors, while a laser range finder would determine the range measurement below 100 m altitude. The problem would then be treated as rendezvousing with the target markers via closed loop guidance. (Ref. Kubota et al. (2003))

Two attitude control reaction wheels failed prior to the descent operations, which caused the LIDAR (Light Detection and Ranging) to have abnormally large measurement errors. These failures made it impossible for the spacecraft to approach Itokawa as planned autonomously. As a result, the descent phase guidance and navigation operations were redesigned. New simulations were designed on the ground to facilitate guiding and navigating the vehicle from the ground, taking advantage of the extensive surface mapping. The vehicle was driven to a point near the target by the ground in semi-real time as the communication delay was 20 minutes one-way. Upon reaching a point near the target, the vehicle was transferred over to the final descent phase which dropped and then rendezvoused with the target markers. (Ref. Yoshimitsua et al. (2009))

Prior to descent, Hayabusa remained in close proximity to Itokawa for three months, mapping the surface. These results were turned into high fidelity shape models and fully characterized the asteroid. Itokawa is significantly smaller than Eros, on the order of 560 x 300 x 240 m. Since it is not a perfect triaxial ellipsoid, these are the longest dimensions on each axis. The rotation period is 12 hours. A constant density assumption was used to adequately determine the gravity model. (Ref. Scheeres et al. (2006))

2.1.1.3 Rosetta and Philae

Philae, Rosetta's lander, completed a successful landing on the Comet 67P / Churyumov-Gerasimenko (average radius 2 km). Comet outgassing was an additional challenge that the descent trajectory and analysis dealt with on top of the asteroid landing challenges. As the mission has just completed, final data on the actual descent is limited and there were probably small adjustments made to the plans that are discussed below.

Upon arriving at the comet, Rosetta will begin a phase to investigate and characterize the comet nucleus for seven months. The data from this will assist in finalizing the descent trajectory parameters. Rosetta will drop to 1 km altitude prior to Philae separation. The entire landing trajectory is ballistic with the only adjustments being Philae's velocity upon ejection from Rosetta. The planned ejection velocity is 18.7 cm/s, which is the same imparted by the back-up spring. Stabilization during descent is provided by flywheel. The expected velocity upon impact is 1 m/s. Early analysis looked at including one maneuver during the descent trajectory instead of being a purely passive descent. This decreased impact velocity at latitudes smaller than 60 deg. However, this was not the method used for the mission. An active descent system was included on the vehicle, though after final selection of the landing site it was no longer required. (Ref. Ulamec et al. (2004); Bernard et al. (2002); Ulamec and Biele (2009); Ulamec et al. (2015))

2.1.2 Proposed Candidate Missions

There are four missions that have been proposed and studied over the last few years: Marco Polo, Marco Polo-R, OSIRIS-REx (Origins Spectral Interpretation Resource Identification Security Regolith Explorer) and Hayabusa-2. Their proposed descent approaches are discussed here. As time progresses these missions may or may not be selected for continuation or the designs may change. Both Marco Polo and its replacement Marco Polo-R are listed under former candidate missions by the European Space Agency[1], implying that they are defunct.

MASCOT (Marco Polo Surface Scout) is the lander studied as part of the Marco Polo and Hayabusa-2 missions as a lander package. The main spacecraft would lower itself to 100 m altitude where it would release MASCOT. The lander then flies a ballistic trajectory down to the asteroid surface. Upon releasing the lander, the spacecraft returns to an altitude of 700 - 1000 m. The accuracy of reaching the landing site along with the velocity at impact is driven and controlled by the accuracy of the main spacecraft releasing the lander. Analysis of the Hayabusa-2 mission shows an impact velocity of 15 - 19 cm/s and an large impact ellipse of 180 x 240 m. (Ref. Richter et al. (2009); Dietze et al. (2010))

The Marco Polo-R initial GN&C design assessment revealed that the descent and landing phase is the most critical to mission success. The proposed strategy designs the trajectory on the ground. The spacecraft follows this trajectory open loop until 250 m, where it switches to closed loop. Since it is a touch-and-go sample return, the vehicle free falls to the surface from

---

[1] http://sci.esa.int/home/51459-missions accessed 7/2/2015

a 15 m altitude. The analyses were required to keep the horizontal velocity at impact less than 5 cm/s and the vertical velocity less than 10 cm/s. Two of the studies introduced a hover at 250 m altitude, which reduces impact velocities and allows ground control a chance to abort the landing. (Ref. Gherardi et al. (2013))

OSIRIS-REx is a touch-and-go sample return mission planned for the asteroid Bennu. The vehicle has a safe home orbit at 700 m altitude from which a variety of sorties will be completed in order to map and characterize the asteroid. The start of the descent phase begins with a deorbit burn, followed by maneuvers at two waypoints, referred to as checkpoint and matchpoint. Both of these points are designed on the ground ahead of time containing the vehicle position and velocity state. The checkpoint is at 125 m altitude reached 20 minutes before touchdown and the matchpoint is at 55 m altitude 10 minutes before touchdown. As the vehicle approaches the checkpoint it predicts the vehicle state at the checkpoint. Differences in the predicted state and the designed state are used to adjust the checkpoint and matchpoint maneuvers. A 10 cm/s vertical impact velocity is targeted, with the errors required to be less than 2 cm/s in the vertical and horizontal velocities. The vehicle must be within 25 m of the landing site. Communication delay is expected to be on the order of 15 minutes one-way. (Ref. Berry et al. (2013); May et al. (2014))

2.2 Landing Guidance Algorithms Proposed in Literature

A wide range of methodologies for designing the descent trajectory and for guiding the vehicle to the asteroid surface are found in literature. This variety emphasizes that the area of study is new, as there is not one method that is considered standard, challenging, and interesting to analyze. This section features a large sample of the ideas currently being studied. The landing trajectory design is a two point value boundary problem, as the initial state and final state (landing site) are both known. This fact is used extensively in the design of powered descent trajectories.

The first trajectory design approach assumes that the vehicle acceleration profile is a cubic polynomial. With this assumed profile, the equations of motion, and the boundary points, the majority of the parameters can be solved for analytically. The problem is then reduced to a nonlinear optimization problem of three parameters (time of flight, initial thrust magnitude and initial thrust angle). These combined with any remaining constraints are solved with a modified compass search algorithm. The gravity model is assumed to be the 2x2 triaxial ellipsoid; however, it is suggested that other gravity models could be paired with this method. The computation time is small which is advantageous for loading onto the spacecraft. The main drawback to this method is the assumption of the acceleration profile shape, as this does not allow for the optimal bang-bang thrust profile. (Ref. Lunghi et al. (2015))

A second approach is an early study performed by the authors of the JPL study in Section 2.3.1. This focused on designing pseudo waypoints which could either be used as a reference trajectory or as part of a model predictive control guidance and control algorithm. The gravity model was linearized, in the traditional sense, around a reference trajectory. The dynamical equations used the linearized gravity model, along with pulsed thrusters at a constant thrust level, to form a linear system that was discretized (˜30 sec intervals) into a second order cone program. The optimization problem used a cost function involving minimum energy or minimum fuel, depending on the problem settings, to determine the waypoints and the corresponding feedfoward control. The second order cone program is repeated after updating the dynamics, especially the linearization about the new trajectory, until the control and state represent a feasible solution to the dynamical problem. These waypoints are not the traditional waypoints as they account for gravity and yield valid solutions to the dynamics. (Ref. Carson and Acikmese (2006))

A third approach in literature focuses on the problem as formulated by Optimal Control Theory. For this study, a combination of a direct method which optimizes the cost function and an indirect method which integrates the costate equations and solves them with the boundary conditions is used. The direct method is robust but computationally intensive, whereas the indirect method is fast computationally, yet very sensitive to initial conditions. By combining these two methods, the robustness remains while the computational time difference between the direct and the combined method decreases drastically as the number of evaluated trajectory points increases. The gravity model is the spherical harmonics model which transitions to the polyhedron model near the Brillouin sphere. One interesting result of this study is the cost function sensitivity. Two versions of the cost function were formulated, a minimum time problem and a minimum fuel problem. The minimum fuel problem was significantly less sensitive to applied disturbances. (Ref. Lantoine and Braun (2007))

A closed loop approach loads the latitude, longitude, and altitude of the landing site onto the vehicle and nulls out the difference between the current spacecraft position and the targeted position. As the spacecraft descends, there are waypoints or gates that it targets in the same manner and must reach before moving on to the next gate and ultimately the landing site. Each waypoint is represented in terms of latitude, longitude, altitude, and descent velocity. The paper's example used a waypoint at 300 m and 200 m altitude prior to targeting the landing site. The acceleration profile is based on zeroing out the errors (differences). Prior to starting this closed loop guidance around 500 m altitude, a lookup table consisting of position and velocity vectors at predetermined times is used to guide the spacecraft. The closed loop acceleration profile also removes errors accumulated in the open loop phase. The waypoints and the lookup table are designed on the ground and uploaded into the vehicle prior to landing initialization. This algorithm uses the spherical harmonics gravity model and switches to the polyhedron method, with a proposal to use the polyhedron method onboard. In-depth analysis shows that uncertainties in the vehicle's velocity knowledge overwhelm the other disturbances that were investigated. (Ref. Kaidy et al. (2010))

Variations on sliding mode control theory have been adapted into guidance laws for the asteroid powered descent problem. From a stability and controllability point of view sliding mode control is a robust and stable control law in the face of disturbances; however, there is a significant amount of switching or chattering (high frequency oscillations) in the solution. One method is to use multiple sliding surfaces to drive the spacecraft to the landing site. This does not use a predefined trajectory. The dynamics of the problem are included in the definition of the sliding surfaces. Incorporating advances in the area of high-order sliding control helped alleviate the chatter. The acceleration profiles did well with no observed chattering. Observations from this analysis showed performance sensitivity to tuning the gains and parameters. Underestimating the flight time had an adverse effect on fuel consumption, thus the problem achieved better success when using longer flight times. (Ref. Furfaro et al. (2013)) A different approach to sliding mode control was to design the trajectory and then apply a sliding mode control surface in each direction to reduce errors in the system from disturbances. A saturation function was used in place of the sign function in the sliding mode control formulation to alleviate the chattering problem. This approach tracked the trajectory well, including the bang-bang thrust profile from the designed trajectory. (Ref. Yang et al. (2013)). A variation on this approach is to use a nonsingular terminal sliding mode approach on a predesigned trajectory in order to track the trajectory. The results showed decreased oscillations as compared to the standard sliding mode control approach. (Ref. Lan et al. (2014))

Two of the sliding mode control approaches used predesigned trajectories. One approach used a homotopic method along with successive solutions to solve the two point boundary problem. The original differential equations and co-state differential equations from Optimal Control Theory are solved via shoot-out methods. Since this may run into difficulties when solving the problem, a variable was introduced to modify and relax the problem. The value of this variable starts at 1 and decreases to 0 where it becomes the original problem. When it is 1 the problem is easier to solve, and the solution of that problem becomes the starting point of the next iteration. This solved the problem effectively. (Ref. Yang et al. (2013)) The second study assumed the acceleration profile was a cubic polynomial and solved the two point boundary problem with that assumption. (Ref. Lan et al. (2014))

An additional method involving polynomials assumes that the position profile is a cubic polynomial. Three polynomials, one for each unit direction, are constructed and the coefficients are determined based on the boundary conditions and a fixed flight time. The velocity profiles are the corresponding derivatives of the position polynomials. A proportional plus derivative guidance control law is used to track the designed trajectory, both the position and velocity components. The thrust was pulsed which led to oscillations in the velocity profile. The gravity model assumed a 4x4 spherical harmonics model for a triaxial ellipsoid. (Ref. Shuang et al. (2006))

A closed loop approach involving ZEM/ZEV (zero effort miss, zero effort velocity), while adapting the OSIRIS-REx two waypoint strategy was developed. Using the ZEM/ZEV algorithms the vehicle was actively guided to the two waypoints. The second waypoint is at an altitude of 30 m, with a coast trajectory from this point down to a soft landing on the surface, in order to avoid surface contamination from the vehicle's thrusters. The ZEM/ZEV drives the position and velocity vectors to the targeted position and velocity vectors. Due to the feedback involved, ZEM/ZEV can alleviate initial state errors along with other disturbances significantly better than flying open loop to the waypoints. Closed loop relies on vehicle state estimation from the various sensors onboard the vehicle. This method proposes a 0.1 HZ state estimation rate in order to have adequate time for calculations and measurements. A 1500 second hover was introduced at the 30 m waypoint followed by a 30 second burn. This hover counteracts the effects of velocity errors and the low frequency of the state estimation updates. The thrust is pulsed and assumed to be full thrust in the positive or negative directions on the axes or zero. The analysis assumed the asteroid was a 350 x 287 x 250 m constant density triaxial ellipsoid. (Ref. Gaudet and Furfaro (2013))

Another approach involving ground designed waypoints, assigns each waypoint a specific time and descent rate. Guidance computes the thrust profile to reach the next waypoint at the designated time. The trajectory between the current spacecraft point and the waypoint is discretized, so that each segment is linear time invariant creating a piecewise linear time invariant dynamical system that can be easily integrated. The gravity model is also linearized. The discretized system is turned into a constrained optimization problem that minimizes the total acceleration magnitude. The problem is first solved with impulsive thrust, in order to produce an initial starting point for the optimization problem. (Ref. Gil-Fernadez and Graziano (2010))

An early predecessor to the Hayabusa mission proposed the use of proportional guidance to softly land on an asteroid. The thrust direction is proportional to the line of sight rate. This line of sight rate is combined into an aligned intercept scheme. The aligned intercept drove the angle between the line of sight and the prescribed approach direction to zero. This scheme guaranteed an intercept with the velocity vector vertical upon touchdown. Also included in the GN&C proposal was a descent rate control, to ensure that the vehicle decreased the velocity to 0.1 m/s upon landing. (Ref. Kawaguchi et al. (1997))

2.3 Foundational Background

Two sets of research created the foundation of this research by demonstrating techniques and methodologies that could be applied to the asteroid powered descent problem. Neither of these sets designed trajectories that land on asteroids. The first set of papers comes from extensive research done by the Jet Propulsion Laboratory (JPL) over the last decade focusing on Mars powered descent trajectories. The second set of research was completed at Iowa State University (ISU) over the last few years and focused on rendezvous and proximity trajectories.

2.3.1 Research at Jet Propulsion Laboratory

Over the last decade researchers from the Jet Propulsion Laboratory (JPL) have published several papers discussing powered descent landing on Mars using convex optimization. The first paper in the series discusses in detail how to turn the nonlinear powered descent problem into a second order cone program (SOCP), which can be solved in polynomial time, thus bounding the algorithm computation time. A primal dual interior point method was chosen to solve the problem.

The researchers convert the nonlinear powered descent problem into a series of problem formulations. First, the problem is relaxed with a slack variable. By applying Optimal Control Theory and the Maximum Principle, the researchers proved that the relaxed problem is equivalent to the original problem. As part of this proof, it was shown that the magnitude of the thrust will always be on its maximum or minimum bound. Next a change of variables is applied, along with a Taylor series expansion, to convexify the thrust magnitude constraints. For the vehicle and trajectories that were analyzed, less than a 2% difference occurred when approximating the mass with the Taylor series expansion. Since the analysis was focused on Mars, a constant gravity field was applied and the rotation of Mars was not taken into account. These are valid assumptions for close proximity operations around Mars. However, these will need to be accounted for when working with asteroids. The glide slope constraint was included in the optimization problem, actually required, otherwise the trajectory went below the Martian surface. (Ref. Acikmese and Ploen (2007))

A set of basis functions was used to integrate the continuous equations of motion between discrete nodes when discretizing the system. The choice of functions and discretization method led to a cubic polynomial for the position vector between nodes. The focus on this paper was the minimum fuel problem for a fixed flight time. Propellant usage as a function of flight time was shown to be unimodal (one minimum point), which led to an outer loop optimization that finds the optimal flight time via the golden search method. Rotation effects were briefly considered and lumped with the gravity terms as a piecewise function. Excluding the rotation effects caused landing site errors on the order 30 - 40 m from the targeted landing site. (Ref. Acikmese and Ploen (2007); Acikmese et al. (2008))

Continuing with the convexification investigation, the authors completed an in-depth study of vehicle pointing constraints levied as thrust pointing constraints. Approaching the problem from a different point of view, they were able to successfully prove that lossless convexification occurs when the thrust constraints are included in the problem. For this proof vehicle controllability was required, which is reasonable as most vehicles are controllable. (Ref. Acikmese et al. (2013))

A comparison study was performed with three other guidance laws. These laws are the Apollo guidance, a modified version of the Apollo guidance and a third order polynomial. The Apollo landing guidance assumed a fixed time descent and a quadratic acceleration profile. This created a deterministic system that could be solved. The modified Apollo guidance turned the problem into a free final time problem. A line search was used to determine the flight time that yields minimum energy. The third order polynomial increased the acceleration polynomial to a cubic to create an underdetermined system. The descent problem for this law turns out to be a weighted norm problem, which has an analytical solution. Again, a line search was used to find the optimal flight time. These three algorithms are computationally less expensive than the convex optimization powered descent algorithm. A disadvantage is that they do not take into account constraints on the problem such as thrust constraints, glide slope and subsurface flight. These constraints limit the range of starting conditions that yield a valid trajectory. Fortunately, the convex optimization powered descent algorithm accounts for these constraints as part of the problem. Comparing the span of valid initial downrange and altitude starting points showed that the convex optimization method had the largest envelope of valid starting conditions. It is a significant improvement over the other three guidance methods. The original Apollo algorithm had the smallest envelope, followed by the modified Apollo and then the cubic polynomial had the second largest. As a result, this study showed that it is worth the complexity to consider the convex optimization method. (Ref. Ploen et al. (2006))

For the rare case when the vehicle does not have enough propellant to reach the landing site, a technique was developed to find the trajectory that minimizes the error to the landing site. Two convex optimization problems are solved in succession, the first to determine where the vehicle will land by minimizing the distance to the targeted landing site. The second convex optimization problem uses this new landing site to design the minimum propellant trajectory. The second convex optimization problem is necessary, because the relaxation employed in the first convex optimization problem does not guarantee the optimal solution to the non-relaxed minimum landing error problem. This second convex optimization problem is the same relaxed problem that was first investigated, just using a different landing site. (Ref. Blackmore et al. (2010))

2.3.2 Research at Iowa State University

A second set of research performed at Iowa State University (ISU) focused on trajectory planning for rendezvous and proximity operations and yielded techniques that were applicable to powered descent trajectory design. An optimization problem was set up with the goal of minimizing the total thrust magnitude which is proportional to minimum propellant consumed, so this is a minimum fuel problem. In a rendezvous and proximity operations trajectory, the main spacecraft flies to and then approaches the target vehicle. The target vehicle trajectory is deterministic, as the vehicle is in a known orbit and non-propulsive during the mission. As the target is in motion, this is no longer a two point value boundary problem. The end conditions require the difference between the two vehicles to be zero. The main vehicle dynamical equations, formulated in an inertial coordinate system, include a Newtonian gravity model and vehicle thrust. The goal was to formulate a second order cone program (SOCP) that can be solved to generate the trajectory.

The problem constraints are different from that of a powered descent trajectory. There is an upper bound on the thrust, but no lower bound. The trajectory design includes determining the number of burn and coast arcs, in addition to their placement and length. The optimization problem determines this automatically by allowing the thrust to be zero. There is an approach cone around the docking axis once the vehicles are within 200 meters of one another. Also, a thrust plume constraint is applied to avoid plume impingement on the target vehicle. These two constraints are similar to the glide slope and thrust pointing constraints in the landing problem.

As in the JPL analysis, the problem is relaxed by the introduction of a slack variable. Theoretical equivalence of the relaxed problem and the original problem was proved. The equivalence proof included the case when the state constraints are active for a finite time period. This is significant, as the JPL study assumed that the constraints were active for at most an instant. A change of variables was required to turn the problem into a SOCP.

The Newtonian gravity field is a higher fidelity model than the constant gravity field used in the JPL analysis. It is nonlinear as $\vec{g} = -\frac{\mu}{\|\vec{r}\|^3}\vec{r}$, which is handled through a successive solution method. A series of SOCPs are solved using the trajectory from the previous solution to evaluate the nonlinear terms. This forms linear continuous equations of motion for the current iteration. The equations of motion are discretized and propagated using the trapezoidal rule. While theoretical proof of convergence of the SOCP iterations was not obtained, in-depth analysis showed good convergence. A short discussion of formulating drag and J2 effects for inclusion into the equations of motion and the successive solutions was included. However, this was not included in the results and analysis. (Ref. Lu and Liu (2013))

Continuation of the research led to methodologies for handling concave inequality constraints and nonlinear terminal constraints. After applying these new techniques, these constraints were included in the successive solution process with great success. Three different types of problems were solved showing robustness and applicability of the successive solution method. The first problem was the rendezvous and proximity operations, though now with keepout zones included. The second problem was an orbital transfer, with the third application being the upper stage flight of an ascent trajectory. Another item of note, some of the optimization problems that were successfully solved with these methods could not be solved using other optimization methods. (Ref. Liu and Lu (2014))

CHAPTER 3. GRAVITATIONAL POTENTIAL AND GRAVITATIONAL ACCELERATION

Asteroids come in a wide variety of sizes and shapes, which are rarely spherical. Therefore, the standard gravity models of constant gravity and Newtonian gravity that are used as good approximations in powered descent algorithms on Earth, Moon, and Mars are poor models for an asteroid powered descent mission. The best way to model the gravitational potential for an asteroid is still a hotly researched topic with a wide range of models under study and new papers being published on a regular basis.

A good starting model is the 2x2 spherical harmonics model for a homogenous triaxial ellipsoid. From Scheeres, “It has also been found in previous studies that the second degree and order gravity field accounts for the majority of the perturbations on the dynamical system, and thus this model can be taken as a simple stand-in for a more general system.” (p. 45, Ref. Scheeres (2012)) The 2x2 model will be used for characterizing and developing the algorithms.

Following the 2x2 model description, there will be a discussion on the limitations of that model along with a brief review of available models. Finally, a higher fidelity model will be presented for use in the powered descent algorithm that is suitable for use on the spacecraft.

3.1 2x2 Spherical Harmonics Gravity Model for a Triaxial Ellipsoid

The standard spherical harmonics gravitational potential model is given in Equation 3.1. It is a readily available model and can be found in a variety of textbooks including Vallado. (Ref. Vallado (2013)) This model is commonly used for modeling Earth's gravity when high fidelity is needed.

$$U = \frac{\mu}{r}\sum_{l=0}^{\infty}\sum_{m=0}^{l}\left(\frac{r_0}{r}\right)^l P_{l,m}\left[\sin\delta\right]\left\{C_{l,m}\cos\left(m\lambda\right) + S_{l,m}\sin\left(m\lambda\right)\right\} \tag{3.1}$$

The gravitational potential (U) for a spacecraft is based on the distance from the gravitational body's center of mass to the spacecraft or radius (r), as well as the latitude (δ) and the longitude (λ) of the spacecraft. The coefficients $C_{l,m}$ and $S_{l,m}$ are unique to the body under investigation, aka the planet, moon, or asteroid of interest. These coefficients can be determined in a number of ways. The reference radius (r_0) is associated with the body and the determination of the coefficients. It is typically taken to be the maximum radius of the body or the Brillouin sphere radius. The gravitational constant (μ) is also unique to the body of interest. $P_{l,m}$ is the associated Legendre function, which is found in a variety of textbooks. The summing coefficient l is referred to as order and m as the degree. While the potential function is an infinite sum, the summation can be truncated and still yield reasonable accuracy. The desired accuracy dictates the order and degree of the model.

A good initial model for an asteroid is to use a 2x2 model and assume a perfect triaxial asteroid with constant density. The potential expression for a 2x2 model, which has a maximum order and degree of 2, is located in Equation 3.2.

$$U = \frac{\mu}{r}\sum_{l=0}^{2}\sum_{m=0}^{l}\left(\frac{r_0}{r}\right)^l P_{l,m}\left[\sin\delta\right]\left\{C_{l,m}\cos\left(m\lambda\right) + S_{l,m}\sin\left(m\lambda\right)\right\} \tag{3.2}$$

By placing the coordinate system's origin at the asteroid's center of mass, the coefficients $C_{1,1}$, $S_{1,1}$ and $C_{1,0}$ are all zero. They would only be nonzero if the center of mass and origin are not co-located. Assuming that the ellipse is homogenous in density and symmetric causes the only nonzero coefficients to be the $C_{l,m}$ coefficients that have an even l and m. For the 2x2 model only $C_{0,0}$, $C_{2,0}$ and $C_{2,2}$ are nonzero. By definition $C_{0,0} = 1$. The associated Legendre functions that will be used in this model are listed in Equation 3.3.

$$\begin{aligned} P_{0,0}\left[\sin\delta\right] &= 1 \\ P_{2,0}\left[\sin\delta\right] &= \tfrac{3}{2}\sin^2\delta - \tfrac{1}{2} \\ P_{2,2}\left[\sin\delta\right] &= 3\cos^2\delta \end{aligned} \tag{3.3}$$

Substituting in all the terms, the gravitational potential for a triaxial ellipsoid with the origin located at the center of mass is given in Equation 3.4.

$$U = \frac{\mu}{r}\left\{1 + \left(\frac{r_0}{r}\right)^2 \left[C_{2,0}\left(\frac{3}{2}\sin^2\delta - \frac{1}{2}\right) + C_{2,2}\left(3\cos^2\delta\right)\cos\left(2\lambda\right)\right]\right\} \tag{3.4}$$

Now that the gravitational potential has been determined, the gravitational acceleration can be calculated. Gravitational acceleration is the gradient of the gravitational potential with respect to the position vector in the Cartesian coordinate system. The chain rule is applied, finding the partial of the potential with respect to the position vector in spherical coordinates (r, δ, λ) and then multiplying by the partial of the position vector in polar coordinates with respect to the position vector in Cartesian coordinates (r_x, r_y, r_z). The conversion between the vehicle position in spherical coordinates and the Cartesian position vector is located in Equation 3.5.

$$\begin{aligned} r &= \left(r_x^2 + r_y^2 + r_z^2\right)^{\frac{1}{2}} \\ \delta &= \sin^{-1}\left(\tfrac{r_z}{r}\right) \\ \lambda &= \tan^{-1}\left(\tfrac{r_y}{r_x}\right) \end{aligned} \tag{3.5}$$

The acceleration due to gravity in the Cartesian coordinate system is given in Equation 3.6.

$$\begin{aligned} \frac{\partial U}{\partial r_x} &= -\frac{\mu}{r^3} r_x + -\frac{\mu}{r^3}\left(G_1 r_x + G_2 \frac{r_x r_z}{\left(r_x^2 + r_y^2\right)^{0.5}}\right) + \frac{\mu}{r} G_3 r_y \\ \frac{\partial U}{\partial r_y} &= -\frac{\mu}{r^3} r_y + -\frac{\mu}{r^3}\left(G_1 r_y + G_2 \frac{r_y r_z}{\left(r_x^2 + r_y^2\right)^{0.5}}\right) - \frac{\mu}{r} G_3 r_x \\ \frac{\partial U}{\partial r_z} &= -\frac{\mu}{r^3} r_z + -\frac{\mu}{r^3}\left(G_1 r_z + G_2 \frac{r_z^2}{\left(r_x^2 + r_y^2\right)^{0.5}}\right) + \frac{\mu}{r} \frac{G_2}{\left(r_x^2 + r_y^2\right)^{0.5}} \end{aligned} \tag{3.6}$$

The terms G_1, G_2, and G_3 are for convenience. These are groupings of terms that are used repeatedly and are listed in Equation 3.7.

$$\begin{aligned} G_1 &= \frac{r_0^2}{r^2}\left\{3C_{2,0}\left[1.5\sin^2\left(\delta\right) - 0.5\right] + 9C_{2,2}\cos\left(\delta\right)\cos\left(2\lambda\right)\right\} \\ G_2 &= \frac{r_0^2}{r^2}\left\{1.5C_{2,0}\sin\left(2\delta\right) - 3C_{2,2}\sin\left(2\delta\right)\cos\left(2\lambda\right)\right\} \\ G_3 &= \frac{r_0^2}{r^2}\left\{\frac{1}{r_x^2 + r_y^2} 6C_{2,2}\cos^2\left(\delta\right)\sin\left(2\lambda\right)\right\} \end{aligned} \tag{3.7}$$

The gravitational acceleration vector is highly nonlinear and nonconvex in terms of the spacecraft position vector. When $C_{2,0}$ and $C_{2,2}$ are zero, Equation 3.6 becomes the standard Newtonian definition of acceleration, Equation 3.8.

$$\frac{\partial U}{\partial \vec{r}} = -\frac{\mu}{r^3}\vec{r} \tag{3.8}$$

3.1.1 Homogeneous Triaxial Coefficients

Gravitational coefficients $C_{l,m}$ and $S_{l,m}$ can be calculated based on the asteroid's shape and density or estimated through measurements. More commonly, a high fidelity shape model is developed from observations and measurements. Combining the shape model and the assumption of uniform (homogeneous) density, the coefficients can be determined.

The triaxial ellipsoid symmetry allows analytical expressions for the coefficients based solely on the lengths of the three semi-major axes. This allows for a reasonable gravity model, if the coefficients cannot be obtained through other methods. The nonzero coefficients for a 2x2 homogenous triaxial asteroid are located in Equations 3.9 and 3.10.

$$C_{2,0}\, r_0^2 = \frac{1}{5}\left(\gamma^2 - \frac{\alpha^2+\beta^2}{2}\right) \tag{3.9}$$

$$C_{2,2}\, r_0^2 = \frac{1}{20}\left(\alpha^2 - \beta^2\right) \tag{3.10}$$

The longest asteroid semi-major axis length is represented by α, the intermediate length by β and the smallest length by γ. This form of the coefficients does not require the reference radius to be determined as it will replace both the $C_{l,m}$ and r_0^2 terms in the gravitational acceleration equations. (Ref. Scheeres (2012))

3.1.2 Triaxial Ellipsoid Limitations

The 2x2 spherical harmonics gravitational model formulated for a perfect triaxial homogeneous asteroid contained several assumptions. First, the coefficients were designed assuming symmetric mass distribution in the shape of an ellipsoid. Second, the coordinate system was fixed exactly at the center of mass and each axis was perfectly aligned with the principal moments of inertia. These assumptions can be removed by including all the coefficients in the gravitational expansion and calculating the coefficients based on shape models.

However, there is an underlying implicit assumption in the spherical harmonics expansion. It assumes that the mathematical series representing the gravitational field converges to the actual gravitational field. If the point where the field is evaluated is outside the maximum radius of mass distribution for the asteroid this assumption is valid, but when a point is evaluated inside the maximum radius of mass distribution the mathematical series diverges from the true gravitational field. The sphere circumscribing the asteroid mass is called the Brillouin sphere. An example of the Brillouin sphere with an irregularly shaped asteroid is shown in Figure 3.1. The spherical harmonics potential model is valid outside of the Brillouin sphere, thus it is referred to as an exterior gravity model. Inside the Brillouin sphere a different model must be used. The more irregularly shaped the asteroid, or the deeper the valleys near the landing site, the worse the divergence. An ellipsoid with an eccentricity less than $1/\sqrt{2}$ will not see divergence inside the Brillouin sphere and can use the spherical harmonics model down to the surface. (Ref. Takahashi et al. (2013); Scheeres (2012))

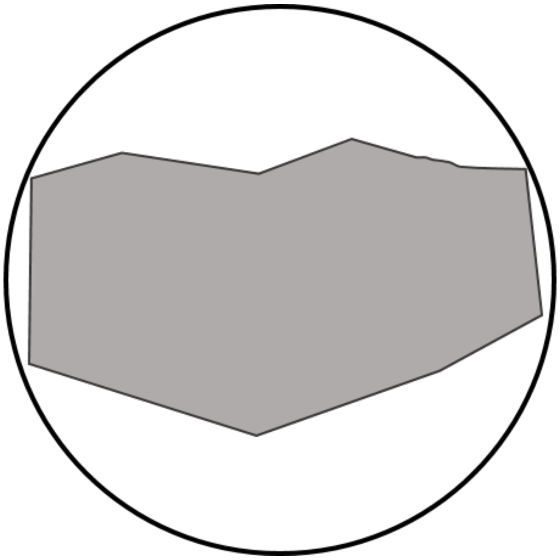

Figure 3.1: Brillouin sphere surrounding an irregularly shaped asteroid.

3.2 Higher Fidelity Gravity Models

The 2x2 spherical harmonics model assuming a triaxial ellipsoid is a good model for testing algorithms and determining trends. Nonetheless, a large number of asteroids have valleys that are of interest for landing, cannot align the axes perfectly with the semi-major axes, or are irregularly shaped. A common class of asteroids that are irregularly shaped are binary asteroids. These asteroids are dumbbell shape, or two small asteroids so close together that their gravity fields interact.

For the asteroids that are not nearly spherical, a higher fidelity gravity model will be needed both outside the Brillouin sphere and inside. The high fidelity model that will be used in the asteroid powered descent formulation will be the 4x4 spherical harmonics gravitational model outside the Brillouin sphere and the interior spherical Bessel model inside the Brillouin sphere and at the Brillouin sphere boundary. This combined model will be referred to as 4x4 Bessel.

3.2.1 Alternative Gravity Models

A wide range of gravitational models pertaining to asteroids have been published over the last few decades, with new ones appearing every couple of years. Some of the more widely recognized models are the homogeneous polyhedron (Ref. Werner (1994); Werner and Scheeres (1997)), mascon model (briefly discussed in Ref. Scheeres (2012); Werner and Scheeres (1997); Werner (2010)) and several interior models (Ref. Takahashi and Scheeres (2014); Werner (2010); Takahashi et al. (2013)).

The mascon model fills the asteroid shape with point masses, each with its own distinct mass to represent the true mass and gravity field. The advantage is the elimination of divergence in the mathematical closed form model. The disadvantages are trying to determine how to fill the shape with the point masses and the accuracy is poor near the surface of the asteroid. Far from the surface it is less accurate than the spherical harmonics expansion. In order to increase the accuracy, the number of point masses included in the model must increase into the thousands, which becomes computationally expensive. (Ref. Scheeres (2012); Werner and Scheeres (1997); Werner (2010))

The polyhedron method is considered to be the most accurate asteroid gravity model and is used as the benchmark for comparing new gravity models to determine their accuracy. In this model the entire shape of the asteroid is mapped as a series of triangles covering the entire surface, detailing ridges, valleys, and any possible topographical feature. The more triangles used, the more accurate the model becomes. The number of triangles is normally on the order of thousands. As an example, the binary asteroid Castalia used 3300 triangle faces in its model. Calculations sum over every triangle face and edge connecting the faces over the entire asteroid to determine the acceleration at one point. This is a very computationally expensive proposition for an entire trajectory. This model can be used on the ground with fast computers and plenty of time to design the trajectory, but is not suitable for a flight computer and the need for rapid trajectory design. Therefore, it is not a candidate for the autonomous powered descent trajectory design. Another feature of the polyhedron method is that it can be used to determine the coefficients for the spherical harmonics gravity model and the interior gravity models. (Ref. Werner (1994); Werner and Scheeres (1997))

An interior gravity model is any model that exists only inside a predetermined sphere. The interior model seen in Ref. Werner (2010); Takahashi et al. (2013) is a type of spherical harmonics expansion that is valid inside a sphere. This sphere touches the asteroid at a single point, on its boundary. This means the sphere and its corresponding coefficients are only valid in a small area surrounding the site. In order to cover multiple landing sites, multiple sets of coefficients would need to be loaded onto the vehicle and a switch between coefficients would be required if the spacecraft diverged from the original sphere.

Another interior model is the interior spherical Bessel gravity model published in Ref. Takahashi and Scheeres (2014). This model is valid in the interior of the Brillouin sphere down to the surface of the asteroid including all the peaks and valleys. This model relies on associated Legendre functions and spherical Bessel functions to formulate a summation series. The summation is over power, degree, and order and can be truncated similarly to the spherical harmonics model. The similarities between the spherical harmonics and the spherical Bessel is one reason why this model was chosen as the gravity model inside the Brillouin sphere. Unlike other interior models, this is valid for the entire surface of the asteroid without requiring new coefficients for different landing sites.

The spherical Bessel model is a very accurate model as compared to other asteroid gravity models, bar the polyhedron model. The polyhedron model was considered truth in the following analysis. The interior spherical Bessel performed within 10% of truth for Bennu, a near spherical asteroid, and 30% for Castalia, an elongated binary asteroid, when the coefficients were analytically converted from the spherical harmonics coefficients. While 30% may appear large, it is significantly smaller than the errors at the surface when using exterior models which are over 100%. A second approach to determining the coefficients involves a least squares fit to the polyhedron gravity model in order to find the optimal coefficients. Bennu error was less than 5%, while Castalia decreased to less than a 10% error. With a good polyhedron model and effort, coefficients can be derived to produce a highly accurate spherical Bessel model. This can be time consuming due to the large number of computations, though it only has to be calculated once per asteroid. This type of accuracy cannot be achieved with the exterior models. Since the spherical Bessel model is significantly less computationally complex than the polyhedron, it makes a good candidate for use onboard the spacecraft given that it can achieve similar accuracy to the polyhedron model.

The final high fidelity model, that will be used in the optimal powered descent algorithm, is a 4x4 spherical harmonics expansion outside the Brillouin sphere and the spherical Bessel model at the Brillouin sphere and inside the sphere. When the coefficients for both models are derived together from the corresponding polyhedron model, there will be a seamless transition in the values between the two models. However, in the case where the coefficients are not derived from the same source the descent algorithm works fine with a small discontinuity in the gravitational acceleration at the Brillouin sphere as the equations of motion are discretized.

3.2.2 4x4 Spherical Harmonics Gravity Model

The farther the spacecraft is from the asteroid surface the more accurate the gravitational spherical harmonics model is. When the spacecraft is outside the Brillouin sphere, the 4x4 spherical harmonics gravity model is accurate and for near spherical asteroids the model is adequate down to the surface. The more irregularly shaped the asteroid, the less accuracy inside the Brillouin sphere. A full 4x4 expansion was chosen for the high order model as opposed to the 2x2 model to increase the accuracy for irregularly shaped asteroids outside the Brillouin sphere. For this 4x4 model all the gravitational coefficients are included, thus removing assumptions of the coordinate axes located at the center of mass, alignment of the axes with the semi-major axes and assumptions of symmetry.

The equations of the spherical harmonics gravitational potential is located in Equation 3.1. For the 4x4 model, the summation goes to 4 instead of the ∞. The gravitational acceleration for the 4x4 model, which is the gradient of the gravitational potential model, is calculated using the chain rule, seen in Equations 3.11 through 3.13.

$$\frac{\partial U}{\partial r_x} = \frac{\partial U}{\partial r}\frac{\partial r}{\partial x} + \frac{\partial U}{\partial \delta}\frac{\partial \delta}{\partial x} + \frac{\partial U}{\partial \lambda}\frac{\partial \lambda}{\partial x} \tag{3.11}$$

$$\frac{\partial U}{\partial r_y} = \frac{\partial U}{\partial r}\frac{\partial r}{\partial y} + \frac{\partial U}{\partial \delta}\frac{\partial \delta}{\partial y} + \frac{\partial U}{\partial \lambda}\frac{\partial \lambda}{\partial y} \tag{3.12}$$

$$\frac{\partial U}{\partial r_z} = \frac{\partial U}{\partial r}\frac{\partial r}{\partial z} + \frac{\partial U}{\partial \delta}\frac{\partial \delta}{\partial z} + \frac{\partial U}{\partial \lambda}\frac{\partial \lambda}{\partial z} \tag{3.13}$$

The position vector in terms of the Cartesian coordinates are represented by x, y, z and in terms of the spherical coordinates by r, $\delta\,\lambda$. The definitions of the spherical coordinates in terms of the Cartesian are located in Equation 3.5. The partials of the spherical coordinates with respect to the Cartesian coordinates are located in Equations 3.14 through 3.22.

$$\frac{\partial r}{\partial x} = \frac{r_x}{r} \tag{3.14}$$

$$\frac{\partial r}{\partial y} = \frac{r_y}{r} \tag{3.15}$$

$$\frac{\partial r}{\partial z} = \frac{r_z}{r} \tag{3.16}$$

$$\frac{\partial \delta}{\partial x} = \frac{-r_x r_z}{r^2\sqrt{r_x^2 + r_y^2}} \tag{3.17}$$

$$\frac{\partial \delta}{\partial y} = \frac{-r_y r_z}{r^2\sqrt{r_x^2 + r_y^2}} \tag{3.18}$$

$$\frac{\partial \delta}{\partial z} = \frac{1}{\sqrt{r_x^2 + r_y^2}}\left(1 - \frac{r_z^2}{r^2}\right) \tag{3.19}$$

$$\frac{\partial \lambda}{\partial x} = \frac{-r_y}{r_x^2 + r_y^2} \tag{3.20}$$

$$\frac{\partial \lambda}{\partial x} = \frac{r_x}{r_x^2 + r_y^2} \tag{3.21}$$

$$\frac{\partial \lambda}{\partial z} = 0 \tag{3.22}$$

The magnitude of the radius from the center of the asteroid to the vehicle is represented by r, while the Cartesian components of the position vector are denoted by the subscripts.

The partial of the gravitational potential with respect to the spherical coordinate system is where the gravitational coefficients and the summation expansion occur, as seen in Equations 3.23 to 3.25.

$$\frac{\partial U}{\partial r} = \sum_{l=0}^{4}\sum_{m=0}^{l} -(l+1)\frac{\mu}{r^2}\left(\frac{r_0}{r}\right)^l P_{l,m}\left[\sin\delta\right]\left\{C_{l,m}\cos\left(m\lambda\right)+S_{l,m}\sin\left(m\lambda\right)\right\} \tag{3.23}$$

$$\frac{\partial U}{\partial \delta} = \sum_{l=0}^{4}\sum_{m=0}^{l} \frac{\mu}{r}\left(\frac{r_0}{r}\right)^l \left\{C_{l,m}\cos\left(m\lambda\right)+S_{l,m}\sin\left(m\lambda\right)\right\}\frac{\partial P_{l,m}\left[\sin\delta\right]}{\partial\delta} \tag{3.24}$$

$$\frac{\partial U}{\partial \lambda} = \sum_{l=0}^{4}\sum_{m=0}^{l} \frac{\mu}{r}\left(\frac{r_0}{r}\right)^l mP_{l,m}\left[\sin\delta\right]\left\{-C_{l,m}\sin\left(m\lambda\right)+S_{l,m}\cos\left(m\lambda\right)\right\} \tag{3.25}$$

The gravitational coefficients $C_{l,m}$ and $S_{l,m}$ are specific to the asteroid under investigation and are tied to the reference radius r_0. This r_0 tends to be the radius of the Brillouin sphere, especially when switching models at the Brillouin sphere boundary. The coefficients used in Equations 3.23 to 3.25 are nondimensionalized by r_0 and not normalized. The associated Legendre functions are represented by $P_{l,m}\left[\sin\delta\right]$, and their associated partials with respect to latitude are represented by $\frac{\partial P_{l,m}[\sin\delta]}{\partial\delta}$. The associated Legendre functions can never have a $m > l$. For summations where this occurs, the value of the function is zero. The equations for the associated Legendre functions and their derivatives are located in Table 3.1. The 4x4 spherical harmonics gravity model uses through index 4,4. The indices with $l = 5$ are for the spherical Bessel gravity model (next subsection) which does not use the corresponding derivative, thus their absence in the table.

3.2.3 Interior Spherical Bessel Gravitational Model

The original equations for the interior spherical Bessel gravity model were published in Ref. Takahashi and Scheeres (2014). The equations have been rearranged and rewritten in this section to clarify the equations and formulate them in a programmable manner. The interior spherical Bessel gravitational model is also a series expansion, with three different summations over: l - power, n - degree, and m - order. The bar over the coefficients and other terms in the equations implies that the term has be normalized by Equation 3.26.

$$N_{n,m} = \sqrt{\frac{(2-\delta_{0,m})\,(2n+1)\,(n-m)!}{(n+m)!}} \tag{3.26}$$

The Kronecker delta, $\delta_{i,j}$, is 1 when the subscripts are equal and 0 otherwise.

A basis function (Equation 3.27) utilizing spherical Bessel functions is created to form the gravitational potential function as the series expansion. The use of spherical Bessel functions is what gives the gravity model its name.

$$\bar{\beta}_{n,m}\left(\alpha_{l,n}\right) = j_n\left(\frac{\alpha_{l,n} r}{R_b}\right) \bar{H}_{n,m} \tag{3.27}$$

$$\bar{H}_{n,m} = \begin{cases} N_{n,m} P_{n,m}\left[sin(\phi)\right] e^{im\lambda} & n \geq m \geq 0 \\ 0 & otherwise \end{cases} \tag{3.28}$$

The spherical Bessel function is represented by $j_n\left(x\right)$. The variable $\bar{H}_{n,m}$ is for convenience, as that term will be used frequently in the gravitational acceleration model. The associated Legendre polynomials that are used in the spherical harmonics gravity model also appear in the spherical Bessel model as $P_{n,m}\left[sin(\phi)\right]$. These are located in Table 3.1, by substituting the n for l. In order to prevent confusion between the latitude and the Kronecker delta, latitude will be represented by ϕ in this subsection. The radius of the Brillouin sphere is R_b, comparable to r_0 in the spherical harmonics gravity model, and the radius from the asteroid center to the spacecraft is r. The term i represents an imaginary number, as opposed to a summation index.

The total gravitational acceleration or the partial of the gravitational potential with respect to the Cartesian coordinate system is located in Equations 3.29 through 3.31.

$$\frac{\partial U}{\partial r_x} = \frac{\mu}{R_b} \sum_{l=0}^{\infty} \sum_{n=0}^{\infty} \sum_{m=0}^{n} Re\left[\frac{\partial}{\partial x}\left(\bar{\beta}_{n,m}\left(\alpha_{l,n}\right)\right)\right] \bar{A}_{l,n,m} + Im\left[\frac{\partial}{\partial x}\left(\bar{\beta}_{n,m}\left(\alpha_{l,n}\right)\right)\right] \bar{B}_{l,n,m} \tag{3.29}$$

$$\frac{\partial U}{\partial r_y} = \frac{\mu}{R_b} \sum_{l=0}^{\infty} \sum_{n=0}^{\infty} \sum_{m=0}^{n} Re\left[\frac{\partial}{\partial y}\left(\bar{\beta}_{n,m}\left(\alpha_{l,n}\right)\right)\right] \bar{A}_{l,n,m} + Im\left[\frac{\partial}{\partial y}\left(\bar{\beta}_{n,m}\left(\alpha_{l,n}\right)\right)\right] \bar{B}_{l,n,m} \tag{3.30}$$

$$\frac{\partial U}{\partial r_z} = \frac{\mu}{R_b} \sum_{l=0}^{\infty} \sum_{n=0}^{\infty} \sum_{m=0}^{n} Re\left[\frac{\partial}{\partial z}\left(\bar{\beta}_{n,m}\left(\alpha_{l,n}\right)\right)\right] \bar{A}_{l,n,m} + Im\left[\frac{\partial}{\partial z}\left(\bar{\beta}_{n,m}\left(\alpha_{l,n}\right)\right)\right] \bar{B}_{l,n,m} \tag{3.31}$$

The normalized gravitational coefficients $\bar{A}_{l,n,m}$ and $\bar{B}_{l,m,n}$ are asteroid specific, similar to the $C_{l,m}$ and $S_{l,m}$ in the spherical harmonics model. As the acceleration vector must be real, the imaginary basis vector is parsed into its real and imaginary portions. The values of these portions are represented by the Re and Im, thus returning to a real equation.

The partials of the basis function are given in Equations 3.32 to 3.34.

$$\frac{\partial}{\partial x}\left(\bar{\beta}_{n,m}\left(\alpha_{l,n}\right)\right)=\begin{cases} -\frac{\alpha_{l,n}r_x}{R_b r}\,j_{n+1}\left[\frac{\alpha_{l,n}r}{R_b}\right]\bar{H}_{n,0} & \\ \quad -2\bar{\mathscr{F}}_1\left(n,m\right)\frac{1}{r}\,j_n\left[\frac{\alpha_{l,n}r}{R_b}\right]N_{n-1,1}P_{n-1,1}\left[sin(\phi)\right]cos\lambda & m=0 \\ -\frac{\alpha_{l,n}r_x}{R_b r}\,j_{n+1}\left[\frac{\alpha_{l,n}r}{R_b}\right]\bar{H}_{n,m}-\bar{\mathscr{F}}_1\left(n,m\right)\frac{1}{r}\,j_n\left[\frac{\alpha_{l,n}r}{R_b}\right]\bar{H}_{n-1,m+1}+ & \\ \quad \bar{\mathscr{F}}_2\left(n,m\right)\frac{1}{r}\,j_n\left[\frac{\alpha_{l,n}r}{R_b}\right]\bar{H}_{n-1,m-1} & m>0 \end{cases} \tag{3.32}$$

$$\frac{\partial}{\partial y}\left(\bar{\beta}_{n,m}\left(\alpha_{l,n}\right)\right)=\begin{cases} -\frac{\alpha_{l,n}r_y}{R_b r}\,j_{n+1}\left[\frac{\alpha_{l,n}r}{R_b}\right]\bar{H}_{n,0} & \\ \quad -2\bar{\mathscr{F}}_1\left(n,m\right)\frac{1}{r}\,j_n\left[\frac{\alpha_{l,n}r}{R_b}\right]N_{n-1,1}P_{n-1,1}\left[sin(\phi)\right]sin\lambda & m=0 \\ -\frac{\alpha_{l,n}r_y}{R_b r}\,j_{n+1}\left[\frac{\alpha_{l,n}r}{R_b}\right]\bar{H}_{n,m}+\bar{\mathscr{F}}_1\left(n,m\right)\frac{1}{r}\,j_n\left[\frac{\alpha_{l,n}r}{R_b}\right]i\,\bar{H}_{n-1,m+1}+ & \\ \quad \bar{\mathscr{F}}_2\left(n,m\right)\frac{1}{r}\,j_n\left[\frac{\alpha_{l,n}r}{R_b}\right]i\,\bar{H}_{n-1,m-1} & m>0 \end{cases} \tag{3.33}$$

$$\frac{\partial}{\partial z}\left(\bar{\beta}_{n,m}\left(\alpha_{l,n}\right)\right)=-\frac{\alpha_{l,n}r_z}{R_b r}\,j_{n+1}\left[\frac{\alpha_{l,n}r}{R_b}\right]\bar{H}_{n,m}+\bar{\mathscr{F}}_3\left(n,m\right)\frac{1}{r}\,j_n\left[\frac{\alpha_{l,n}r}{R_b}\right]\bar{H}_{n-1,m} \tag{3.34}$$

The magnitude of the radius from the center of the asteroid to the vehicle is represented by r, while the Cartesian components of the position vector are denoted by the subscripts. The latitude of the vehicle is ϕ and the longitude is λ. The $\bar{H}_{n,m}$ terms are evaluated with Equation 3.28. Note that the subscripts for $\bar{H}_{n,m}$ and $P_{n,m}$ must be positive and the second subscript can never be larger than the first. If either of these conditions occur in the summation, these terms are treated as zero. Also when $m = 0$, the partial derivatives in Equations 3.32 and 3.33 use a different expression than for $m > 0$. Once the eigenvalue of the spherical Bessel function ($\alpha_{l,n}$) has been calculated it will remain the same throughout the use of the gravity model, independent of the asteroid. Table 3.2 contains the the eigenvalues courtesy of Ref. Takahashi and Scheeres (2014). The terms $\bar{\mathscr{F}}_1\left(n,m\right)$, $\bar{\mathscr{F}}_2\left(n,m\right)$ and $\bar{\mathscr{F}}_3\left(n,m\right)$ are for convenience and given in Equation 3.35.

$$\begin{aligned}
\bar{\mathscr{F}}_1\left(n,m\right) &= \frac{1}{2}\sqrt{\frac{\left(2-\delta_{0,m}\right)\left(2n+1\right)\left(n-m\right)\left(n-m-1\right)}{2\left(2n-1\right)}} \\
\bar{\mathscr{F}}_2\left(n,m\right) &= \frac{1}{2}\sqrt{\frac{\left(2-\delta_{0,m}\right)\left(2n+1\right)\left(n+m\right)\left(n+m-1\right)}{\left(2-\delta_{1,m}\right)\left(2n-1\right)}} \\
\bar{\mathscr{F}}_3\left(n,m\right) &= \sqrt{\frac{\left(2n+1\right)\left(n+m\right)\left(n-m\right)}{2n-1}}
\end{aligned} \tag{3.35}$$

The spherical Bessel functions used in the gravity model are listed in Equations 3.36 through 3.42, where $x = \left[\frac{\alpha_{l,n} r}{R_b}\right]$ in the basis function partial derivatives. (Ref. Rade and Westergren (1999))

$$j_0\left(x\right) = \frac{1}{x}\sin x \tag{3.36}$$

$$j_1\left(x\right) = \frac{1}{x^2}\sin x - \frac{1}{x}\cos x \tag{3.37}$$

$$j_2\left(x\right) = \left[\frac{3}{x^3} - \frac{1}{x}\right]\sin x - \frac{3}{x^2}\cos x \tag{3.38}$$

$$j_3\left(x\right) = \left[\frac{15}{x^4} - \frac{6}{x^2}\right]\sin x + \left[-\frac{15}{x^3} + \frac{1}{x}\right]\cos x \tag{3.39}$$

$$j_4\left(x\right) = \left[\frac{105}{x^5} - \frac{45}{x^3} + \frac{1}{x}\right]\sin x + \left[-\frac{105}{x^4} + \frac{10}{x^2}\right]\cos x \tag{3.40}$$

$$j_5\left(x\right) = \left[\frac{945}{x^6} - \frac{420}{x^4} + \frac{15}{x^2}\right]\sin x + \left[-\frac{945}{x^5} + \frac{105}{x^3} - \frac{1}{x}\right]\cos x \tag{3.41}$$

$$j_6\left(x\right) = \left[\frac{10395}{x^7} - \frac{4725}{x^5} + \frac{210}{x^3} - \frac{1}{x}\right]\sin x + \left[-\frac{10395}{x^6} + \frac{1260}{x^4} - \frac{21}{x^2}\right]\cos x \tag{3.42}$$

The best truncation of the summation series, which corresponds to the available coefficients, goes to a power of 2, order and degree of 5. ($l_{max} = 2$, $n_{max} = 5$, $m_{max} = 5$). The dominant term is the sum of the order and degree equal to zero over the 3 powers. These are the terms associated with the following three triplets (l, n, m): 0,0,0; 1,0,0; 2,0,0. This is equivalent to the dominant term ($C_{0,0}$) in the spherical harmonics model.

Table 3.1: Associated Legendre functions and their derivatives for use in the gravity models. The derivatives for 5,0 - 5,5 are not required, thus their absence.

l	m	$P_{l,m}\left[\sin\delta\right]$	$\frac{\partial P_{l,m}[\sin\delta]}{\partial\delta}$
0	0	1	0
1	0	$\sin\delta$	$\cos\delta$
1	1	$\cos\delta$	$-\sin\delta$
2	0	$\frac{1}{2}\left\{3\sin^2\delta-1\right\}$	$3\sin\delta\cos\delta$
2	1	$3\sin\delta\cos\delta$	$-3\sin^2\delta+3\cos^2\delta$
2	2	$3\cos^2\delta$	$-6\sin\delta\cos\delta$
3	0	$\frac{1}{2}\left\{5\sin^3\delta-3\sin\delta\right\}$	$\frac{15}{2}\sin^2\delta\cos\delta-\frac{3}{2}\cos\delta$
3	1	$\frac{1}{2}\cos\delta\left\{15\sin^2\delta-3\right\}$	$-\frac{15}{2}\sin^3\delta+\frac{3}{2}\sin\delta+15\sin\delta\cos^2\delta$
3	2	$15\sin\delta\cos^2\delta$	$-30\sin^2\delta\cos\delta+15\cos^3\delta$
3	3	$15\cos^3\delta$	$-45\sin\delta\cos^2\delta$
4	0	$\frac{1}{8}\left\{35\sin^4\delta-30\sin^2\delta+3\right\}$	$\frac{35}{2}\sin^3\delta\cos\delta-\frac{15}{2}\sin\delta\cos\delta$
4	1	$\frac{5}{2}\cos\delta\left\{7\sin^3\delta-3\sin\delta\right\}$	$-\frac{35}{2}\sin^4\delta+\frac{15}{2}\sin^2\delta+\frac{105}{2}\sin^2\delta\cos^2\delta-\frac{15}{2}\cos^2\delta$
4	2	$\frac{15}{2}\cos^2\delta\left\{7\sin^2\delta-1\right\}$	$-105\sin^3\delta\cos\delta+15\sin\delta\cos\delta+105\sin\delta\cos^3\delta$
4	3	$105\sin\delta\cos^3\delta$	$-315\sin^2\delta\cos^2\delta+105\cos^4\delta$
4	4	$105\cos^4\delta$	$-420\sin\delta\cos^3\delta$
5	0	$\frac{63}{8}\sin^5\delta-\frac{35}{4}\sin^3\delta+\frac{15}{8}\sin\delta$	NA
5	1	$\frac{315}{8}\sin^4\delta\cos\delta-\frac{105}{4}\sin^2\delta\cos\delta+\frac{15}{8}\cos\delta$	NA
5	2	$-\frac{105}{2}\sin\delta\cos^2\delta+\frac{315}{2}\sin^3\delta\cos^2\delta$	NA
5	3	$\frac{945}{2}\sin^2\delta\cos^3\delta-\frac{105}{2}\cos^3\delta$	NA
5	4	$945\sin\delta\cos^4\delta$	NA
5	5	$945\cos^5\delta$	NA

Table 3.2: Spherical Bessel eigenvalues, in place of 0.0, 1.00E-12 is used to prevent numerical errors.

l	n	$\alpha_{l,n}$
0	0	1.5708
0	1	3.1416
0	2	1.00E-12
0	3	1.00E-12
0	4	1.00E-12
0	5	1.00E-12
1	0	4.7124
1	1	6.2832
1	2	4.4934
1	3	5.7635
1	4	6.9879
1	5	8.1826
2	0	7.854
2	1	9.4248
2	2	7.7253
2	3	9.095
2	4	10.4171
2	5	11.7049
3	0	10.9956
3	1	12.5664
3	2	10.9041
3	3	12.3229
3	4	13.698
3	5	15.0397
4	0	14.1372
4	1	15.708
4	2	14.0662
4	3	15.5146
4	4	16.9236
4	5	18.3013
5	0	17.2788
5	1	18.8496
5	2	17.2208
5	3	18.689
5	4	20.1218
5	5	21.5254

CHAPTER 4. POWERED DESCENT PROBLEM FORMULATION

First, the vehicle's equations of motion during the powered descent are formulated. These equations are the dynamics in the minimum propellant optimization problem. Second, the original nonlinear minimum propellant optimization problem is formulated. The solution to this optimization problem defines the desired vehicle trajectory. This version of the optimization problem is nonconvex.

4.1 Equations of Motion

The equations of motion are derived from Newton's second law, Equation 4.1.

$$\vec{F} = m\vec{a} \tag{4.1}$$

The asteroid's gravitational force and the vehicle thrust are the forces included in $\vec{F}$. All other forces on the vehicle such as gravity from other bodies and solar radiation pressure are considered marginal during the descent burn. The vehicle acceleration vector ($\vec{a}$) is with respect to an inertial frame in Equation 4.1, but the working coordinate system is fixed in the asteroid and rotates with the asteroid. This rotation must be accounted for when calculating the acceleration vector.

The asteroid and its coordinate system rotate around the spin vector ($\vec{\omega}$), with the spin rate equivalent to the magnitude of the spin vector. The spin vector is defined in terms of the Cartesian coordinate system and is assumed to be any possible axis, Equation 4.2

$$\vec{\omega} = \omega_x \hat{x} + \omega_y \hat{y} + \omega_z \hat{z} \tag{4.2}$$

Most asteroids in the uniform rotator class rotate about their maximum moment of inertia, along Z; however, to accommodate asteroids that do not rotate perfectly aligned with the Z axis, the full rotation vector will be included in the derivation and analysis. This will allow flexibility if the coordinate system does not perfectly align with the maximum moment of inertia or the asteroid is a rare case that does not rotate around that axis. The spin vector will be allowed to be nonconstant to accommodate tumbling asteroids in the derivation.

The inertial acceleration, including the acceleration due to the rotating coordinate frame, is located in Equation 4.3.

$$\vec{a} = \frac{d\vec{v}}{dt} + 2\vec{\omega} \times \vec{v} + \dot{\vec{\omega}} \times \vec{r} + \vec{\omega} \times (\vec{\omega} \times \vec{r}) \tag{4.3}$$

The $\vec{r}$ and $\vec{v}$ are the spacecraft position and velocity vectors in the asteroid centered fixed coordinate system.

Applying Newton's second law (Equation 4.1) gives the equation of motion for the system in vector form, Equation 4.4.

$$\vec{T} + m\nabla U(\vec{r}) = m\left(\frac{d\vec{v}}{dt} + 2\vec{\omega} \times \vec{v} + \dot{\vec{\omega}} \times \vec{r} + \vec{\omega} \times (\vec{\omega} \times \vec{r})\right) \tag{4.4}$$

In the above equation, $\vec{T}$ is the vehicle thrust, m is the vehicle mass and ∇U is the gradient of the gravitational potential. The gradient of gravitational potential is the acceleration due to gravity and is taken with respect to the asteroid centered fixed coordinate system. The methods for determining the gravitational acceleration are discussed in Chapter 3. For now, consider it a generic vector that is a function of the vehicle position vector.

The easiest form of the equations of motion to work with is a system of first order differential equations. These can be propagated to determine the entire vehicle state at any point in time given the control vector. The state vector consists of position vector ($\vec{r} = [r_x, r_y, r_z]$), velocity ($\vec{v} = [v_x, v_y, v_z]$), and mass (m). The control vector is the vehicle thrust ($\vec{T} = [T_x, T_y, T_z]$). Rearranging Equation 4.4 yields the equations of motion as a set of first order differential equations, Equation 4.5, in vector form.

$$\begin{aligned}
\dot{\vec{r}} &= \vec{v} \\
\dot{\vec{v}} &= \frac{\vec{T}}{m} - 2\vec{\omega} \times \vec{v} - \dot{\vec{\omega}} \times \vec{r} - \vec{\omega} \times (\vec{\omega} \times \vec{r}) + \nabla U(\vec{r}) \\
\dot{m} &= -\frac{1}{v_{ex}}\left\|\vec{T}\right\|
\end{aligned} \tag{4.5}$$

The mass flowrate (bottom line in Equation 4.5) is a standard calculation involving the thrust magnitude and the vehicle exit velocity (v_{ex}).

4.2 Original Nonlinear Optimization Problem

The soft landing problem is a two point boundary optimization problem. The initial vehicle state is known along with the targeted landing site, which yields a two point value boundary problem. The optimization part comes from minimizing the propellant (fuel) usage. This is achieved by maximizing the mass of the vehicle when it touches down, thus minimizing propellant consumption. To accomplish this, the cost function (Equation 4.6) is the negative of the vehicle mass at the landing site. The full optimization problem is located in Equations 4.6 through 4.18, referred to as Problem P1.

$$\min -m(t_f) \tag{4.6}$$

$$s.t.\ \dot{\vec{r}} = \vec{v} \tag{4.7}$$

$$\dot{\vec{v}} = \frac{\vec{T}}{m} - 2\vec{\omega} \times \vec{v} - \dot{\vec{\omega}} \times \vec{r} - \vec{\omega} \times (\vec{\omega} \times \vec{r}) + \nabla U(\vec{r}) \tag{4.8}$$

$$\dot{m} = -\frac{1}{v_{ex}} \left\| \vec{T} \right\| \tag{4.9}$$

$$T_{min} \le \left\| \vec{T} \right\| \le T_{max} \tag{4.10}$$

$$\|\vec{r} - \vec{r}_f\| \cos\theta - (\vec{r} - \vec{r}_f)^T \hat{n} \le 0 \tag{4.11}$$

$$m \ge m_{dry} \tag{4.12}$$

$$\vec{r}\,(0) = \vec{r}_0 \tag{4.13}$$

$$\vec{v}\,(0) = \vec{v}_0 \tag{4.14}$$

$$m\,(0) = m_{wet} \tag{4.15}$$

$$\vec{r}\,(t_f) = \vec{r}_f \tag{4.16}$$

$$\vec{v}\,(t_f) = \vec{v}_f \tag{4.17}$$

$$t_f \ \text{ given} \tag{4.18}$$

Once the engine has been turned on it is throttleable between a minimum and maximum range and cannot be turned off until the descent burn is complete. This is accounted for by inequality constraints on the thrust magnitude, Equation 4.10. The constraint in Equation 4.11 is called a glide slope constraint. Currently the angle θ is set at 90.0 deg to prevent the spacecraft from going below the surface of the asteroid. $\hat{n}$ is the unit vector normal to the landing site. The final constraint 4.12 is to ensure that the trajectory does not use more than the available propellant.

The above optimization problem is nonlinear and nonconvex. The nonlinear terms are the norm of the thrust vector and dividing by the mass. The gravitational acceleration is highly nonlinear in terms of the position vector.

The thrust constraint, Equation 4.10, can be divided into the two constraints located in Equation 4.19.

$$\begin{aligned} T_{min} &\leq \left\| \vec{T} \right\| \\ \left\| \vec{T} \right\| &\leq T_{max} \end{aligned} \tag{4.19}$$

The bottom inequality expression is convex and a valid inequality for a convex optimization problem, while the top inequality is not. The bottom inequality expression is the only nonlinear term in the optimization problem that is viable for a convex optimization problem. Therefore, the remaining nonlinearities will need to be handled with a variety of techniques in order to create a convex optimization problem.

CHAPTER 5. CONVEXIFICATION

The ultimate goal is to create an optimization problem that is in the form of a convex optimization problem, so that available convex solvers can be used to determine the solution. An added bonus occurs if the problem can be turned into a second order cone program, as more solvers and techniques are available. In order to keep the problem as generic as possible, the focus will be on turning the nonlinear powered descent optimization problem into a convex optimization problem, thus allowing a larger variety of constraints and situations.

Convexification is the process of turning the nonconvex optimization problem into a convex optimization problem. The first technique applied to the problem is a relaxation of the problem by introducing a slack variable. Change of variables is the second technique applied.

5.1 Exact Relaxation of the Problem

The magnitude of the thrust vector or norm of the thrust vector is one of the nonlinearities in the original problem. In order to remove nonlinearities, a slack variable referred to as T_m will become a fourth control vector to supplement $\vec{T}$. In the optimization problem this variable is completely separate from the thrust vector and only related through a new constraint, Equation 5.1.

$$\left\| \vec{T} \right\| \leq T_m \tag{5.1}$$

This slack variable represents the magnitude of the thrust vector and is substituted where the norm of the thrust occurred. The optimization problem is now formulated as Problem P2 located in Equations 5.2 through 5.15.

$$\min -m(t_f) \tag{5.2}$$

$$s.t.\ \dot{\vec{r}} = \vec{v} \tag{5.3}$$

$$\dot{\vec{v}} = \frac{\vec{T}}{m} - 2\vec{\omega} \times \vec{v} - \dot{\vec{\omega}} \times \vec{r} - \vec{\omega} \times (\vec{\omega} \times \vec{r}) + \nabla U(\vec{r}) \tag{5.4}$$

$$\dot{m} = -\frac{1}{v_{ex}} T_m \tag{5.5}$$

$$\left\| \vec{T} \right\| \leq T_m \tag{5.6}$$

$$T_{min} \leq T_m \leq T_{max} \tag{5.7}$$

$$\left\| \vec{r} - \vec{r}_f \right\| \cos\theta - \left(\vec{r} - \vec{r}_f \right)^T \hat{n} \leq 0 \tag{5.8}$$

$$m \geq m_{dry} \tag{5.9}$$

$$\vec{r}\,(0) = \vec{r}_0 \tag{5.10}$$

$$\vec{v}\,(0) = \vec{v}_0 \tag{5.11}$$

$$m\,(0) = m_{wet} \tag{5.12}$$

$$\vec{r}\,(t_f) = \vec{r}_f \tag{5.13}$$

$$\vec{v}\,(t_f) = \vec{v}_f \tag{5.14}$$

$$t_f \ \text{ given} \tag{5.15}$$

Problems P1 and P2 are identical when the inequality in Equation 5.6 is active, specifically when $\left\| \vec{T} \right\| = T_m$. When the two problems are identical, the minimum point in Problem P2 is a feasible solution to Problem P1 and indeed the minimum of both Problems P1 and P2. With the introduction of the slack variable Equations 5.5 and 5.7 are now linear and Equation 5.6 is convex. The remaining nonlinearities are the first and last terms on the right-hand side of Equation 5.4.

Proposition: Problems P1 and P2 are identical when the inequality in Equation 5.6 is active, i.e., $\left\| \vec{T} \right\| = T_m$. Moreover, the solution to Problem P2 is the same as the solution to Problem P1.

Proof: For brevity of the proof, the glide slope constraint Equation 5.8 is removed from the problem under investigation. The first part of the Proposition is straightforward. It is immediately clear that when the constraint in Equation 5.6 is active, Problem P2 reduces to Problem P1. To prove the second part of the Proposition, apply the Minimum Principle from Optimal Control Theory and form the Hamiltonian in a vector and matrix format that removes the cross products, Equation 5.16. Note, that the cost function is only dependent on the mass at the final time, $\phi\left(t_f\right) = -m(t_f)$. The dynamics of the system are autonomous causing the Hamiltonian to be constant during the entire flight.

$$
\begin{gathered}
H = \vec{p}_r^{\,T}\vec{v} + \vec{p}_v^{\,T}\left(\frac{1}{m}\vec{T} - 2W_1\vec{v} - W_2\vec{r} - W_3\vec{r} + \nabla U\left(\vec{r}\right)\right) - p_m\frac{1}{v_{ex}}T_m \\
W_1 = \begin{bmatrix} 0 & -\omega_z & \omega_y \\ \omega_z & 0 & -\omega_x \\ -\omega_y & \omega_x & 0 \end{bmatrix} \quad W_2 = \begin{bmatrix} 0 & -\dot{\omega}_z & \dot{\omega}_y \\ \dot{\omega}_z & 0 & -\dot{\omega}_x \\ -\dot{\omega}_y & \dot{\omega}_x & 0 \end{bmatrix} \\
W_3 = \begin{bmatrix} -\omega_y^2 - \omega_z^2 & \omega_x\omega_y & \omega_x\omega_z \\ \omega_x\omega_y & -\omega_x^2 - \omega_z^2 & \omega_y\omega_z \\ \omega_x\omega_z & \omega_y\omega_z & -\omega_x^2 - \omega_y^2 \end{bmatrix}
\end{gathered} \tag{5.16}
$$

The states are $\vec{r}$, $\vec{v}$, m, and the corresponding costates are $\vec{p}_r$, $\vec{p}_v$, p_m. The control vector $\mathscr{C}$ consists of the thrust vector and slack variable, along with the constraints on the control vector as described in Equation 5.17.

$$
\mathscr{C} = \left\{\left(\vec{T}, T_m\right) \mid \left\|\vec{T}\right\| \leq T_m,\ T_{min} \leq T_m,\ T_m \leq T_{max}\right\} \tag{5.17}
$$

From Optimal Control Theory, the differential equations for the costates are listed in Equation 5.18 through Equation 5.20.

$$
\dot{\vec{p}}_r = W_2^T\vec{p}_v + W_3^T\vec{p}_v - \vec{p}_v^{\,T}\nabla^2 U(\vec{r}) \tag{5.18}
$$

$$
\dot{\vec{p}}_v = -\vec{p}_r + 2W_1^T\vec{p}_v \tag{5.19}
$$

$$
\dot{p}_m = \vec{p}_v^{\,T}\vec{T}\left(\frac{1}{m^2}\right) \tag{5.20}
$$

The problem is a fixed final time problem. Applying the end point constraints and the transversality conditions yields one useful equation, Equation 5.21.

$$
p_m\left(t_f\right) = -1 \tag{5.21}
$$

From the Minimum Principle, the optimal solution is determined by minimizing the Hamiltonian with respect to the control vector ($\mathscr{C}$) subject to the constraints in Equation 5.17. The Hamiltonian is linear in terms of the control vector, therefore the minimum will be on the boundary of the admissible control set. This can be turned into a constrained optimization problem which minimizes the Hamiltonian by applying the Karush-Kuhn-Tucker (KKT) conditions. First, the terms in the Hamiltonian expression that are not dependent on the control vector can be removed from the optimization problem, as they have no effect on the solution. These terms are $\vec{p}_r^T\vec{v} + \vec{p}_v^T\left(-2W_1\vec{v} - W_2\vec{r} - W_3\vec{r} + \nabla U\left(\vec{r}\right)\right)$. It is interesting to note that as long as the gravitational potential remains solely a function of spacecraft position, it does not influence the minimization of the Hamiltonian. Increasing the complexity of the gravity model will not invalidate these arguments.

The point-wise minimization problem with respect to $\vec{T}$, T_m is stated in Equation 5.22.

$$\begin{aligned} \min \ & \tfrac{1}{m}\vec{p}_v^T\vec{T} - \tfrac{1}{v_{ex}}p_m T_m \\ s.t. \ & \left\|\vec{T}\right\| \le T_m,\ T_{min} \le T_m,\ T_m \le T_{max} \end{aligned} \tag{5.22}$$

This is a convex optimization problem that has a global optimal solution. The Lagrangian for the constrained optimization problem is listed in Equation 5.23.

$$\mathscr{L} = \frac{1}{m}\vec{p}_v^T\vec{T} - \frac{1}{v_{ex}}p_m T_m + \lambda_1\left(\left\|\vec{T}\right\| - T_m\right) + \lambda_2\left(T_{min} - T_m\right) + \lambda_3\left(T_m - T_{max}\right) \tag{5.23}$$

The variables λ_1, λ_2, λ_3 are the Lagrange multipliers associated with the inequality constraints on $\vec{T}$, T_m. From the KKT conditions, a constraint is active when $\lambda_i \geq 0$, while a constraint can only be inactive when $\lambda_i = 0$. Applying the KKT conditions yields Equation 5.24 and Equation 5.25.

$$\frac{\partial \mathscr{L}}{\partial \vec{T}} = \frac{1}{m}\vec{p}_v + \lambda_1\frac{\vec{T}}{\left\|\vec{T}\right\|} = 0 \tag{5.24}$$

$$\frac{\partial \mathscr{L}}{\partial T_m} = -\frac{1}{v_{ex}}p_m - \lambda_1 - \lambda_2 + \lambda_3 = 0 \tag{5.25}$$

Now examine the problem as two specific cases: when $\vec{p}_v$ is nonzero almost everywhere (a.e.) in $[0, t_f]$ and when it is zero in a finite time interval. For the first case it will be shown that $\lambda_1 \neq 0$, therefore the solutions to Problems P1 and P2 are the same. Then by contradiction, show that $\vec{p}_v$ cannot be zero for a finite time interval.

Suppose that $\vec{p_v} \neq 0$ in any finite time interval. From Equation 5.24, when $\vec{T} \neq 0$, then λ_1 must be nonzero ($\lambda_1 \neq 0$); otherwise, Equation 5.24 necessitates $\vec{p_v} = 0$, since mass is nonzero, contradicting the assumption that $\vec{p_v} \neq 0$. When $\vec{T} = 0$, $\vec{T}/||\vec{T}||$ is a finite vector. The same argument applies to ascertain that $\lambda_1 \neq 0$. Therefore, the corresponding constraint must be active, $\left\|\vec{T}\right\| = T_m$. Consequently, the solution to Problem P2 is also the solution to Problem P1.

Next look at the case when $\vec{p_v} = 0$ for a finite time period. If $\vec{p_v} = 0$ in a finite time interval, its derivative must also be zero simultaneously. From the costate equations in Equation 5.18 through Equation 5.20, this implies that $\vec{p_r} = 0$ and p_m is a constant. Because the costate system in Equation 5.18 through Equation 5.20 is a homogeneous linear system in $\vec{p_r}$ and $\vec{p_v}$, it follows that $\vec{p_r} = \vec{p_v} = 0$ in the entire interval $[0, t_f]$, and p_m is constant. From the transversality condition in Equation 5.21, $p_m(t) = -1$. The Hamiltonian reduces to Equation 5.26.

$$H = \frac{1}{v_{ex}} T_m \tag{5.26}$$

The minimum of the Hamiltonian with respect to $\mathscr{C}$ is the smallest admissible T_m, which is $T_{min} > 0$, therefore $T_m = T_{min}$. Thus the Hamiltonian becomes Equation 5.27.

$$H = \frac{1}{v_{ex}} T_{min} \tag{5.27}$$

Since $T_{min} > 0$ and $v_{ex} > 0$, then $H > 0$. If $\vec{p_v} = 0$ in a finite interval, the constancy condition of the Hamiltonian, Equation 5.27, should always hold, regardless of the initial conditions, landing site, or the specified final time, t_f. In particular, if the value of t_f happens to be equal to t_f^*, the optimal flight time in a free time problem, which is the same as Problem P2 except that the final time is free, the Hamiltonian is zero along the optimal trajectory from the Minimum Principle. The nonzero constancy condition in Equation 5.27 then constitutes a contradiction in this case. Therefore, the condition that $\vec{p_v} = 0$ in a finite interval cannot happen. Since this case is invalid, the case of $\vec{p_v} \neq 0$ a.e. on $[0, t_f]$ is the only possibility, which in turn means that $\left\|\vec{T}\right\| = T_m$ in the solution to Problem P2. This solution is also the solution to Problem P1. (Ref. Pontryagin et al. (1962))

As the glide slope constraint was not included explicitly, checks on the slack variable will be made to ensure that the two problems are identical. A related proof involving thrust pointing constraints for the Mars landing problem is found in Ref. Acikmese et al. (2013).

5.2 Change of Variables

The next step of the process that turns Problems P1 and P2 into a convex optimization problem is a change of variables. Two different types of variable changes are applied. The first changes all thrust variables into acceleration due to thrust through the conversion seen in Equation 5.28.

$$\begin{aligned} \vec{a}_t &= \frac{\vec{T}}{m} \\ a_{tm} &= \frac{T_m}{m} \end{aligned} \tag{5.28}$$

This change effects Equations 5.4 through 5.7 in Problem P2, changing them into Equations 5.29 through 5.32.

$$\dot{\vec{v}} = \vec{a}_t - 2\vec{\omega} \times \vec{v} - \dot{\vec{\omega}} \times \vec{r} - \vec{\omega} \times (\vec{\omega} \times \vec{r}) + \nabla U(\vec{r}) \tag{5.29}$$

$$\dot{m} = -\frac{1}{v_{ex}} a_{tm} m \tag{5.30}$$

$$\|\vec{a}_t\| \leq a_{tm} \tag{5.31}$$

$$T_{min} \leq a_{tm} m \leq T_{max} \tag{5.32}$$

This turned Equation 5.29 into a linear equation in state except for the gravitational acceleration term, handled later. Unfortunately, Equations 5.30 and 5.32 are now nonlinear.

A second change of variables is completed to handle the nonlinearities in Equations 5.30 and 5.32. A new mass variable is introduced as seen in Equation 5.33.

$$q = \ln(m) \tag{5.33}$$

This change affects the cost function. The maximum mass occurs at the same time as the maximum of q, due to the natural log function properties. The derivative of the above equation is calculated in Equation 5.34 and will replace the flowrate equation (Equation 5.30) in the equations of motion.

$$\dot{q} = \frac{\dot{m}}{m} = \frac{-a_{tm} m}{m\, v_{ex}} = -\frac{a_{tm}}{v_{ex}} \tag{5.34}$$

This is linear in terms of state.

Manipulation of Equation 5.32 with the mass variable change results in the following two inequalities.

$$\begin{aligned} T_{min}\,\mathrm{e}^{-q} &\leq a_{tm} \\ a_{tm} &\leq T_{max}\,\mathrm{e}^{-q} \end{aligned} \tag{5.35}$$

Taylor series expansion will be applied to e^{-q} in order to turn the top inequality into a quadratic equation in state and the bottom into a linear. This effectively creates a second order cone constraint and a linear constraint, which are both convex. A quadratic cannot be used on the bottom constraint as that would not turn it into a convex constraint. The new constraints (Equation 5.36) are equivalent to the old as long as the Taylor series expansion does not deviate from the vehicle mass. Spot checking shows the difference is on the order of a few grams, which is negligible to ensuring the thrust bounds are not exceeded.

$$\begin{gathered} T_{min}\,\mathrm{e}^{-q_o}\left[1-(q-q_o)+0.5\,(q-q_o)^2\right] \leq a_{tm} \\ a_{tm} \leq T_{max}\,\mathrm{e}^{-q_o}\left[1-(q-q_o)\right] \end{gathered} \tag{5.36}$$

The point about which the expansion occurs (q_o) is calculated ahead of time. It is the expected mass at the same time in the trajectory, if the vehicle has been running at minimum thrust for the entire flight, Equation 5.37.

$$q_o = \ln\left(m_{wet} - \frac{T_{min}}{v_{ex}}\triangle t\right) \tag{5.37}$$

In the above equation Δt is the time elapsed from the start of the burn.

After the above manipulation the optimization problem becomes Problem P3 found in Equations 5.38 through 5.52

$$\min -q(t_f) \tag{5.38}$$

$$s.t.\ \ \dot{\vec{r}} = \vec{v} \tag{5.39}$$

$$\dot{\vec{v}} = \vec{a}_t - 2\vec{\omega} \times \vec{v} - \dot{\vec{\omega}} \times \vec{r} - \vec{\omega} \times (\vec{\omega} \times \vec{r}) + \nabla U\left(\vec{r}\right) \tag{5.40}$$

$$\dot{q} = -\frac{1}{vex} a_{tm} \tag{5.41}$$

$$\|\vec{a}_t\| \leq a_{tm} \tag{5.42}$$

$$T_{min}\, \mathrm{e}^{-q_o} \left[1 - (q - q_o) + 0.5\,(q - q_o)^2\right] \leq a_{tm} \tag{5.43}$$

$$a_{tm} \leq T_{max}\, \mathrm{e}^{-q_o} \left[1 - (q - q_o)\right] \tag{5.44}$$

$$\|\vec{r} - \vec{r}_f\| \cos\theta - \left(\vec{r} - \vec{r}_f\right)^T \hat{n} \leq 0 \tag{5.45}$$

$$q \geq q_{dry} \tag{5.46}$$

$$\vec{r}\,(0) = \vec{r}_0 \tag{5.47}$$

$$\vec{v}\,(0) = \vec{v}_0 \tag{5.48}$$

$$q\,(0) = \ln\left(m_{wet}\right) \tag{5.49}$$

$$\vec{r}\,(t_f) = \vec{r}_f \tag{5.50}$$

$$\vec{v}\,(t_f) = \vec{v}_f \tag{5.51}$$

$$t_f \ \text{ given} \tag{5.52}$$

Problem P3 is equivalent to Problem P2 as long as the Taylor series expansion is a close approximation. The optimal point for Problem P3 is the optimal solution of Problem P2 and thus Problem P1. With the exception of the gravitational acceleration, the dynamics are linear in state and control and the constraints are linear or second order cones, yielding a convex optimization problem. The gravitational acceleration term will be handled via the successive solution method.

CHAPTER 6. SUCCESSIVE SOLUTION METHOD

The gravitational acceleration is the most challenging aspect to manipulate into a convex form. Previous chapters used a generic gravity model, now the problem will focus on the 2x2 spherical harmonics gravity model for the homogenous triaxial ellipsoid, with extension to the higher fidelity models in Section 6.3. Recall that the 2x2 spherical harmonics gravity model is highly nonlinear in the position vector, including radius raised to the fifth power and cross multiplication of position components (Section 3.1).

The best way to handle these nonlinearities is to introduce a successive solution method (iterations). In the successive solution method a series of convex optimization problems are solved with each one using data from the previous solution, also known as iterations. The equations of motion from Problem P3, found in Equations 5.39 through 5.41, can be rearranged as in Equation 6.1, where (k) is the current iteration and (k-1) is the previous iteration.

$$\dot{\vec{x}}^{(k)} = A\left(\vec{r}^{\,(k-1)}\right)\vec{x}^{(k)} + B\vec{u}^{(k)} + c\left(\vec{r}^{\,(k-1)}\right) \tag{6.1}$$

The full state is represented by $\vec{x} = \left[\vec{r}^{\,T},\, \vec{v}^{\,T},\, q\right]^T$ and the control vector $\vec{u} = \left[\vec{a}_t^{\,T},\, a_{tm}\right]^T$. The superscript index notates with which iteration the variables are evaluated.

The terms in the gravitational acceleration are divided between the A matrix and c vector and evaluated with the previous iteration's solution (position vector). Five different arrangements of the terms were tried; see Section 6.1 for the corresponding analysis. The best one placed the Newtonian terms in the A matrix and all the remaining terms in the c vector as shown in Equation 6.6. Thus c can be thought of as a vector of higher order terms. Also, this arrangement makes it easy to swap out the 2x2 model for the 4x4 and 4x4 Bessel.

Since the only nonlinear terms in the gravitational acceleration are functions of the vehicle position, A and c are functions of position. For the first iteration, the position vector is taken to be the initial condition for the entire flight time, equivalent to assuming the spacecraft hovered at the initial point. Iterations continue until the current iteration and previous iteration match within a specified tolerance. At this point they are close enough to be called equivalent and the gravitational acceleration used to develop the current trajectory is no longer an approximation. By using the previous trajectory to evaluate the gravitational acceleration, the dynamics are now linear. Note, that this linearization was not completed in the traditional sense and does not have approximations due to linearization in the final iteration. With linear dynamics, the problem is a convex optimization problem, as well as a second order cone program formulation. In order to keep the problem generic and allow for additional constraints or dynamics, a convex optimizer will be used. A second order cone program is also an option for solving the problem as it is currently set up.

6.1 Dynamic Equations in State Dependent Linear Form

Five arrangements of the nonlinear gravity terms in A and c were analyzed. The first four placed the majority of the gravity model terms in A, and alternated in which columns to place the cross-couple terms, while the fifth method placed the Newtonian part in A and all the higher order terms in c. The five options are listed below; Option 1: Equation 6.2, Option 2: Equation 6.3, Option 3: Equation 6.4, Option 4: Equation 6.5 and Option 5: Equation 6.6. These options are formulated assuming that the asteroid is rotating around the +Z axis at a rate of ω. The full rotation vector can be placed in the A matrix corresponding to the dynamic equations, when needed.

$$A = \begin{bmatrix} 0 & 0 & 0 & 1 & 0 & 0 & 0 \\ 0 & 0 & 0 & 0 & 1 & 0 & 0 \\ 0 & 0 & 0 & 0 & 0 & 1 & 0 \\ \omega^2 - \frac{\mu}{r^3}\left(1 + G_1 + G_2\tau_1\right) & \frac{\mu}{r}G_3 & 0 & 0 & 2\omega & 0 & 0 \\ -\frac{\mu}{r}G_3 & \omega^2 - \frac{\mu}{r^3}\left(1 + G_1 + G_2\tau_1\right) & 0 & -2\omega & 0 & 0 & 0 \\ 0 & 0 & -\frac{\mu}{r^3}\left(1 + G_1 + G_2\tau_1\right) & 0 & 0 & 0 & 0 \\ 0 & 0 & 0 & 0 & 0 & 0 & 0 \end{bmatrix}^{(k-1)}$$

$$B = \begin{bmatrix} 0 & 0 & 0 & 0 \\ 0 & 0 & 0 & 0 \\ 0 & 0 & 0 & 0 \\ 1 & 0 & 0 & 0 \\ 0 & 1 & 0 & 0 \\ 0 & 0 & 1 & 0 \\ 0 & 0 & 0 & -\frac{1}{v_{ex}} \end{bmatrix} \qquad c = \begin{bmatrix} 0 \\ 0 \\ 0 \\ 0 \\ 0 \\ \frac{\mu}{r}\frac{1}{\sqrt{r_x^2+r_y^2}}G_2 \\ 0 \end{bmatrix}^{(k-1)} \qquad \tau_1 = \frac{r_z}{\sqrt{r_x^2+r_y^2}} \tag{6.2}$$

$$A = \begin{bmatrix} 0 & 0 & 0 & 1 & 0 & 0 & 0 \\ 0 & 0 & 0 & 0 & 1 & 0 & 0 \\ 0 & 0 & 0 & 0 & 0 & 1 & 0 \\ \omega^2 - \frac{\mu}{r^3}\left(1 + G_1\right) & \frac{\mu}{r} G_3 & -\frac{\mu}{r^3} G_2 \tau_2 r_x & 0 & 2\omega & 0 & 0 \\ -\frac{\mu}{r} G_3 & \omega^2 - \frac{\mu}{r^3}\left(1 + G_1\right) & -\frac{\mu}{r^3} G_2 \tau_2 r_y & -2\omega & 0 & 0 & 0 \\ 0 & 0 & -\frac{\mu}{r^3}\left(1 + G_1 + G_2 r_z \tau_2\right) & 0 & 0 & 0 & 0 \\ 0 & 0 & 0 & 0 & 0 & 0 & 0 \end{bmatrix}^{(k-1)} \tag{6.3}$$

$$B = \begin{bmatrix} 0 & 0 & 0 & 0 \\ 0 & 0 & 0 & 0 \\ 0 & 0 & 0 & 0 \\ 1 & 0 & 0 & 0 \\ 0 & 1 & 0 & 0 \\ 0 & 0 & 1 & 0 \\ 0 & 0 & 0 & -\frac{1}{v_{ex}} \end{bmatrix} \qquad c = \begin{bmatrix} 0 \\ 0 \\ 0 \\ 0 \\ 0 \\ \frac{\mu}{r} \frac{1}{\sqrt{r_x^2 + r_y^2}} G_2 \\ 0 \end{bmatrix}^{(k-1)} \qquad \tau_2 = \frac{1}{\sqrt{r_x^2 + r_y^2}}$$

$$A = \begin{bmatrix} 0 & 0 & 0 & 1 & 0 & 0 & 0 \\ 0 & 0 & 0 & 0 & 1 & 0 & 0 \\ 0 & 0 & 0 & 0 & 0 & 1 & 0 \\ \omega^2 - \frac{\mu}{r^3}\left(1 + G_1 + G_2\tau_1\right) & \frac{\mu}{r}G_3 & 0 & 0 & 2\omega & 0 & 0 \\ -\frac{\mu}{r}G_3 & \omega^2 - \frac{\mu}{r^3}\left(1 + G_1\right) & -\frac{\mu}{r^3}G_2\tau_2 r_y & -2\omega & 0 & 0 & 0 \\ 0 & 0 & -\frac{\mu}{r^3}\left(1 + G_1 + G_2\tau_1\right) & 0 & 0 & 0 & 0 \\ 0 & 0 & 0 & 0 & 0 & 0 & 0 \end{bmatrix}^{(k-1)} \tag{6.4}$$

$$B = \begin{bmatrix} 0 & 0 & 0 & 0 \\ 0 & 0 & 0 & 0 \\ 0 & 0 & 0 & 0 \\ 1 & 0 & 0 & 0 \\ 0 & 1 & 0 & 0 \\ 0 & 0 & 1 & 0 \\ 0 & 0 & 0 & -\frac{1}{v_{ex}} \end{bmatrix} \qquad c = \begin{bmatrix} 0 \\ 0 \\ 0 \\ 0 \\ 0 \\ \frac{\mu}{r}\frac{1}{\sqrt{r_x^2+r_y^2}}G_2 \\ 0 \end{bmatrix}^{(k-1)}$$

$$\tau_1 = \frac{r_z}{\sqrt{r_x^2+r_y^2}}$$

$$\tau_2 = \frac{1}{\sqrt{r_x^2+r_y^2}}$$

$$A = \begin{bmatrix} 0 & 0 & 0 & 1 & 0 & 0 & 0 \\ 0 & 0 & 0 & 0 & 1 & 0 & 0 \\ 0 & 0 & 0 & 0 & 0 & 1 & 0 \\ \omega^2 - \frac{\mu}{r^3}\left(1+G_1\right) & \frac{\mu}{r}G_3 & -\frac{\mu}{r^3}G_2\tau_2 r_x & 0 & 2\omega & 0 & 0 \\ -\frac{\mu}{r}G_3 & \omega^2 - \frac{\mu}{r^3}\left(1+G_1+G_2\tau_1\right) & 0 & -2\omega & 0 & 0 & 0 \\ 0 & 0 & -\frac{\mu}{r^3}\left(1+G_1+G_2\tau_1\right) & 0 & 0 & 0 & 0 \\ 0 & 0 & 0 & 0 & 0 & 0 & 0 \end{bmatrix}^{(k-1)}$$

$$B = \begin{bmatrix} 0 & 0 & 0 & 0 \\ 0 & 0 & 0 & 0 \\ 0 & 0 & 0 & 0 \\ 1 & 0 & 0 & 0 \\ 0 & 1 & 0 & 0 \\ 0 & 0 & 1 & 0 \\ 0 & 0 & 0 & -\frac{1}{v_{ex}} \end{bmatrix} \qquad c = \begin{bmatrix} 0 \\ 0 \\ 0 \\ 0 \\ 0 \\ \frac{\mu}{r}\frac{1}{\sqrt{r_x^2+r_y^2}}G_2 \\ 0 \end{bmatrix}^{(k-1)} \qquad \begin{aligned} \tau_1 &= \frac{r_z}{\sqrt{r_x^2+r_y^2}} \\ \tau_2 &= \frac{1}{\sqrt{r_x^2+r_y^2}} \end{aligned} \tag{6.5}$$

$$A = \begin{bmatrix} 0 & 0 & 0 & 1 & 0 & 0 & 0 \\ 0 & 0 & 0 & 0 & 1 & 0 & 0 \\ 0 & 0 & 0 & 0 & 0 & 1 & 0 \\ \omega^2 - \frac{\mu}{r^3} & 0 & 0 & 0 & 2\omega & 0 & 0 \\ 0 & \omega^2 - \frac{\mu}{r^3} & 0 & -2\omega & 0 & 0 & 0 \\ 0 & 0 & -\frac{\mu}{r^3} & 0 & 0 & 0 & 0 \\ 0 & 0 & 0 & 0 & 0 & 0 & 0 \end{bmatrix}^{(k-1)} \qquad B = \begin{bmatrix} 0 & 0 & 0 & 0 \\ 0 & 0 & 0 & 0 \\ 0 & 0 & 0 & 0 \\ 1 & 0 & 0 & 0 \\ 0 & 1 & 0 & 0 \\ 0 & 0 & 1 & 0 \\ 0 & 0 & 0 & -\frac{1}{v_{ex}} \end{bmatrix}$$

$$c = \begin{bmatrix} 0 \\ 0 \\ 0 \\ -\frac{\mu}{r^3}\left(G_1 r_x + G_2 \frac{r_x r_z}{\sqrt{r_x^2+r_y^2}}\right) + \frac{\mu}{r} G_3 r_y \\ -\frac{\mu}{r^3}\left(G_1 r_y + G_2 \frac{r_y r_z}{\sqrt{r_x^2+r_y^2}}\right) - \frac{\mu}{r} G_3 r_x \\ -\frac{\mu}{r^3}\left(G_1 r_z + G_2 \frac{r_z^2}{\sqrt{r_x^2+r_y^2}}\right) + \frac{\mu}{r} \frac{1}{\sqrt{r_x^2+r_y^2}} G_2 \\ 0 \end{bmatrix}^{(k-1)} \tag{6.6}$$

A set of flight time parameter sweeps was completed to determine if any of the gravity term options performed better or had advantages or disadvantages. For these parameter sweeps, the flight time was varied and the number of iterations required for convergence of the successive solution method was recorded. Fewer iterations is preferable as it decreases the number of computations and simulation run time. Two trajectories were examined, one landing on the Z axis (NP) and one landing on the X axis (EQ) of A1 with an 8 hr period. For more information on the trajectories see Section 8.4. Table 6.1 contains the iteration data for the EQ trajectory, while Table 6.2 corresponds to the NP trajectory. Option 2, Option 3 and Option 4 failed to converge on a solution after 12 iterations for a flight time of 760 seconds and are labeled NS for no solution. For these cases the trajectory alternated between two trajectories, never approaching a final answer. Increasing the maximum allowed number of iterations would not have yielded a successful trajectory. By failing to produce a solution these three options were eliminated from consideration. Even if these three had not been eliminated because of this failure, those options tended to take more iterations than the remaining options for the NP trajectories. For the EQ trajectories, Option 1 and Option 5 used the same number of iterations. However, for the NP trajectories Option 5 used slightly fewer iterations than Option 1 overall. Option 5 has all the higher order terms in the c vector, which makes it more convenient for changing to a higher order fidelity gravity model. Option 5 was chosen as the arrangement of gravity terms for the 2x2 spherical harmonics model. When not specifically stated, Option 5 is the one used in the presented results for the remainder of the dissertation. Note, that for this comparison an option placing the entire gravity model in c was not evaluated.

6.2 Dynamic Equations with the Gravity Model Removed from the State Matrix

In preparation for extending the 2x2 gravity model to the higher fidelity models, a sixth option of gravity term arrangement was analyzed. In Option 6, all the gravitational terms are placed in the c vector. This is equivalent to evaluating the gravitational acceleration in a separate model instead of parsing out the dominant term (Newtonian) in the A matrix (Option 5). The dynamics in the A matrix would be solely the asteroid's rotation and the relationship between position and velocity. The A, B and c for Option 6 are located in Equation 6.7.

$$A = \begin{bmatrix} 0 & 0 & 0 & 1 & 0 & 0 & 0 \\ 0 & 0 & 0 & 0 & 1 & 0 & 0 \\ 0 & 0 & 0 & 0 & 0 & 1 & 0 \\ \omega^2 & 0 & 0 & 0 & 2\omega & 0 & 0 \\ 0 & \omega^2 & 0 & -2\omega & 0 & 0 & 0 \\ 0 & 0 & 0 & 0 & 0 & 0 & 0 \\ 0 & 0 & 0 & 0 & 0 & 0 & 0 \end{bmatrix}^{(k-1)} \qquad B = \begin{bmatrix} 0 & 0 & 0 & 0 \\ 0 & 0 & 0 & 0 \\ 0 & 0 & 0 & 0 \\ 1 & 0 & 0 & 0 \\ 0 & 1 & 0 & 0 \\ 0 & 0 & 1 & 0 \\ 0 & 0 & 0 & -\frac{1}{v_{ex}} \end{bmatrix} \tag{6.7}$$

$$c = \begin{bmatrix} 0 \\ 0 \\ 0 \\ -\frac{\mu}{r^3}\left(r_x + G_1 r_x + G_2 \frac{r_x r_z}{\sqrt{r_x^2+r_y^2}}\right) + \frac{\mu}{r} G_3 r_y \\ -\frac{\mu}{r^3}\left(r_y + G_1 r_y + G_2 \frac{r_y r_z}{\sqrt{r_x^2+r_y^2}}\right) - \frac{\mu}{r} G_3 r_x \\ -\frac{\mu}{r^3}\left(r_z + G_1 r_z + G_2 \frac{r_z^2}{\sqrt{r_x^2+r_y^2}}\right) + \frac{\mu}{r} \frac{1}{\sqrt{r_x^2+r_y^2}} G_2 \\ 0 \end{bmatrix}^{(k-1)}$$

Comparison of the iterations required in the successive solution method between Option 5 and Option 6 are located in Table 6.3 for the NP and EQ trajectories. The successive solution method was able to design the trajectory for all the cases using Option 6. However, for shorter flight times Option 6 tended to require one more iteration than Option 5. Overall, Option 5 is a better method when it is feasible. When using the higher fidelity models it will be best to place the dominant term, such as the Newtonian, in the A matrix as opposed to placing the entire gravity model in the c vector. In the case where it is not possible to separate out the dominant term, such as when using a predefined gravity algorithm, the successive solution method will work adequately, though it may require more computation time.

6.3 Generalization to Higher Fidelity Gravity Models

In the previous section, it was shown that the best arrangement of terms between the matrix A and the vector c is to place the dominant gravitational acceleration term in A and the higher order terms in c. In the 4x4 spherical harmonics model the dominant term is the Newtonian, while for the spherical Bessel model it is the summation of the zero order and degree pairings over all the powers. The dominant term that belongs in the A matrix is the same for each vector component, as it is multiplied by the corresponding state component in the linear equation form. The position components are evaluated with the previous iteration. The dominant term for the 4x4 spherical harmonics model is listed in Equation 6.8, while the dominant term for the spherical Bessel is listed in Equation 6.9. The final arrangement of the terms for A, B and c are listed in Equation 6.10. The c contains the entire gravity model after the dominant terms have been removed.

$$dom = -\frac{\mu}{r^3} \tag{6.8}$$

$$dom = \alpha_{0,0} j_1 \left(\frac{\alpha_{0,0} r}{R_b} \right) \bar{A}_{0,0,0} + \alpha_{1,0} j_1 \left(\frac{\alpha_{1,0} r}{R_b} \right) \bar{A}_{1,0,0} + \alpha_{2,0} j_1 \left(\frac{\alpha_{2,0} r}{R_b} \right) \bar{A}_{2,0,0} \tag{6.9}$$

$$A = \begin{bmatrix} 0 & 0 & 0 & 1 & 0 & 0 & 0 \\ 0 & 0 & 0 & 0 & 1 & 0 & 0 \\ 0 & 0 & 0 & 0 & 0 & 1 & 0 \\ \omega^2 + dom & 0 & 0 & 0 & 2\omega & 0 & 0 \\ 0 & \omega^2 + dom & 0 & -2\omega & 0 & 0 & 0 \\ 0 & 0 & dom & 0 & 0 & 0 & 0 \\ 0 & 0 & 0 & 0 & 0 & 0 & 0 \end{bmatrix}^{(k-1)} \quad B = \begin{bmatrix} 0 & 0 & 0 & 0 \\ 0 & 0 & 0 & 0 \\ 0 & 0 & 0 & 0 \\ 1 & 0 & 0 & 0 \\ 0 & 1 & 0 & 0 \\ 0 & 0 & 1 & 0 \\ 0 & 0 & 0 & -\frac{1}{v_{ex}} \end{bmatrix}$$

$$c = \begin{bmatrix} 0 \\ 0 \\ 0 \\ \frac{\partial U}{\partial r_x} - dom \\ \frac{\partial U}{\partial r_y} - dom \\ \frac{\partial U}{\partial r_z} - dom \\ 0 \end{bmatrix}^{(k-1)} \tag{6.10}$$

Table 6.1: Required iterations comparison for the five arrangements of gravity terms, EQ trajectory.

Option 1		Option 2		Option 3		Option 4		Option 5	
tf (s)	iter	tf (s)	iter	tf (s)	iter	tf (s)	iter	tf (s)	iter
300	2	300	2	300	2	300	2	300	2
320	2	320	2	320	2	320	2	320	2
340	2	340	2	340	2	340	2	340	2
360	2	360	2	360	2	360	2	360	2
380	2	380	2	380	2	380	2	380	2
400	3	400	3	400	3	400	3	400	3
420	3	420	3	420	3	420	3	420	3
440	3	440	3	440	3	440	3	440	3
460	3	460	3	460	3	460	3	460	3
480	3	480	3	480	3	480	3	480	3
500	3	500	3	500	3	500	3	500	3
520	3	520	3	520	3	520	3	520	3
540	3	540	3	540	3	540	3	540	3
560	3	560	3	560	3	560	3	560	3
580	3	580	3	580	3	580	3	580	3
600	3	600	3	600	3	600	3	600	3
620	3	620	3	620	3	620	3	620	3
640	3	640	3	640	3	640	3	640	3
660	3	660	3	660	3	660	3	660	3
680	3	680	3	680	3	680	3	680	3
700	3	700	3	700	3	700	3	700	3
720	3	720	3	720	3	720	3	720	3
740	3	740	3	740	3	740	3	740	3
760	3	760	NS	760	NS	760	NS	760	3
780	3	780	3	780	3	780	3	780	3
800	3	800	3	800	3	800	3	800	3
820	3	820	3	820	3	820	3	820	3
840	3	840	3	840	3	840	3	840	3
860	3	860	3	860	3	860	3	860	3
880	3	880	3	880	3	880	3	880	3
900	3	900	3	900	3	900	3	900	3
920	3	920	3	920	3	920	3	920	3
940	3	940	3	940	3	940	3	940	3
960	3	960	3	960	3	960	3	960	3
980	3	980	3	980	3	980	3	980	3
1000	3	1000	3	1000	3	1000	3	1000	3

Table 6.2: Required iterations comparison for the five arrangements of gravity terms, NP trajectory.

Option 1		Option 2		Option 3		Option 4		Option 5	
tf (s)	iter	tf (s)	iter	tf (s)	iter	tf (s)	iter	tf (s)	iter
300	3	300	3	300	3	300	3	300	3
320	3	320	3	320	3	320	3	320	3
340	3	340	3	340	3	340	3	340	3
360	3	360	3	360	3	360	3	360	3
380	3	380	3	380	3	380	3	380	3
400	3	400	3	400	3	400	3	400	3
420	3	420	3	420	3	420	3	420	3
440	3	440	3	440	3	440	3	440	4
460	3	460	3	460	3	460	3	460	4
480	4	480	4	480	4	480	4	480	4
500	4	500	4	500	4	500	4	500	4
520	5	520	5	520	5	520	5	520	4
540	5	540	5	540	5	540	5	540	4
560	4	560	5	560	4	560	5	560	4
580	4	580	5	580	4	580	5	580	4
600	4	600	4	600	4	600	4	600	4
620	4	620	4	620	4	620	4	620	4
640	4	640	4	640	4	640	4	640	4
660	4	660	4	660	4	660	4	660	4
680	4	680	4	680	4	680	4	680	4
700	5	700	4	700	5	700	5	700	4
720	5	720	5	720	5	720	4	720	4
740	4	740	4	740	4	740	4	740	4
760	4	760	5	760	4	760	5	760	4
780	4	780	4	780	4	780	4	780	4
800	4	800	4	800	4	800	4	800	4
820	4	820	5	820	4	820	5	820	4
840	5	840	5	840	5	840	5	840	4
860	5	860	5	860	5	860	5	860	4
880	5	880	5	880	5	880	5	880	4
900	5	900	5	900	5	900	5	900	4
920	5	920	5	920	5	920	5	920	4
940	5	940	5	940	5	940	5	940	4
960	5	960	5	960	5	960	5	960	4
980	5	980	5	980	5	980	5	980	4
1000	5	1000	5	1000	5	1000	5	1000	4

Table 6.3: Required iterations comparison between Option 5 and Option 6 for NP and EQ trajectory.

NP Option 5		NP Option 6		EQ Option 5		EQ Option 6	
tf (s)	iter	tf (s)	iter	tf (s)	iter	tf (s)	iter
300	3	300	3	300	2	300	3
320	3	320	4	320	2	320	3
340	3	340	4	340	2	340	2
360	3	360	3	360	2	360	3
380	3	380	3	380	2	380	3
400	3	400	3	400	3	400	2
420	3	420	3	420	3	420	3
440	4	440	4	440	3	440	3
460	4	460	4	460	3	460	3
480	4	480	5	480	3	480	3
500	4	500	4	500	3	500	3
520	4	520	4	520	3	520	3
540	4	540	4	540	3	540	3
560	4	560	4	560	3	560	3
580	4	580	4	580	3	580	3
600	4	600	4	600	3	600	3
620	4	620	4	620	3	620	3
640	4	640	4	640	3	640	3
660	4	660	4	660	3	660	3
680	4	680	4	680	3	680	3
700	4	700	4	700	3	700	3
720	4	720	4	720	3	720	3
740	4	740	4	740	3	740	3
760	4	760	4	760	3	760	3
780	4	780	4	780	3	780	3
800	4	800	4	800	3	800	3
820	4	820	4	820	3	820	3
840	4	840	4	840	3	840	3
860	4	860	4	860	3	860	3
880	4	880	4	880	3	880	3
900	4	900	4	900	3	900	3
920	4	920	4	920	3	920	3
940	4	940	4	940	3	940	3
960	4	960	4	960	3	960	3
980	4	980	4	980	3	980	3
1000	4	1000	4	1000	3	1000	3

CHAPTER 7. DISCRETIZATION AND SCALING

Two items are needed to finalize the powered descent convex optimization algorithm, discretization and scaling. An optimizer works in discrete time with discrete trajectory steps, but the equations of motion are in continuous time. Therefore, the continuous equations of motion must be discretized. Scaling the parameters in the optimization problem proved to have a significant effect on the solver and successive solution method convergence.

7.1 Discretization

The equations of motion, while linear, are in continuous time; however, optimizers require the problem to be in discrete time points. To form a discrete system the problem is divided into n number of time points with a fixed dt time step between each point. Trapezoidal rule is used to propagate the trajectory between the points as demonstrated in Equation 7.1.

$$\vec{x}_j = \vec{x}_{j-1} + 0.5dt \left(A_j \vec{x}_j + A_{j-1} \vec{x}_{j-1} + B_j \vec{u}_j + B_{j-1} \vec{u}_{j-1} + c_j + c_{j-1} \right) \tag{7.1}$$

Each of the n points is represented this way, with j being the current point and $j-1$ the previous point. The problem can be rearranged (Equation 7.2), so that it is a function of the previous point and the coefficient matrices.

$$\vec{x}_j = \left[I - 0.5dtA_j \right]^{-1} \left[\left(I + 0.5dtA_{j-1} \right) \vec{x}_{j-1} + 0.5dt \left(B_j \vec{u}_j + B_{j-1} \vec{u}_{j-1} + c + c_{j-1} \right) \right] \tag{7.2}$$

This form replaces the continuous dynamics in Problem P3 as $n-1$ additional equality constraints levied on the problem. The first point, $j = 1$, corresponds to the known initial conditions.

In the analysis, a time step of 2.0 seconds was used. This was compared to smaller time steps of 1.0 second and 0.5 second, with negligible change in the results. The smaller time steps increase the number of equality constraints levied on the problem, thus increasing the number of calculations and simulation run time. Table 7.1 (NP trajectory) and Table 7.2 (EQ trajectory) contain comparisons of the propellant usage and number of required iterations for the 0.5 sec, 1.0 sec and 2.0 sec time steps landing on A1 with an 8 hr period. There is no appreciable difference between the time steps in terms of propellant used and iterations, as the difference in propellant usage appears in the fourth decimal place. A comparison of the position vectors for the NP trajectory between the 2.0 and 0.5 second time step is located in Figure 7.1. The difference is less than 0.5 m. Two seconds yields good accuracy, while containing a fourth of the number of equality constraints as the 0.5 sec case. Care should be taken to balance out the propagation accuracy and the number of equality constraints. If the flight time of the trajectory is not exactly divisible by the fixed time step, the time step will be adjusted slightly to allow each time step to be identical.

Table 7.1: Comparison of time step for NP case.

0.5 sec			1.0 sec			2.0 sec		
Flight Time (sec)	Prop Used (kg)	Iterations	Flight Time (sec)	Prop Used (kg)	Iterations	Flight Time (sec)	Prop Used (kg)	Iterations
400	5.40518	3	400	5.40524	3	400	5.40553	3
440	5.24067	2	440	5.24074	3	440	5.24084	2
480	5.16113	3	480	5.16119	3	480	5.16141	3
520	5.13941	3	520	5.13944	3	520	5.13955	3
560	5.18692	3	560	5.18695	3	560	5.18704	3
600	5.43829	3	600	5.43829	3	600	5.43829	3

7.2 Scaling

The algorithm variables, especially the vehicle state, were scaled to keep the values near one and to keep any variable from having extra emphasis or weighting due to its magnitude. Proper scaling is critical to convergence and optimizer success, so care must be taken when choosing the scale factors. Scaling is a common technique with optimization solvers.

All distance parameters are scaled by R_{sc}, velocity by v_{sc}, acceleration by g_{sc}, time by t_{sc},

Table 7.2: Comparison of time step for EQ case.

0.5 sec			1.0 sec			2.0 sec		
Flight Time (sec)	Prop Used (kg)	Iterations	Flight Time (sec)	Prop Used (kg)	Iterations	Flight Time (sec)	Prop Used (kg)	Iterations
400	5.52362	2	400	5.52369	2	400	5.52386	2
440	5.36071	3	440	5.36076	3	440	5.36101	3
480	5.28639	3	480	5.28645	3	480	5.28664	3
520	5.27109	3	520	5.27111	3	520	5.27122	3
560	5.31409	3	560	5.31412	3	560	5.31419	3
600	5.43829	3	600	5.43829	3	600	5.43829	3

angular rate by ω_{sc} and thrust by T_{sc}, as defined in Equations 7.3 through 7.10. The scale factors are applied by dividing the original value by the scale factor, ex. $\vec{r} = \vec{r}/R_{sc}$. Variable names have not been changed to indicate scaled or not scaled. The scaled version of the variable is used in all of the algorithm calculations when coded.

$$R_{sc} = \gamma \tag{7.3}$$

$$g_{sc} = \frac{\mu}{R_{sc}^2} \tag{7.4}$$

$$v_{sc} = \sqrt{R_{sc} g_{sc}} \tag{7.5}$$

$$t_{sc} = \sqrt{\frac{R_{sc}}{g_{sc}}} \tag{7.6}$$

$$\omega_{sc} = \sqrt{\frac{g_{sc}}{R_{sc}}} \tag{7.7}$$

$$m_{sc} = 1 \tag{7.8}$$

$$\mu_{sc} = \mu \tag{7.9}$$

$$T_{sc} = g_{sc} m_{sc} \tag{7.10}$$

The distance scale factor is set to the smallest semi-major axis value (γ), or an approximation of the shortest axis for nonellipsoidal asteroids. The mass is not scaled as indicated by setting the mass scale factor, m_{sc}, to 1. The mass variable used in the formulation, q, is the natural log of mass. The natural log function acts as a scaling function and keeps q near one.

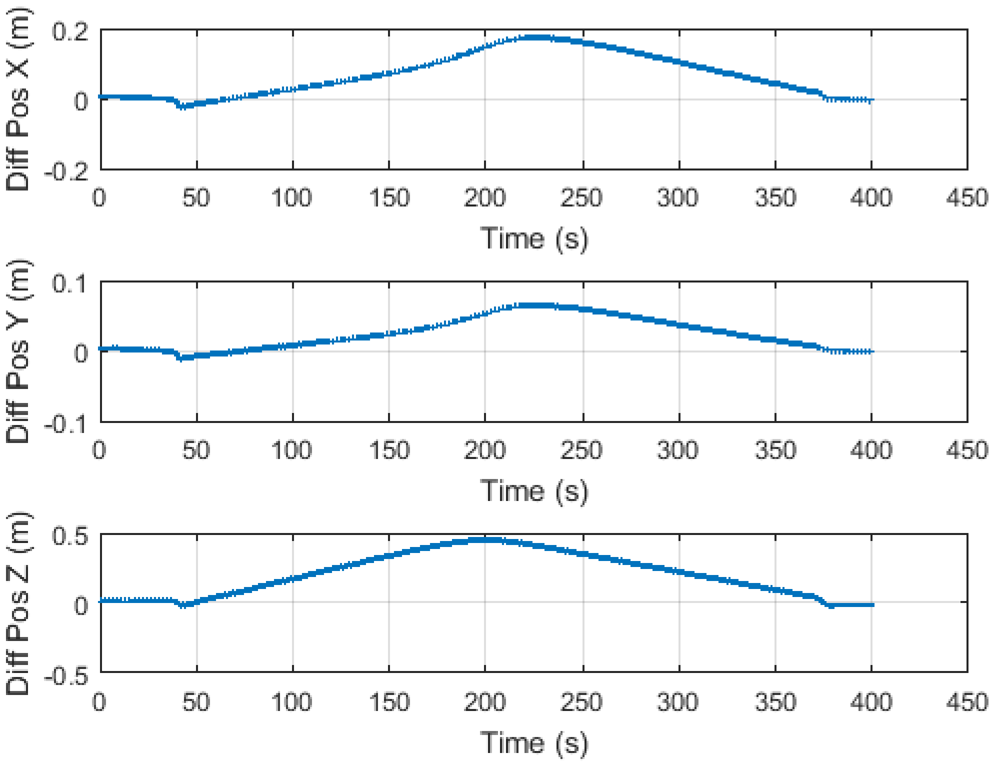

Figure 7.1: Comparison between time step of 0.5 sec and 2.0 sec for a 400 sec NP trajectory.

Special cases of parameters in their scaled form are listed in Equations 7.11 through 7.14.

$$v_{ex} = \frac{v_{ex}}{v_{sc}} \tag{7.11}$$

$$dt = \frac{dt}{t_{sc}} \tag{7.12}$$

$$\mu = \frac{\mu}{\mu_{sc}} = 1 \tag{7.13}$$

$$C_{l,m} r_0^2 = \frac{C_{l,m} r_0^2}{R_{sc}^2} \tag{7.14}$$

The exit velocity and time step between nodes are scaled as in Equations 7.11 and 7.12. The gravitational constant is scaled by itself, so that anywhere it is used in the equations it is now equal to 1, Equation 7.13. All the gravitational coefficients used in the 2x2 triaxial ellipsoid gravitational model are scaled as indicated in Equation 7.14, in order to keep the gravity model scaled properly. The coefficients based on the asteroid size replaced two terms in the gravity model, including a position squared term, thus requiring the scaling. In the 4x4 spherical harmonics and spherical Bessel gravity models the coefficients are nondimensional and therefore not scaled. Instead the reference radius (r_0) and the radius of the Brillouin sphere (r_B) are scaled by the distance scale factor to ensure proper scaling of the gravity model.

Proper scaling is critical to the optimizer success and the convergence success of the successive solution method. Originally, the problem was run without scaling and the optimizer had difficulty finding a feasible solution. Upon scaling, the optimizer no longer had cases where it failed to find a solution. Furthermore, the algorithm is sensitive to the choice of R_{sc}. When scaled by the asteroid's largest semi-major axis (α) there were several cases that oscillated between two trajectories, so that the successive solution method never converged after 12 iterations. Scaling by the smallest semi-major axis (γ) did not have any cases where the solver failed nor the successive solution method failed.

Asteroids are nonspherical and small, which cause the difference in semi-major axis length to be significant between the largest and smallest semi-major axes. When the vehicle flies below the largest semi-major axis length, the scaled radius vector is less than one when scaled by the largest semi-major axis length. The scaled gravity models have numerous multiples of this scaled radius vector in the denominator, causing the scaled gravitational acceleration magnitude to grow rapidly near the surface. An example of the scaled gravitational acceleration from the Newtonian model for a vehicle landing on the smallest semi-major axis of 250 m is located in Figure 7.2. The corresponding largest semi-major axis is 1000 m. The difference in magnitude near the surface of the asteroid is pronounced, 16 versus 1. The purpose of scaling is to keep the values near one, which scaling by the largest semi-major axis fails to do. The higher order terms for the gravity models include additional multiples of the radius in the denominator, which will cause the difference between the two scale factors to grow exponentially.

Tables 7.3 and 7.4 contain data for the NP and EQ trajectories highlighting the differences between no scaling, scaling with α and with γ. These trajectories used the Option 1 arrangement of the gravity terms, Equation 6.2, and landed on A1 with an 8 hr period. The smallest semi-major axis cases used fewer iterations than scaling by the largest semi-major axis, for cases that had solutions.

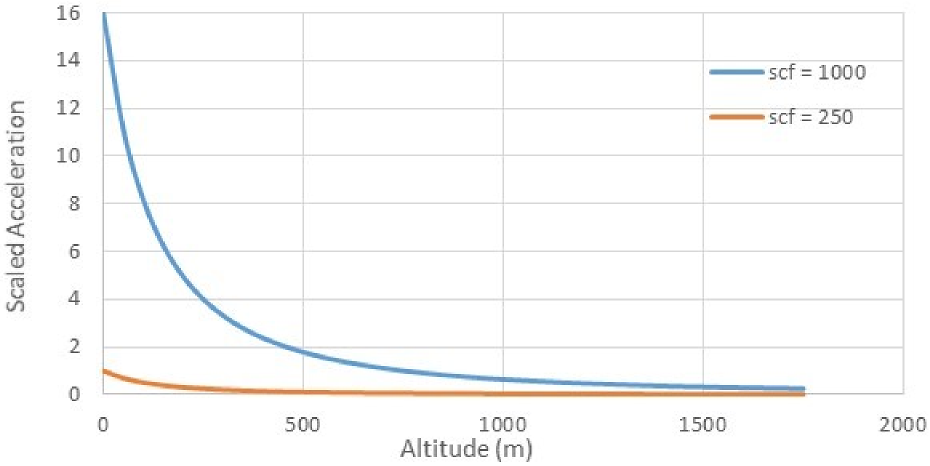

Figure 7.2: Scaled gravitational acceleration magnitude for a Newtonian gravity model with a scale factor of 1000 m and a scale factor of 250 m. Landing site located at a radius of 250 m.

Table 7.3: Iterations required for no scaling, scaling with the largest semi-major axis and scaling with the smallest semi-major axis, NP trajectory.

Not Scaled		Scaled by α		Scaled by γ	
tf (s)	iter	tf (s)	iter	tf (s)	iter
500	4	500	5	500	4
520	5	520	12	520	5
540	CF	540	4	540	5
560	CF	560	4	560	4
580	CF	580	4	580	4
600	CF	600	5	600	4
620	CF	620	6	620	4
640	CF	640	8	640	4
660	CF	660	4	660	4
680	CF	680	8	680	4
700	CF	700	6	700	5
720	5	720	8	720	5
740	NS	740	NS	740	4
760	5	760	NS	760	4
780	6	780	NS	780	4
800	CF	800	NS	800	4

CF: CVX solver failed to converge.

NS: successive solution method failed to converge.

Table 7.4: Iterations required for no scaling, scaling with the largest semi-major axis and scaling with the smallest semi-major axis, EQ trajectory.

Not Scaled		Scaled by α		Scaled by γ	
tf (s)	iter	tf (s)	iter	tf (s)	iter
500	3	500	5	500	3
520	3	520	12	520	3
540	3	540	4	540	3
560	3	560	4	560	3
580	CF	580	4	580	3
600	CF	600	5	600	3
620	CF	620	6	620	3
640	CF	640	8	640	3
660	3	660	4	660	3
680	3	680	8	680	3
700	3	700	6	700	3
720	3	720	8	720	3
740	3	740	NS	740	3
760	3	760	NS	760	3
780	3	780	NS	780	3
800	5	800	NS	800	3

CF: CVX solver failed to converge.

NS: successive solution method failed to converge.

CHAPTER 8. OPTIMIZATION SOLVER, VEHICLE, ASTEROID, AND TRAJECTORY MODELS

The algorithm formulated in the previous chapters was rigorously analyzed. A testbed was programmed in Matlab using the solver CVX. In order to show robustness, a variety of asteroid sizes, asteroid rotation speeds, and landing sites were examined. The nomenclature described in this chapter will be used throughout the dissertation to describe the analyzed cases. This is a three degree of freedom (3-DOF) analysis, so only the translational motion is investigated. A tolerance of 0.5 m was used in the successive solution method to verify that the final trajectory and the trajectory immediately preceding it are close enough for the gravity model representation. Smaller tolerances are achievable at the cost of more iterations.

8.1 Convex Optimization Solver

The convex optimization solver used in the analysis was CVX. CVX is a publicly available convex optimization package.[1] It is based in Matlab and works with Matlab as a plug-in, levying the programming and computational advantages of Matlab. CVX is designed to handle a wide range of convex optimization problems, which it refers to as disciplined convex programs. The disciplined convex programs applies a rule set that allows the program to easily recognize a convex problem. (Ref. Grant and Boyd (2011))

The CVX package contains two free optimization solvers, SDPT3 and SeDuMi. SDPT3 has been used in the analysis and performs admirably. SDPT3 is a conic optimizer originally designed to solve semi-definite quadratic linear problems. The admissible set of state variables is a convex cone, which is the product of positive semi-definite matrices, second order cones and

---

[1] http://cvxr.com/cvx/download/ v2.0 released 9/12/2013

non-negative orthants. The conic optimization problems include semidefinite program, second order cone program and linear program. (Ref. Tutuncu et al. (2003))

8.2 Vehicle Model

The vehicle is represented as a point mass, without physical dimensions and sizes, since this is a 3-DOF analysis. Only the basic characteristics of the vehicle: mass, thrust, and Isp are truly needed for the analysis. The vehicle's mass is 1400 kg with 400 kg devoted to propellant. The 1000 kg of dry mass is devoted to vehicle structure and hardware along with payload. The engines have an Isp of 225 sec and range in thrust with a maximum of 80 N and a minimum of 20 N. While this is considered low thrust, an analysis set was run with lower thrust, a maximum of 20 N and a minimum of 5 N. This case is referred to as lower thrust (LT). The vehicle exit velocity in the problem formulation is calculated in Equation 8.1.

$$v_{ex} = isp * g_0 \tag{8.1}$$

This is the product of the vehicle Isp and the reference sea level gravity (g_0) on Earth. Earth is used even though the vehicle is around an asteroid and far from Earth.

8.3 Asteroids

It was desired to show algorithm robustness by running it through a range of asteroids, starting with homogenous triaxial ellipsoidal asteroids and then extending to the binary asteroid, Castalia. The majority of the analysis and trends were completed with the triaxial ellipsoidal asteroids.

Three homogenous triaxial ellipsoidal asteroid sizes were examined, 1000 x 500 x 250 m (A1), 750 x 500 x 250 m (A2) and 500 x 500 x 250 m (A3). The three asteroids are depicted in Figure 8.1. The gravitational coefficients calculated with Equations 3.9 and 3.10 are located in Table 8.1.

The asteroids rotate at a constant spin rate along the +Z axis. The amount of time that it takes for the asteroid to complete one revolution is the rotation period. A period of 12 hours, 8 hours, 4 hours, and 2 hours was examined. These speeds are typical for asteroids. The

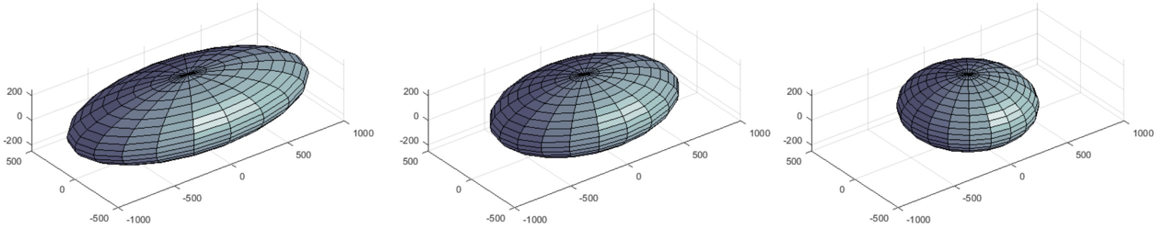

Figure 8.1: Three asteroids under investigation. 1000 x 500 x 250 m (left), 750 x 500 x 250 m (middle), 500 x 500 x 250 m (right)

Table 8.1: Triaxial ellipsoidal asteroid gravitational coefficients.

	$C_{2,0}r_0^2$ (m^2)	$C_{2,2}r_0^2$ (m^2)
A1	-112,500	37,500
A2	-68,750	15,625
A3	-37,500	0

corresponding rotation speeds, that is the magnitude of $\vec{\omega}$ in the equations of motion, are listed in Table 8.2

Table 8.2: Asteroid rotation speed.

	12 hr	8 hr	4 hr	2 hr
ω (rad/s)	$0.145\text{x}10^{-3}$	$0.218\text{x}10^{-3}$	$0.436\text{x}10^{-3}$	$0.873\text{x}10^{-3}$

The asteroid 4769 Castalia was examined using the higher fidelity gravity model, 4x4 Bessel, in order to test the algorithm with a real asteroid. Castalia is an elongated binary asteroid that has been under investigation over the last couple of decades and has high fidelity shape models, allowing the calculation of gravitational parameters. A mesh model, courtesy of Ref. Neese (2004)[2], shows the asteroid shape along with the Cartesian coordinate system used in this research. In order to keep the orientation of the asteroid similar to subsequent plots, the -Y axis is shown with the +X and +Z axes in the diagram. The rotation period is 4.07 hours along the +Z axis with a rotation speed of $0.429\text{x}10^{-3}$ rad/s.

Castalia is one of the asteroids used as a test of the spherical Bessel gravity model and has coefficients available for it and the 4x4 spherical harmonics gravity model. The Castalia

---

[2] http://sbn.psi.edu/pds/resource/rshape.html accessed 3/17/2016

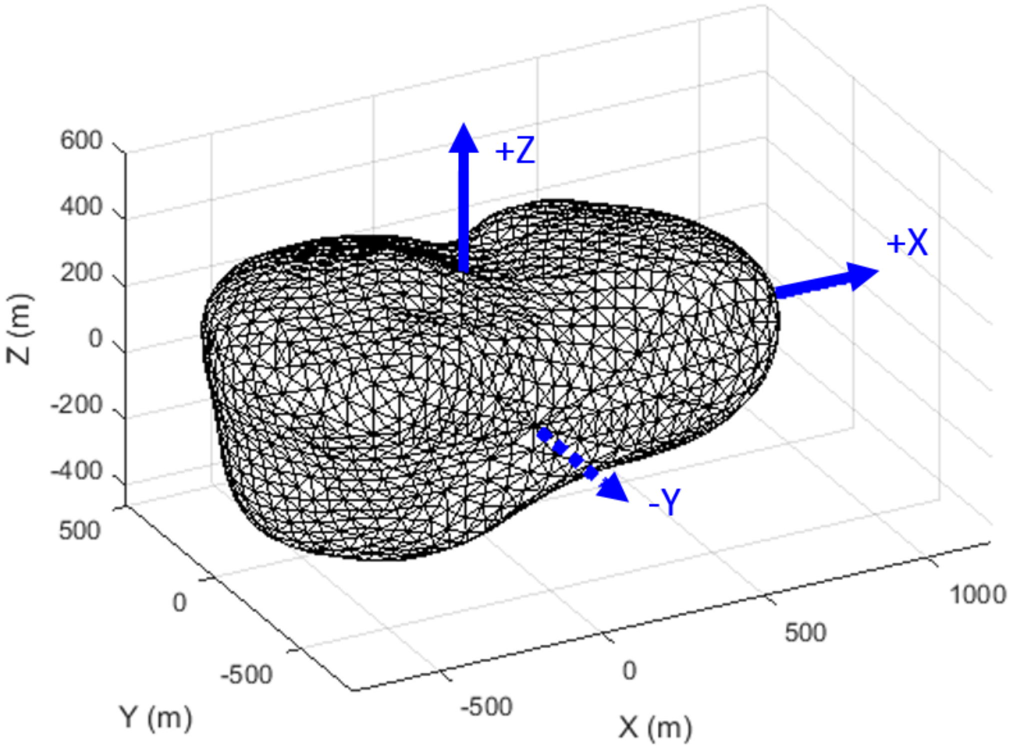

Figure 8.2: Asteroid Castalia with coordinate system axes. Note: -Y is shown as opposed to +Y.

coefficients for the 4x4 spherical harmonics gravity model are listed in Table 8.3, in the form used by the gravity model equations in Section 3.2.2. The original coefficients, found in Ref. Scheeres et al. (1996), were normalized with Equation 8.2 and nondimensionalized by a reference radius of 543.1 m. In order to switch the models at the Brillouin sphere (radius of 879 m), the coefficients were adjusted so that they are now nondimensionalized by a reference radius of 879 m. Also, the normalization has been removed.

$$N_{l,m} = \sqrt{\frac{(2-\delta_{0,m})\,(2l+1)\,(l-m)!}{(l+m)!}} \tag{8.2}$$

The coefficients for the spherical Bessel model are from Ref. Takahashi and Scheeres (2014) and located in Table 8.7. These coefficients are normalized by the $N_{n,m}$ which is equivalent to Equation 8.2 where l is replaced by n. The equations in Section 3.2.3 require the normalized coefficients, so no modification of the coefficients is required.

Table 8.3: Spherical harmonics coefficients for Castalia nondimensionalized by r_0 of 879 m.

l	m	$C_{l,m}$	$S_{l,m}$
0	0	1	0
1	0	0	0
1	1	0	0
2	0	-0.0941530721226227000	0
2	1	0	0
2	2	0.0386221708802032000	0
3	0	-0.0094306960553867600	0
3	1	-0.0096646530144642400	0.0003085249716756610
3	2	0.0005095733510737160	0.0000496280133219619
3	3	0.0006764919241294330	-0.0004510932876038110
4	0	0.0160148134554870000	0
4	1	0.0003741215783250580	0.0000562703186911672
4	2	-0.0016737827782259100	0.0001286873467518270
4	3	0.0000534752798894485	-0.0000152151977144734
4	4	0.0001549890964672470	-0.0000210587362565960

8.4 Triaxial Ellipsoidal Asteroid Landing Trajectories

Two landing sites were chosen for the triaxial ellipsoidal asteroid analysis to bound landing on the asteroid. The north pole (NP) trajectory lands on the +Z axis. The pole of the asteroid is where the gravitational acceleration is the strongest, including the largest change of gravitational acceleration over the trajectory. The north pole is on the spin axis, so effects of rotation are not felt. The second landing site on the +X axis, corresponds to an equatorial trajectory (EQ). This axis experiences the largest effects of the rotation spin, as the largest centripetal force occurs here with the longest semi-major axis. Also, the landing site does not stay at a fixed point in space and the trajectory end point must match the landing site's rotational speed. Sample trajectories for the NP and EQ are depicted in Figure 8.3.

The trajectories cover 1000 m altitude from the initial starting conditions until reaching the landing site. As the asteroid size changes, the starting conditions are based off the semi-major axes lengths. The main set of initial conditions include uprange and out of plane position and velocity components that will need to be eliminated. The initial conditions for the NP and EQ are located in the top two rows in Table 8.4. A second set of initial conditions correspond to

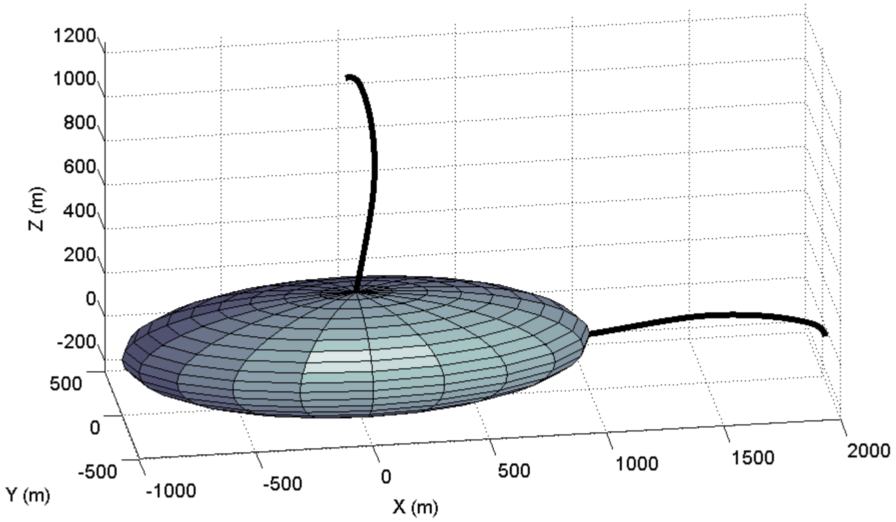

Figure 8.3: NP (top) and EQ (right) trajectories.

hover trajectories. This type of trajectory starts directly over the landing site where the vehicle has remained fixed over the landing site for a significant amount of time prior to the burn start. In order to remain fixed over the landing site, the velocity must match the rotational speed of the landing site determined from the asteroid rotation vector and vehicle initial position vector. Hover trajectories are commonly seen in literature. The bottom two rows in Table 8.4 contain the initial conditions for these trajectories, which will be denoted with a _hov. The NP_LT and EQ_LT trajectories have the same starting conditions as the NP and EQ.

Table 8.4: Initial conditions for the trajectories.

	r_{0_x} (m)	r_{0_y} (m)	r_{0_z} (m)	v_{0_x} (m/s)	v_{0_y} (m/s)	v_{0_z} (m/s)
NP, NP_LT	-50	-50	$1000+\gamma$	2	1	0
EQ, EQ_LT	$1000+\alpha$	-50	-50	0	2	1
NP_hov	0	0	$1000+\gamma$	$\vec{\omega} \times \vec{r}_0$		
EQ_hov	$1000+\alpha$	0	0	$\vec{\omega} \times \vec{r}_0$		

γ is the semi-major axis length corresponding to the Z axis.
α is the semi-major axis length corresponding to the X axis.

8.5 Castalia Landing Trajectories

Three landing sites on Castalia were provided in Ref. Takahashi and Scheeres (2014). All three of these sites were analyzed and are referred to as LS1, LS2 and LS3 to distinguish them from the equatorial and north pole landing sites used on the ellipsoidal asteroids. The sites move away from pure polar and equatorial sites due to the geometry of the asteroid and the site's locations. The coordinates of the landing sites are listed in Table 8.5 and marked on the asteroid in Figure 8.4. The velocity of the landing site is the speed due to the rotation of the asteroid ($\vec{\omega} \times \vec{r}_f$), listed in Table 8.5.

The initial locations of the vehicle were chosen to mirror the initial starting points in Section 8.4. The trajectories all start at an altitude of 1000 m. The out of plane and uprange cases were offset in position in the direction of basis vectors determining the landing site plane, one in the longitudinal direction and one in the latitudinal direction. Initial velocity components were applied in the direction of the basis vectors. The initial position and velocity magnitudes are the same as the ellipsoidal trajectories in Table 8.4. The hover trajectories start over the landing site with a velocity that keeps the vehicle directly over the site. The values for the initial vehicle states are located in Table 8.6.

Table 8.5: Castalia landing site coordinates and associated velocity.

	r_{f_x} (m)	r_{f_y} (m)	r_{f_z} (m)	v_{f_x} (m/s)	v_{f_y} (m/s)	v_{f_z} (m/s)
LS1	-345	-67	370	0.0287	-0.148	0
LS2	459	23.5	302	-0.0101	0.197	0
LS3	41.8	-348	-168	0.149	0.0179	0

Table 8.6: Initial conditions for the Castalia trajectories.

	r_{0_x} (m)	r_{0_y} (m)	r_{0_z} (m)	v_{0_x} (m/s)	v_{0_y} (m/s)	v_{0_z} (m/s)
LS1, LS1_LT	-1066.1	-157.5	1060.6	1.097	-1.823	0.689
LS2, LS2_LT	1323.3	18.2	809.8	-0.652	1.969	0.835
LS3, LS3_LT	97.6	-1227.8	-645.3	2.037	-0.190	0.902
LS1_hov	-1020.9	-199.6	1095.0	0.086	-0.438	0
LS2_hov	1293.3	66.7	851.6	-0.029	0.555	0
LS3_hov	149.8	-1243.3	-600.2	0.533	0.064	0

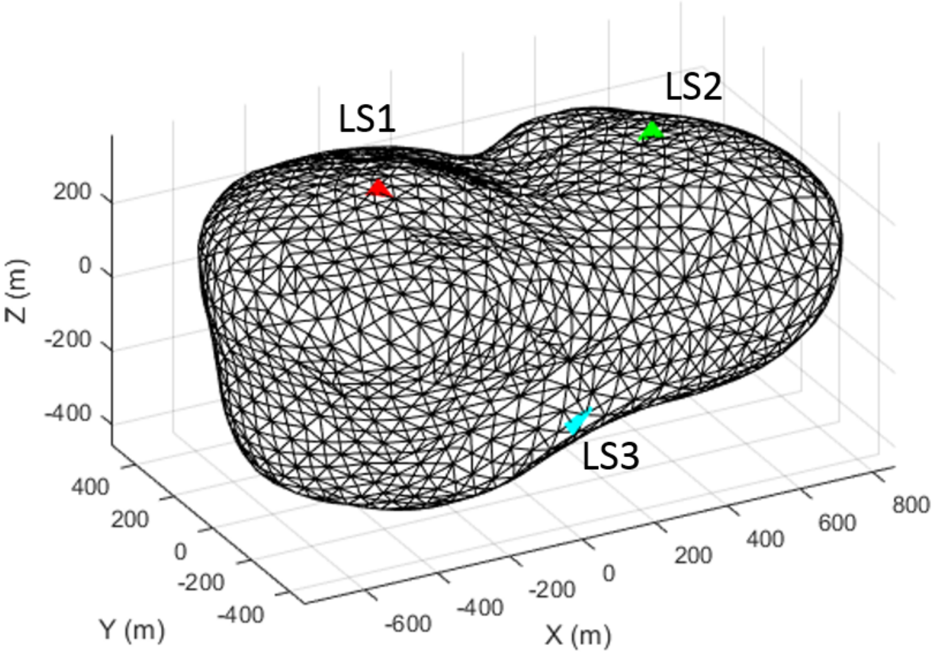

Figure 8.4: Castalia with the three landing sites highlighted.

Table 8.7: Normalized interior spherical Bessel coefficients for Castalia nondimensionalized by r_B of 879 m.

l	n	m	$\bar{A}_{l,n,m}$	$\bar{B}_{l,n,m}$
0	0	0	1.802974690E+00	0.000000000E+00
0	1	0	-1.735007668E-02	0.000000000E+00
0	1	1	-7.131813697E-02	1.362482061E-04
1	0	0	7.391186806E-01	0.000000000E+00
1	1	0	-6.119001962E-02	0.000000000E+00
1	1	1	-2.455384409E-01	-1.169035081E-02
1	2	0	-3.371599844E-01	0.000000000E+00
1	2	1	1.180985071E-02	6.489313919E-03
1	2	2	4.615366023E-01	7.966833023E-03
1	3	0	-2.479669965E-02	0.000000000E+00
1	3	1	-6.776972878E-02	-2.154017728E-03
1	3	2	-1.242368501E-02	-1.469634423E-02
1	3	3	1.646083195E-02	-3.564784335E-02
1	4	0	8.533444910E-02	0.000000000E+00
1	4	1	8.902368720E-03	-3.112486340E-03
1	4	2	-1.212298075E-01	1.113145643E-02
1	4	3	2.067640881E-02	6.400094817E-03
1	4	4	1.211059773E-01	8.463361733E-03
1	5	0	3.018500456E-02	0.000000000E+00
1	5	1	7.178322357E-02	7.861637879E-04
1	5	2	-1.826079507E-02	6.890550646E-03
1	5	3	-3.846474551E-02	6.227751644E-03
1	5	4	-1.010549987E-02	-1.977976238E-02
1	5	5	-1.127225191E-02	-3.851601031E-02

Table 8.7 continued from previous page. Normalized interior spherical Bessel coefficients for Castalia nondimensionalized by r_B of 879 m.

l	n	m	$\bar{A}_{l,n,m}$	$\bar{B}_{l,n,m}$
2	0	0	5.155596040E-02	0.000000000E+00
2	1	0	-4.271461929E-02	0.000000000E+00
2	1	1	-1.802760480E-01	-3.275896829E-02
2	2	0	-3.029474832E-01	0.000000000E+00
2	2	1	6.068636081E-02	2.979474150E-02
2	2	2	3.650090715E-01	1.558292408E-02
2	3	0	1.609467527E-02	0.000000000E+00
2	3	1	1.892772671E-02	-1.133832717E-02
2	3	2	-8.062631405E-02	-7.173968387E-02
2	3	3	-6.812518249E-02	-5.601270273E-02
2	4	0	8.246146486E-02	0.000000000E+00
2	4	1	-8.723520344E-03	-1.831448635E-02
2	4	2	-1.200619102E-01	3.344907003E-02
2	4	3	4.474184742E-02	4.650009823E-02
2	4	4	1.262690634E-01	4.623192337E-02
2	5	0	1.559764022E-02	0.000000000E+00
2	5	1	4.641755365E-02	9.536984724E-03
2	5	2	1.862640789E-02	4.615891556E-02
2	5	3	-1.649314982E-03	-8.760890819E-03
2	5	4	-3.571548246E-02	-8.785179345E-02
2	5	5	-5.760270197E-02	-6.099876735E-02

CHAPTER 9. TRAJECTORY ANALYSIS FOR OUT OF PLANE AND UPRANGE CASES

Flight time is fixed for the optimal propellant problem in the trajectory design algorithm. Parameter sweeps were performed by varying the flight time to see the effect of flight time on propellant usage and number of iterations required in the successive solution method. The small number of required iterations shows stability in the successive solution method. Ultimately, the flight time that consumes the least amount of propellant over all the flight times, optimal flight time, is desired. Parameter sweeps were performed for all four spin rates on the three triaxial ellipsoidal asteroids. Propellant usage is a tiny fraction of the propellant onboard the spacecraft. This implies that in the future less mass needs to be allocated towards propellant and more can be allocated for payload. A discussion of thrust profiles for the various trajectories and the need for a 2x2 gravity model follows the flight time parameters sweeps and the sample designed trajectories.

9.1 Flight Time Parameter Sweeps for a North Pole Landing

The flight time parameter sweeps for the NP trajectories are located in Figures 9.1 through 9.4. Comparison of the four periods for A1 (largest asteroid) is located in Figure 9.1 and for A3 (smallest asteroid) in Figure 9.2. The spin rate, determined by the period, has no effect on propellant usage for the NP cases. This is expected as the NP landing site is located on the spin axis, thus the landing site is stationary. The NP trajectories are sensitive to the asteroid size as seen in Figure 9.3, which compares the three asteroid sizes for the 8 hour period. Similar trends are seen in Figure 9.4, which compares the asteroid sizes for the 2 hour period. The asteroid size determines the gravitational attraction, which is strongest at the NP landing site. Also, the change in acceleration during the descent burn is largest for the north pole landings.

Comparison of iterations required for the successive solution method is located in Figures 9.5 and 9.6. The majority of trajectories required 3 or 4 iterations with a small number requiring 2 or 5 iterations. The top bar chart in Figure 9.5 is for A1, 1000 x 500 x 250 m, the bottom chart for A2, 750 x 500 x 250 m, and A3, 500 x 500 x 250 m, is located in Figure 9.6. Each color represents a rotational period. Unlike propellant usage, there are no clear trends with respect to flight time, spin rate, nor asteroid size.

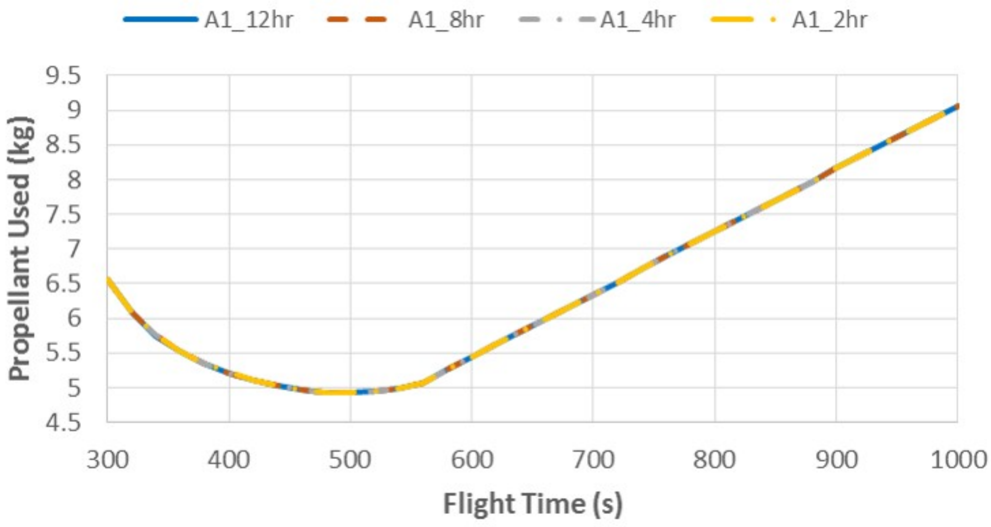

Figure 9.1: NP trajectory propellant usage parameter sweep for A1 (1000 x 500 x 250 m) with all four spin rates.

9.2 Flight Time Parameter Sweeps for a Equatorial Landing

The flight time parameter sweeps for the EQ trajectories are located in Figures 9.7 through 9.10. Propellant usage for the EQ trajectories is sensitive to the spin rate. The EQ landing site is the fastest spinning location on the asteroid surface as it is on the longest axis. Parameter sweep comparison of the four periods for A1 (largest asteroid) is located in Figure 9.7 and for A3 (smallest asteroid) in Figure 9.8. Clear differences are seen between the speeds. The fastest spinning cases require more propellant than the slower ones. EQ trajectories are fairly

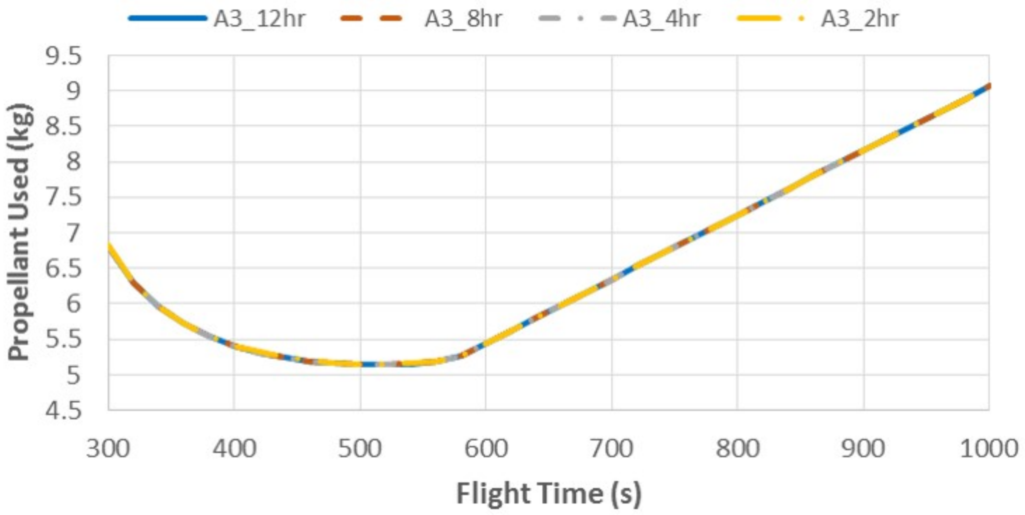

Figure 9.2: NP trajectory propellant usage parameter sweep for A3 (500 x 500 x 250 m) with all four spin rates.

insensitive to the asteroid size. Figure 9.9, which compares the three asteroid sizes for the 8 hour period, shows no changes in propellant usage between the asteroid sizes. Figure 9.10, which compares the asteroid sizes for the 2 hour period, indicates tiny changes in propellant usage between the three asteroids. These changes are not significant to show sensitivity to the asteroid size.

Comparison of iterations required for the successive solution method is located in Figures 9.11 and 9.12. The EQ trajectories required 2 or 3 iterations. The top bar chart in Figure 9.11 is for A1, 1000 x 500 x 250 m, the bottom chart for A2, 750 x 500 x 250 m, and A3, 500 x 500 x 250 m, is located in Figure 9.12. Each color represents a rotational period. Unlike propellant usage, there are no clear trends with respect to flight time, spin rate, nor asteroid size. The one noticeable trend is that EQ cases require the same or fewer number of iterations than the NP.

9.3 Designed Trajectories

Figures 9.13 through 9.15 take an in-depth look at a single EQ trajectory landing on A1 with an 8 hour period corresponding to the optimal flight time of 512 seconds. The position vector

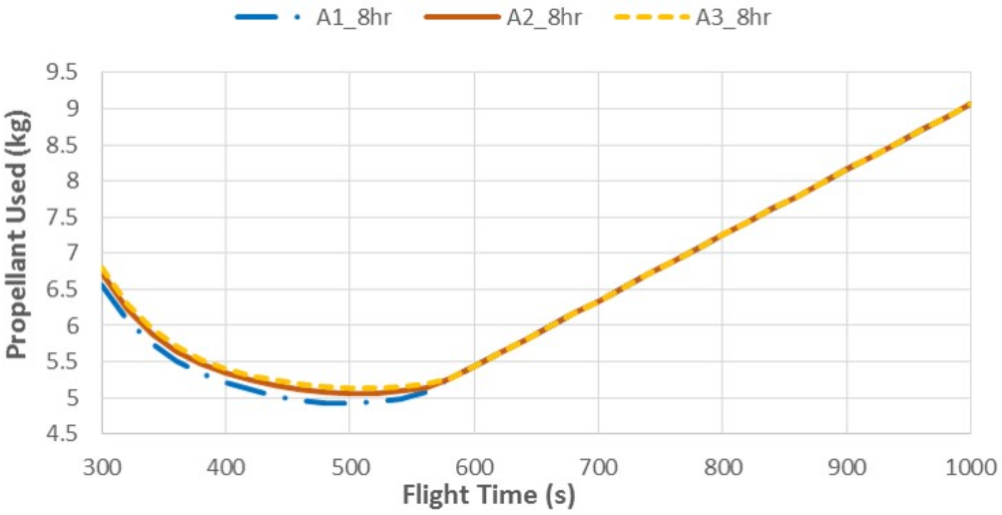

Figure 9.3: NP trajectory propellant usage parameter sweep with an 8 hour period for the three asteroid sizes.

as it changes throughout the iterations is shown in Figure 9.13. The initial trajectory that feeds the gravity model on the first successive solution is shown in green and uses the initial point for the entire trajectory. After the first iteration is complete, the maximum position difference between the initial trajectory and the first iteration's trajectory is 1002 m, the distance from the landing site to the initial vehicle state. The second and third iterations are very close to the first iteration. The maximum position difference between the first and second iterations is 1.53 m. When the trajectory design is completed the maximum distance between the second and third iterations is 0.006 m. The thrust magnitude for all three iterations is shown in Figure 9.14, with no noticeable difference. Once the first iteration's trajectory is designed, the remaining iterations contain minor corrections.

All the trajectory parameters for the final designed EQ trajectory are located in Figure 9.15. The vehicle position vector is shown relative to the asteroid and the corresponding landing site. The velocity vector is successfully designed to have zero velocity relative to the landing site, thus achieving a soft landing. The difference between the slack variable and the acceleration vector magnitude is on the order of $2\text{x}10^{-9}$ m/s^2, proving that the relaxed problem is identical to the original problem for the designed trajectory. The individual thrust components are the profile that would feed the vehicle controller, when flying the profile as designed.

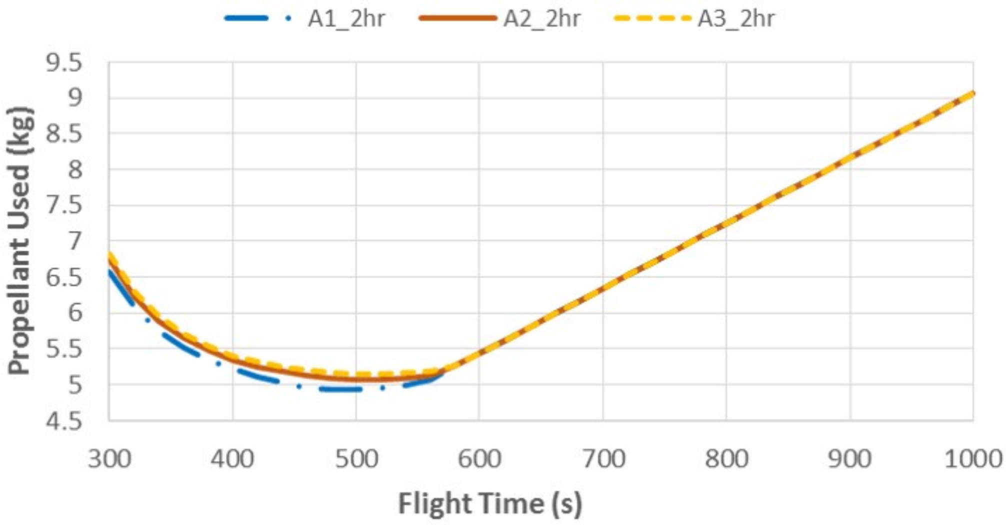

Figure 9.4: NP trajectory propellant usage parameter sweep with a 2 hour period for the three asteroid sizes.

The NP optimal propellant usage trajectory for A1 with an 8 hour period corresponds to a flight time of 488 seconds. This trajectory requires four iterations in the successive solution method, while the EQ required three. After the first iteration is complete the maximum position difference between the initial trajectory and the first iteration's trajectory is 1002 m, the distance from the landing site to the initial vehicle state. There are small differences in the position vector between the first iteration's solution and the remaining iterations as seen in Figure 9.16. The first iteration throttled down to the minimum thrust level slightly after the other iterations and throttled back up to the maximum thrust at the end of flight, see Figure 9.17. The later iterations did not return to the maximum thrust at the end of flight. The maximum difference in distance between the first and second iterations is 38.34 m and 0.95 m between the second and third iterations. When the trajectory design is completed, the maximum distance between the third and fourth iterations is 0.18 m. The trajectory parameters for the final designed NP trajectory are located in Figure 9.18. Like the EQ trajectory, the difference between the slack variable and the acceleration vector magnitude is on the order of $2\text{x}10^{-9}$ m/s^2.

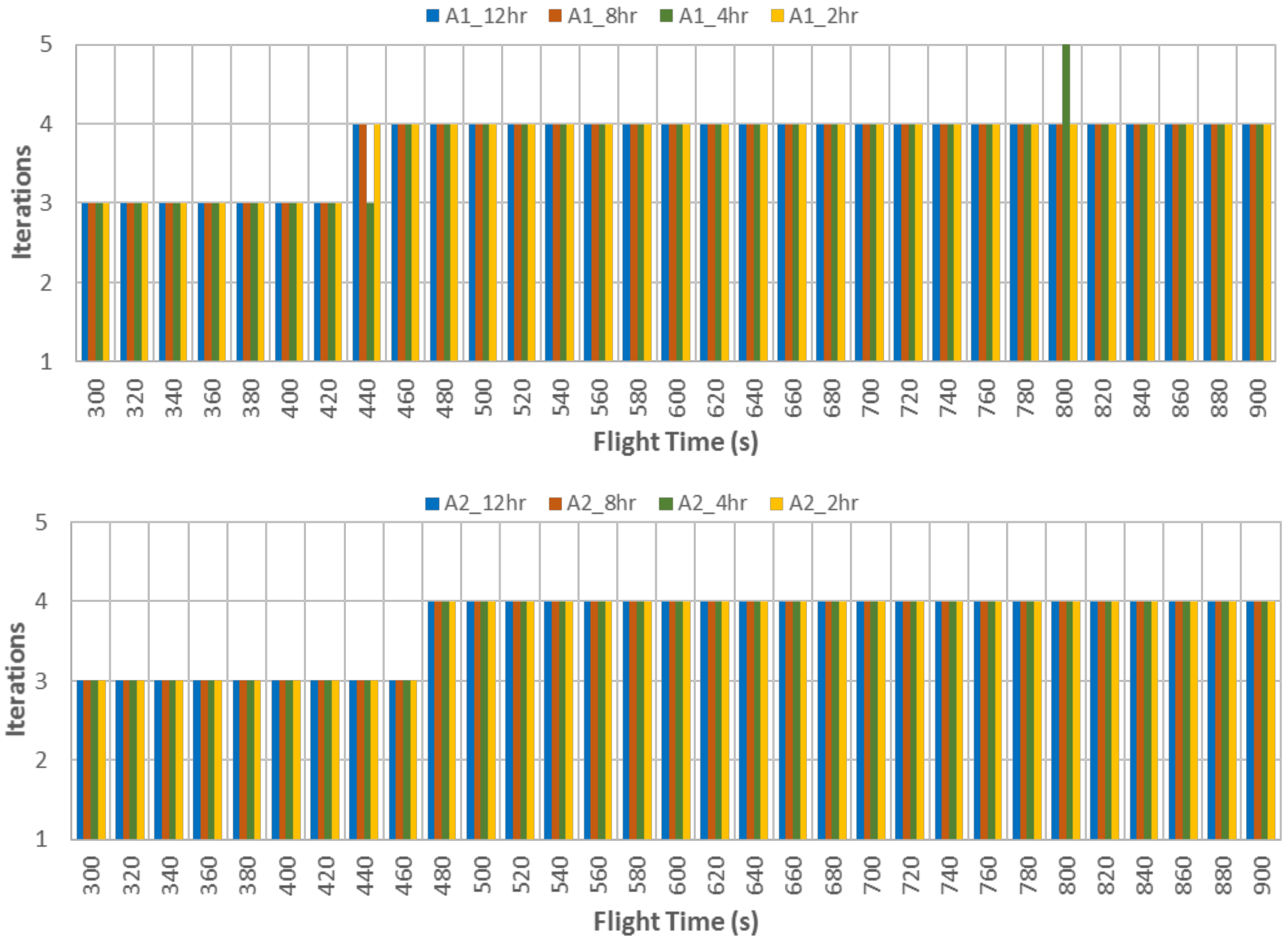

Figure 9.5: NP comparison of trajectory iterations required for the four spin rates with A1 (top) and A2 (bottom).

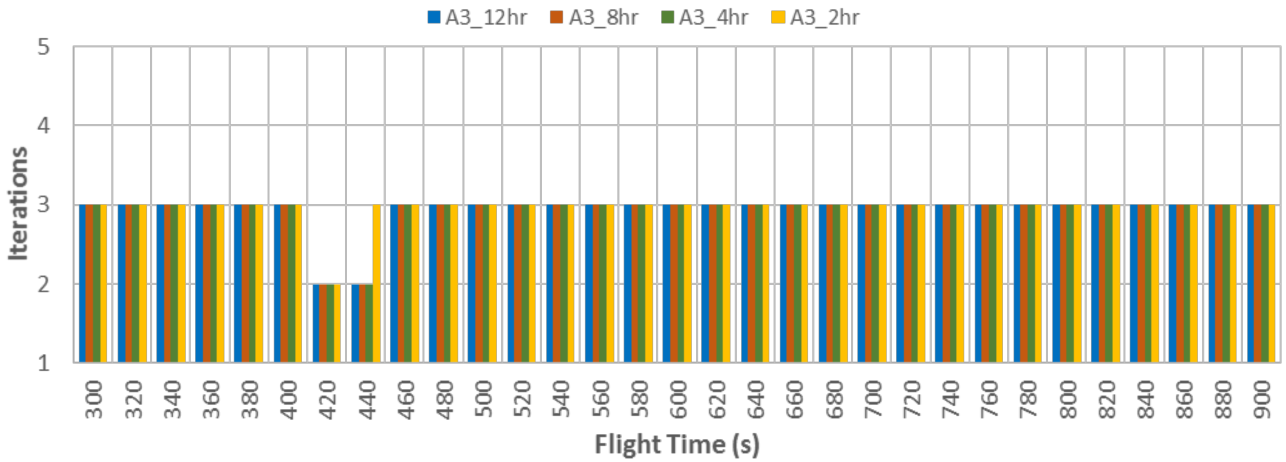

Figure 9.6: NP comparison of trajectory iterations required for the four spin rates with A3 (bottom).

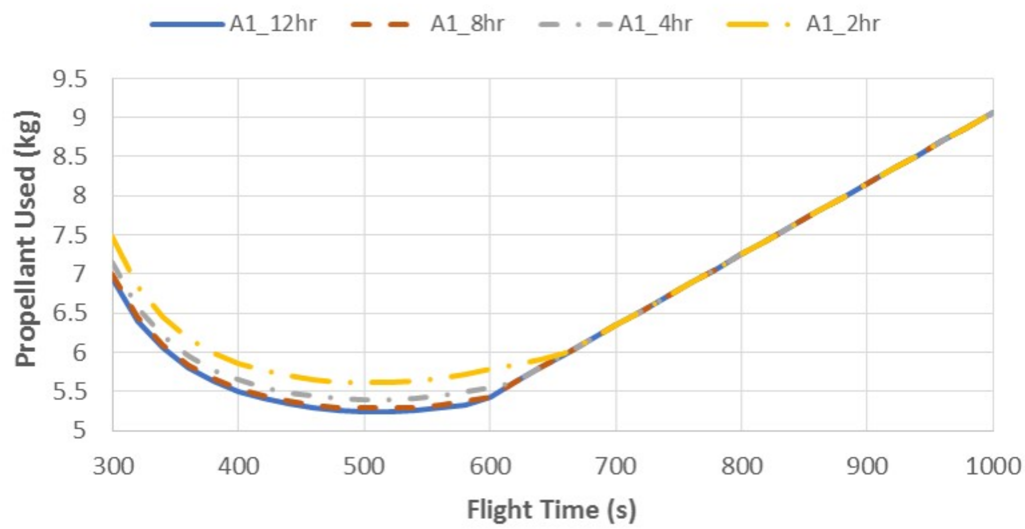

Figure 9.7: EQ trajectory propellant usage parameter sweep for A1 (1000 x 500 x 250 m) with all four spin rates.

9.4 Optimal Thrust Magnitude Profile

The thrust magnitude profile during flight follows the traditional bang-bang as dictated by Optimal Control Theory. This bang-bang refers to the thrust magnitude following the maximum or minimum thrust value and then rapidly changing to the other thrust bound. The trajectories fell into three categories: maximum-minimum-maximum, maximum-minimum and minimum for the entire flight. An example for each of the three categories is located in Figure 9.19. The shortest flight times followed the maximum-minimum-maximum and the longest flight times were all minimum.

On the right-hand side of the plots in Figures 9.1 through 9.4 and 9.7 through 9.11 all the parameter sweeps align and use the same amount of propellant. At this point the trajectories have reached the all minimum thrust profile. For these long flight times, the trajectory is swinging out to consume excess time, so it never needs to use maximum thrust. The effects of consuming the excess time dominates the effects of asteroid size and rotation speed.

Table 9.1 contains the flight times corresponding to the switches between the thrust profile categories. This is for the A1 asteroid with an 8 hr period for all six trajectories. The middle row corresponds to the start of the maximum-minimum thrust profile and the bottom row

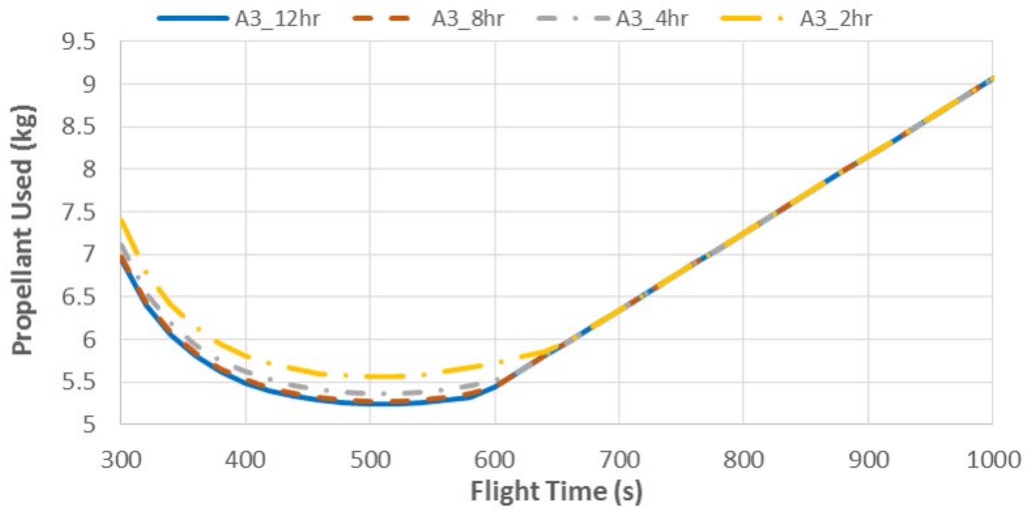

Figure 9.8: EQ trajectory propellant usage parameter sweep for A3 (500 x 500 x 250 m) asteroid with all four spin rates.

corresponds to the switch to all minimum. The top line is the optimal flight time, smallest propellant usage. The optimal flight time occurs before the switch to maximum-minimum for the equatorial cases and after the switch for the north pole cases. This switch is within 30 seconds of the optimal flight time for the higher thrust cases and 90 seconds for the lower thrust case. Propellant usage is flat in this region, so the difference in optimal propellant usage and propellant usage at the switch to maximum-minimum is within 0.5% for all cases except NP_LT which is 1.5%, (see Table 9.2) . This switch point is a reasonable first cut at determining the optimal flight time, if no other methods are readily available. Table 9.2 is the propellant used percentage difference between the optimal flight time and the thrust profile switches.

The optimal flight time occurs before the switch to the all minimum thrust profile for all the trajectories. The propellant usage difference is within 2.5% between the all minimum and the optimal flight time for the higher thrust cases. However, the propellant usage has a steeper slope at the switch to all minimum. This is seen in the 19% difference for the lower thrust cases. Therefore, it is advantageous to ensure that the mission flight time is before the switch to all minimum.

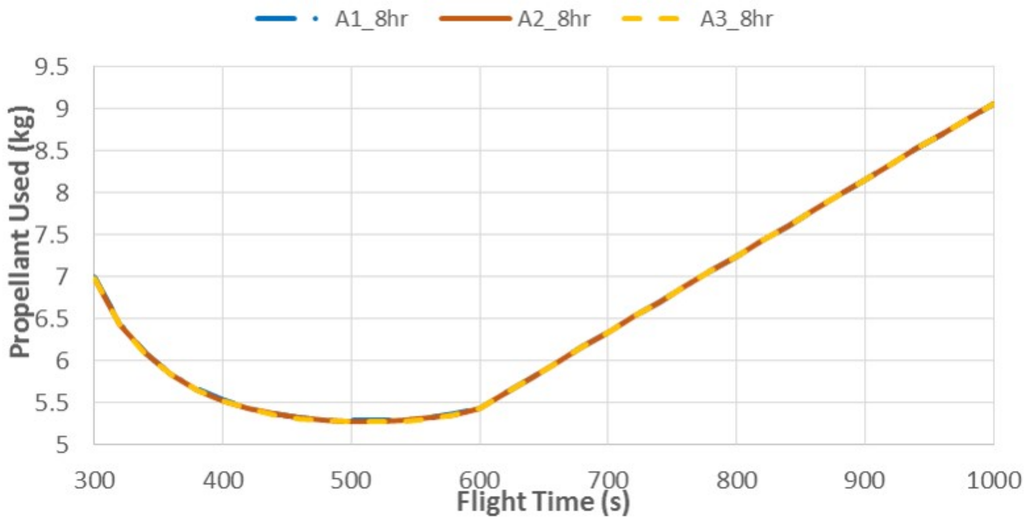

Figure 9.9: EQ trajectory propellant usage parameter sweep with an 8 hour period for the three asteroid sizes.

Table 9.1: Flight times corresponding to the optimal flight time and thrust profile switches.

(s)	NP	EQ	NP_hov	EQ_hov	NP_LT	EQ_LT
optimal propellant	488	512	501	525	897	1044
start maximum-minimum	465	521	474	529	811	1100
start all minimum	553	598	502	536	1503	1758

9.5 Effects of Non-Newtonian Gravity Terms

In order to show that a minimum of a 2x2 gravity model is required in the asteroid trajectory design, the trajectory was designed with lower fidelity models and then run open loop in a 2x2 environment. The open loop simulates the translational dynamics of the vehicle following the designed thrust profile, assuming perfect navigation and control. No corrections are made if the vehicle drifts off the trajectory due to disturbances in the environment. For this particular open loop run, the only disturbance is the 2x2 gravity model. The simulation ends when the vehicle reaches zero altitude. If the designed thrust profile ends before this point, the last thrust value and direction is held.

The trajectory was designed using the same processes with the only difference being the gravity model. Three gravity models were used: a constant gravity model, the Newtonian

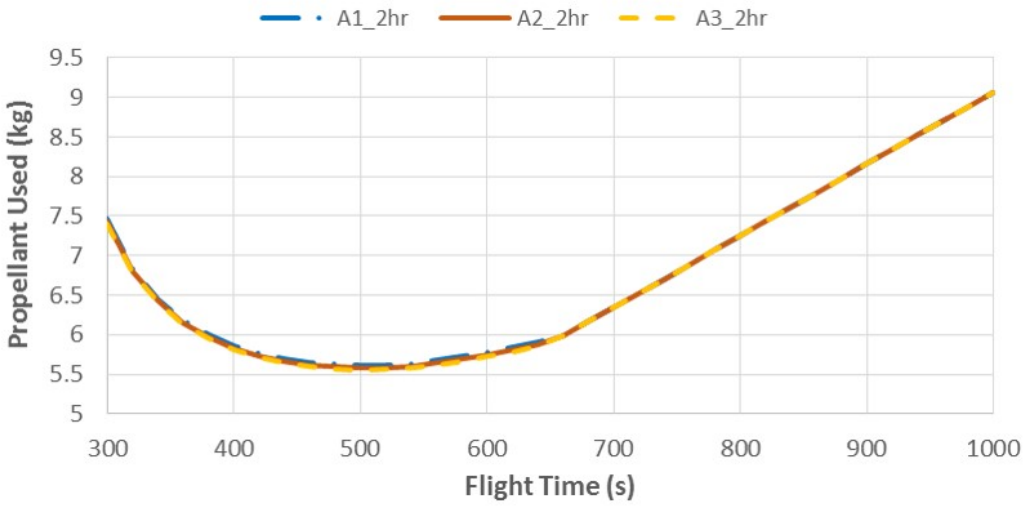

Figure 9.10: EQ trajectory propellant usage parameter sweep with a 2 hour period for the three asteroid sizes.

Table 9.2: Percent difference in propellant used from the optimal propellant case.

	NP	EQ	NP_hov	EQ_hov	NP_LT	EQ_LT
start maximum-minimum	0.33%	0.019%	0.45%	0.002%	1.5%	0.16%
start all minimum	1.8%	2.5%	0.17%	0.19%	18.7%	18.8%

model and the 2x2 model. The constant gravitational model magnitude uses the acceleration at the landing site, with the acceleration vector perpendicular to the landing site. Newtonian gravitational acceleration is given in Equation 3.8. The 2x2 trajectory was designed and run through the open loop simulation to show that the open loop simulation is an adequate way to test the lower fidelity models.

Both the NP trajectory and the EQ trajectory were tested in this fashion with a flight time of 480 seconds for A1 with an 8 hour period. The NP case was unable to design a trajectory using the constant gravity model as the optimization method failed. The EQ was able to design a trajectory with constant gravity, though it consumed 2.5 times more propellant in the design than the 2x2 trajectory. When the EQ was flown open loop it never reached the asteroid surface, in fact the altitude never decreased always increasing for all of flight. Figure 9.20 shows the increase in altitude throughout flight (top) and compares the open loop position vector to

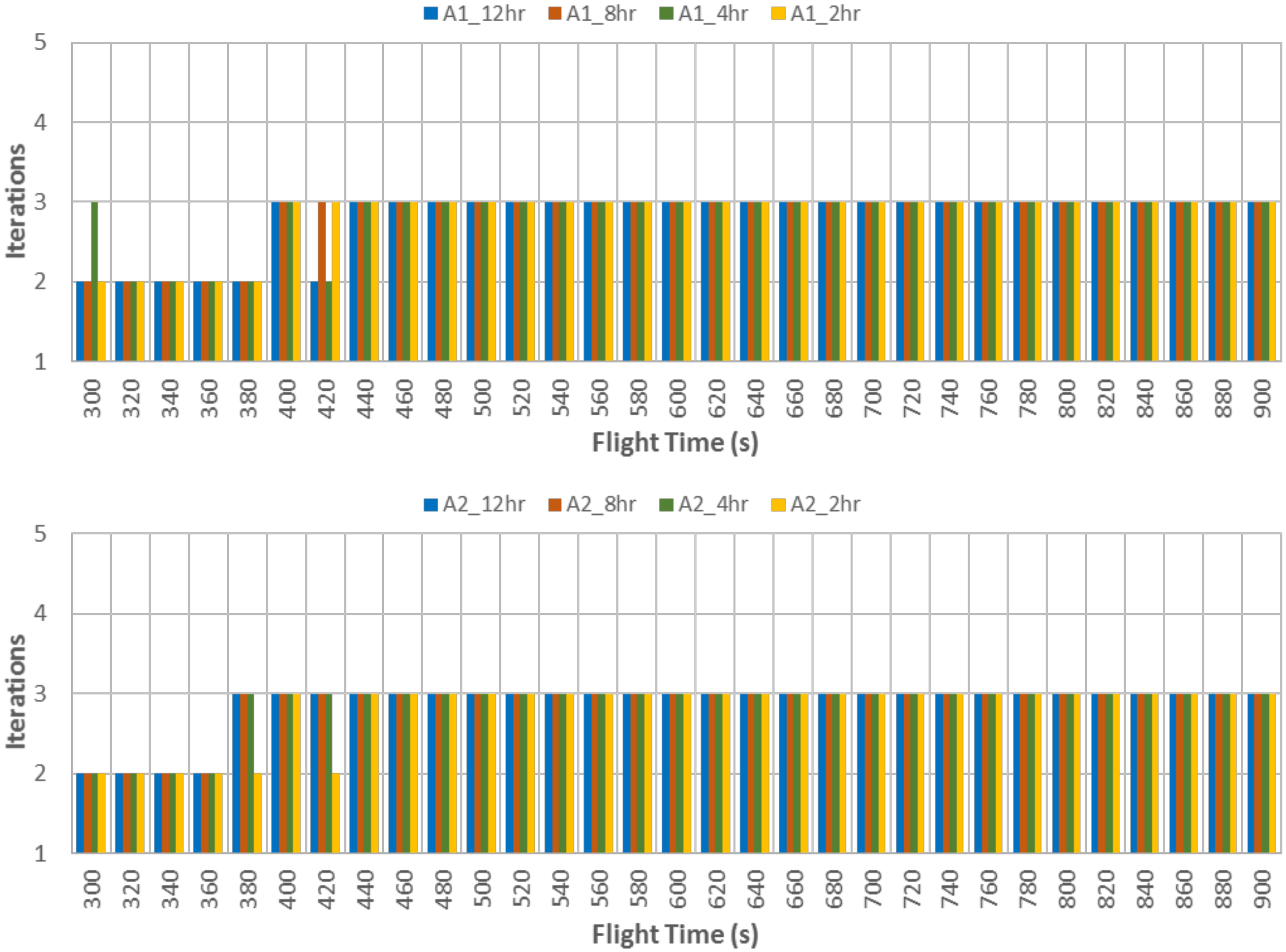

Figure 9.11: EQ comparison of trajectory iterations required for the four spin rates with A1 (top) and A2 (bottom).

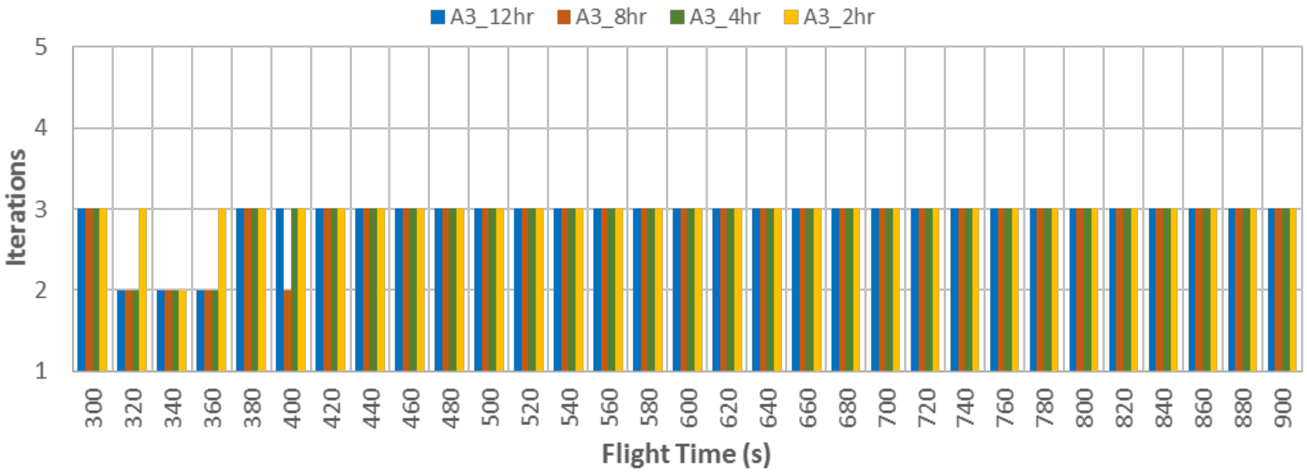

Figure 9.12: EQ comparison of trajectory iterations required for the four spin rates with A3.

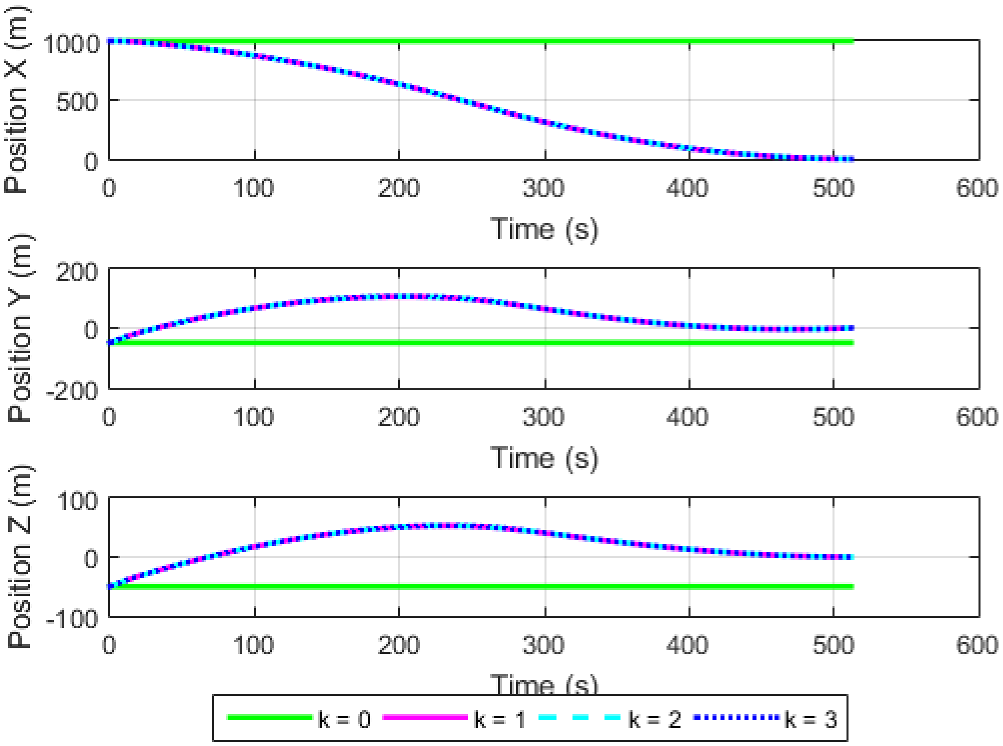

Figure 9.13: Position vector comparison for the different iterations with an EQ trajectory on A1, 8 hr period, 512 sec flight time. k=0 feeds the gravity model for the first optimization.

the designed trajectory, the input to the open loop (bottom). Clearly, a constant gravity model is not feasible when designing an asteroid powered descent trajectory.

Table 9.3 contains the position and velocity errors relative to the landing site upon reaching zero altitude. The Newtonian NP is not listed as it also never reached the landing site. The altitude plot (top) along with a comparison of the NP open loop results to the designed trajectory (bottom) are shown in Figure 9.21. Thirty seconds from the end of flight the open loop begins diverging from the designed trajectory. The lowest altitude that the vehicle achieved was 32 m. The 2x2 reached the landing site with minimum error, which is expected. The EQ Newtonian case also reached the landing site with decent accuracy. As expected, it was farther from the landing site than the 2x2 case. However, since the NP Newtonian did not reach the landing site, Newtonian is not an adequate model for asteroid powered descent trajectory design.

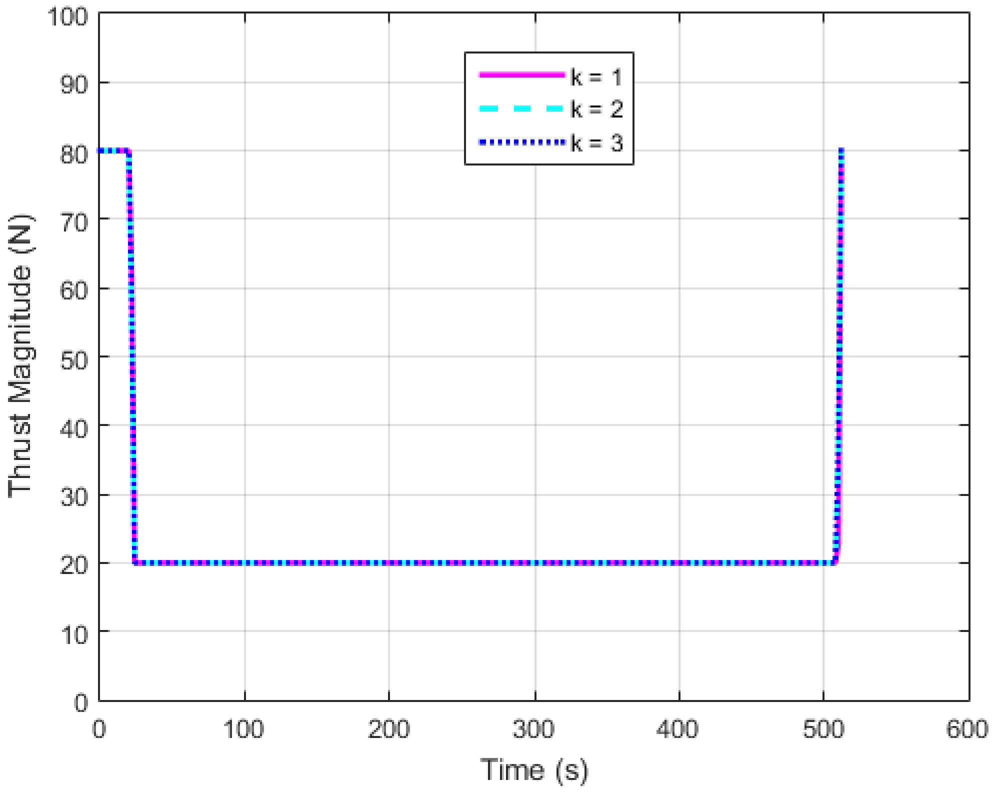

Figure 9.14: Thrust magnitude comparison for the different iterations with an EQ trajectory on A1, 8 hr period, 512 sec flight time.

Table 9.3: Open loop gravity models results. Error is with respect to the landing site.

	NP 2x2	EQ 2x2	EQ Newtonian
Position Error x (m)	-0.009	0.000	0.000
Position Error y (m)	-0.003	-0.367	-1.076
Position Error z (m)	0.000	-0.001	0.109
Velocity Error x (m/s)	-0.006	-0.027	-0.359
Velocity Error y (m/s)	-0.002	-0.010	-0.111
Velocity Error z (m/s)	-0.021	-0.004	-0.047
Prop Used (kg)	4.934	5.306	5.519

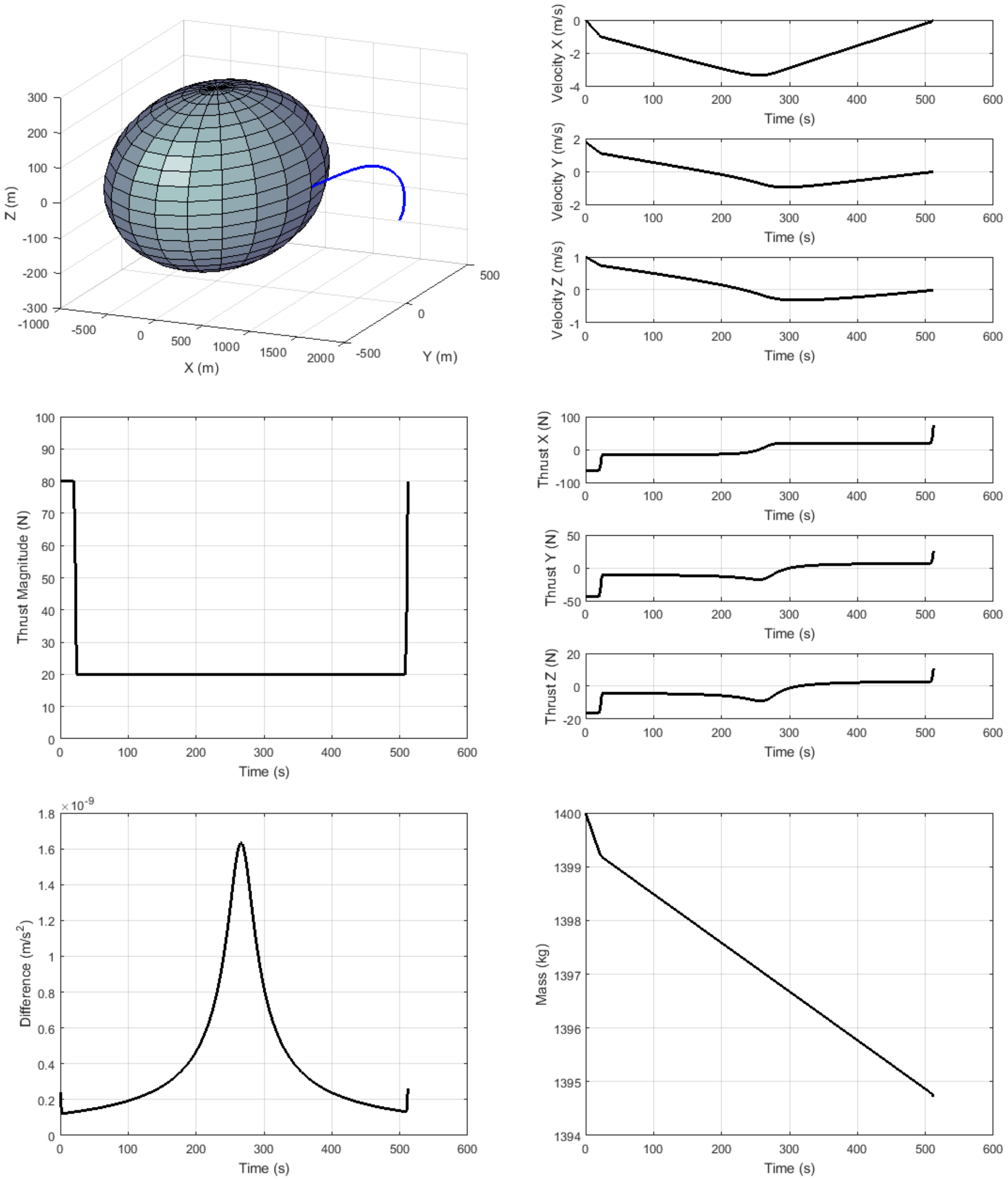

Figure 9.15: A1 8 hr period EQ trajectory for a 512 sec flight time. Top left: 3-D vehicle position, Top right: velocity components relative to the landing site, Middle left: thrust magnitude, Middle right: thrust components, Bottom left: difference between the slack variable and the acceleration vector, Bottom right: mass profile.

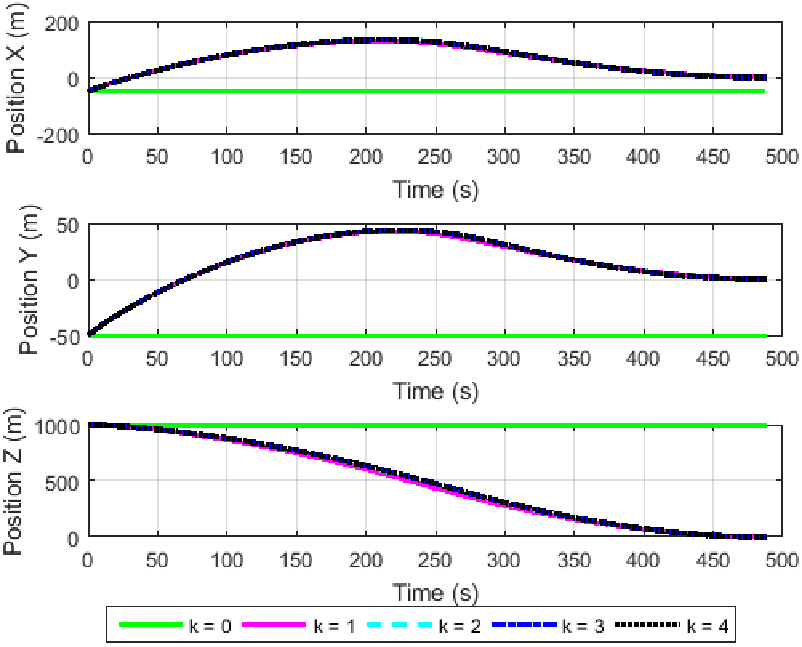

Figure 9.16: Position vector comparison for the different iterations with a NP trajectory on A1, 8 hr period, 488 sec flight time. k=0 feeds the gravity model for the first optimization.

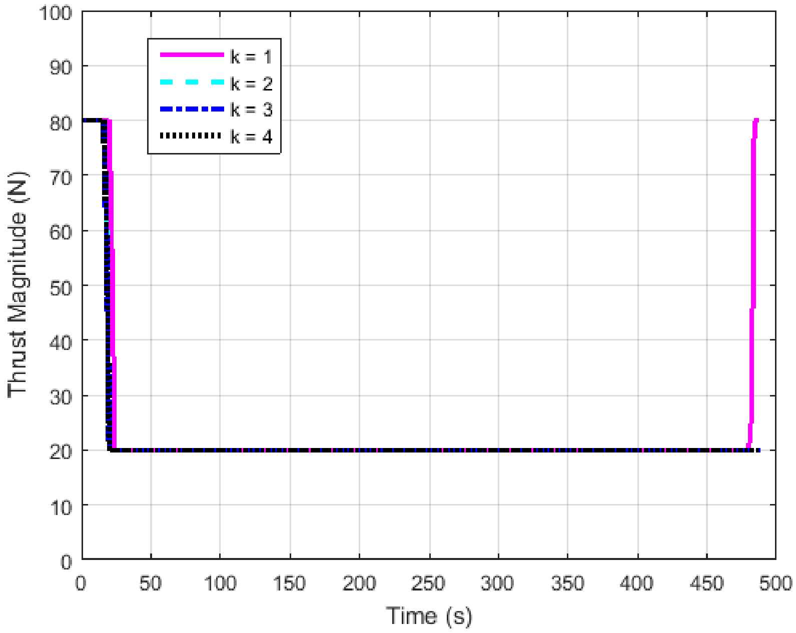

Figure 9.17: Thrust magnitude comparison for the different iterations with a NP trajectory on A1 8 hr period with a 488 sec flight time.

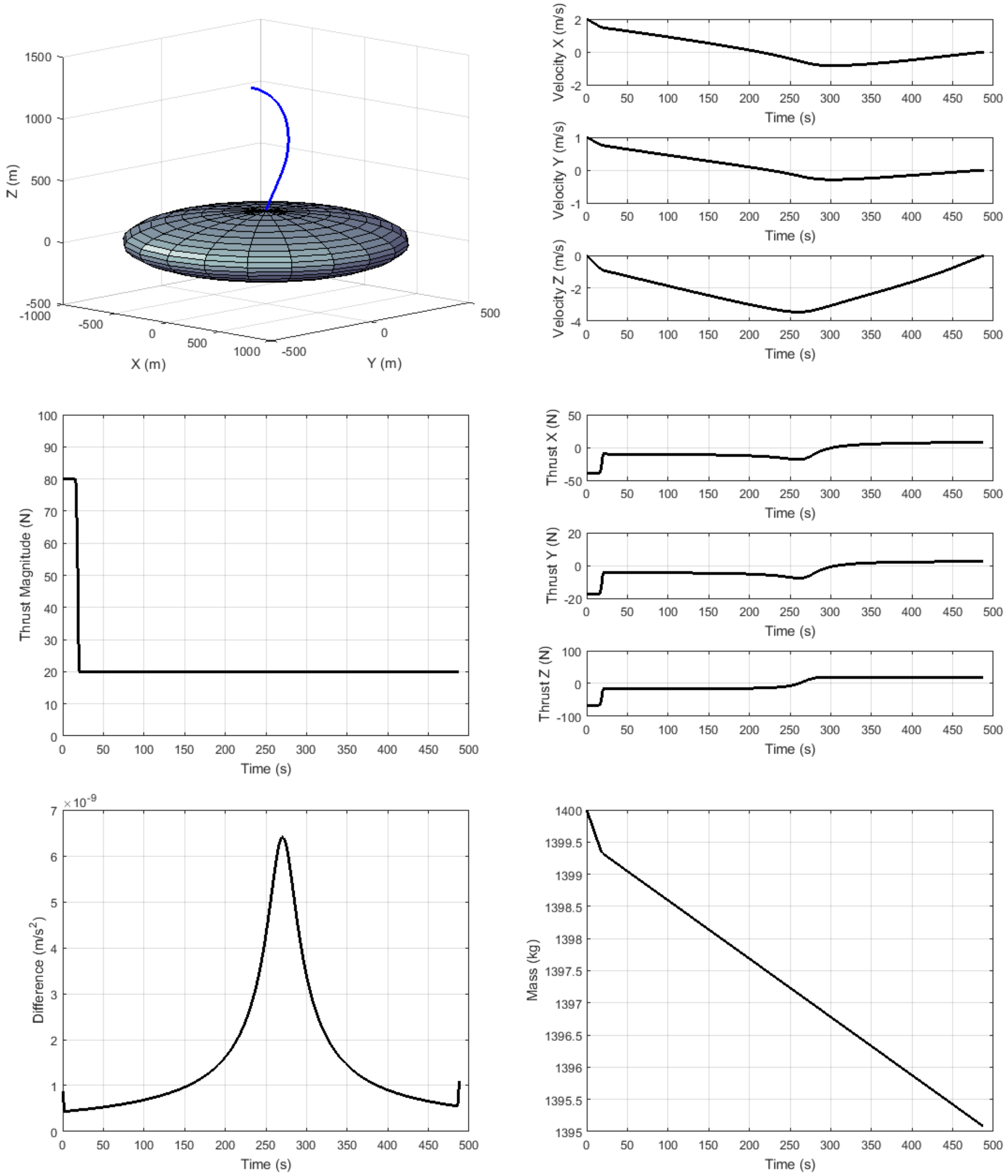

Figure 9.18: A1 8 hr period NP trajectory for a 488 sec flight time. Top left: 3-D vehicle position, Top right: velocity components relative to the landing site, Middle left: thrust magnitude, Middle right: thrust components, Bottom left: difference between the slack variable and the acceleration vector, Bottom right: mass profile.

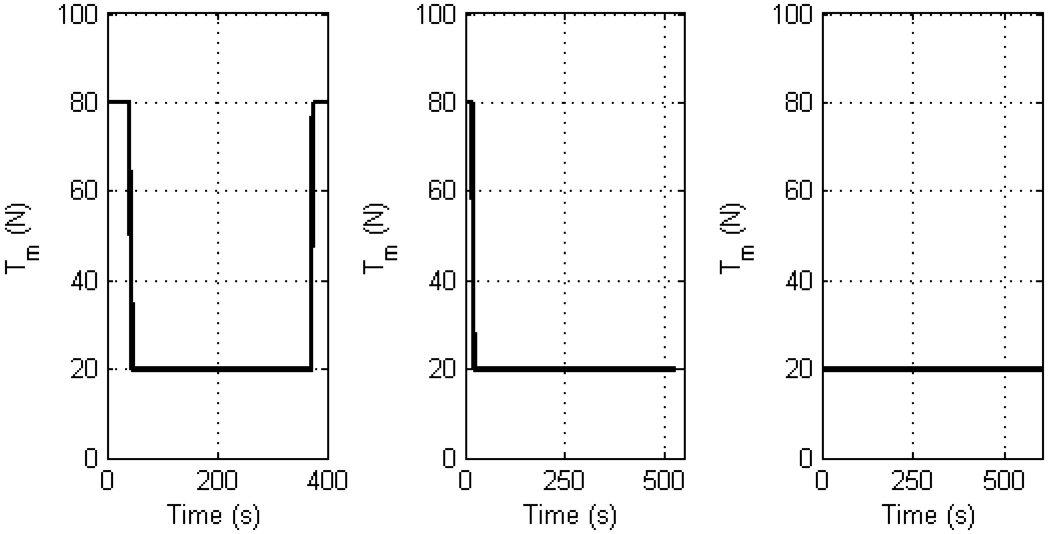

Figure 9.19: Thrust profiles for EQ A1 with a 400 sec (left), 525 sec (middle), and 600 sec (right) flight time, showing the three different categories of thrust profiles.

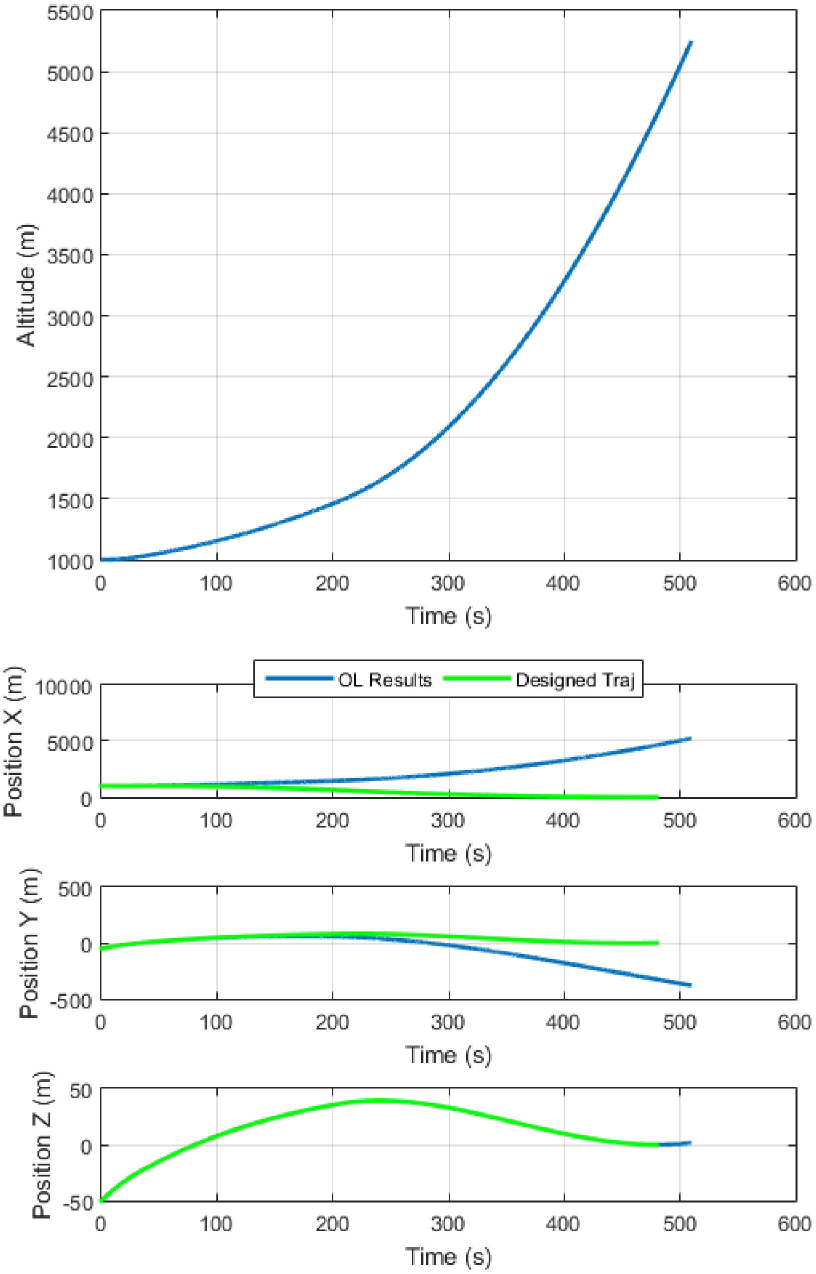

Figure 9.20: Open loop gravity model results for the EQ constant gravity, altitude (top) and position component comparison (bottom).

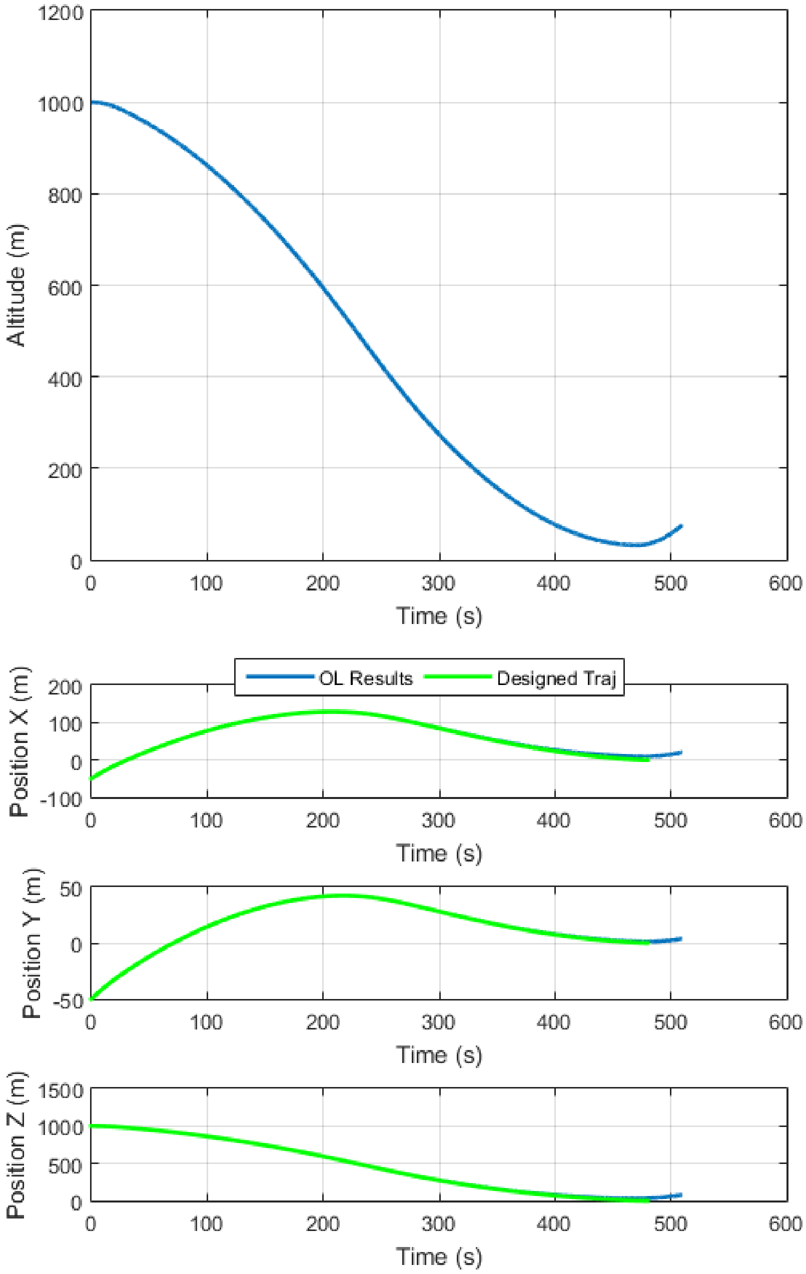

Figure 9.21: Open loop gravity model results for the NP Newtonian gravity, altitude (top) and position component comparison (bottom).

CHAPTER 10. TRAJECTORY ANALYSIS FOR HOVER CASES

The hover cases (NP_hov and EQ_hov) differ from the out of plane and uprange cases in Chapter 9 by the initial vehicle state. Flight time parameter sweeps were performed for the four rotation periods on all three triaxial ellipsoidal asteroids. Overall, the trends seen in the parameters sweeps for the hover cases are similar to the out of plane and uprange cases. The data for the thrust profile categories and switches between categories are included in Section 9.4.

10.1 Flight Time Parameter Sweeps for a North Pole Landing from a Hovering Initial Condition

The parameter sweep data for the NP_hov trajectories is compiled in Figures 10.1 through 10.5. As expected, the spin rate has no effect on propellant usage as seen in Figures 10.1 and 10.2. NP_hov is sensitive to the asteroid size, Figure 10.3 and 10.4. A1 (largest asteroid) requires the least amount of propellant. The difference in propellant required between A1 and A2 is larger than the difference between A2 and A3.

Comparison of iterations required to design the trajectory for the NP_hov case is located in Figures 10.5 (A1 - top and A2 - bottom) and 10.6 (A3). Each color represents a spin period. For NP_hov, all four rotation speeds for each flight time used the same number of iterations. This is seen on all three asteroid sizes, though different number of iterations appear for the different asteroid sizes. This is not true for the out of plane and uprange cases. A3 (smallest asteroid) needed 3 iterations for every flight time. A1 and A2 needed 3 or more iterations. The pattern of the smallest asteroid needing the fewest iterations is also seen in the NP case, but not the EQ nor EQ_hov cases.

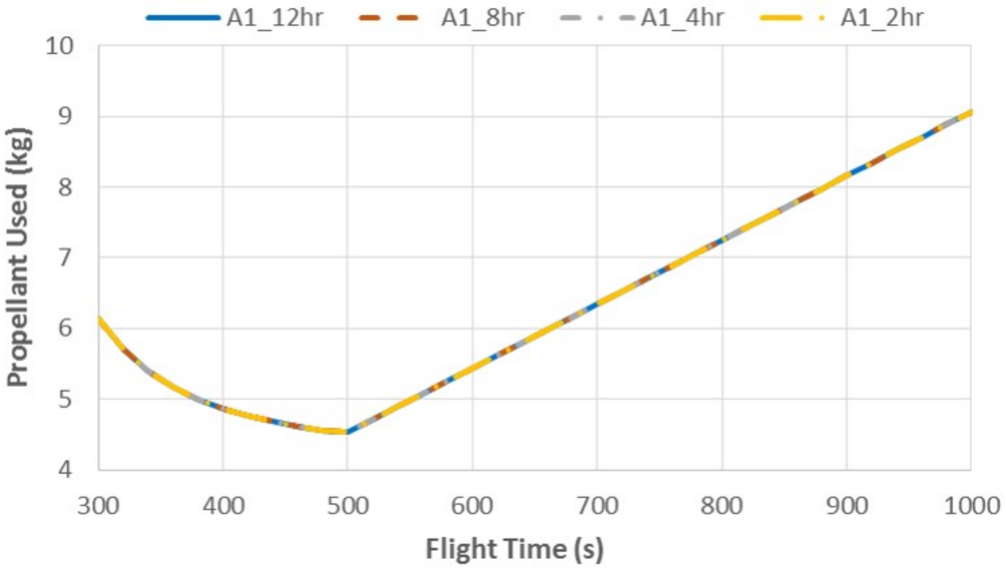

Figure 10.1: NP_hov trajectory propellant usage parameter sweep for A1 (1000 x 500 x 250 m) with all four spin rates.

10.2 Flight Time Parameter Sweeps for an Equatorial Landing from a Hovering Initial Condition

The EQ_hov parameter sweep data is located in Figures 10.7 through 10.11. Spin rate clearly impacts the propellant usage, with the 2 hr spin rate needing significantly more propellant for the shorter flight times, see Figures 10.7 and 10.8. Figure 10.7 trajectories land on A1 (largest asteroid) and Figure 10.8 land on A3 (smallest). The difference between the 2 hr and the 12 hr periods is more pronounced for the hover cases as compared to the out of plane and uprange cases. EQ_hov trajectories are insensitive to asteroid size, especially for the 8 hr period, Figure 10.9. There is a slight difference between the largest and smallest asteroids for the 2 hr spin rate, Figure 10.10.

Comparison of iterations required to design the trajectory for the EQ_hov case is located in Figures 10.11 (A1 - top and A2 - bottom) and 10.12 (A3). Each color represents a spin period. There are no perceivable trends for number of iterations required for the EQ_hov cases with respect to flight time, asteroid size, and rotation speed. Generally, EQ_hov requires fewer iterations than NP_hov, though there is a one flight time that requires more iterations.

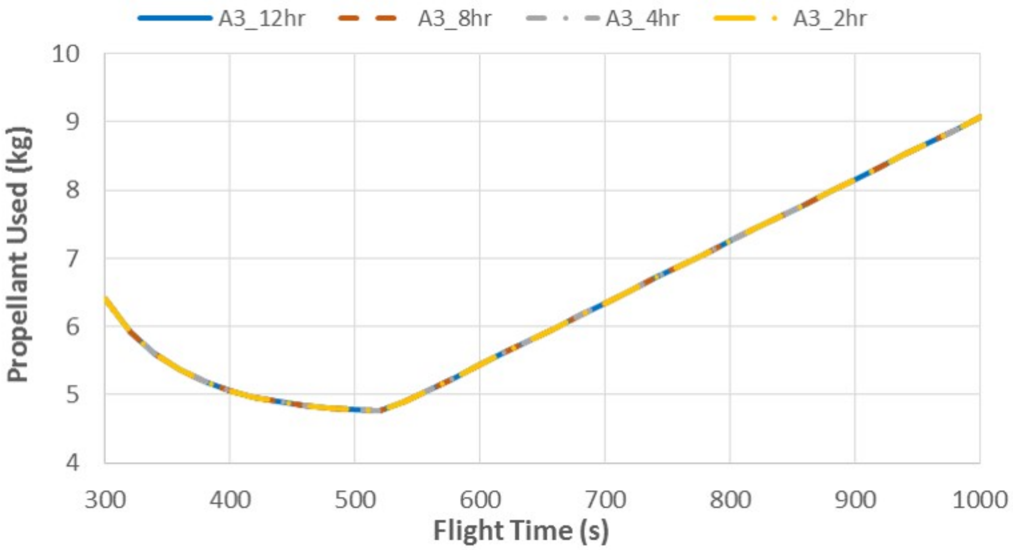

Figure 10.2: NP_hov trajectory propellant usage parameter sweep for A3 (500 x 500 x 250 m) with all four spin rates.

10.3 Designed Trajectories

The parameters from the EQ_hov optimal flight time of 525 sec for A1 with an 8 hr period are located in Figures 10.13 through 10.15. This case required three iterations to successfully design the trajectory. The vehicle position vector for the three iterations, along with the initial position vector for the gravity model is shown in Figure 10.13. The maximum position difference after the first iteration is 1000 m, the altitude at burn start. The maximum position difference between the first and second iterations was 1.51 m and the position difference between the second and third iterations is 0.0068 m. All three iterations designed the same thrust magnitude profile, seen in Figure 10.14. The trajectory parameters for the final designed trajectory are depicted in Figure 10.15. For the hover case, the vehicle starts directly over the landing site. However, the vehicle does not remain directly over it during the descent burn, due to the landing site's motion. This is seen by the movement in the Y component of position and velocity. The vehicle does remain in the X-Y plane with no motion toward the poles. The difference between the slack variable and magnitude of the acceleration vector is on the order of $1.2\text{x}10^{-8}$ m/s^2.

The parameters from the NP_hov optimal flight time of 501 sec for A1 with an 8 hr period

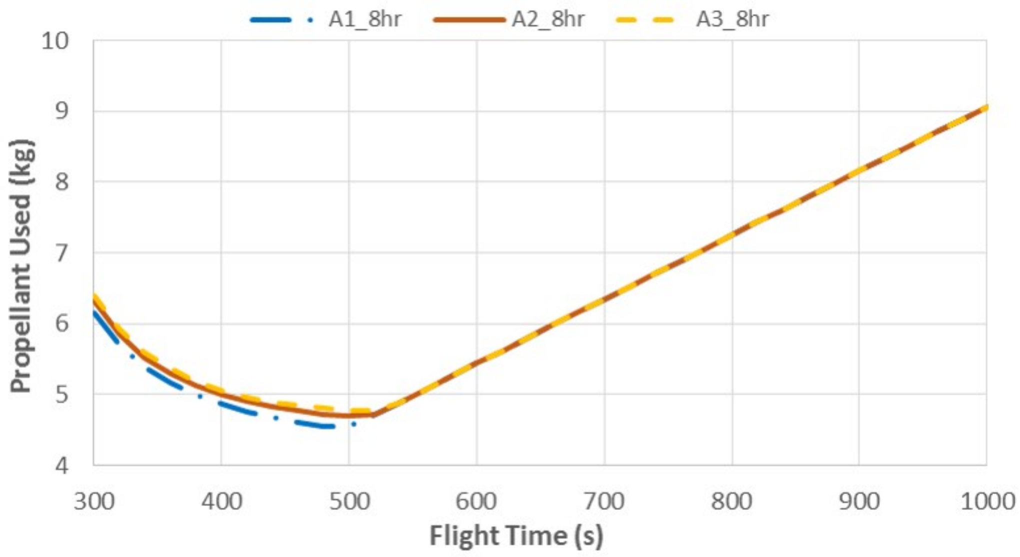

Figure 10.3: NP_hov trajectory propellant usage parameter sweep with an 8 hour period for the three asteroid sizes.

are located in Figures 10.16 through 10.18. The maximum position difference after the first trajectory is 1000 m, the altitude at burn start. The maximum position difference between the first and second iterations was 46.6 m and the difference between the second and third iterations is 0.885 m. The position difference between the third and fourth (final) iterations is 0.235 m. The thrust magnitude from the four iterations is located in Figure 10.17. The thrust magnitude for the first iteration is a maximum-minimum-maximum profile while it is a maximum-minimum profile for the remaining iterations. The initial starting thrust differs between the first, second, and third iterations. The third and fourth iterations have the same profile. The NP_hov optimal flight time occurs immediately before the switch to all minimum, which is evident as the highest thrust at the beginning is not the full maximum thrust value.

The parameters from the final designed NP_hov trajectory are plotted in Figure 10.18. The position starts directly above the landing site and comes straight down vertically. There is no motion in the X and Y components of the position vector as evident by no thrust and thus no velocity in the X and Y components. The large spike in the difference between the slack variable and the acceleration magnitude occurs where the thrust vector is switching from -Z to +Z, accelerating the vehicle to decelerating the vehicle. With the exception of this time frame,

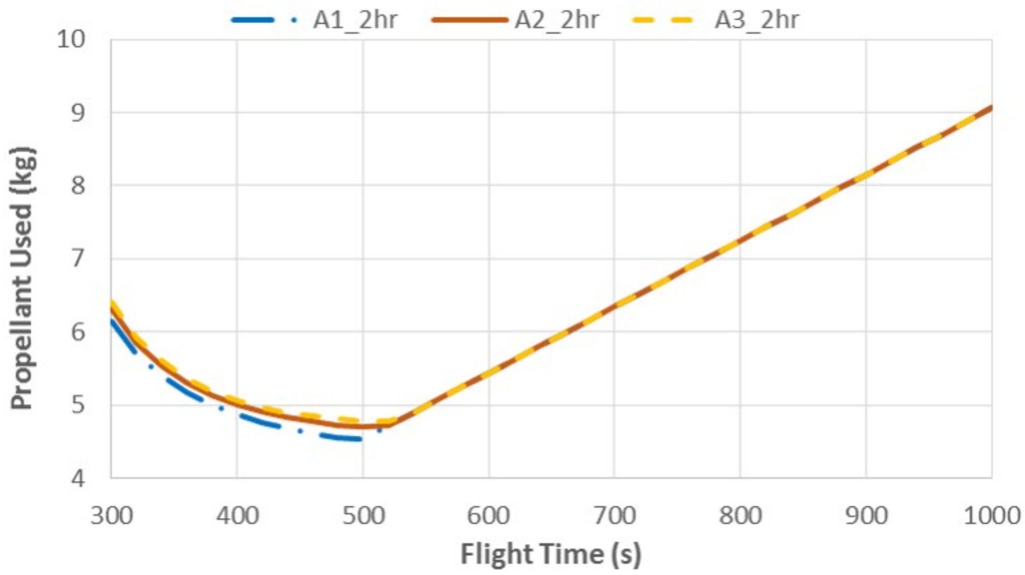

Figure 10.4: NP_hov trajectory propellant usage parameter sweep with a 2 hour period for the three asteroid sizes.

the difference is less than 2x10^{-7} m/s^2. Overall, the evidence points to the relaxed problem solution being the optimal solution to the original problem.

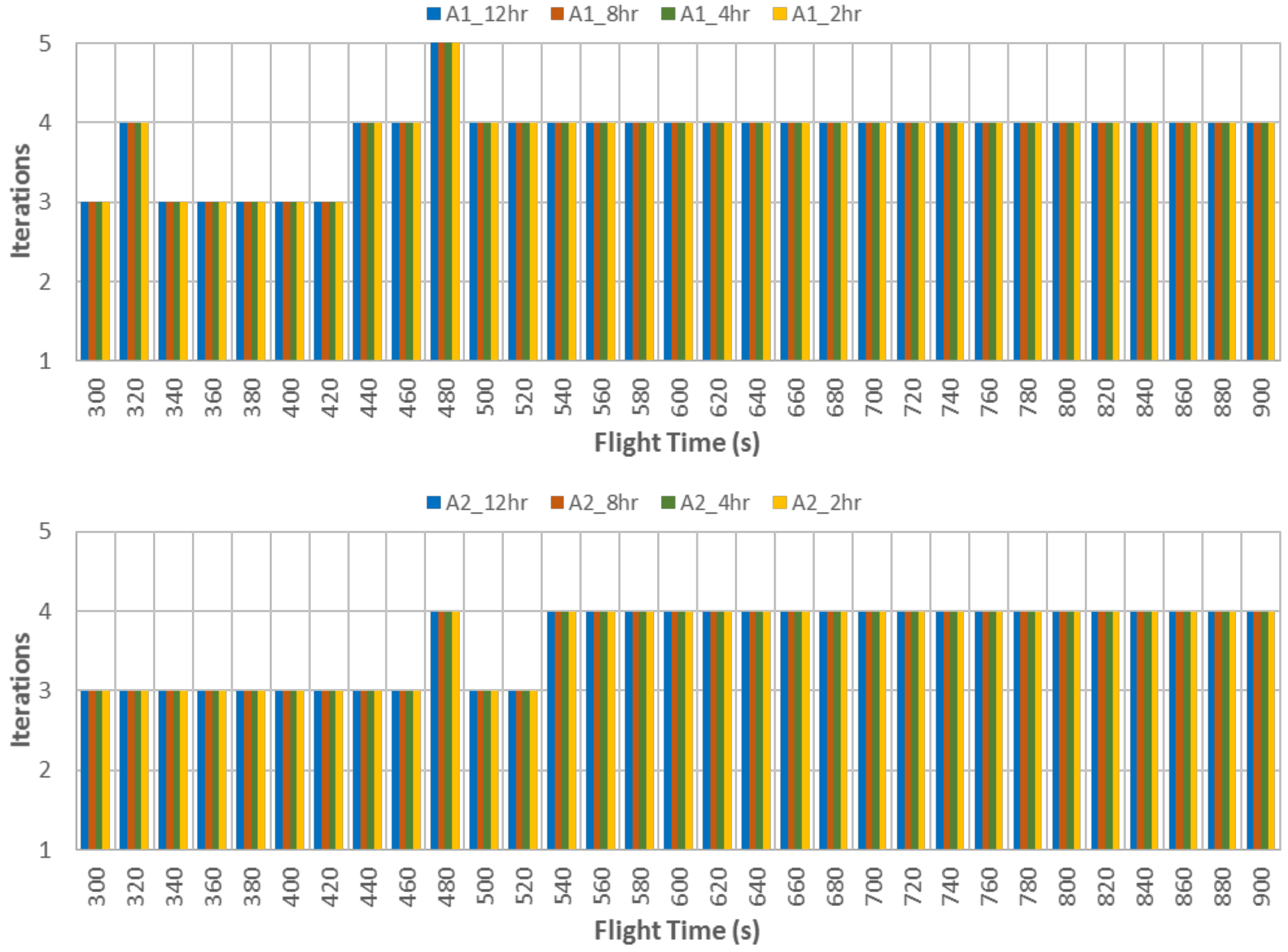

Figure 10.5: NP_hov comparison of trajectory iterations required for the four spin rates with A1 (top) and A2 (bottom).

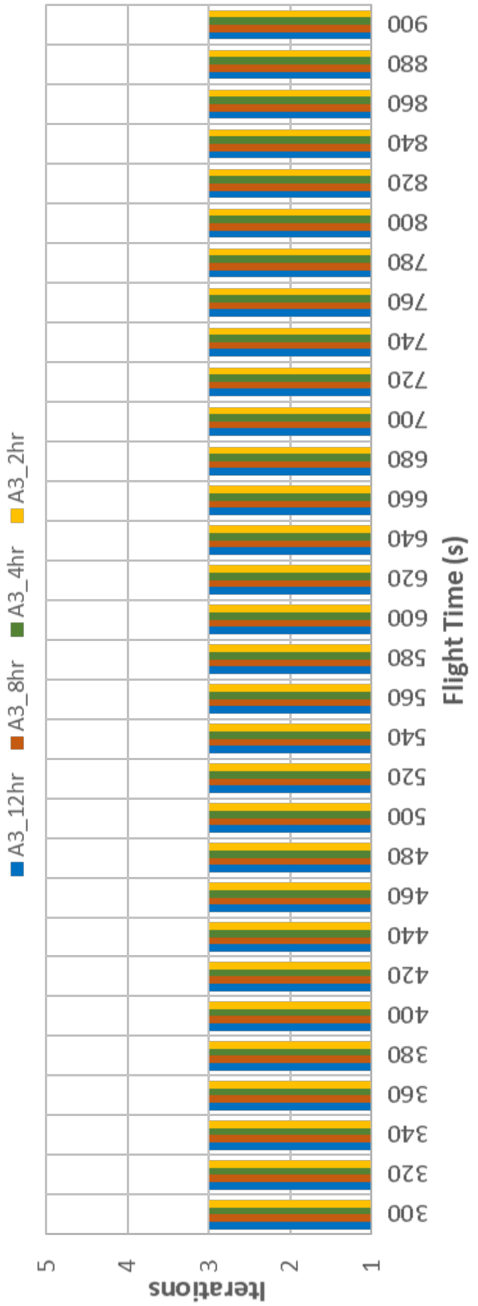

Figure 10.6: NP_hov comparison of trajectory iterations required for the four spin rates with A3.

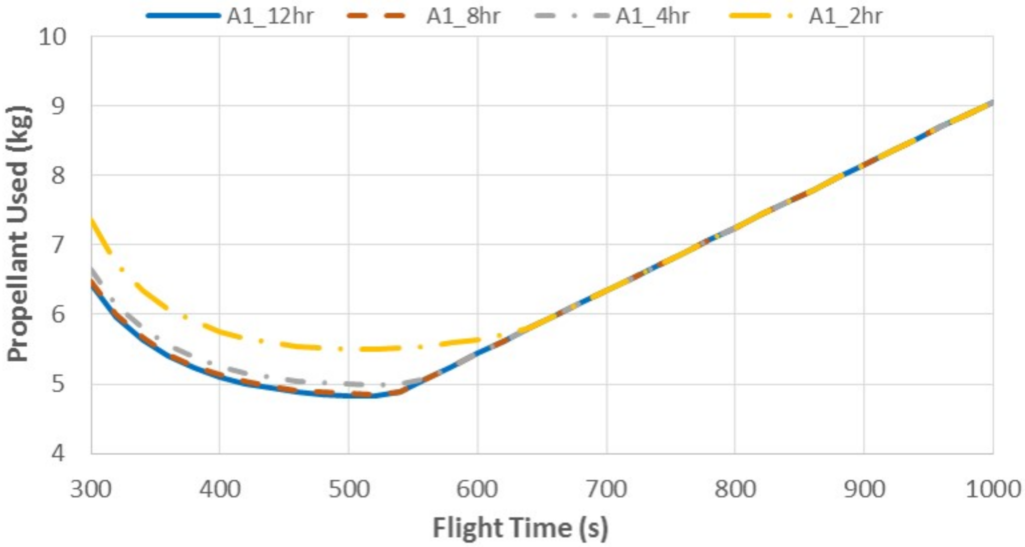

Figure 10.7: EQ_hov trajectory propellant usage parameter sweep for A1 (1000 x 500 x 250 m) with all four spin rates.

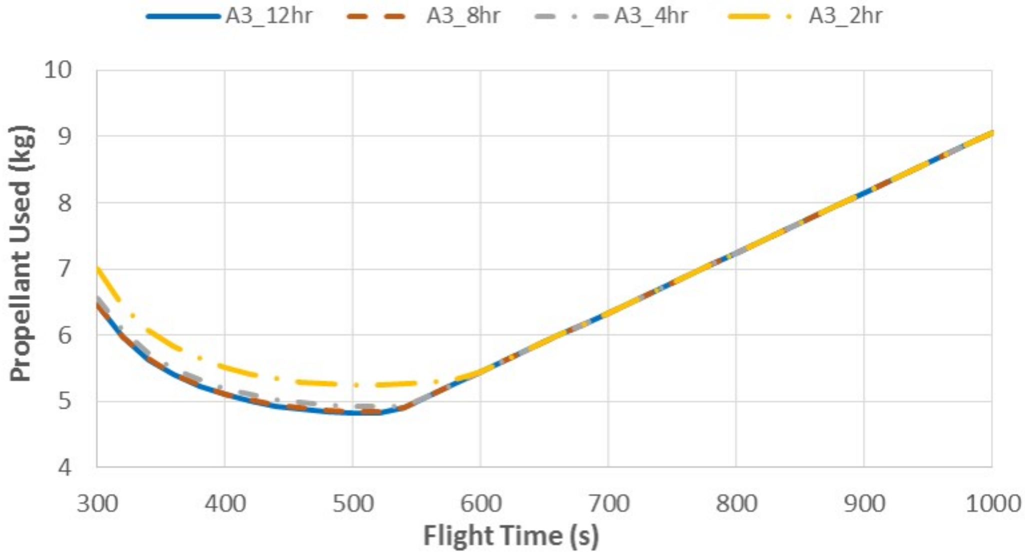

Figure 10.8: EQ_hov trajectory propellant usage parameter sweep for A3 (500 x 500 x 250 m) with all four spin rates.

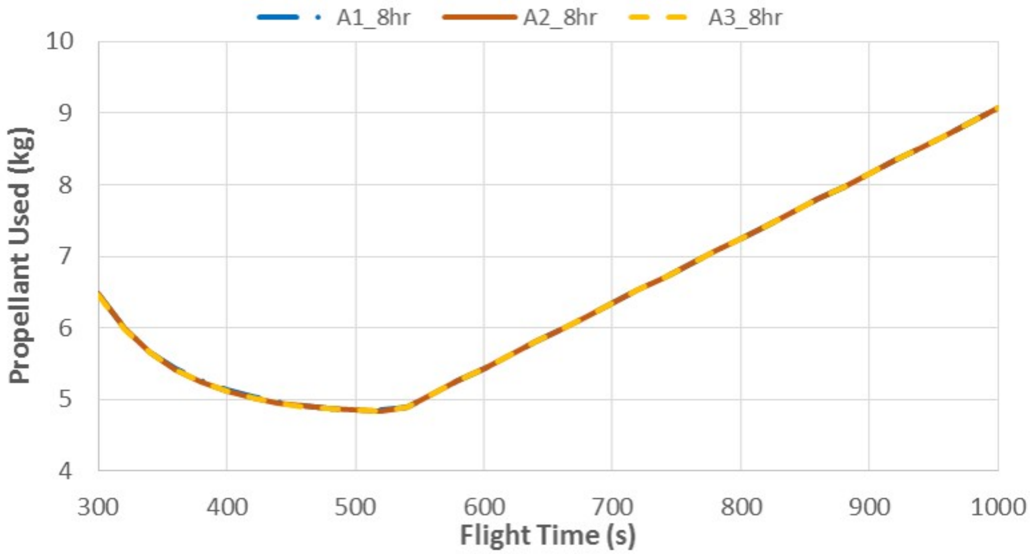

Figure 10.9: EQ_hov trajectory propellant usage parameter sweep with an 8 hour period for the three asteroid sizes.

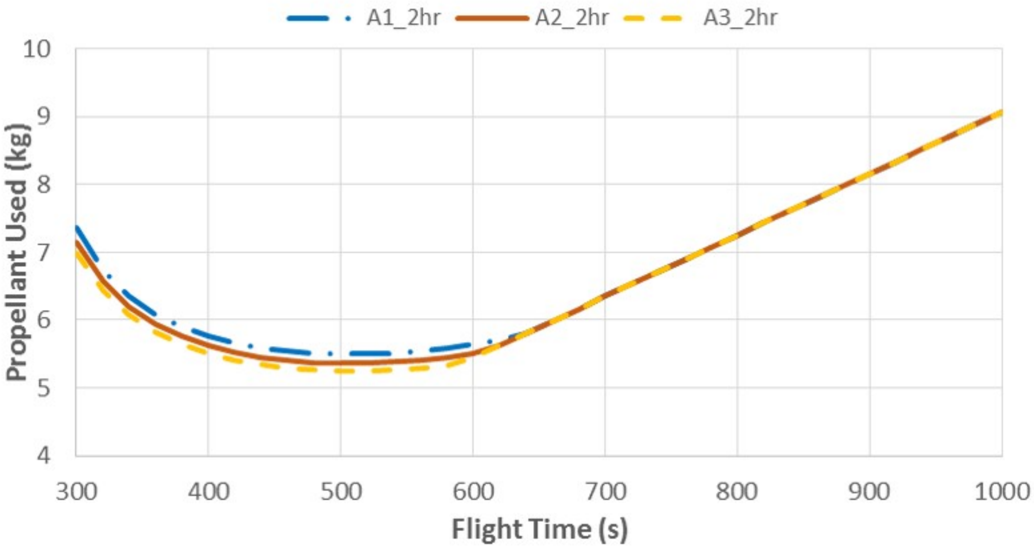

Figure 10.10: EQ_hov trajectory propellant usage parameter sweep with a 2 hour period for the three asteroid sizes.

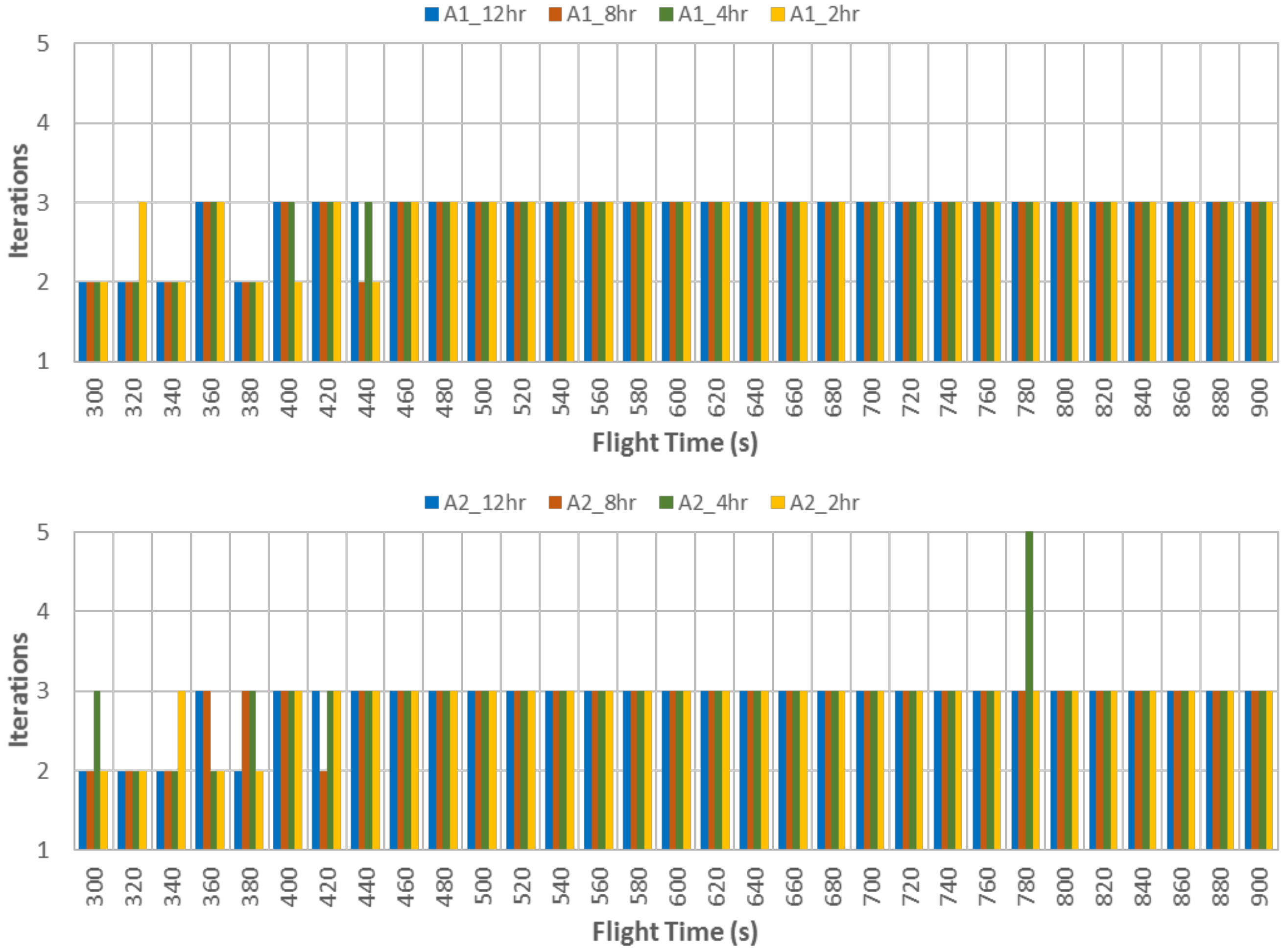

Figure 10.11: EQ_hov comparison of trajectory iterations required for the four spin rates with A1 (top) and A2 (bottom).

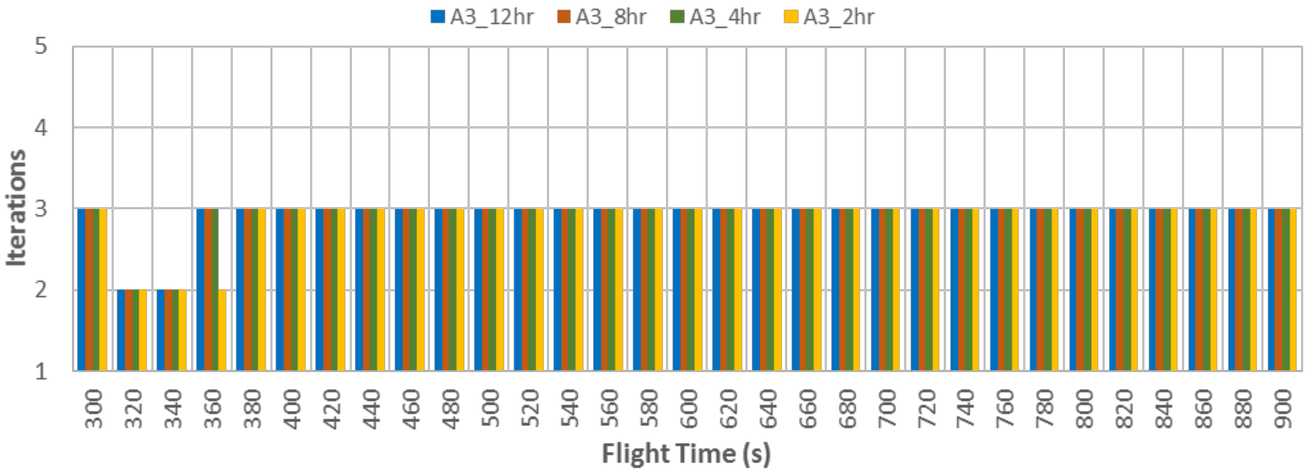

Figure 10.12: EQ_hov comparison of trajectory iterations required for the four spin rates with A3 (bottom).

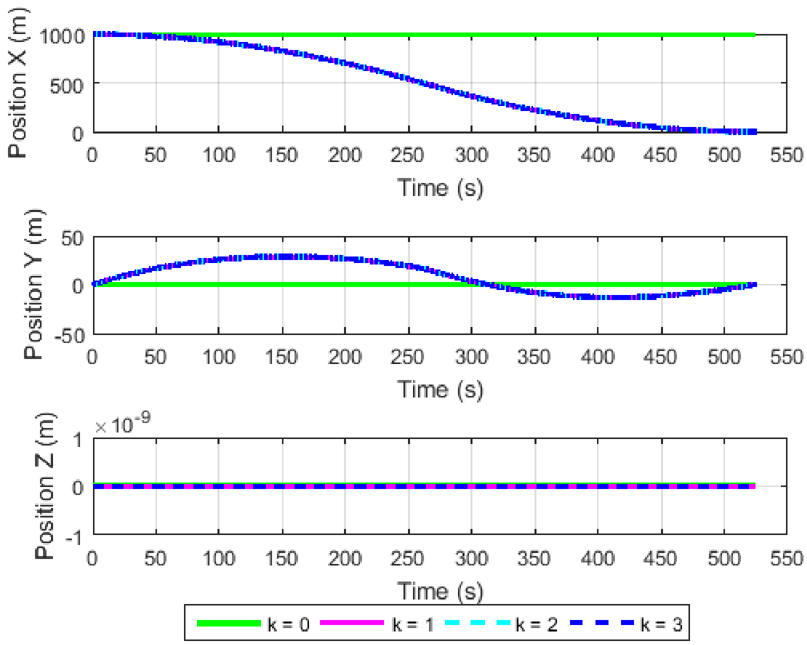

Figure 10.13: Position vector comparison for the different iterations with an EQ_hov trajectory on A1, 8 hr period, 525 sec flight time. k=0 feeds the gravity model for the first optimization.

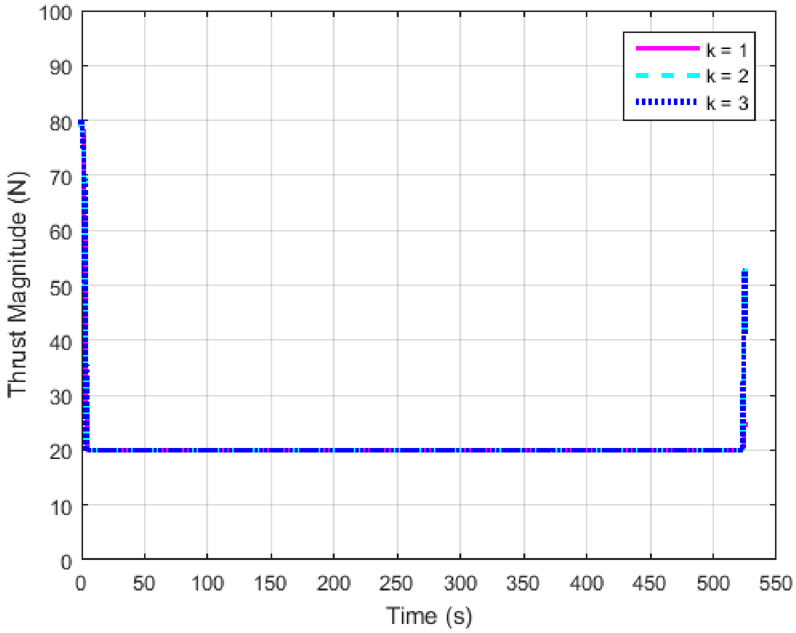

Figure 10.14: Thrust magnitude comparison for the different iterations with an EQ_hov trajectory on A1, 8 hr period, 525 sec flight time.

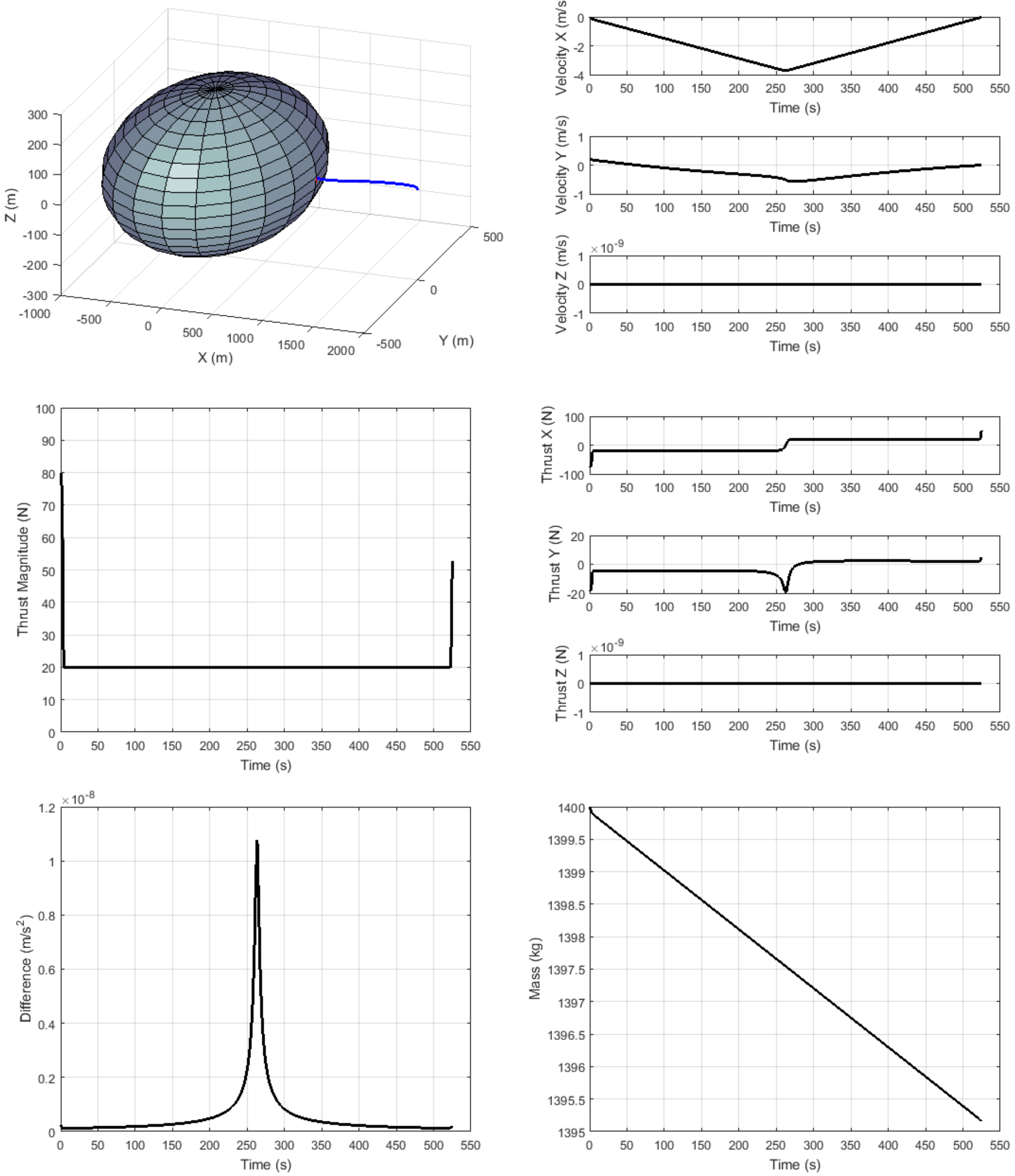

Figure 10.15: A1 8 hr period EQ_hov trajectory for a flight time of 525 sec. Top left: 3-D vehicle position, Top right: velocity components relative to the landing site, Middle left: thrust magnitude, Middle right: thrust components, Bottom left: difference between the slack variable and the acceleration vector, Bottom right: mass profile.

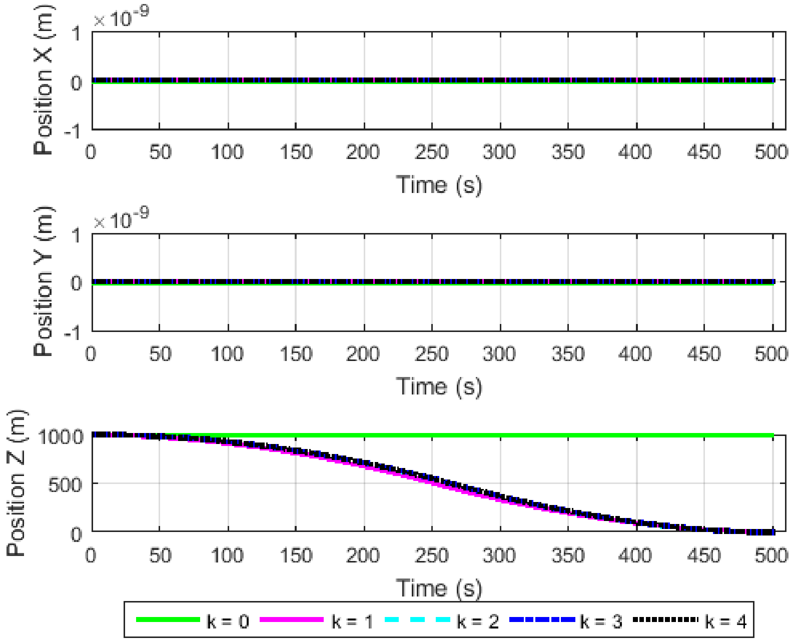

Figure 10.16: Position vector comparison for the different iterations with a NP_hov trajectory on A1, 8 hr period, 501 sec flight time. k=0 feeds the gravity model for the first optimization.

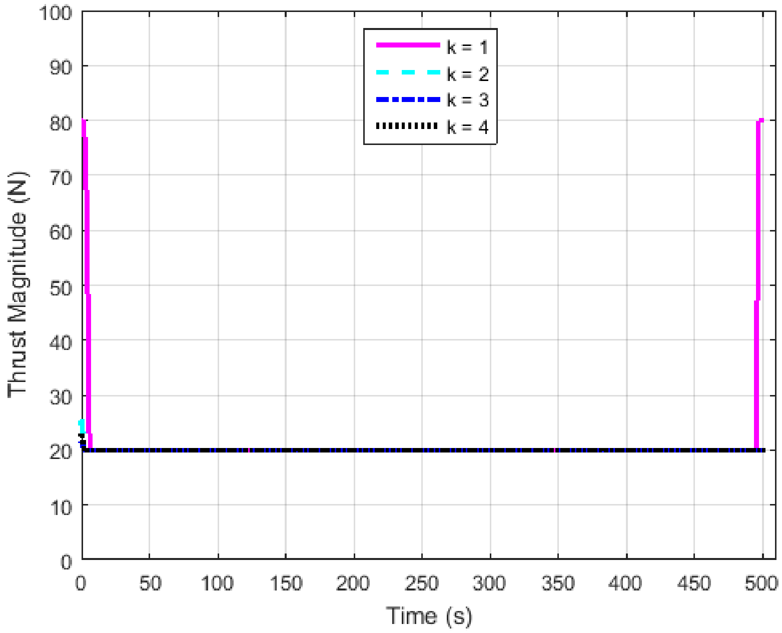

Figure 10.17: Thrust magnitude comparison for the different iterations with a NP_hov trajectory on A1, 8 hr period, 501 sec flight time.

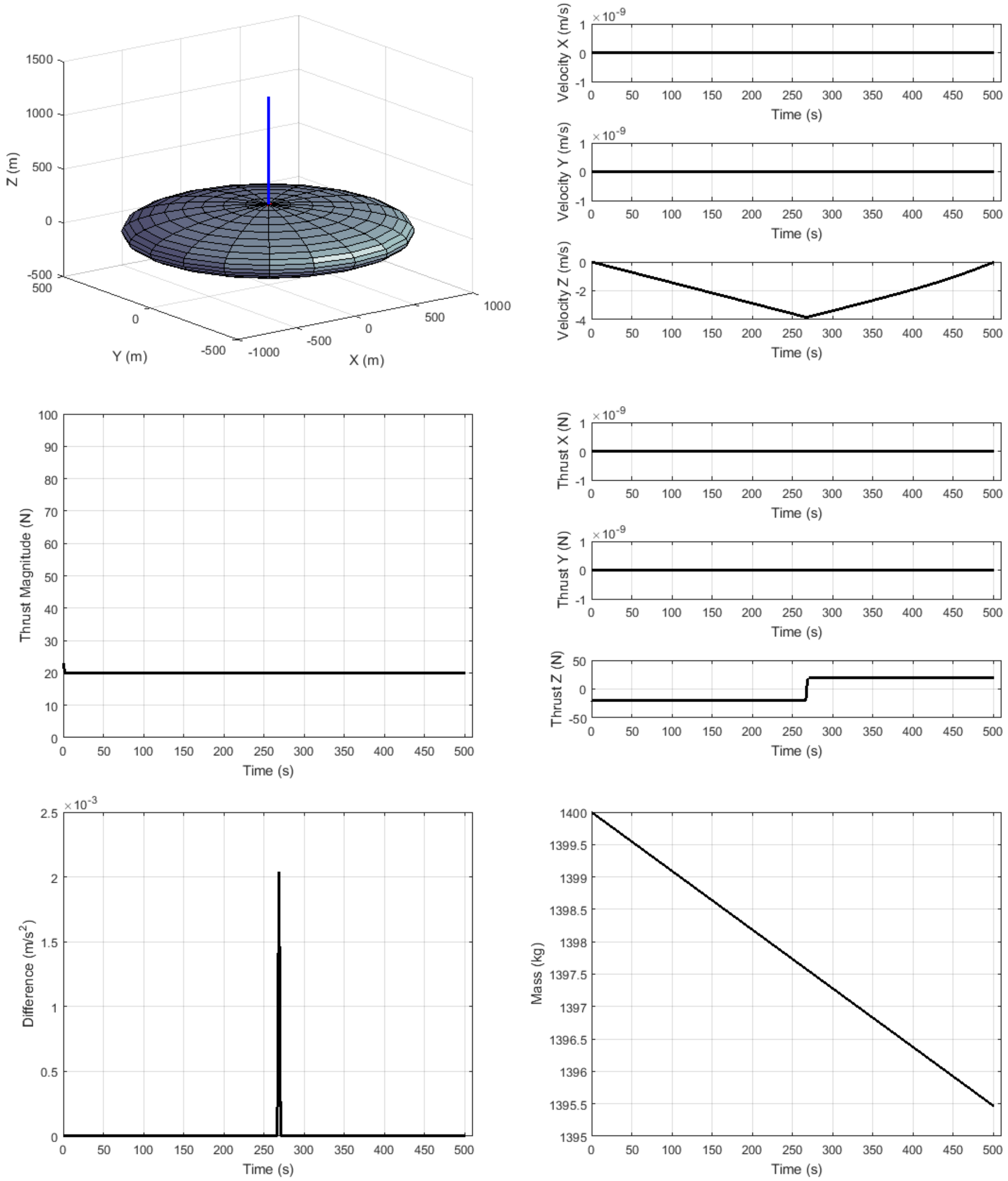

Figure 10.18: A1 8 hr period NP_hov trajectory for a flight time of 501 sec. Top left: 3-D vehicle position, Top right: velocity components relative to the landing site, Middle left: thrust magnitude, Middle right: thrust components, Bottom left: difference between the slack variable and the acceleration vector, Bottom right: mass profile.

CHAPTER 11. TRAJECTORY ANALYSIS FOR THE EVEN LOWER THRUST CASES

The previous out of plane and uprange cases and the hover cases used a fraction of the propellant onboard the vehicle. The thrust profiles for the optimal flight time tended to stay near the minimum thrust value for most of flight. This led to analyzing an even lower thrust vehicle. For these lower thrust cases, the maximum thrust is 20 N, the minimum from the previous cases, and the minimum thrust is 5 N. The initial conditions are the out of plane and uprange; the same as NP and EQ. The lower thrust lengthens the flight time needed to reach the surface, which led to the discretization time step being increased to 5 sec from 2 sec for these cases. The thrust magnitude is a quarter of the original; however, the optimal flight time change between the NP and EQ cases and the NP_LT and EQ_LT cases does not scale by a factor of four. The change is closer to a factor of two. The data for the thrust profile categories are included in Section 9.4. Overall, the trends for the lower thrust cases resemble the trends from the out of plane and uprange cases and the hover cases.

11.1 Flight Time Parameter Sweeps for a North Pole Landing with Lower Thrust

The flight time lengths are longer for the NP_LT cases as compared to the previous two sets of polar trajectories. While the flight times are longer, the overall propellant usage is less. The NP and NP_hov parameter sweeps with flight times ranging from 300 - 1000 sec used 4 to 9.5 kg of propellant. The NP_LT parameter sweeps with flight times ranging from 600 - 1800 sec used 2.7 to 4.5 kg of propellant. The parameter sweep data for the NP_LT trajectories is compiled in Figures 11.1 through 11.4. The comparison of propellant usage data for all four periods is located in Figure 11.1 for A1 (1000 x 500 x 250 m) and Figure 11.2 for A3 (500 x 500 x 250 m). As in the previous cases, the rotation speed has no effect on propellant usage for the missions landing at the north pole. The parameter sweep data comparing the three asteroid sizes for the 8 hour period are located in Figure 11.3 and for the 2 hour period in Figure 11.4, where the influence of the asteroid size is strongly seen. The shape of the parameter sweep changes for the different asteroid sizes, with the optimal flight time occurring at markedly different times. The largest asteroid requires the least amount of propellant to successfully land.

Comparison of iterations required for the successive solution method is located in Figures 11.5 (A1 - top and A2 - bottom) and 11.6 (A3). Each color represents a spin period. The majority of the trajectories required 3 to 5 iterations with a small number requiring 6 or 7 iterations. Unlike propellant usage, there are no clear trends with respect to flight time, spin rate, nor asteroid size. Overall, NP_LT tends to need more iterations than the NP and NP_hov. For the majority of cases, the number of iterations remains in the 2 - 5 range that was seen in the NP and NP_hov. This shows the stability in the successive solution method.

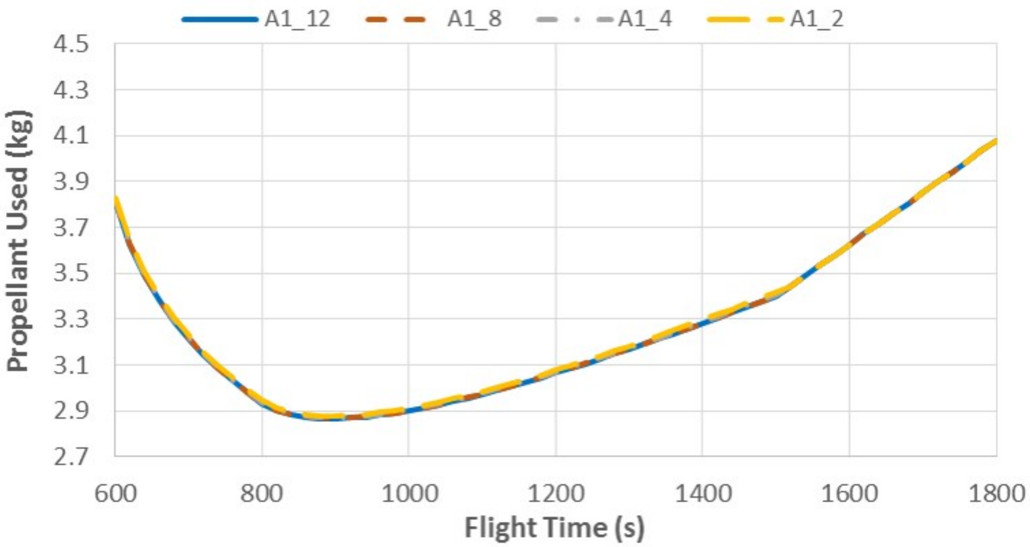

Figure 11.1: NP_LT trajectory propellant usage parameter sweep for A1 (1000 x 500 x 250 m) with all four spin rates.

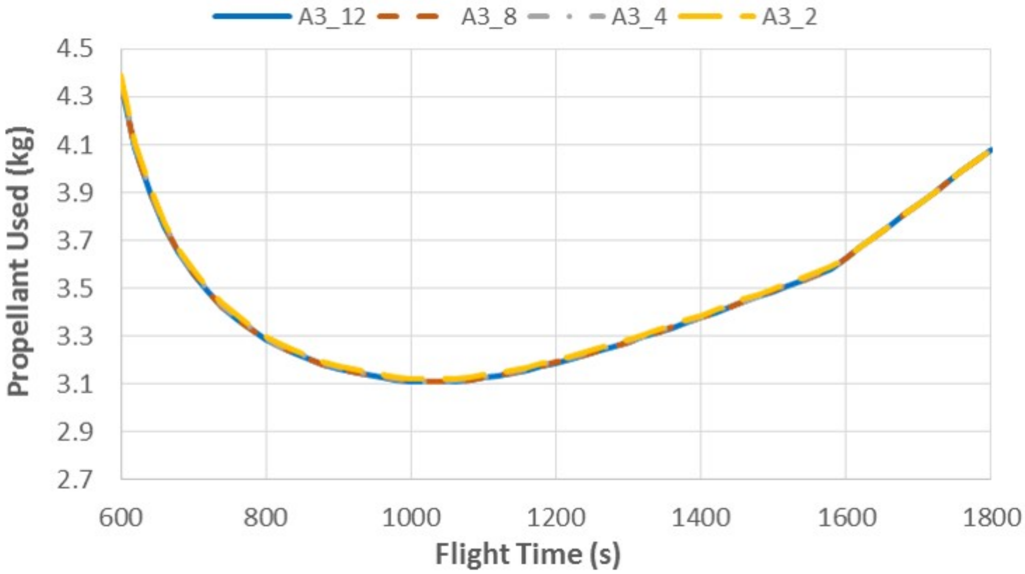

Figure 11.2: NP_LT trajectory propellant usage parameter sweep for A3 (500 x 500 x 250 m) with all four spin rates.

11.2 Flight Time Parameter Sweeps for an Equatorial Landing with Lower Thrust

The flight time lengths are longer for the EQ_LT cases as compared to the previous two sets of equatorial trajectories. While the flight times are longer, the overall propellant usage is less. The EQ and EQ_hov parameter sweeps with flight times ranging from 300 - 1000 sec used 4.5 to 9.5 kg of propellant. The EQ_LT parameter sweeps with the flight times ranging from 600 - 1800 seconds used 3.0 to 5.5 kg of propellant. The parameter sweep data for the EQ_LT trajectories is compiled in Figures 11.7 through 11.10. The comparison of propellant usage data for all four periods is located in Figure 11.7 for A1 (1000 x 500 x 250 m) and Figure 11.8 for A3 (500 x 500 x 250 m). The influence of the rotation speed is strongly seen in these two figures. The fastest spinning asteroid required more propellant. As rotation speed increases, the amount of propellant needed increases and the difference between the curves becomes greater. The parameter sweep data comparing the three asteroid sizes for the 8 hour period are located in Figure 11.9 and for the 2 hour period in Figure 11.10. The asteroid size has a very small effect on the propellant consumption. This effect is seen in the 2 hour period (Figure 11.10),

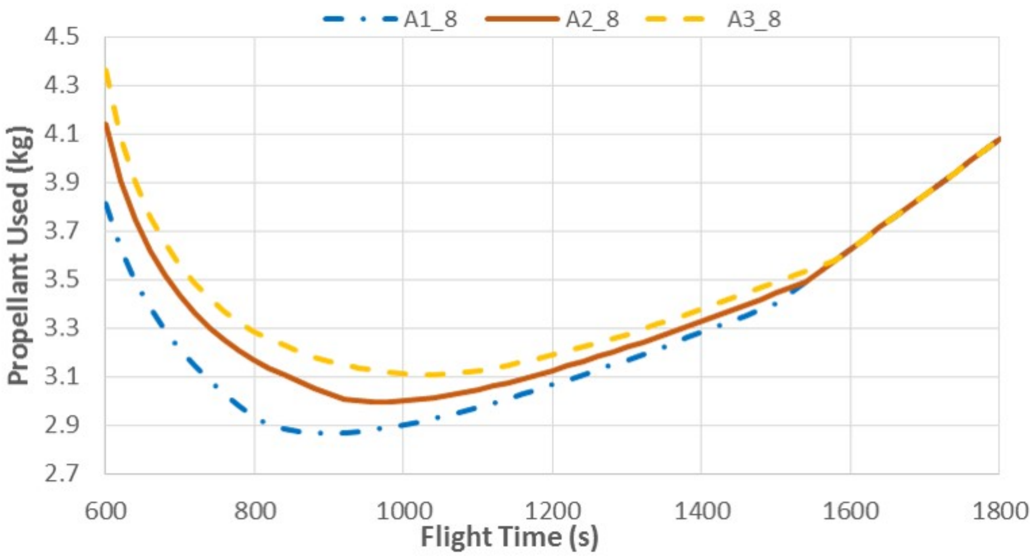

Figure 11.3: NP_LT trajectory propellant usage parameter sweep with an 8 hour period for the three asteroid sizes.

but barely noticeable in the 8 hour period (Figure 11.9). This is more pronounced here, as compared to the EQ case and on the same order as the EQ_hov case.

Comparison of iterations required for the successive solution method is located in Figures 11.11 (A1 - top and A2 - bottom) and 11.12 (A3). Each color represents a spin period. The majority of trajectories required 2 or 3 iterations. Unlike propellant usage, there are no clear trends with respect to flight time, spin rate, nor asteroid size as all the trajectories, except two, used 3 iterations. Generally, EQ_LT requires fewer iterations than NP_LT. EQ_LT's 2 to 3 iterations is similar to the 2 - 5 iterations required for EQ and EQ_hov cases. For all three, the majority of cases required 3 iterations. This shows stability in the successive solution method convergence.

11.3 Designed Trajectories

Figures 11.13 through 11.15 take an in-depth look at a single EQ_LT trajectory landing on A1 (1000 x 500 x 250 m) with an 8 hour period for the optimal flight time of 1044 seconds. The position vector as it changes throughout the iterations is shown in Figure 11.13. The initial trajectory that feeds the gravity model on the first successive solution is shown in green. This

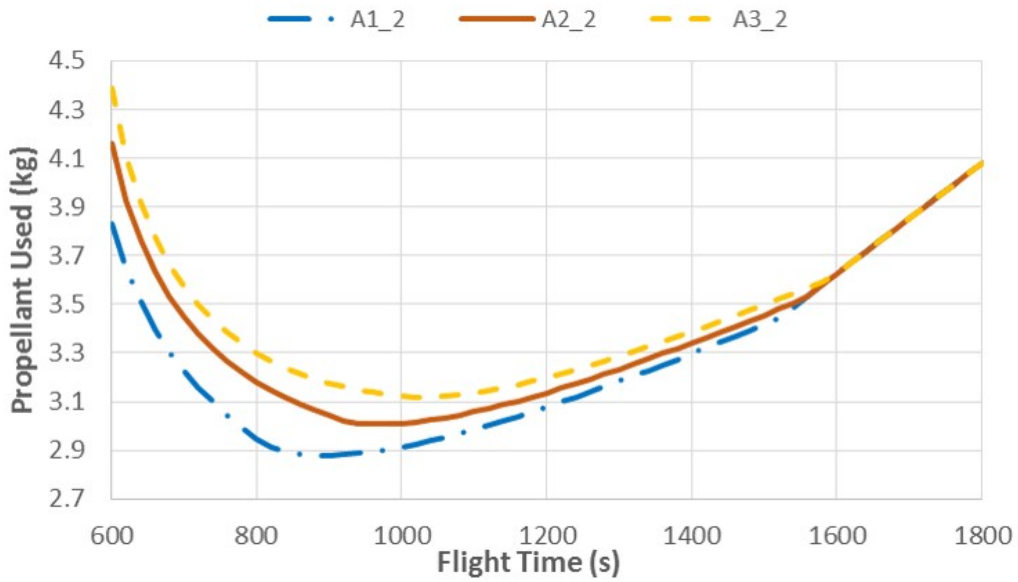

Figure 11.4: NP_LT trajectory propellant usage parameter sweep with a 2 hour period for the three asteroid sizes.

trajectory uses the initial point for the entire trajectory. After the first iteration is complete, the maximum position difference is 1002 m, the distance from the landing site to the initial vehicle state. The second and third iterations are very close to the first iteration. The maximum difference in distance between the first and second iterations is 3.18 m. When the trajectory is designed, the maximum distance between the second and third iterations is 0.026 m. The thrust magnitude for all three iterations is shown in Figure 11.14, with very little difference between the three. The difference is the time at which the throttle back to maximum thrust occurs. Once the first trajectory iteration is designed, the remaining iterations contain minor corrections.

All the trajectory parameters for the final designed trajectory are located in Figure 11.15. The vehicle position vector is shown relative to the asteroid and the corresponding landing site. The velocity vector is successfully designed to have zero relative velocity to the landing site, thus achieving a soft landing. The difference between the slack variable and the acceleration vector magnitude is on the order of 6x10^{-10} m/s^2, proving that the relaxed problem is identical to the original problem for the designed trajectory. The individual thrust components are the profile that would feed the vehicle controller, when flying the profile as designed.

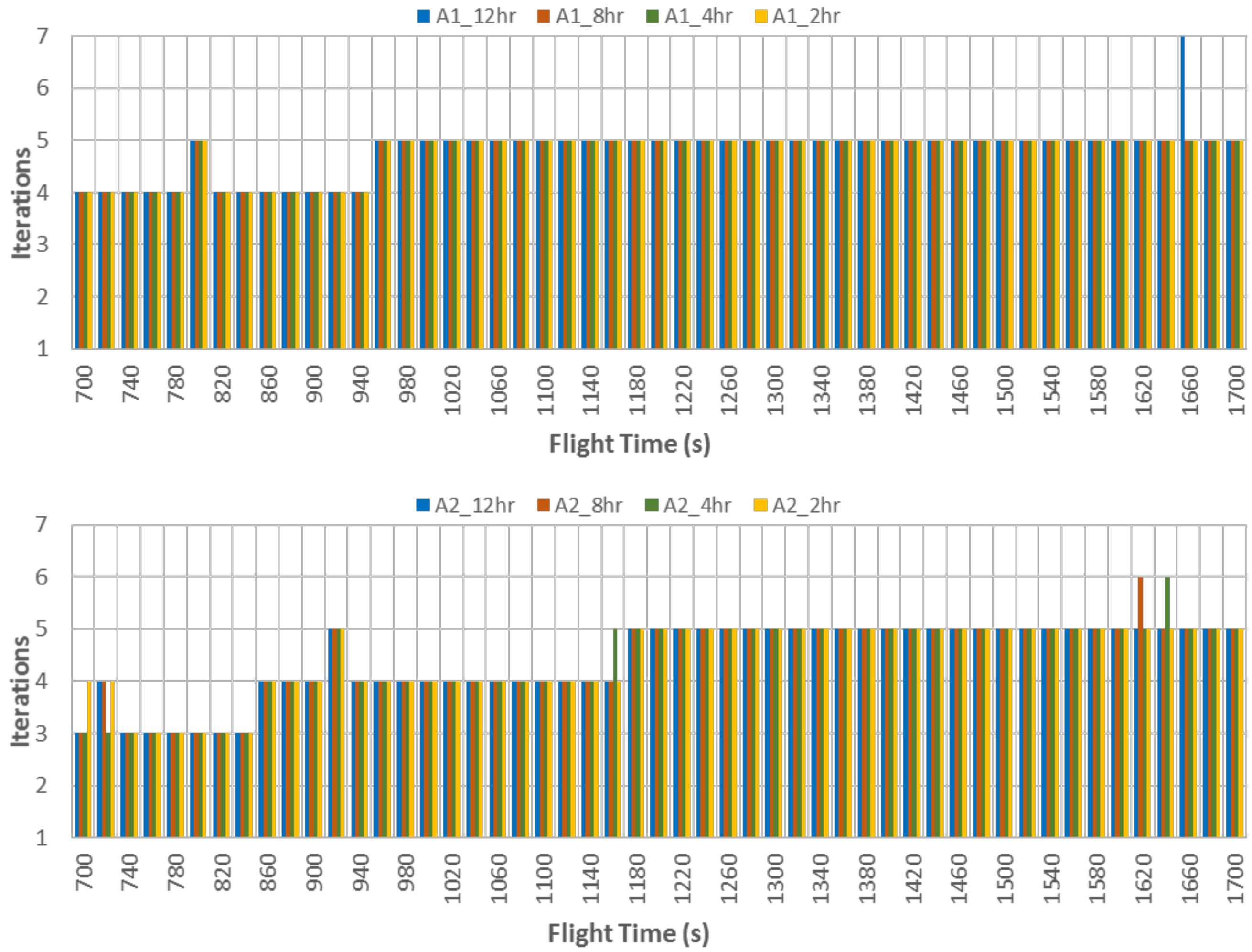

Figure 11.5: NP_LT comparison of trajectory iterations required for the four spin rates with A1 (top) and A2 (bottom).

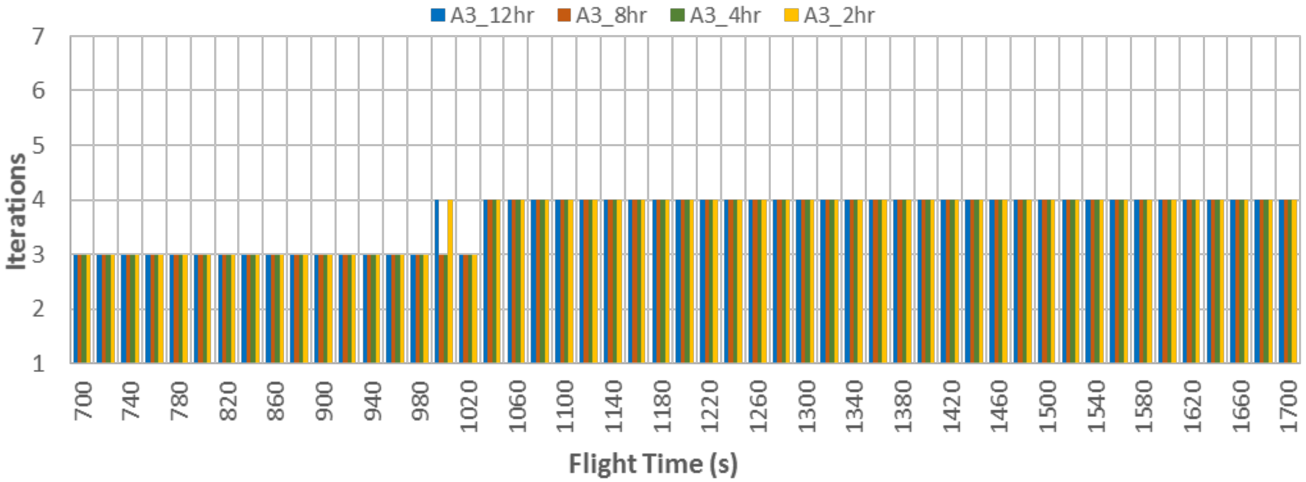

Figure 11.6: NP_LT comparison of trajectory iterations required for the four spin rates with A3.

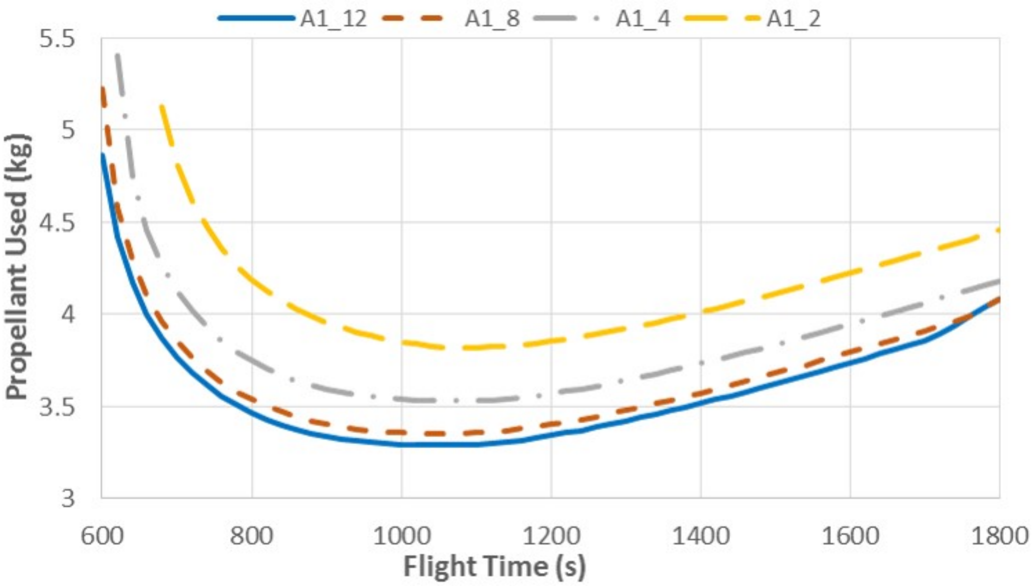

Figure 11.7: EQ_LT trajectory propellant usage parameter sweep for A1with all four spin rates.

The NP_LT optimal propellant usage trajectory for the 8 hour period A1 corresponds to a flight time of 897 seconds. This trajectory requires four iterations in the successive solution method, while the EQ_LT required three. After the first iteration is complete the maximum position difference is 1002 m, the distance from the landing site to the initial vehicle state. The maximum difference in distance between the first and second iterations is 89.14 m and 9.27 m between the second and third trajectories. When the trajectory is designed the maximum distance between the third and fourth iterations is 0.48 m. There are differences in the Z position component between the first iteration's solution and the remaining iterations as seen in Figure 11.16. The first iteration follows the maximum-minimum-maximum thrust profile, while the remaining iterations followed the maximum-minimum thrust profile, see Figure 11.17. The later iterations did not return to maximum thrust at the end of flight. The trajectory parameters for the final designed NP_LT trajectory are located in Figure 11.18. The difference between the slack variable and the acceleration vector magnitude is on the order of $7\text{x}10^{-10}$ m/s^2.

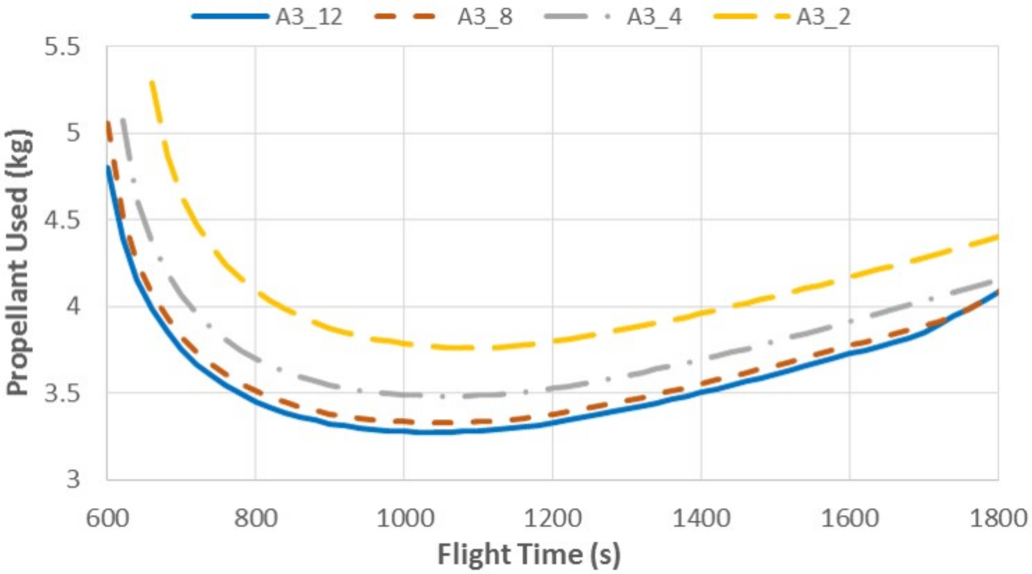

Figure 11.8: EQ_LT trajectory propellant usage parameter sweep for A3 with all four spin rates.

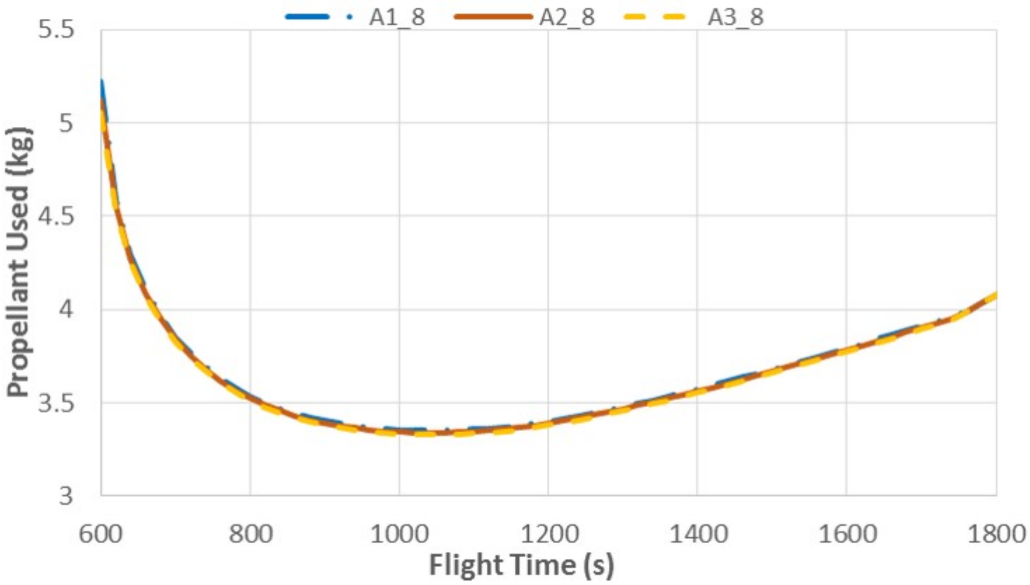

Figure 11.9: EQ_LT trajectory propellant usage parameter sweep with an 8 hour period for the three asteroid sizes.

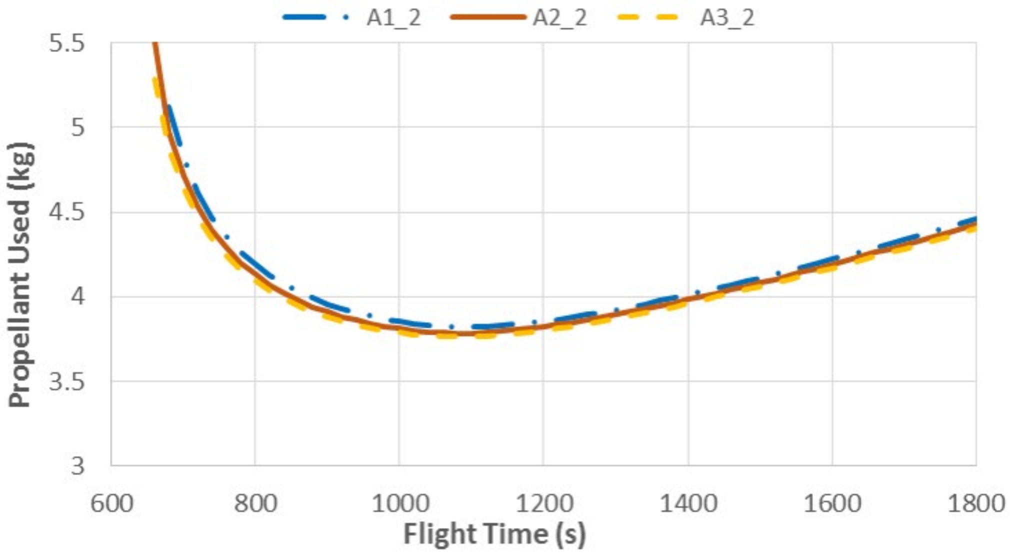

Figure 11.10: EQ_LT trajectory propellant usage parameter sweep with a 2 hour period for the three asteroid sizes.

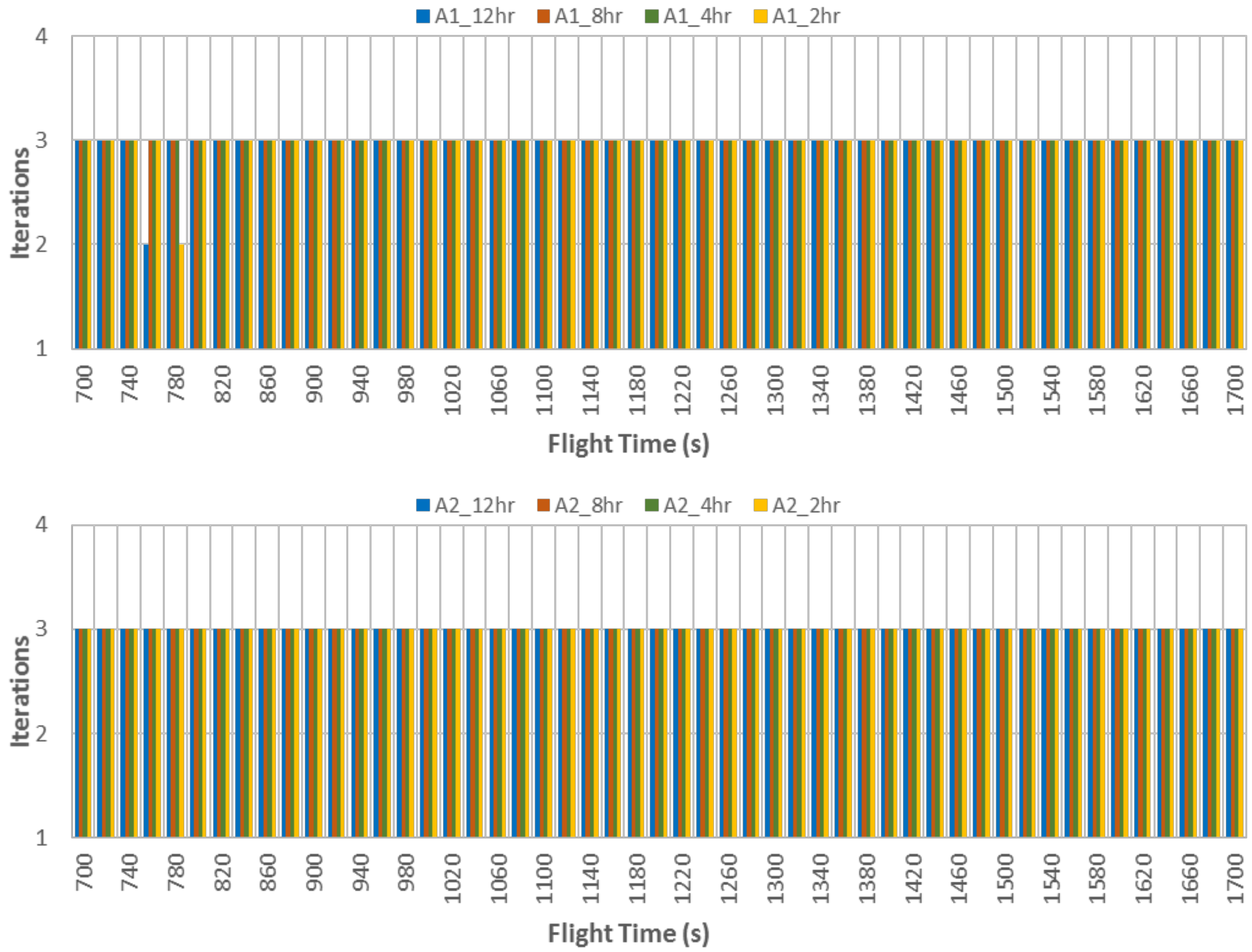

Figure 11.11: EQ_LT comparison of trajectory iterations required for the four spin rates with A1 (top) and A2 (bottom).

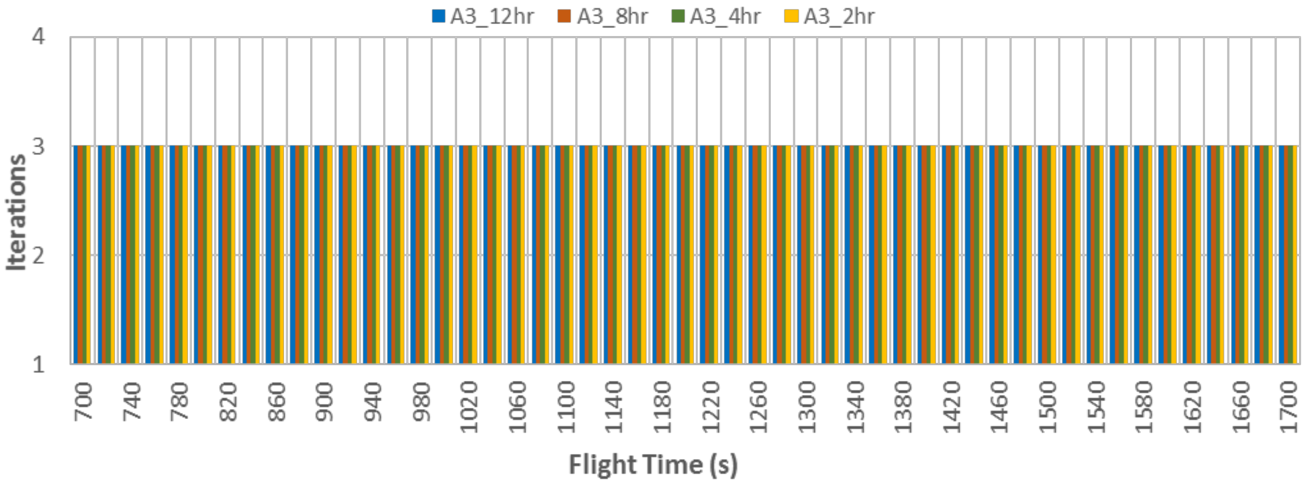

Figure 11.12: EQ_LT comparison of trajectory iterations required for the four spin rates with A3.

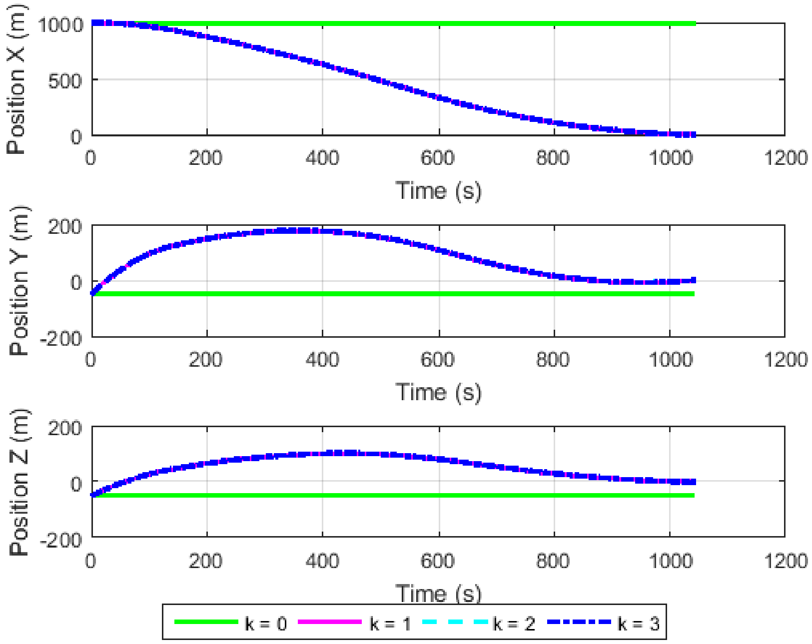

Figure 11.13: Position vector comparison for the different iterations with an EQ_LT trajectory on A1, 8 hr period, 1044 sec flight time. k=0 feeds the gravity model for the first optimization.

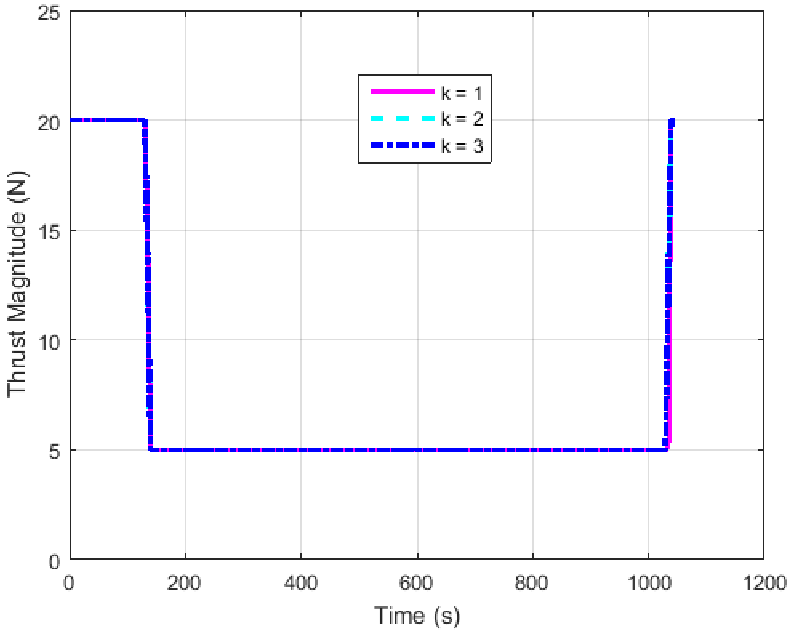

Figure 11.14: Thrust magnitude comparison for the different iterations with an EQ_LT trajectory on A1, 8 hr period, 1044 sec flight time.

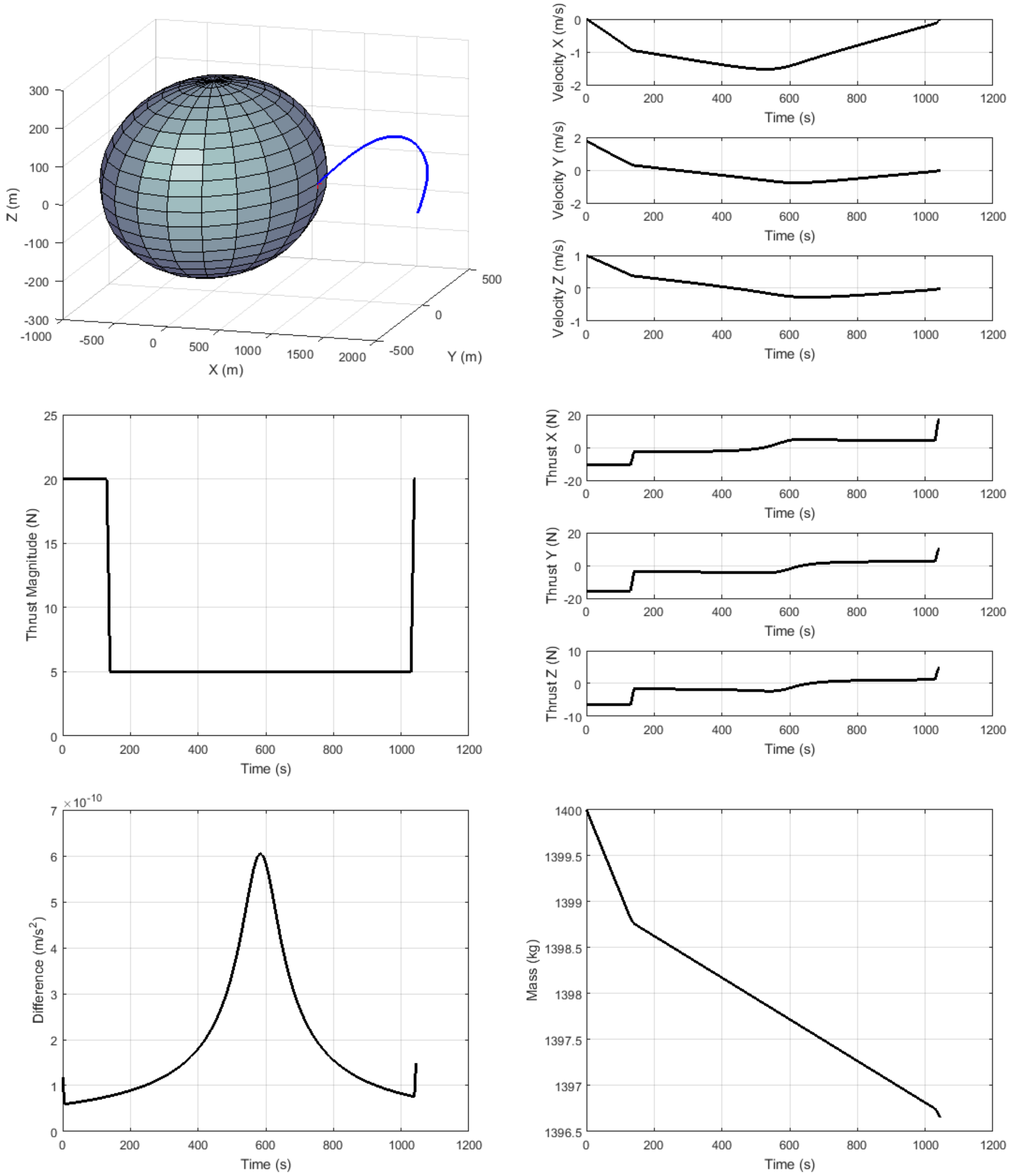

Figure 11.15: A1 8 hr period EQ_LT trajectory for a 1044 sec flight time. Top left: 3-D vehicle position, Top right: velocity components relative to the landing site, Middle left: thrust magnitude, Middle right: thrust components, Bottom left: difference between the slack variable and the acceleration vector, Bottom right: mass profile.

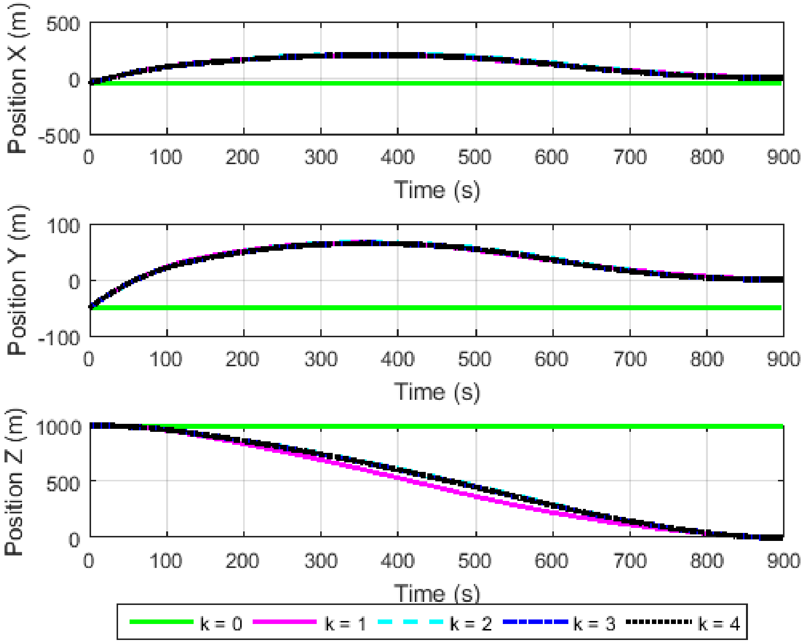

Figure 11.16: Position vector comparison for the different iterations with a NP_LT trajectory on A1, 8 hr period, 897 sec flight time. k=0 feeds the gravity model for the first optimization.

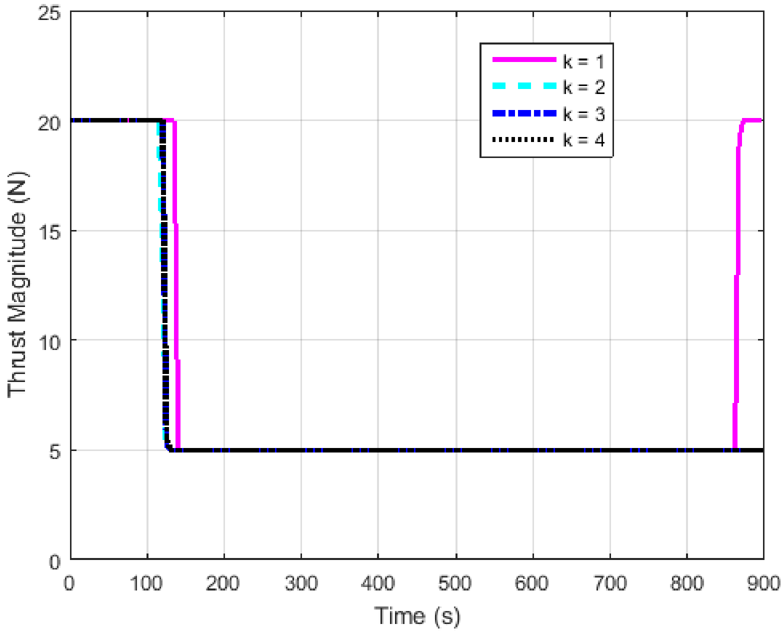

Figure 11.17: Thrust magnitude comparison for the different iterations with the NP_LT trajectory on A1, 8 hr period, 897 sec flight time.

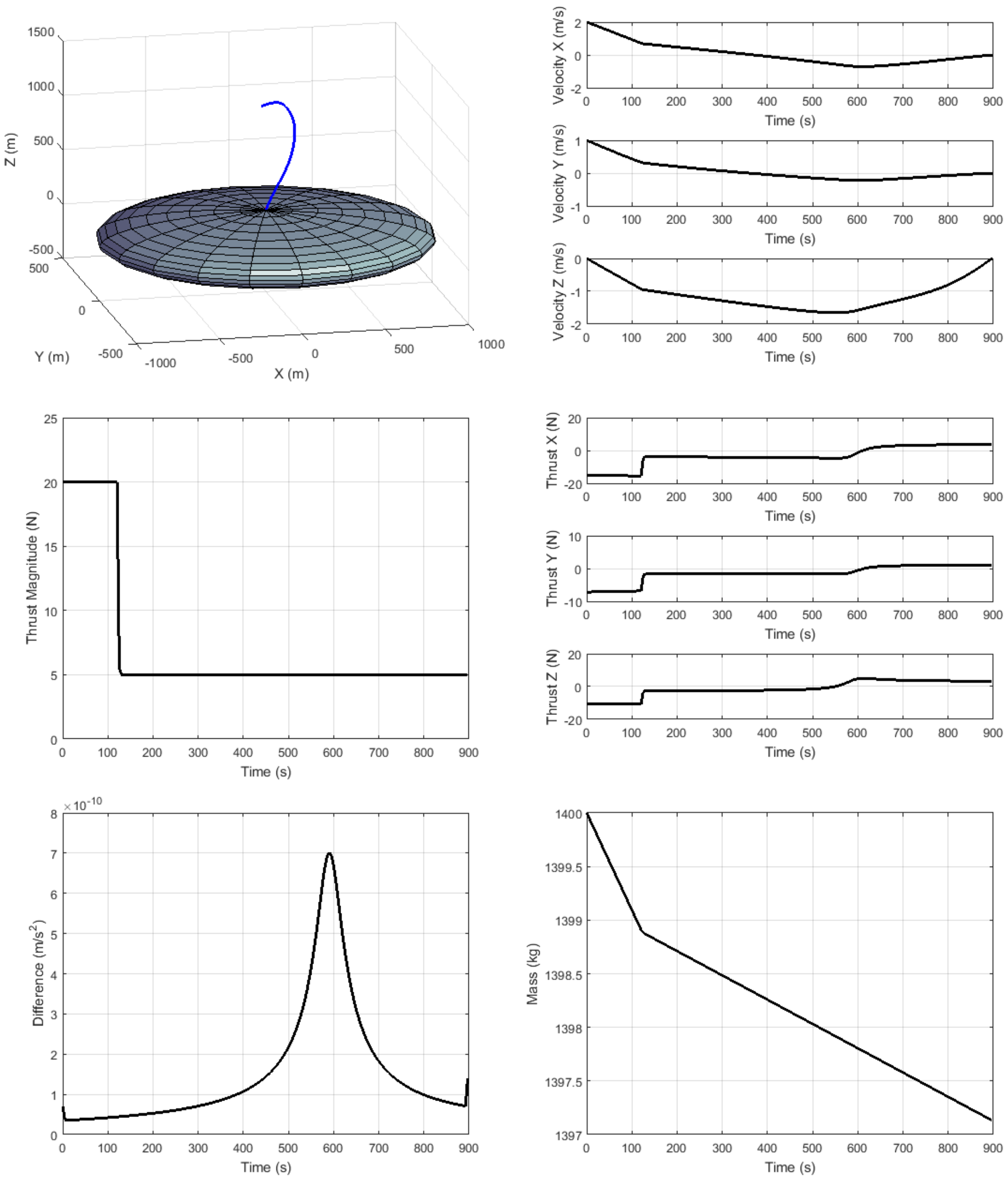

Figure 11.18: A1 8 hr period NP_LT trajectory for a 897 sec flight time. Top left: 3-D vehicle position, Top right: velocity components relative to the landing site, Middle left: thrust magnitude, Middle right: thrust components, Bottom left: difference between the slack variable and the acceleration vector, Bottom right: mass profile.

CHAPTER 12. OPTIMAL FLIGHT TIME DETERMINATION

The propellant optimal convex optimization problem discussed in the previous chapters assumed that a fixed flight time was given to the algorithm. Ultimately, the algorithm should determine the optimal flight time that yields minimum propellant usage over all flight times (tf^*). This is achieved by wrapping the convex optimization problem solved in CVX with an outer optimization loop that minimizes propellant with respect to flight time. Brent's method was selected as the solver routine for this outer optimization loop.

There are two different versions of Brent's method, a root finder and the minimum of a single variable function. The minimum of a single variable is the appropriate version and this function was incorporated based on the code entitled *localmin* found in Chapter 5 Section 8 of Ref. Brent (1973). Brent's method combines golden section search with parabolic interpolation. The golden section search guarantees an approximation of the minimum at linear speed. Parabolic interpolation is faster than golden section search, though it does not guarantee convergence on the minimum. By combining these two methods, Brent's method takes advantage of the parabolic interpolation speed for well-behaved functions, while guaranteeing convergence within a finite number of steps for all functions. This upper bound on the number of required steps can be determined; however, it normally does not need that many steps. Brent's method only requires function evaluations of the convex optimization loop. It does not require a derivative nor an approximation of the derivative through differencing, which is advantageous given the complexity of the inner loop's optimization problem.

For classes of functions that are twice differentiable near the minimum, Brent's method achieves superlinear convergence. Superlinear convergence is faster than the linear convergence found in the golden section search and Fibonacci search. In testing all classes of functions, Brent's method was never more than 5% slower than the Fibonacci search. (Ref. Brent (1973))

Propellant usage as a function of flight time is the one variable function that Brent's method minimizes. This function is demonstrated in the parameter sweeps shown in Figures 9.1 - 9.4, 9.7 - 9.10, 10.1 - 10.4, 10.7 - 10.10, 11.1 - 11.4 and 11.7 - 11.10. This function is unimodal, convex, well-behaved, and smooth near the minimum, which includes it in the class of functions that yields superlinear convergence. This is the reason Brent's method was chosen over golden section search and Fibonacci search.

An upper and lower flight time bounding the minimum is required. Due to the convexity of the propellant usage function, a large range of flight times can be given, so that there is no need to find a tight bounding range around the optimal. The NP, EQ, NP_hov, and EQ_hov cases used a bound of 300 - 1000 seconds, while NP_LT and EQ_LT used 700 - 1800 seconds.

The outer optimization loop using Brent's method calls the CVX optimization package for each function evaluation inside Brent's optimization loop. This continues until the answer cannot be improved within a given tolerance. This tolerance is a combination of relative and absolute tolerances given by Equation 12.1.

$$tol = t_1 \left| x \right| + \epsilon \tag{12.1}$$

In Equation 12.1, ϵ is the absolute tolerance based on machine tolerance (2.23x10^{-16} was used), x is the current approximation of the minimum and t_1 is the tolerance given to the algorithm, which was 0.01 for the NP, EQ, NP_hov, and EQ_hov cases and 0.001 for the NP_LT and EQ_LT cases. The value for t_1 was chosen to be the largest value that will give the same accuracy as the smaller values. The smaller the value the more evaluations of the CVX optimization package are needed, which increases computational cost.

Even with the superlinear convergence, the CVX optimization package will be called multiple times to determine the optimal flight time. In order to save on computation time, the time step inside the CVX package was increased to find the optimal flight time. Then, the propellant optimal problem was solved a final time with the optimal flight time using the original 2.0 sec step size (5.0 sec for lower thrust). A flow diagram of the final algorithm is depicted in Figure 12.1.

Four time steps for the CVX optimization package (inner optimization problem) were ex-

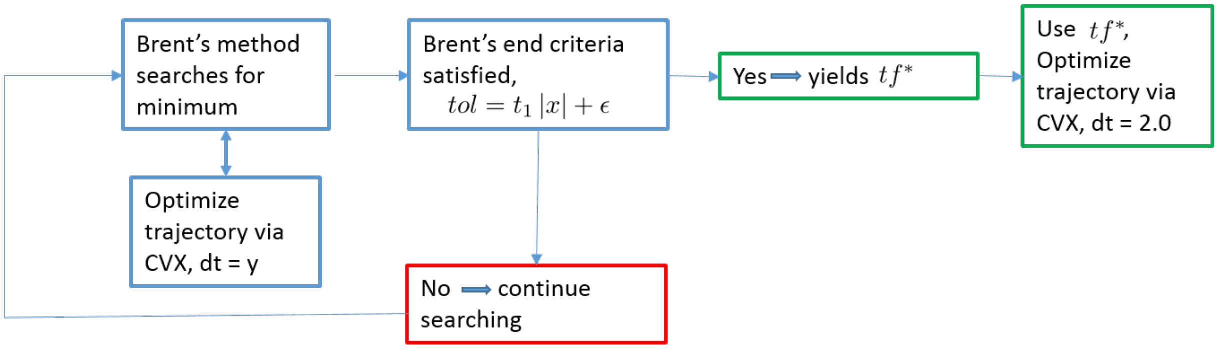

Figure 12.1: Flow diagram for the outer loop interactions with the inner loop.

amined: 2 sec, 5 sec, 10 sec, and 15 sec. For this analysis, when the 2.0 sec time step was used the final call to the CVX package was not necessary. The choice of the best time step is a balance between computational time and optimal flight time accuracy. The data examining these time steps for the NP is located in Table 12.1 and for EQ in Table 12.2, with both cases requiring 7 function evaluations of the inner optimization loop. As the time step increases from 2 sec to 5 sec to 10 sec, the required run time drops significantly to one third of the 2 sec run time, while the change in optimal flight time is less than one second and no difference in propellant usage. The increase to 15 sec does not decrease the run time significantly, while the difference in optimal flight time increases to two seconds. A time step of 10 sec for the initial calls to the inner optimization loop is the best balance between accuracy and computational speed for the NP and EQ trajectories. Since the thrust level and thus flight time is similar for the NP_hov and EQ_hov cases, the 10 sec time step will be used for those trajectories as well.

The data from the NP_LT and EQ_LT time step experiment are located in Tables 12.3 and 12.4, respectively. For only this experiment, 2 sec was used as the finest resolution, instead of the standard 5 sec. The NP_LT required 10 calls to the inner optimization loop, while the

Table 12.1: Time step comparisons for Brent's method, NP trajectory.

Time Step	tf* (s)	Prop Used (kg)	Run Time (min)
2 sec	487.69	4.9228	21.3
5 sec	487.78	4.9228	13.4
10 sec	488.03	4.9228	7.0
15 sec	489.55	4.9228	6.3

Table 12.2: Time step comparisons for Brent's method, EQ trajectory.

Time Step	tf* (s)	Prop Used (kg)	Run Time (min)
2 sec	512.08	5.2868	16.5
5 sec	512.29	5.2868	8.2
10 sec	512.87	5.2868	5.0
15 sec	514.10	5.2868	4.2

EQ_LT required 8. The lower thrust cases showed the same trends as NP and EQ. The run time drops significantly, to less than one third of the original between 2 sec and 10 sec, with less than a four second difference in optimal flight time. The run time does not decrease substantially between the 10 sec and 15 sec. The difference in flight time between the 2 sec and 15 sec time steps is 5.2 sec for the EQ_LT and 2.0 sec for the NP_LT. The NP_LT is a decrease from the 10 sec to 2 sec difference. Overall, it was decided that the 10 second time step is a very good balance for the NP_LT and EQ_LT cases.

Table 12.3: Time step comparisons for Brent's method, NP_LT trajectory.

Time Step	tf* (s)	Prop Used (kg)	Run Time (min)
2 sec	895.05	2.8682	65.5
5 sec	896.51	2.8682	27.8
10 sec	891.31	2.8682	18.9
15 sec	893.10	2.8682	16.6

Table 12.4: Time step comparisons for Brent's method, EQ_LT trajectory.

Time Step	tf* (s)	Prop Used (kg)	Run Time (min)
2 sec	1043.8	3.3531	49.4
5 sec	1045.2	3.3531	23.3
10 sec	1046.0	3.3531	12.2
15 sec	1049.0	3.3531	8.7

CHAPTER 13. ADDITIONAL TRAJECTORY CONSTRAINTS

Two additional trajectory constraints were activated, independently, in the propellant optimal trajectory design problem and analyzed. The first constraint keeps the vehicle directly above the landing site with no lateral motion for the last few seconds of flight, or only allows vertical motion. The second constraint is the glide slope constraint. The original problem included a glide slope constraint; however, it was only used to ensure that the vehicle did not fly subsurface. An in-depth look at applying the glide slope and the ability to keep the vehicle within a small cone around the landing site is included.

13.1 Solely Vertical Motion Near the Landing Site Constraint

As the vehicle nears the landing site it is desirable and advantageous for it to be directly over the landing site with the only motion being a change in altitude. This allows the vehicle to land upright and removes tip over concerns. If the vehicle has lateral motion when it reaches the landing site, the vehicle could be misaligned for an upright landing. A new constraint was applied that eliminates the lateral motion during the last seconds of flight, resulting in solely a change in altitude.

First, the position vector from the landing site to the spacecraft is determined, Equation 13.1.

$$\vec{r}_{ls} = \vec{r} - \vec{r}_f \tag{13.1}$$

The vehicle vertical and lateral motion is with respect to the landing site. Therefore, this position vector, relative to the landing site, is used in the constraint instead of the position vector from the asteroid center to the spacecraft.

The solely vertical motion near the landing site constraint is applied as two new equality constraints, located in Equation 13.2.

$$\begin{aligned} \vec{r}_{ls}^{\,T}\hat{t}_1 &= 0 \\ \vec{r}_{ls}^{\,T}\hat{t}_2 &= 0 \end{aligned} \tag{13.2}$$

The basis describing the plane tangent to the landing site is contained in $\hat{t}_1$ and $\hat{t}_2$. This can be any basis as long as the plane is completely described. A zero dot product with the tangent plane requires the motion to be solely normal to the landing site plane, which would only allow motion in the vertical direction or a change in altitude. The vectors describing the landing site are depicted in Figure 13.1. The basis vectors describing the plane tangent to the landing site are listed in Equation 13.3 for the NP trajectories and in Equation 13.4 for the EQ trajectories.

$$\hat{t}_1 = \begin{bmatrix} 1 \\ 0 \\ 0 \end{bmatrix} \hat{t}_2 = \begin{bmatrix} 0 \\ 1 \\ 0 \end{bmatrix} \tag{13.3}$$

$$\hat{t}_1 = \begin{bmatrix} 0 \\ 1 \\ 0 \end{bmatrix} \hat{t}_2 = \begin{bmatrix} 0 \\ 0 \\ 1 \end{bmatrix} \tag{13.4}$$

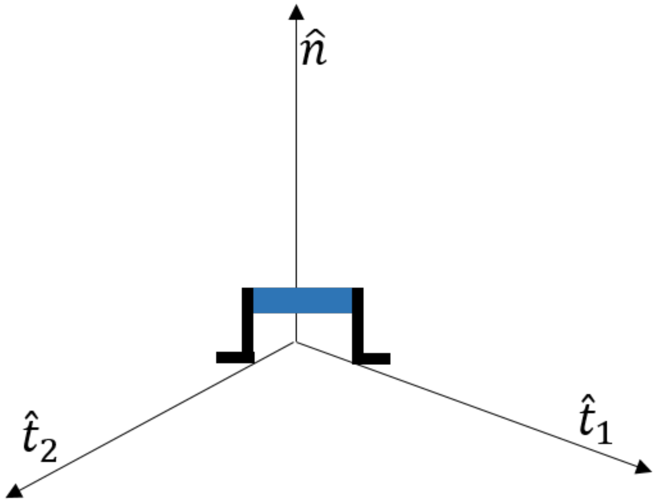

Figure 13.1: Unit vectors describing the landing site. $\hat{n}$ is normal to the landing site, while $\hat{t}_1$ and $\hat{t}_2$ describe the plane tangent to the landing site.

Both the NP and EQ trajectories were examined with the solely vertical motion near the landing site constraint. The NP successfully included and achieved this constraint, while the EQ trajectory had difficulty due to the velocity of the landing site coupled with the low thrust of the vehicle.

A NP trajectory on A1 with an 8 hr period for a 480 second flight time was analyzed. The solely vertical motion constraint is enforced during the last six seconds of flight and then during the last ten seconds. The end portion of flight (approximately the last 20 seconds) is shown in Figure 13.2, comparing the trajectory without this constraint to enforcing for the last six seconds and last ten seconds. The trajectory shape within two meters of altitude above the landing site differs greatly between the three trajectories. The propellant usage changed very slightly between the three cases, with the original case using 4.92 kg, the 6 sec using 4.93 kg, and the 10 sec using 4.94 kg. Required iterations was 4 for the original and 6 sec enforcement, and 3 for the 10 sec enforcement. Addition of this constraint did not adversely affect the successive solution convergence. The difference between the slack variable and the acceleration vector was on the order of $5\text{x}10^{-9}$ m/s^2. This shows that the optimal solution of the relaxed problem is still the optimal solution of the original problem. This constraint was not included in the proof, so spot checking gives confidence that the relaxation holds.

Problems arose when enforcing the solely vertical motion near the landing site constraint for the EQ trajectories. The low thrust of the vehicle (80 N) is not strong enough for the vehicle to match the landing site velocity, while eliminating additional lateral velocity. The velocity required to remain above the landing site changes with altitude. Originally, it was thought that the centripetal acceleration was the driver behind the vehicle being unable to eliminate the lateral motion near the landing site; however, this is not the case. For an 8 hour period on A1 the landing site velocity is 0.22 m/s. If the speed of the landing site is reduced to 0.01 m/s, while leaving the accelerations due to the asteroid rotation (8 hr period) in the optimization problem, the problem can be successfully solved

Unfortunately, the landing site speed cannot be changed without changing the speed of the asteroid and the overall forces on the vehicle. Increasing the rotational period, which decreases both the landing site velocity and the centripetal and Coriolis accelerations allows the problem

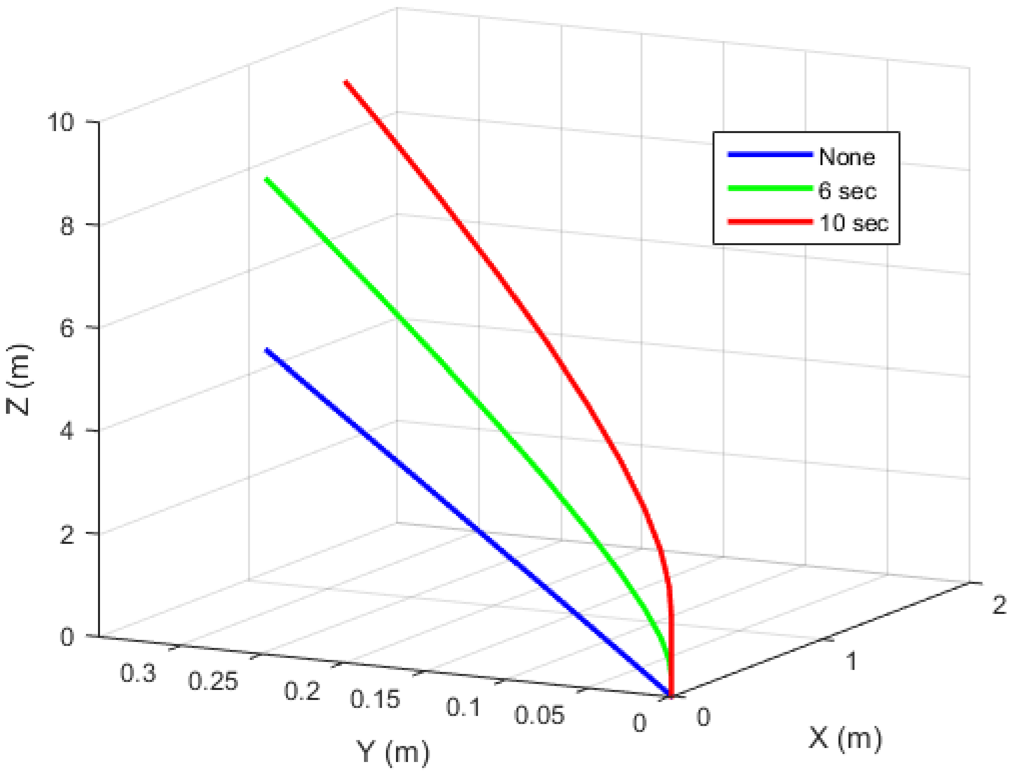

Figure 13.2: End of the A1 8 hr NP 480 sec trajectory without the solely vertical motion constraint, with a 6 sec enforcement, and with a 10 sec enforcement of the constraint. Origin is the landing site.

to be solved. For the A1 asteroid, the rotational period had to be increased to 92 hours in order to enforce the solely vertical motion constraint for the last 6 seconds of flight and 184 hours to enforce the constraint for the last 10 seconds of flight. Figure 13.3 contains the original EQ trajectory without the constraint and these two constrained trajectories. The figure's vertical axis is the altitude above the landing site corresponding to the asteroid +X axis and the horizontal axes are the lateral directions. Since the forces on the vehicle are quite different in the three trajectories, the vehicle approaches the landing site from a different direction for each trajectory. An alternate approach to show that the vehicle thrust is insufficient for the landing site velocity is to increase the thrust of the vehicle until it successfully lands on the asteroid with an 8 hour period. The upper thrust bound must be increased to 920 N as compared to

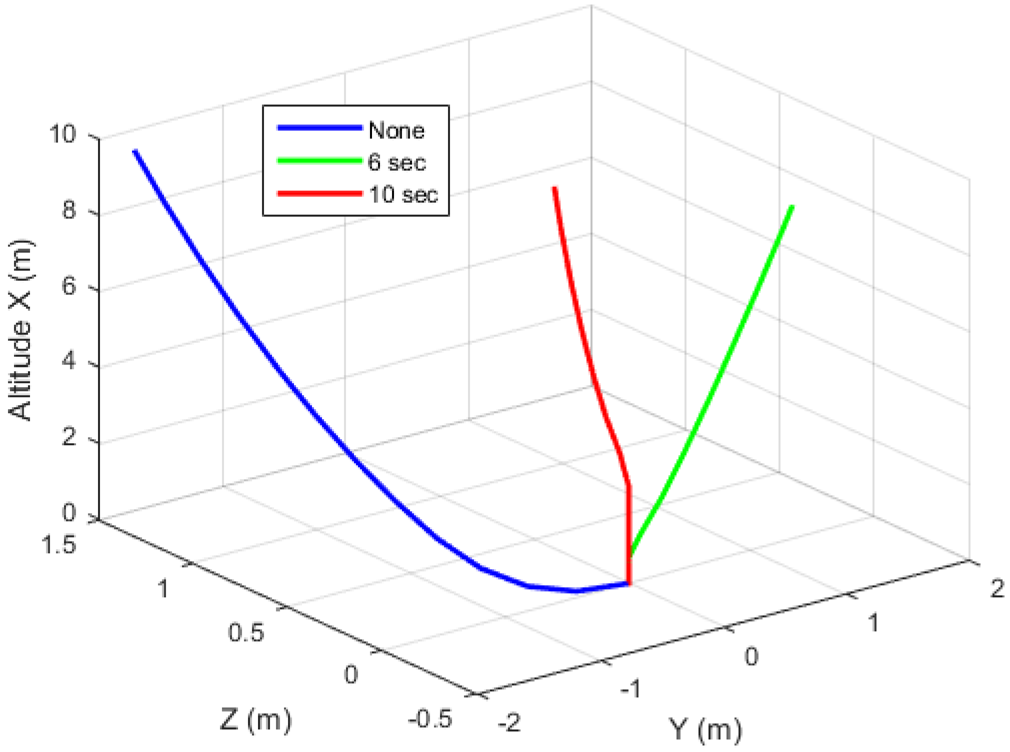

Figure 13.3: End of the A1 EQ 480 sec trajectory without the solely vertical motion constraint, with a 6 sec enforcement (92 hr period) and with a 10 sec enforcement (184 hr period). Origin is the landing site.

80 N to successfully land the vehicle. Equatorial landing is not recommended if the vehicle needs to eliminate lateral motion near the landing site.

13.2 Glide Slope Constraint

The glide slope constraint requires the vehicle to stay inside a cone centered at the landing site as shown in Figure 13.4. The cone is described by the angle θ measured from the vector normal to the landing site, $\hat{n}$. The constraint is a second order cone constraint, given in Equation 13.5.

$$\|\vec{r}-\vec{r}_f\|\cos\theta-(\vec{r}-\vec{r}_f)^T\hat{n}\leq 0 \tag{13.5}$$

This equation is part of the problem formulation in the previous chapters; however, it was only used to prevent the vehicle from flying subsurface, corresponding to an angle of 90 degrees. The constraint is applied to all time points, except the last time point when the vehicle is located at the landing site. Due to machine precision, the vehicle position vector will not exactly equal the landing site location for every single decimal place. This causes problems with enforcing the constraint at this point. Since the vehicle is at the landing site the constraint is not needed. As with the solely vertical motion near the landing site constraint, the glide slope constraint worked well for the NP trajectories, while issues existed for the EQ trajectories.

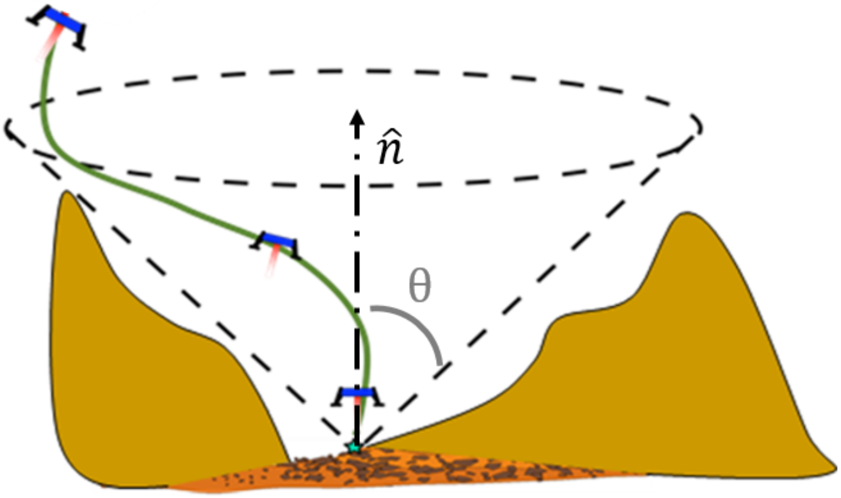

Figure 13.4: Glide slope constraint requires the vehicle to stay within the black cone.

A 480 second A1 8 hr NP trajectory was run without the glide slope constraint (free), then with a cone of 10 degrees around the landing site, and finally with a 5 degree cone around the landing site. The plot in Figure 13.5 compares the angle between the landing site normal vector and the vehicle position vector. The free trajectory had an angle greater than 15 degrees for the last 230 seconds of flight. When the 10 degree cone constraint is included, the entire trajectory takes a different shape with the 10 degree limit only being active for a single point. For the 5 degree cone constraint, the trajectory hovers at the 5 degree limit, though it does leave the bound for the last 150 seconds of flight. The 3-D plot comparing the original trajectory to the 10 deg cone trajectory is located in Figure 13.6. The blue dashed cone represents a 10 degree cone around the landing site. A similar plot for the 5 degree cone constraint is located in Figure 13.7, where the blue dashed cone is a 5 degree cone around the landing site.

The relaxation proof in Chapter 5 did not include the glide slope constraint. In order for the optimal solution of the relaxed problem to be the optimal solution of the original problem, the acceleration slack variable must equal the magnitude of the acceleration vector. Plots showing the difference between these two values are located in Figure 13.8, showing the difference to be less than 7.0x10^{-7} m/s^2. Thus, the relaxation holds for these cases. It is reasonable to assume it will hold for other cases. Proofs including pointing constraints, which are similar to the glide slope constraint, are contained in Ref. Acikmese et al. (2013), which gives confidence in lossless convexification holding for the glide slope constraint.

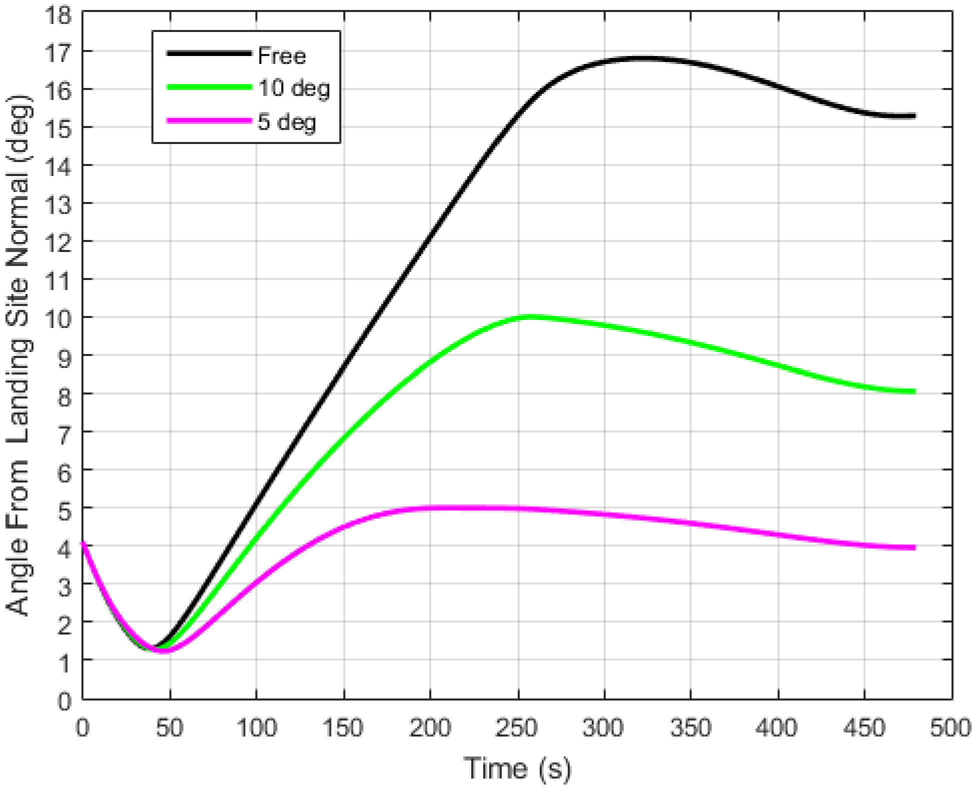

Figure 13.5: Angle from the landing site normal for the NP trajectory on A1 8 hr with a 480 second flight time.

Near the landing site the cone around the landing site narrows and approaches the solely vertical motion near the landing site constraint from Section 13.1. Given this similarity, it is not surprising that the equatorial cases cannot design a trajectory with the glide slope constraint applied for the entire trajectory. Examining the 8 hr A1 EQ with a 480 sec flight time, when

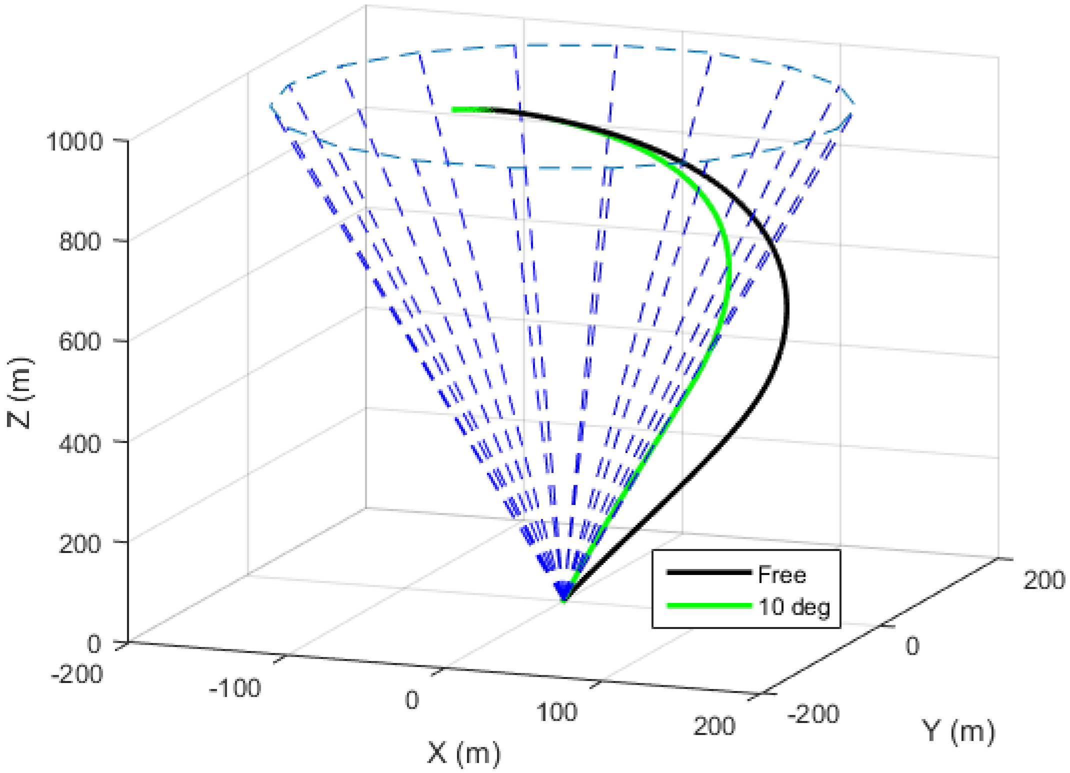

Figure 13.6: Comparison of the trajectory without the glide slope constraint (free) and with a 10 deg cone glide slope constraint for a NP trajectory on A1 8 hr with a 480 second flight time. Origin is the landing site.

the constraint is applied for all but the last 6 seconds a trajectory can be solved, though it flies outside the cone for the last few seconds. For this case, the trajectory flies the 10 degree limit for the last half of the flight until the last 6 seconds where it leaves the cone for about 0.5 meter at the end. The angle between the landing site normal and the position vector for the trajectory without the glide slope constraint (free) and the 10 deg cone glide slope constraint is shown in Figure 13.9. The 3-D plot for the two trajectories is located in Figure 13.10. The bottom plot focuses on where the trajectory leaves the cone for a short distance. The origin is the landing site, with the axes oriented with the altitude along the z axis. The difference between the slack variable and the acceleration vector magnitude is less than 1.0x10^{-7} m/s^2, showing that the relaxation still holds. As in the solely vertical motion near the landing site constraint problem, a slower rotation speed allows the constraint to be levied for the entire

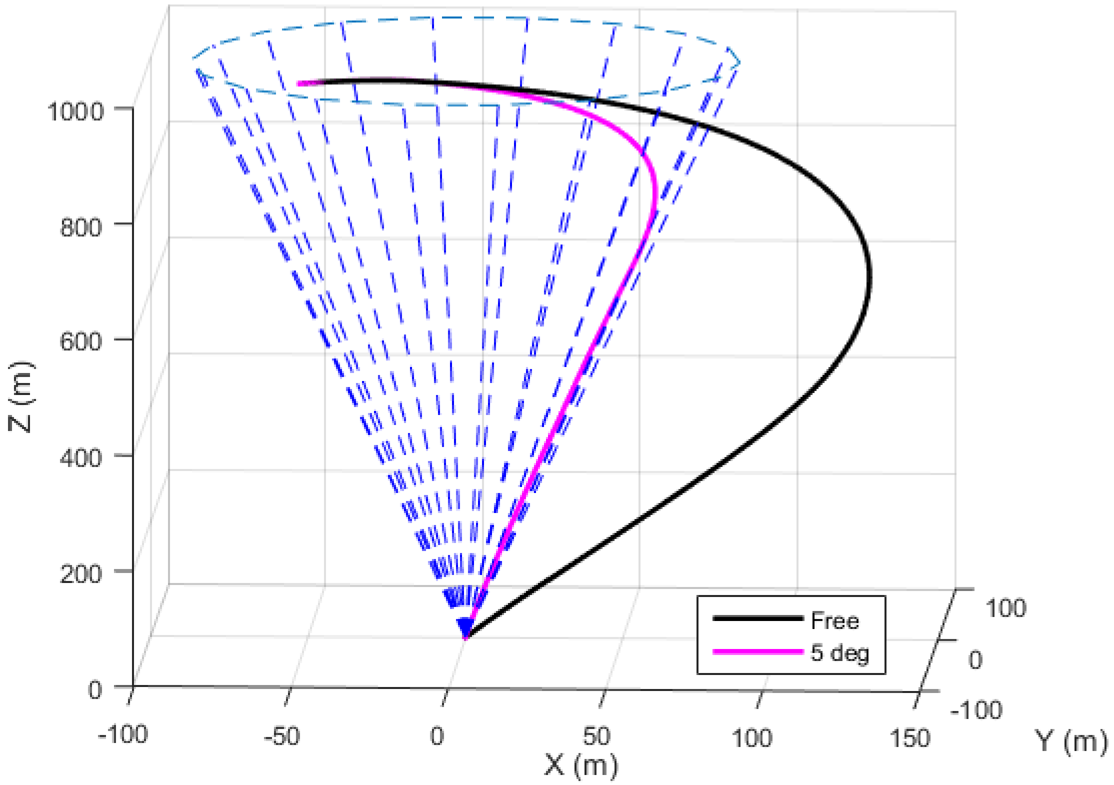

Figure 13.7: Comparison of the trajectory without the glide slope constraint (free) and with a 5 deg cone glide slope constraint for a NP trajectory on A1 8 hr with a 480 second flight time. Origin is the landing site.

trajectory. The landing site velocity can be decreased to 5x10^{-5} m/s while keeping the 8 hour rotation for the centripetal forces or the rotation period can be increased to 36 hours to allow a successful 10 degree glide slope constraint.

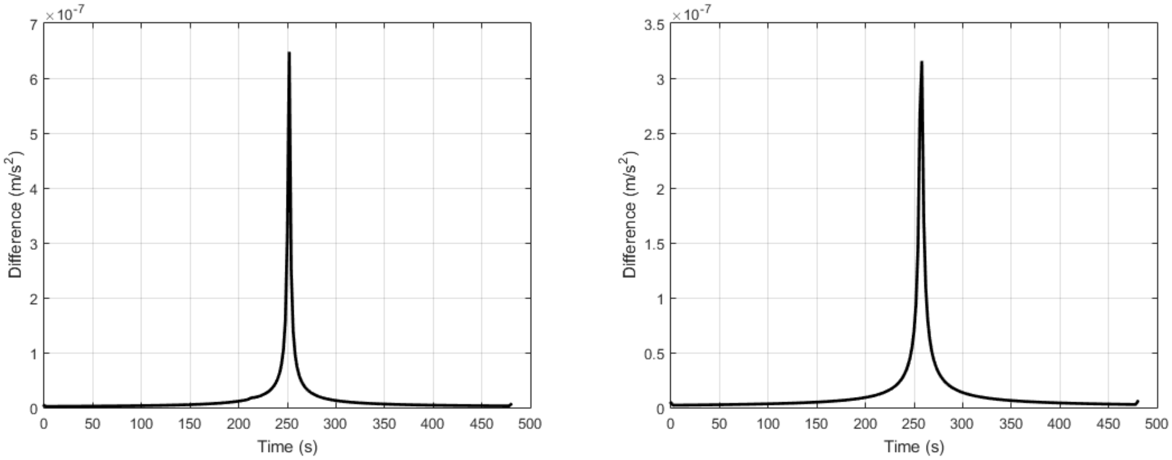

Figure 13.8: Comparison between the slack variable and the magnitude of the acceleration vector for the 5 deg cone constraint (left) and the 10 deg cone constraint (right) for the NP trajectory on A1 8 hr with a 480 second flight time.

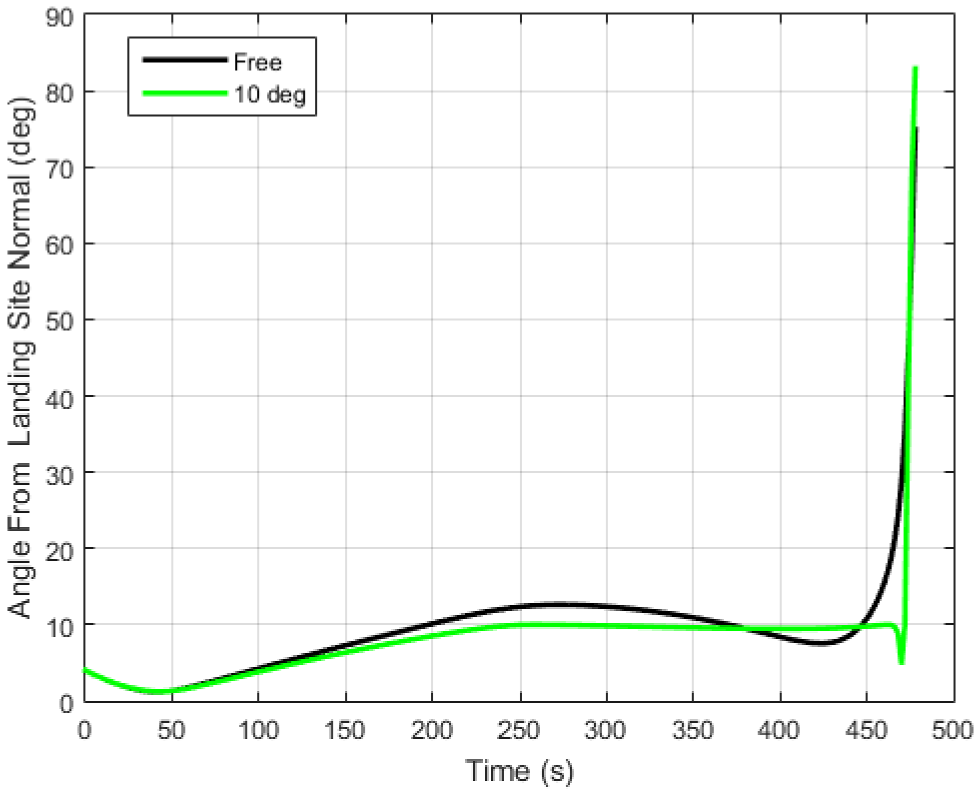

Figure 13.9: Angle from the landing site normal for the EQ trajectory on A1 8 hr with a 480 second flight time.

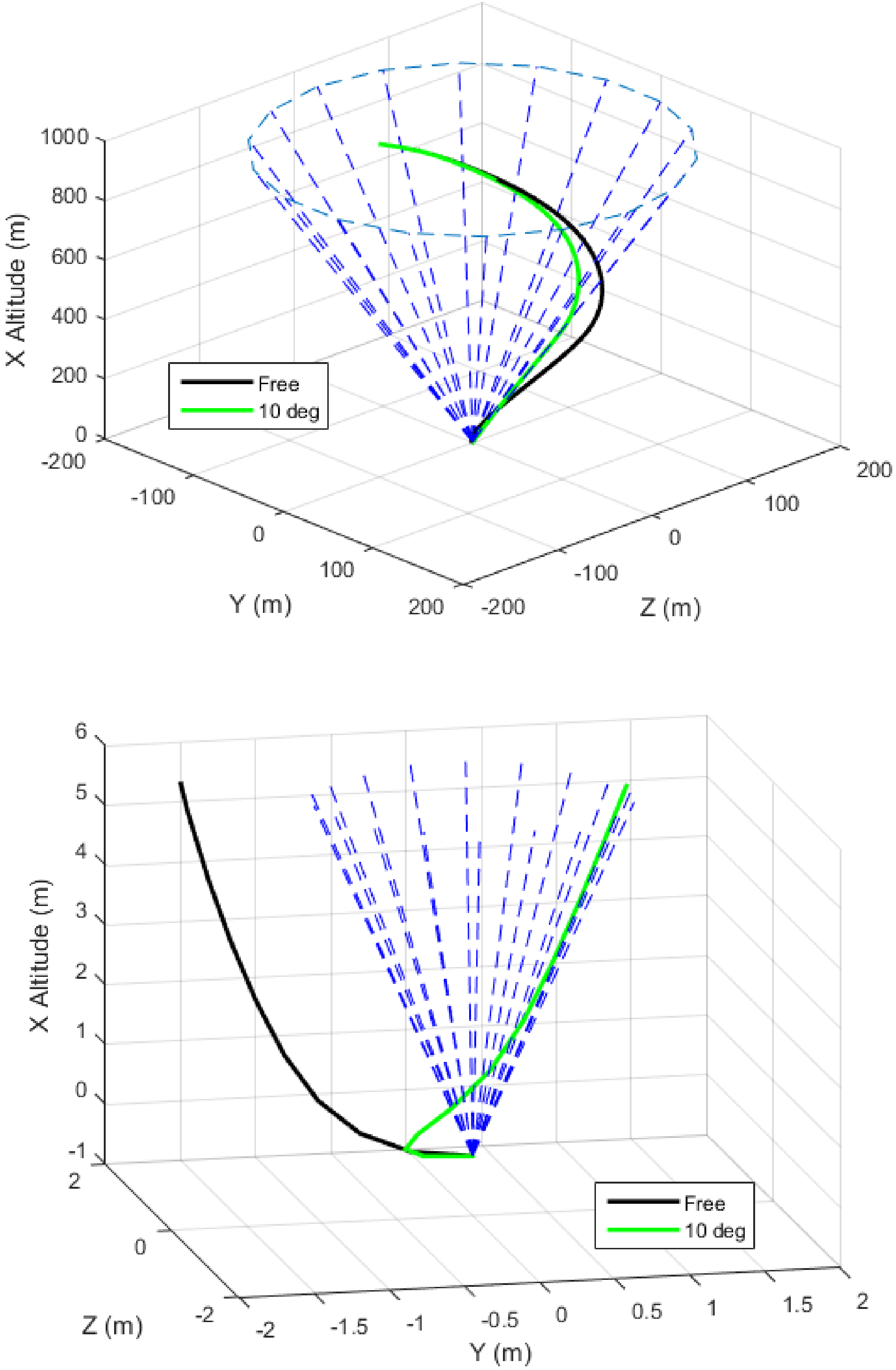

Figure 13.10: Comparison of the trajectory without the glide slope constraint (free) and with a 10 deg cone glide slope constraint for an EQ trajectory on A1 8 hr with a 480 second flight time. Bottom plot zooms in on the landing site. Origin is the landing site.

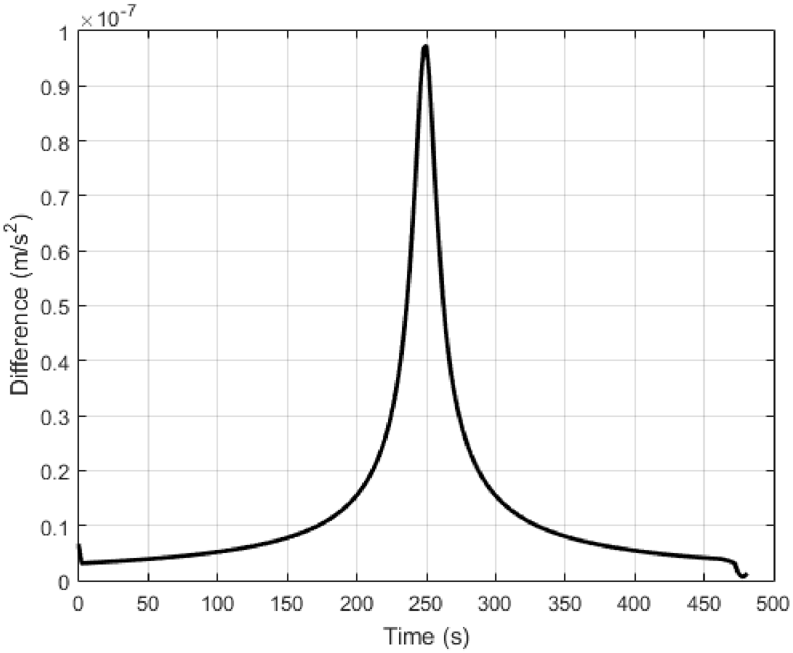

Figure 13.11: Comparison between the slack variable and the magnitude of the acceleration vector with the 10 deg cone constraint for the EQ trajectory on an 8 hr A1 with a 480 second flight time.

CHAPTER 14. CASTALIA TRAJECTORY ANALYSIS

The binary asteroid Castalia is a good example of an irregularly shaped asteroid. It is long and flat which invalidates the triaxial asteroid assumptions and the use of the 2x2 gravitational model, especially near the surface. Section 14.3, demonstrates that this asteroid requires the full high fidelity gravity model, 4x4 Bessel, in order to design a trajectory that successfully reaches the surface. Overall, the trends seen with Castalia and the 4x4 Bessel gravity model incorporated in the algorithm follow the trends seen with the three triaxial asteroids and the different spin periods. As this uses a real asteroid, the size and rotational rates will not be varied to show trends; however, the out of plane and uprange trajectories, the hover trajectories, and the low thrust trajectories were all evaluated and tested.

14.1 Trajectory and Optimization Analysis

Solving the propellant optimal descent problem, the inner loop algorithm in CVX, for the three landing sites on Castalia produces the same trends as the triaxial asteroids. The inner loop algorithm, trajectory design, contains the relaxation of the problem, discretization, and application of the successive solution method along with the 4x4 Bessel gravity model. A parameter sweep varying flight time and designing the trajectory with the inner optimization loop was performed for the out of plane and uprange initial conditions for the three landing sites on Castalia, as shown in Figure 14.1. Propellant usage is similar between the three landing sites, despite their locations being on different parts of the asteroid. The trend confirms that propellant usage is unimodal with respect to flight time; therefore, the outer loop optimization of flight time using Brent's method is still applicable.

The number of required iterations for the different flight times is displayed in Figure 14.2.

For the most part, three iterations were required to design the optimal trajectory, which is similar to the two to four from the triaxial asteroids. A handful of cases required more than three iterations. All the cases analyzed successfully converged on the optimal trajectory, showing stability in the successive solution method.

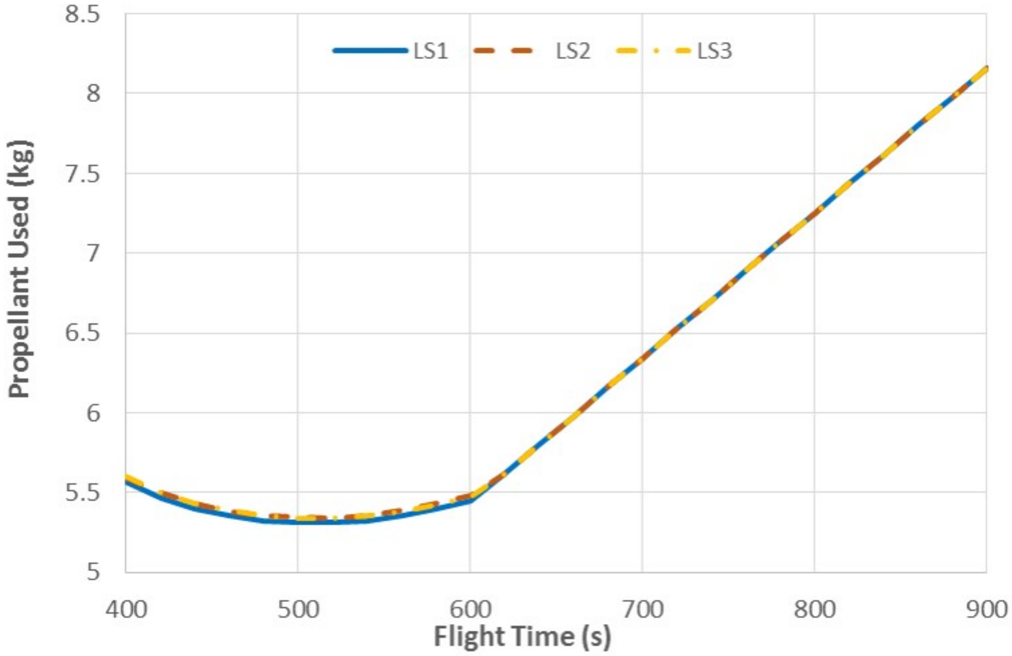

Figure 14.1: Propellant usage from the flight time parameter sweep for the three Castalia landing sites.

The thrust profile remains bang-bang for the designed trajectories. By using the convex optimization coupled with the successive solution method, the thrust profile will follow the profile proposed by Optimal Control Theory. Other research options, discussed in Section 2.2, do not follow this trend when designing powered descent trajectories. A 400 second flight time for LS3 was designed, in order to fully demonstrate a case that clearly designs the bang-bang thrust profile. The plots from this trajectory are located in Figure 14.3. The difference between the slack variable acceleration and the magnitude of the acceleration vector is less than 1.0x10^{-9} m/s^2, demonstrating that lossless convexification is valid and the relaxed problem is the original problem for the optimal solution. This is still true, despite switching to a more complex gravity model.

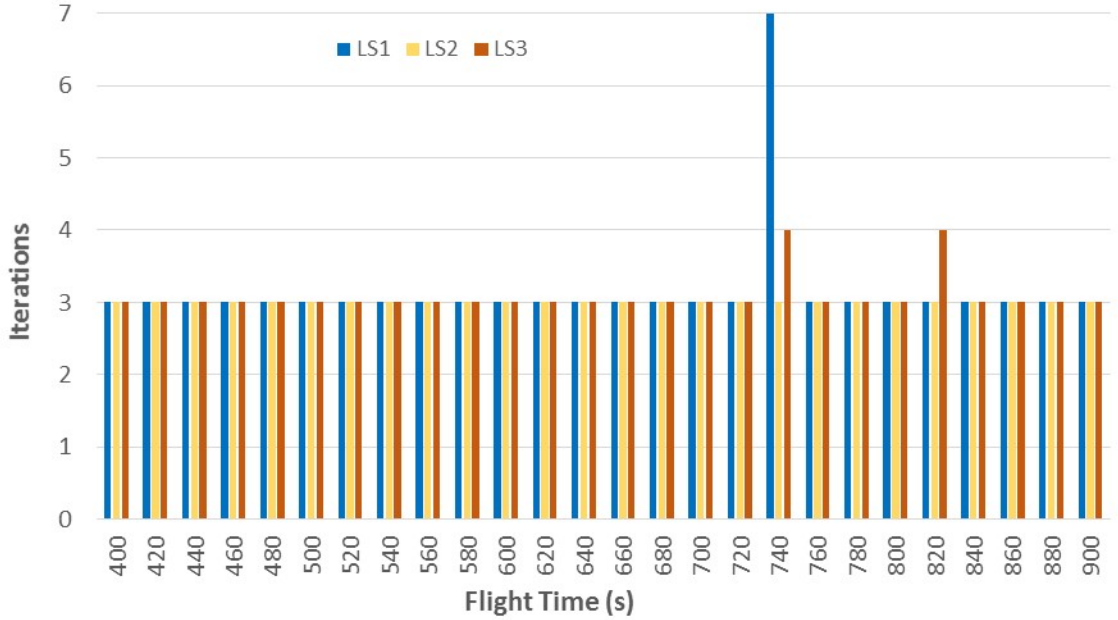

Figure 14.2: Required iterations for the three Castalia landing sites.

The short flight time of 400 seconds showed the maximum-minimum-maximum thrust profile version of bang-bang associated with Optimal Control Theory. As with the triaxial asteroids, the shorter flight times had a maximum-minimum-maximum profile, with the medium flight times designing a maximum-minimum, and the longer times staying at minimum for the entire flight. The flight time at which these switches occurred, along with the optimal propellant usage flight time, is tabulated in Table 14.1. The propellant difference between the optimal propellant flight time case and the switches is located in Table 14.2. For all three landing sites the optimal propellant flight time occurred seven to nine seconds before the switch to maximum-minimum. Since the optimal flight time is very close to the switch to maximum-minimum, only the last few points are at the maximum. The propellant usage difference between the optimal flight time and the switch to maximum-minimum is a fraction of a percent. This is in line with the triaxial asteroid trends. As seen in Figure 14.1, propellant usage is fairly flat near the minimum point; however, after the switch to all minimum the slope becomes steeper. It is best to design the trajectory before the switch to all minimum.

Table 14.1: Flight times corresponding to optimal propellant and thrust profile switches for the asteroid Castalia.

(s)	LS1	LS2	LS3
optimal propellant	513	512	513
start maximum-minimum	520	521	521
start all minimum	602	608	607

Table 14.2: Percent difference in propellant usage from optimal propellant case for the asteroid Castalia.

	LS1	LS2	LS3
start maximum-minimum	0.02%	0.02%	0.01%
start all minimum	2.75%	3.15%	3.04%

14.2 Optimized Flight Time Optimal Propellant Trajectories

As the ultimate goal is to design the optimal propellant trajectory over all flight times and trajectories, the outer loop optimization (Brent's method) wrapping around the inner optimization algorithm (CVX) was tested with the Castalia trajectories. Castalia trajectories used the same tolerances and bounds with Brent's method as the triaxial asteroids. For all sets of trajectories, out of plane and uprange, hover, and lower thrust, the overall optimization method was successful. Table 14.3 contains the optimal flight time and the corresponding propellant used for that flight time. The last column is the number of times the inner loop designed a trajectory. Each of these inner loop executions contained multiple iterations of the successive solution method, normally around three. The hover cases took more inner loop calls than the out of plane and uprange cases using the same vehicle configuration. The lower thrust cases required the most amount of calls to the trajectory design loop. Despite the fact that the three landing sites are in different locations on the asteroid, the optimal flight time was within one second of each other for the nominal thrust cases with propellant usage being less than 0.03 kg difference between the cases. The lower thrust cases had a larger variation in optimal flight time, 25 seconds, yet the propellant difference was still very small, 0.06 kg.

Table 14.3: Comparison of the optimal flight time, propellant used, and number of inner loop executions for all Castalia trajectory configurations.

	Optimal Flight Time (s)	Optimal Propellant Used (kg)	Number of inner loop executions
LS1	512.86	5.31	7
LS2	512.27	5.34	7
LS3	513.35	5.34	7
LS1_hov	527.99	4.86	9
LS2_hov	527.77	4.89	9
LS3_hov	528.77	4.89	9
LS1_LT	1052.0	3.39	10
LS2_LT	1050.6	3.45	11
LS3_LT	1075.6	3.44	9

The propellant optimal designed trajectories corresponding to the optimal flight time for the out of plane and uprange cases are shown in Figure 14.4. The top plot is for LS1, the middle for LS2, and the bottom for LS3. Figure 14.5 compares the magnitude of the vehicle velocity relative to the landing site velocity, the thrust magnitude profile, a check on the slack variable, and the mass profiles for the three trajectories. All three trajectories have the maximum-minimum-maximum thrust profile, though the final maximum is only for a few seconds. The difference between the slack variable and the magnitude of the acceleration vector is less than $4x10^{-9}$ m/s^2. The magnitude of the vehicle velocity is very similar across the cases, though the individual components are not.

The hover case designed trajectories for the optimized flight time are shown in Figure 14.6 with trajectory parameters in Figure 14.7. As this trajectory mainly removes altitude, the trajectory is closer to straight in and does not have the hook that the other trajectories have. Also, the inertial velocity plot has the near perfect triangular shape associated with acceleration followed by braking. An interesting note, the LS2_hov is the only optimized flight time to occur after the switch to maximum-minimum. LS1_hov and LS3_hov are close to this switch as they did not return all the way to maximum thrust in the design. The check on the slack variable shows that the relaxed problem is the original problem for this designed trajectory.

The optimal propellant trajectory corresponding to the lowest propellant usage over all flight times for the lower thrust cases is depicted in Figure 14.8 with the trajectory parameters in Figure 14.9. The trends are similar to the hover and out of plane and uprange cases. The thrust magnitude and velocity magnitude profiles show more variation between the three landing sites when compared to the other cases.

14.3 Gravity Effects from an Irregularly Shaped Asteroid

In order to show that the high fidelity model incorporating both the spherical harmonics and the spherical Bessel gravity models is necessary for trajectory design on an irregularly shaped asteroid, the trajectory was designed with lower fidelity gravity models and then run open loop in the combined 4x4 Bessel environment. The open loop simulates the translational dynamics of the vehicle following the designed thrust profile, assuming perfect navigation and control. No corrections are made if the vehicle drifts off the trajectory due to disturbances in the environment. For this particular open loop run, the only disturbance is the 4x4 Bessel gravity model, which is taken to be the true gravity of the asteroid. The simulation ends when the vehicle reaches zero altitude. If the designed thrust profile ends before this point, the last thrust value and direction is held.

Three gravity models were used: the 2x2 model, the 4x4 model, and the 4x4 Bessel gravity model. Recall from Section 9.5, a minimum of 2x2 was required on a perfect triaxial ellipsoidal asteroid, so at least that high of a fidelity model will be required on an irregularly shaped asteroid. All three Castalia landing sites were studied in this analysis using a 500 second flight time.

When the trajectory designed in the 2x2 gravity model was flown open loop, only the vehicle landing at LS3 reached the surface. The vehicle's lowest altitude for LS1 was 1.3 m and LS2 was 1.6 m with the designed 2x2 trajectory. Altitude plots for these two open loop simulations are located in Figure 14.10 (LS1) and Figure 14.11 (LS2). The accuracy for the LS3 site is located in the fourth column of Table 14.4. The position accuracy is poor, on the order of

3.9 m away from the landing site. Likewise, the only 4x4 designed trajectory that reached the surface was LS3, with its accuracy in the fifth column of Table 14.4. The vehicle landing at LS1 came close to the surface with a lowest altitude of 0.5 m, while the LS2 lowest altitude was 1.3 m. The altitude plots for these two cases are located Figure 14.10 (LS1) and Figure 14.11 (LS2). Overall, for an elongated asteroid such as Castalia the full 4x4 Bessel is required when designing the trajectory in order to complete the mission. The remaining columns in Table 14.4 show the accuracy when flying the designed 4x4 Bessel trajectory in the open loop simulation.

Table 14.4: Open loop results for the asteroid Castalia with a 500 sec flight time.

	LS1 4x4 Bessel	LS2 4x4 Bessel	LS3 2x2	LS3 4x4	LS3 4x4 Bessel
Position Error x (m)	-0.033	0.012	0.40	2.82	-0.180
Position Error y (m)	0.168	-0.230	-1.62	-1.55	-0.022
Position Error z (m)	0.0002	-0.0003	3.47	3.92	0.0006
Velocity Error x (m/s)	0.026	-0.021	-0.14	-0.09	0.064
Velocity Error y (m/s)	-0.049	-0.040	0.45	0.39	0.019
Velocity Error z (m/s)	0.041	0.042	0.17	0.16	0.045
Prop Used (kg)	5.27	5.30	5.04	5.08	5.30

14.4 Additional Trajectory Constraints

The glide slope constraint was applied to demonstrate that it will work with the 4x4 Bessel gravity model in the inner loop trajectory design algorithm. Unfortunately, the Castalia landing sites interact with the glide slope constraint in the same manner as the EQ landing site on the triaxial ellipsoids. The landing site velocity is too large for the vehicle to stay in the cone right at the landing site with the available thrust.

The trajectory was run two different ways with the glide slope constraint enabled to show that including the constraint is feasible and this is a physical limitation not a failure of the method. The first run does not apply the constraint for the last 3 points (4 seconds) for LS1 and LS3 and the last 4 points (6 seconds) for LS2. This allows the vehicle to fly outside the cone near the landing site where the constraint is very tight. The second run adjusted the vehicle thrust and found that the thrust must be at least 320 N in order to fly a 10 deg cone with the glide slope constraint applied. Opening the cone up to higher angles does not help. The cone must be at least 75 degrees to allow the trajectory to successfully solve, which is near the maximum angle that the trajectory designs when the constraint is not active.

A 500 second flight time trajectory was designed for these two runs and a third run where the glide slope constraint is not applied for the three landing sites. In the legend, Free refers to cases without the constraint applied, Point refers to the first set of runs, and Thrust refers to the second set. Figure 14.12 compares the angle between the vehicle position vector relative to the landing site and the landing site normal for LS1. The free trajectory travels outside the 10 degree cone between 200 - 350 seconds, thus requiring the constraint in order to stay within the cone for most of the flight. The 3-D plot of the trajectories and the cone around the landing site is located in Figure 14.15. The zero point is the landing site location. The left plot is the entire trajectory. The vehicle path stays near the cone boundary for most of flight for both of the constrained trajectories, while the free trajectory exceeds the cone. The right plot zooms in on the landing site. While it can be seen that the free trajectory deviates from the cone, the Point trajectory leaves the cone very slightly, so slight that it is not visible. Despite the large angle in Figure 14.12, the vehicle does not deviate by a large distance. Therefore, it is feasible to not constrain the last points and get a trajectory that does not significantly leave the cone around the landing site.

Figures 14.13 and 14.16 contain similar plots for LS2 and Figures 14.14 and 14.17 contain the plots for LS3. As with all these cases, a large angle from the landing site normal appears, but the vehicle does not greatly leave the cone in the constrained cases near the landing site. If larger thrusters are available that will mitigate the necessity of not applying the glide slope constraint to all the trajectory points. Given that the glide slope constraint cannot be applied near the landing site, the solely vertical motion near the landing site constraint also cannot be applied.

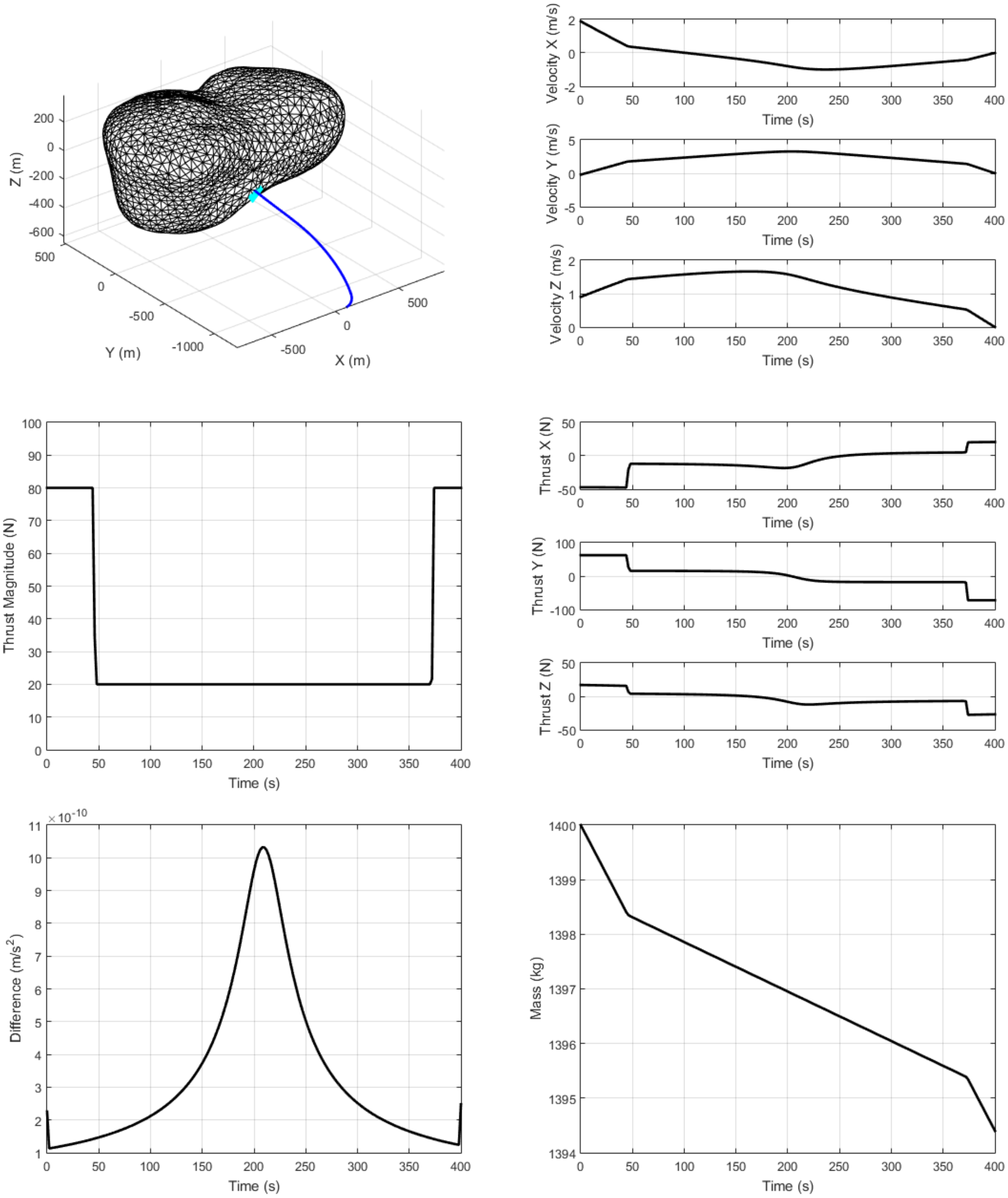

Figure 14.3: LS3 trajectory for a flight time of 400 sec. Top left: 3-D vehicle position, Top right: velocity components relative to the landing site, Middle left: thrust magnitude, Middle right: thrust components, Bottom left: difference between the slack variable and the acceleration vector, Bottom right: mass profile.

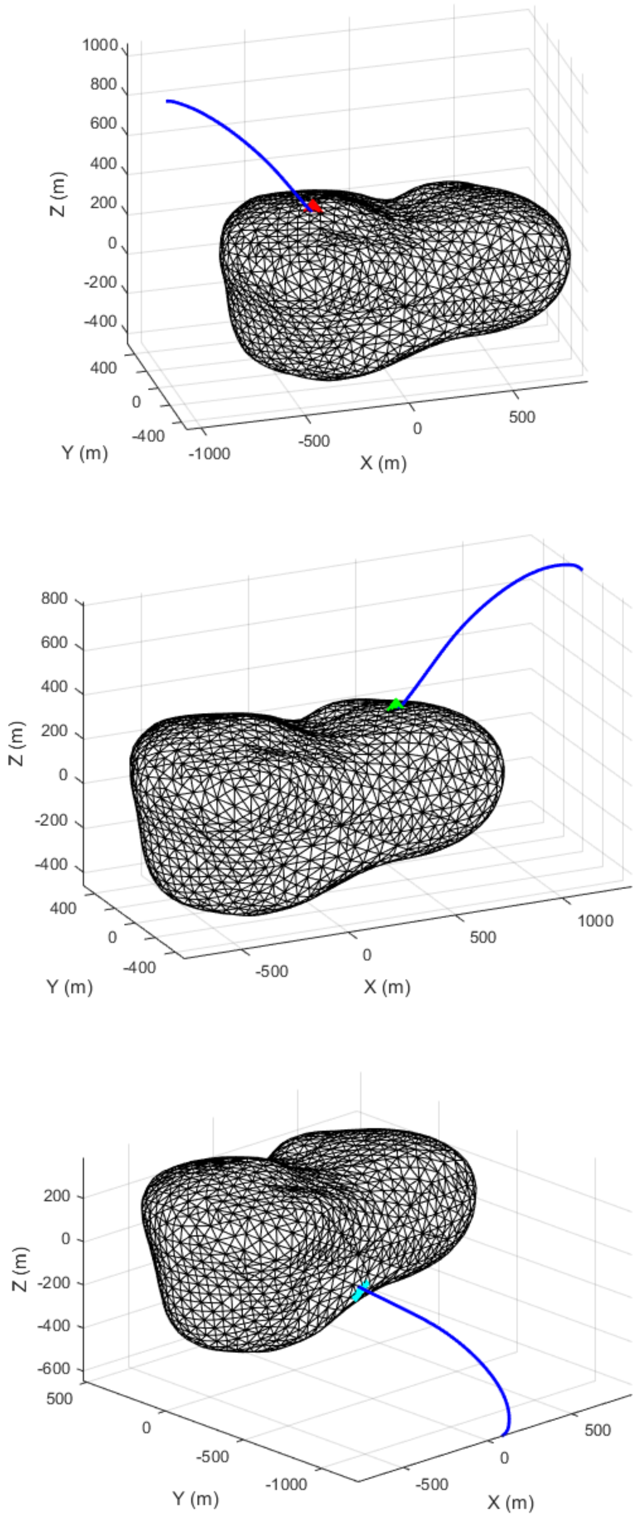

Figure 14.4: Optimal flight time trajectories landing on Castalia for LS1 (top), LS2 (middle), and LS3 (bottom).

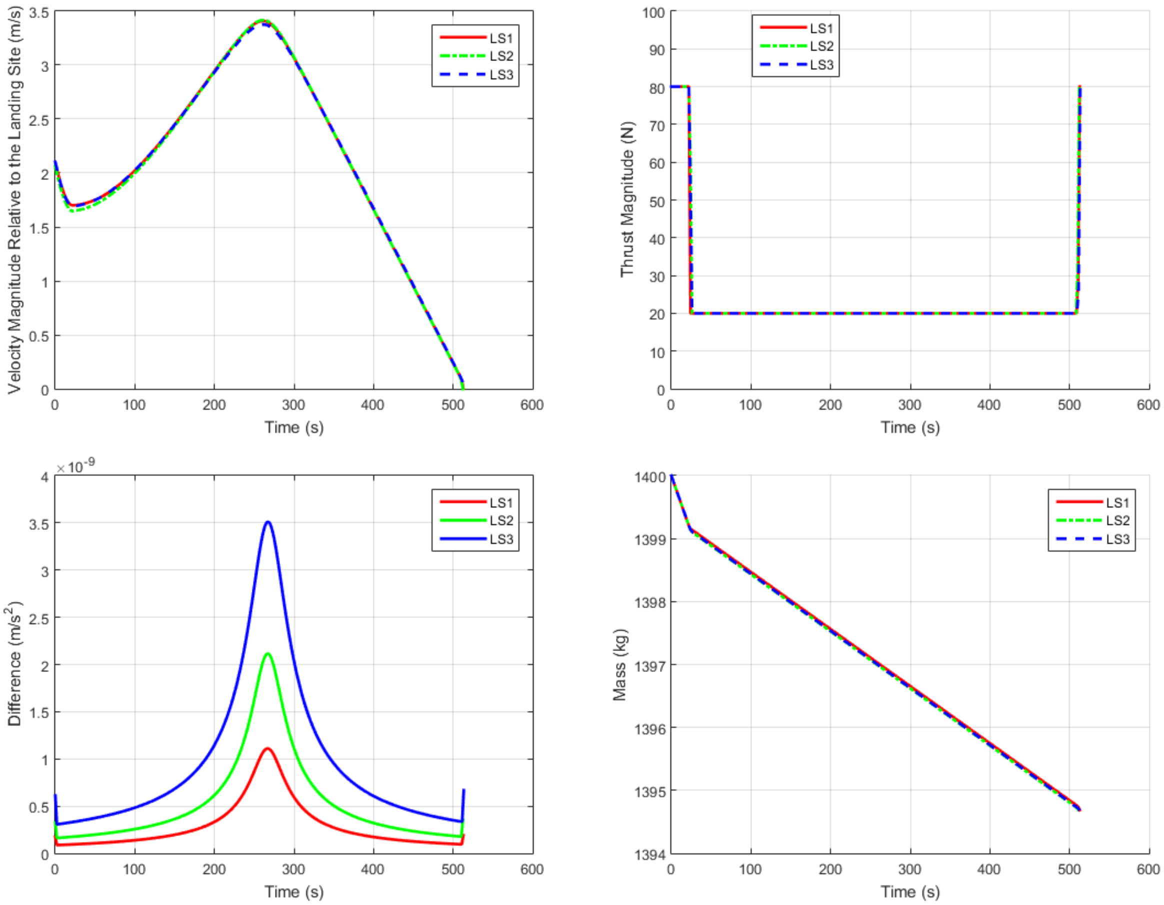

Figure 14.5: Optimal flight time trajectories landing on Castalia comparing the three landing sites. Top left: velocity magnitude relative to the landing site, Top right: thrust magnitude, Bottom left: difference between the slack variable and the acceleration vector, Bottom right: mass profile.

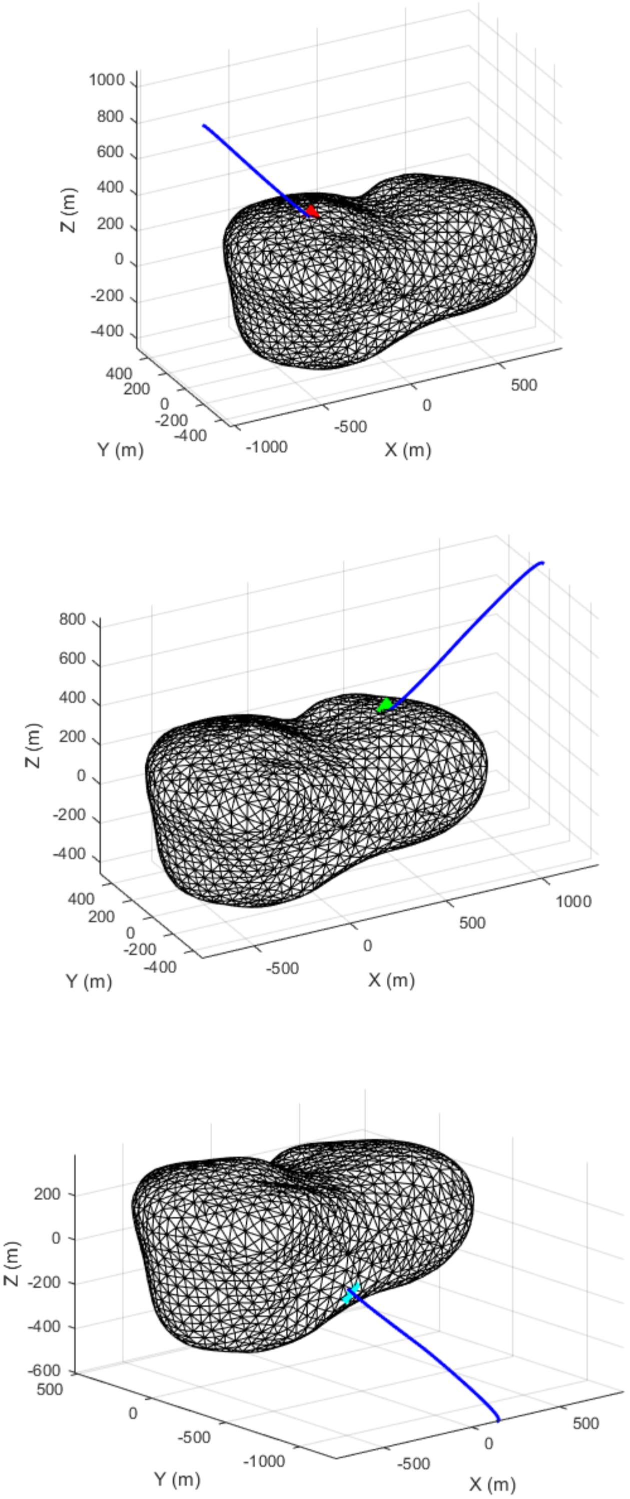

Figure 14.6: Optimal flight time trajectories landing on Castalia for LS1_hov (top), LS2_hov (middle), and LS3_hov (bottom).

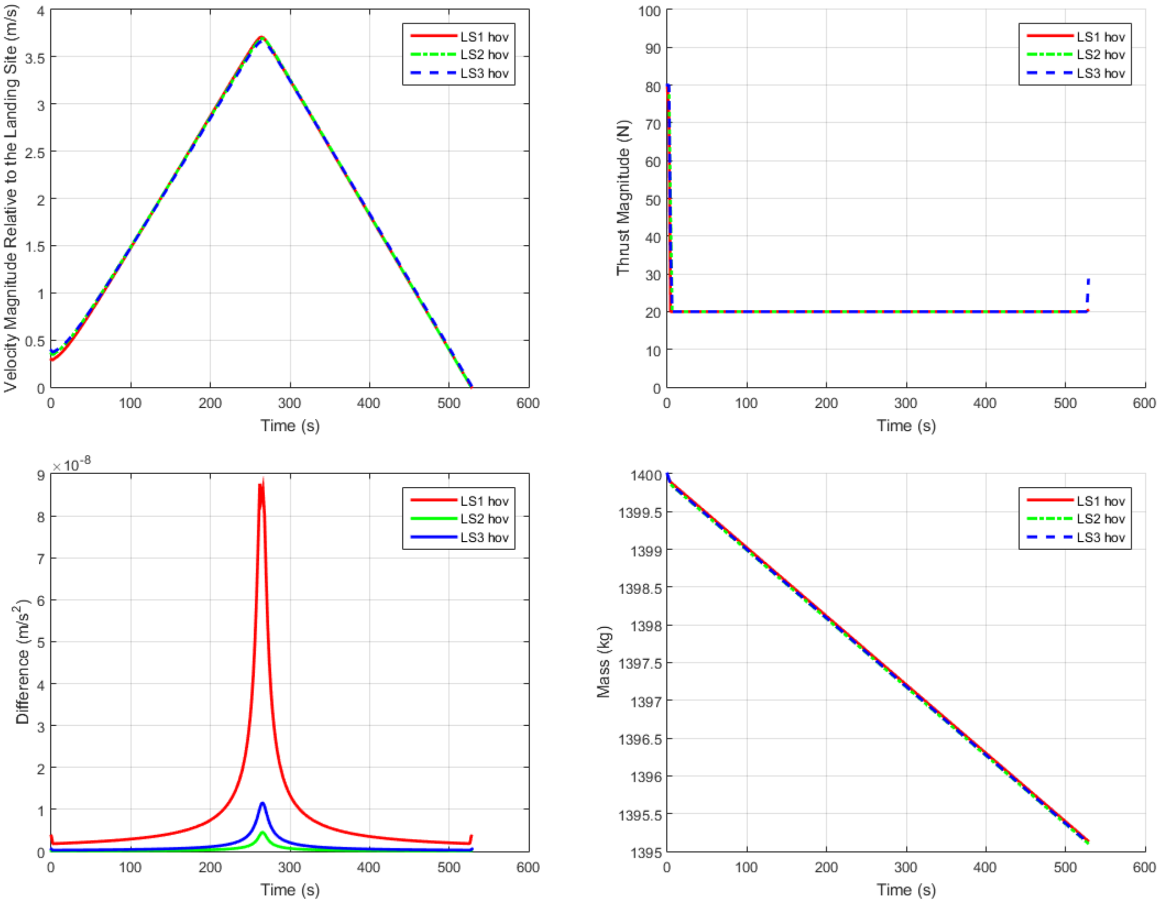

Figure 14.7: Optimal flight time with the hover trajectories landing on Castalia comparing the three landing sites. Top left: velocity magnitude relative to the landing site, Top right: thrust magnitude, Bottom left: difference between the slack variable and the acceleration vector, Bottom right: mass profile.

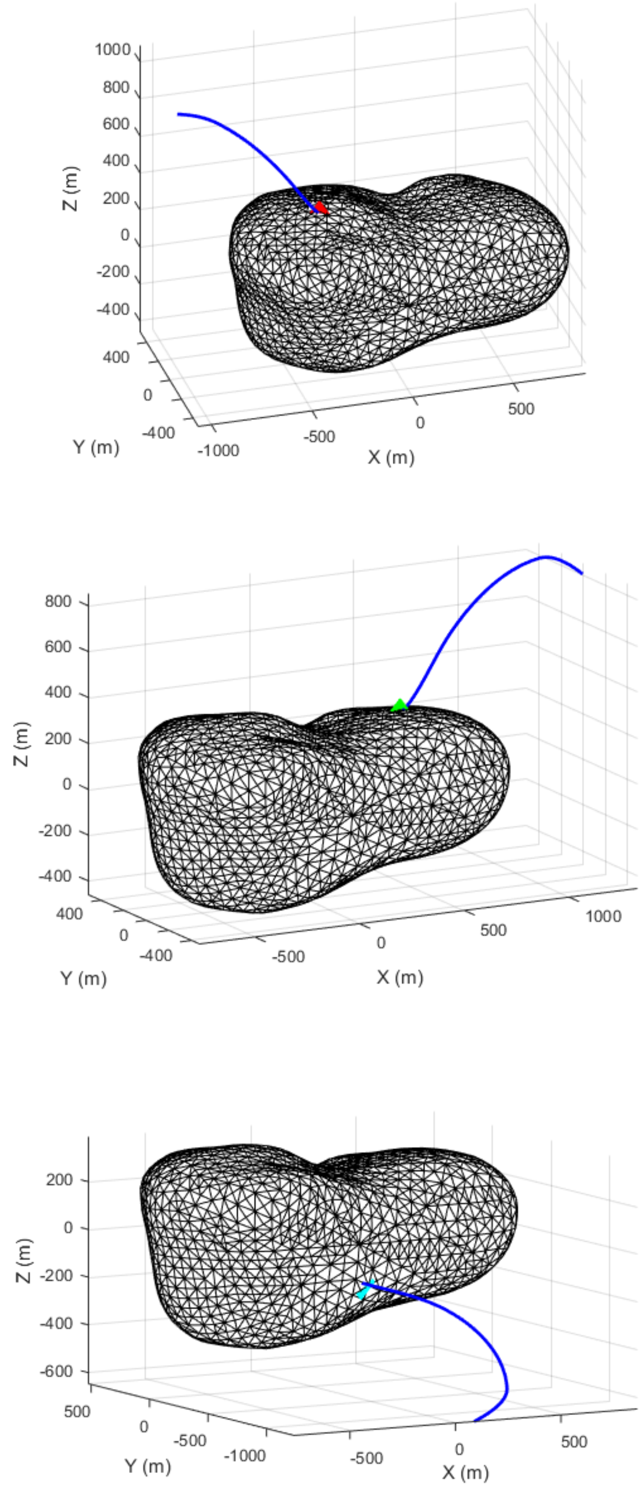

Figure 14.8: Optimal flight time trajectories landing on Castalia for LS1_LT (top), LS2_LT (middle), and LS3_LT (bottom).

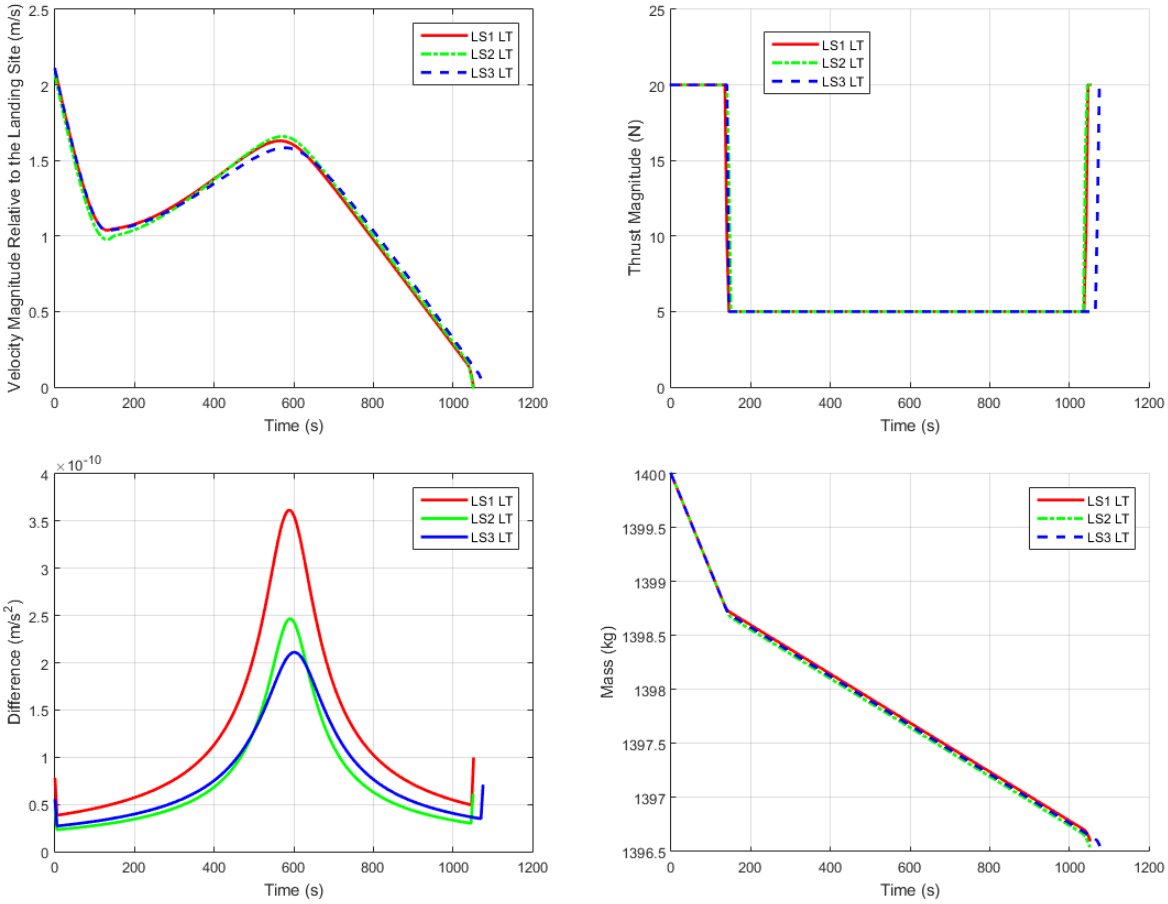

Figure 14.9: Optimal flight time for the lower thrust trajectories landing on Castalia comparing the three landing sites. Top left: velocity magnitude relative to the landing site, Top right: thrust magnitude, Bottom left: difference between the slack variable and the acceleration vector, Bottom right: mass profile.

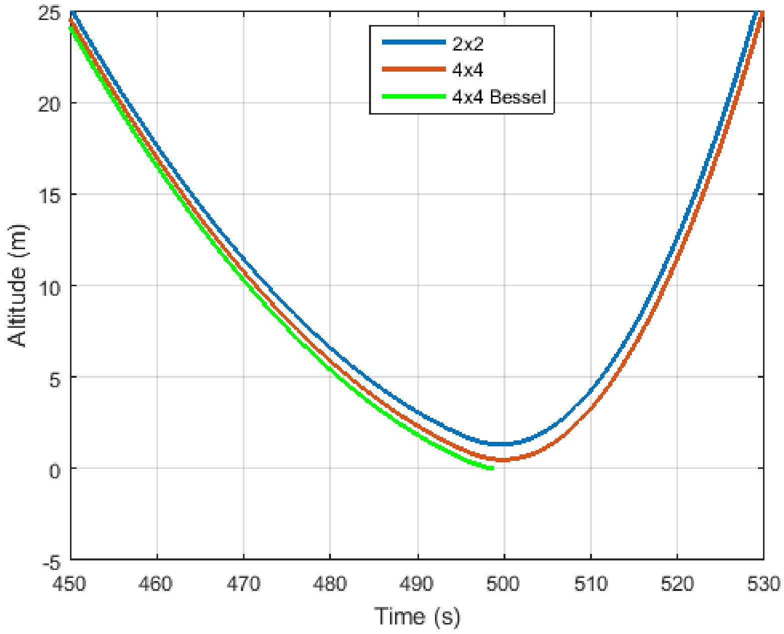

Figure 14.10: Altitude above LS1 from the open loop gravity model test on the asteroid Castalia with a 500 sec flight time.

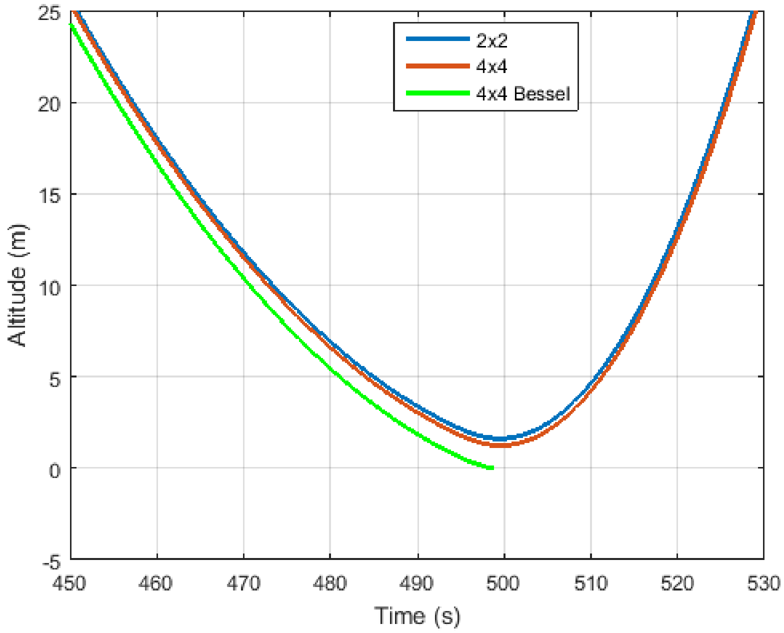

Figure 14.11: Altitude above LS2 from the open loop gravity model test on the asteroid Castalia with a 500 sec flight time.

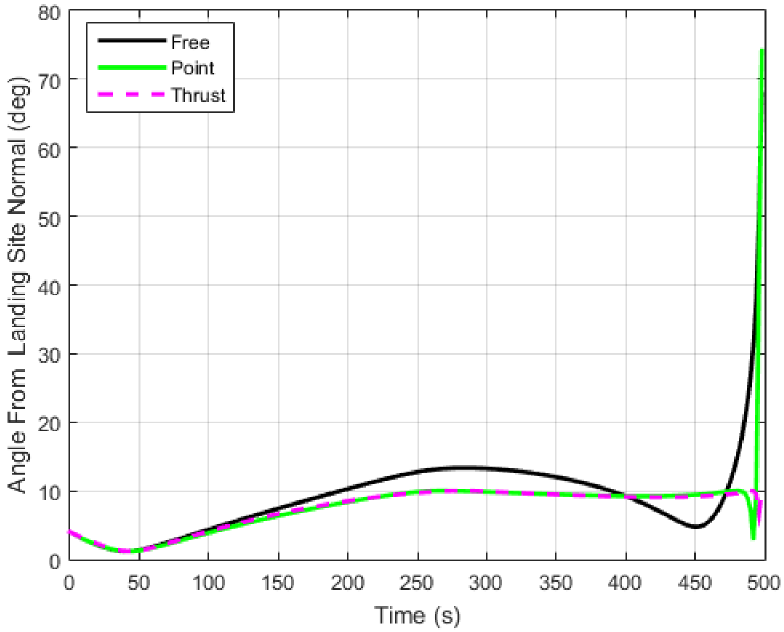

Figure 14.12: Angle from landing site, LS1, normal with a 500 second flight time.

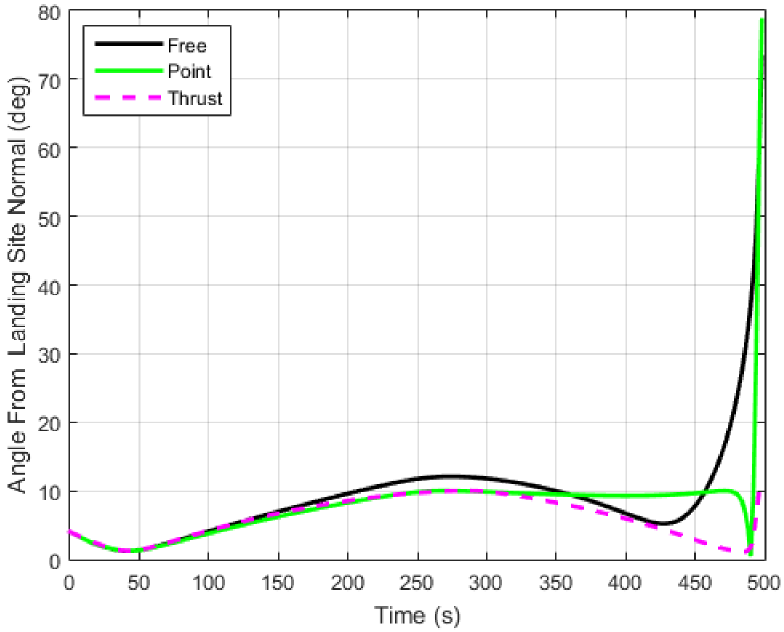

Figure 14.13: Angle from landing site, LS2, normal with a 500 second flight time.

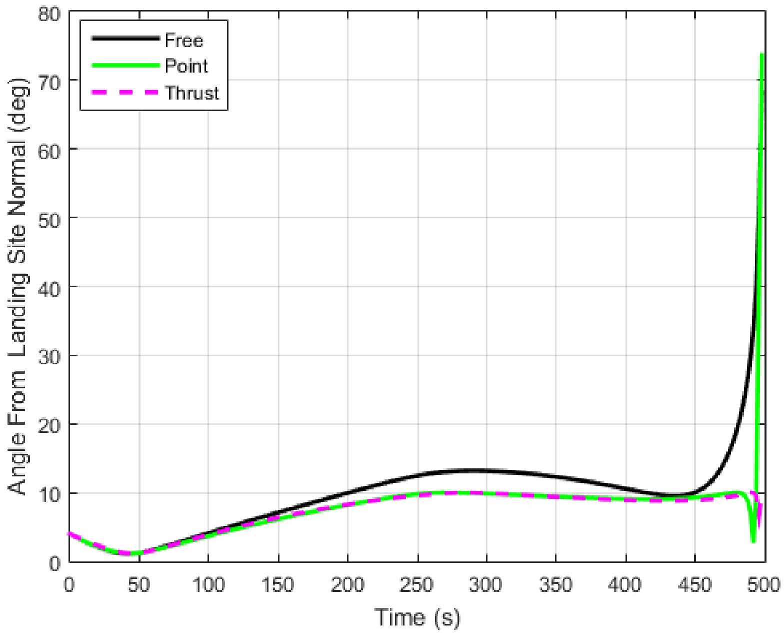

Figure 14.14: Angle from landing site, LS3, normal with a 500 second flight time.

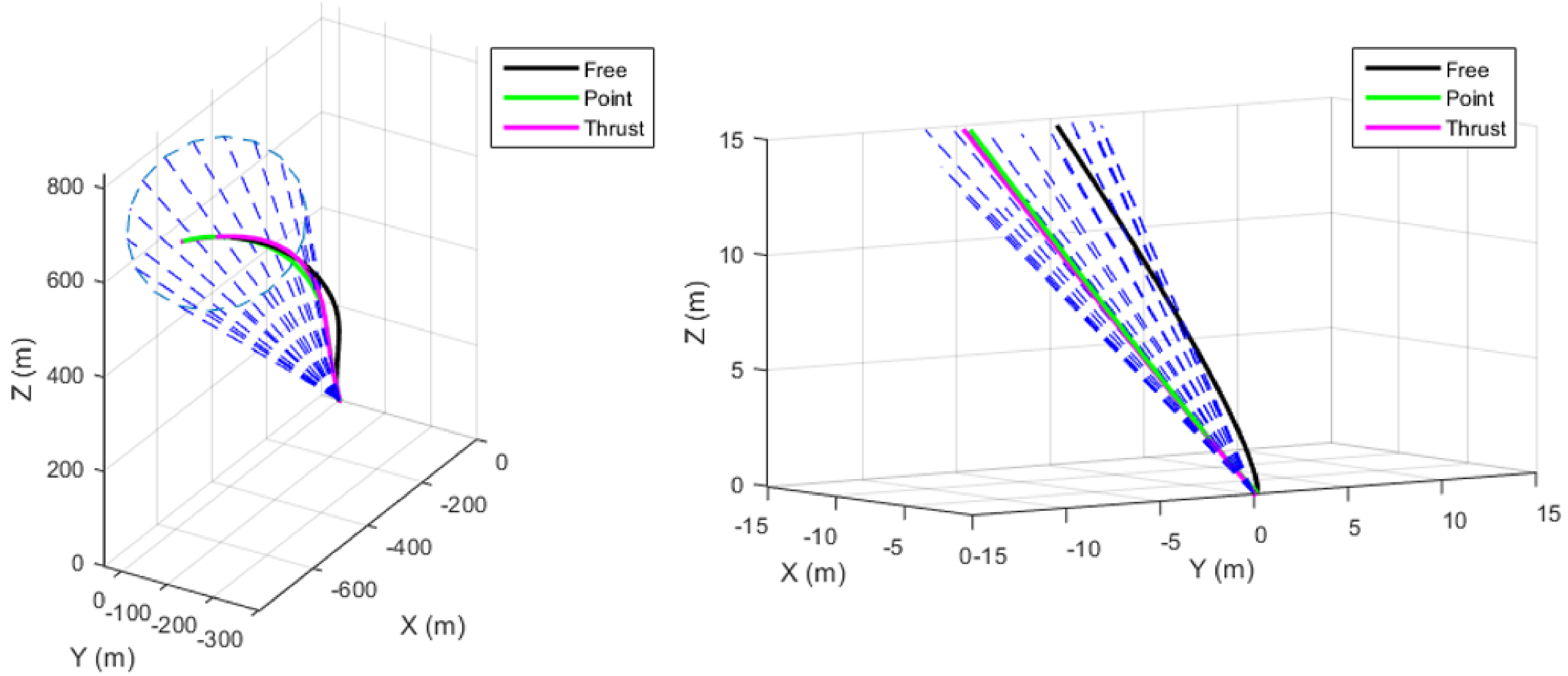

Figure 14.15: 10 deg cone from LS1 around the trajectory with a 500 sec flight time. Right plot is zoomed in on the landing site. Origin is the landing site.

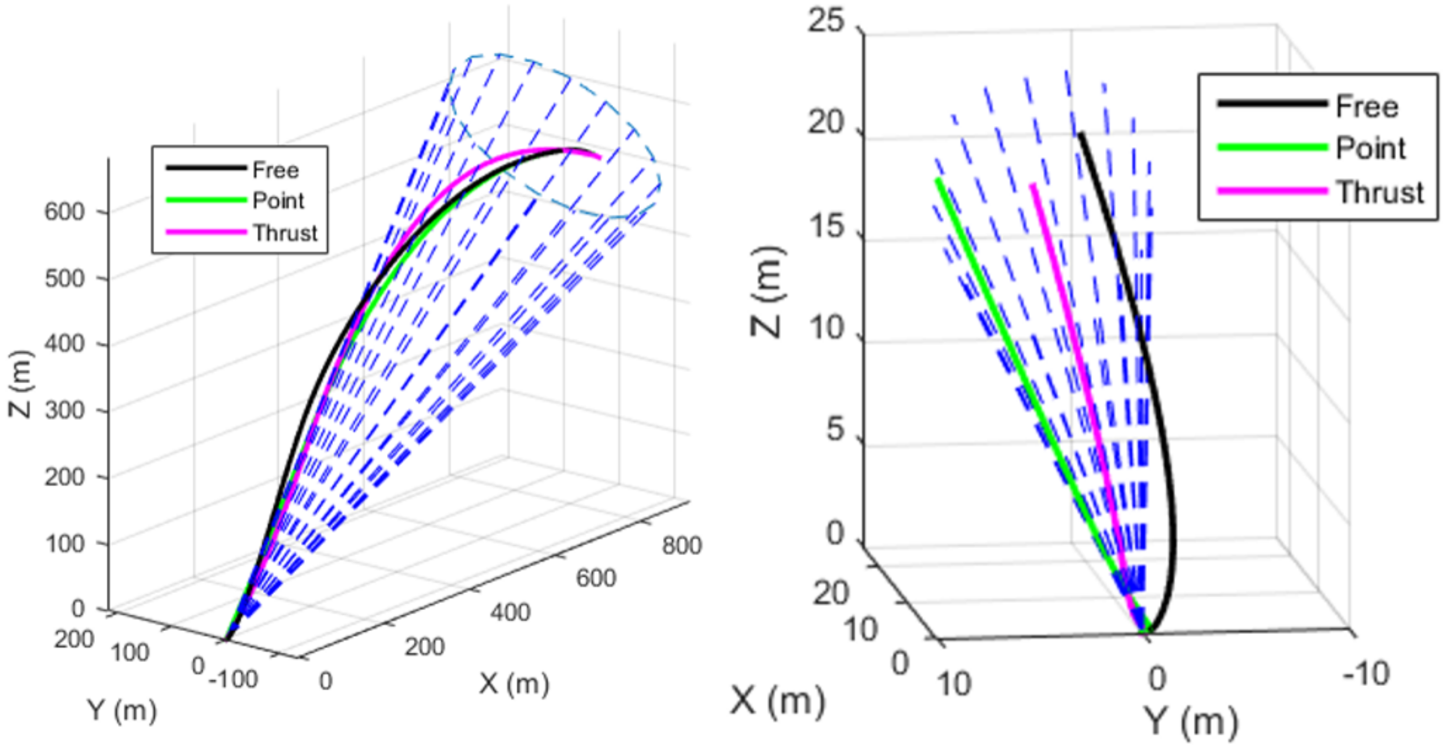

Figure 14.16: 10 deg cone from LS2 around the trajectory with a 500 sec flight time. Right plot is zoomed in on the landing site. Origin is the landing site.

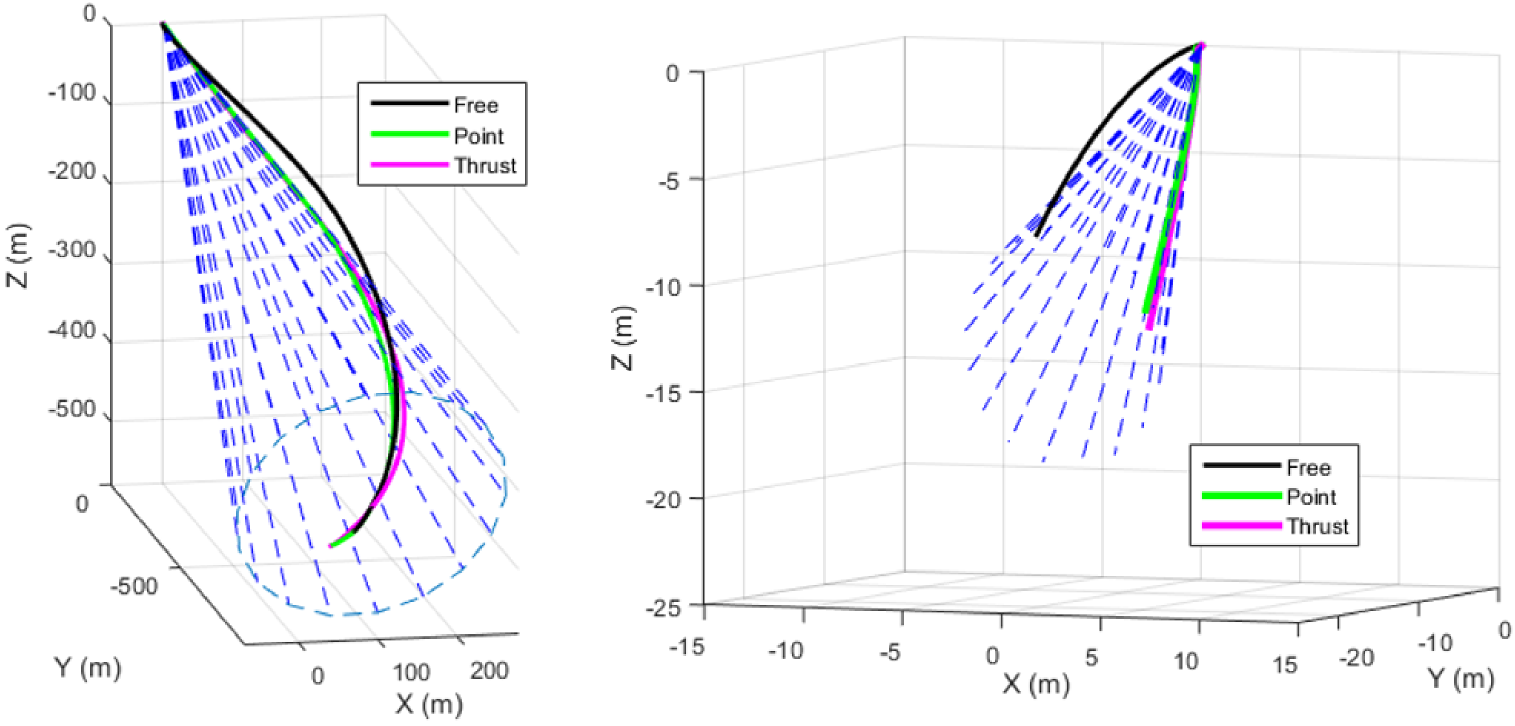

Figure 14.17: 10 deg cone from LS3 around the trajectory with a 500 sec flight time. Right plot is zoomed in on the landing site. Origin is the landing site.

CHAPTER 15. SUMMARY AND CONCLUSIONS

This research set out to answer the following questions: Can convex optimization be used to design the minimum propellant powered descent trajectory for a soft landing on an asteroid? Is this method robust and reliable to allow autonomy onboard the spacecraft without interaction from ground control? This research has shown that a truly optimal propellant trajectory can be designed for a fixed flight time using convex optimization. The solution to the convex optimization problem is the thrust magnitude and direction, which designs and determines the trajectory, including a soft landing. The propellant optimal problem was formulated as a second order cone program, a subset of convex optimization, through relaxation techniques by including a slack variable, change of variables, and incorporation of the successive solution method. Convex optimization solvers, especially second order cone programs, are robust, reliable, and are guaranteed to find the global minimum point provided one exists. In addition, an outer optimization loop using Brent's method determines the optimal flight time corresponding to the minimum propellant usage over all flight times.

Through a theoretical proof involving the Minimum Principle from Optimal Control Theory and the Karush-Kuhn-Tucker (KKT) conditions it was shown that the relaxed problem is identical to the original problem at the minimum point. Therefore, the optimal solution of the relaxed problem is an optimal solution of the original problem, referred to as lossless convexification. A key finding is that this holds for all levels of gravity model fidelity as long as they only depend on the spacecraft's position vector. This proof did not include the glide slope nor the solely vertical motion near the landing site constraints; however, checks on the slack variable showed that the lossless convexification held when these constraints were active.

The first high fidelity gravity model employed was the 2x2 spherical harmonics model assuming a perfect triaxial ellipsoidal asteroid and placement of the coordinate frame at the asteroid's center of mass and aligned with the moments of inertia. This model was used for the initial testing with the three triaxial ellipsoidal asteroids. The spherical harmonics model is not valid inside the Brillouin sphere and this becomes relevant as the asteroids move away from a spherical shape, especially irregularly shaped asteroids. A higher fidelity model was implemented, 4x4 Bessel, which combines the 4x4 spherical harmonics gravity model with the interior spherical Bessel gravity model. The transition between the models occurs at the boundary of the Brillouin sphere. All gravitational terms in the equations of motion are evaluated with the position vector from the previous iteration, creating the successive solution method. The successive solution method formulation places the dominant gravity term, like the Newtonian, in the linear term, while placing the remaining gravity terms in the higher order term. The equations of motion are discretized and then propagated with the trapezoidal rule before using the CVX solver to find the optimal propellant trajectory. Scaling helps ensure convergence for both the convex optimizer and the successive solution method.

Methodology success was shown by applying the algorithm to three triaxial ellipsoidal asteroids with four different rotation speeds using the 2x2 gravity model and to the irregularly shaped asteroid, Castalia using the 4x4 Bessel gravity model. A range of starting conditions, landing sites, and thrust values were used to truly test the algorithm. Trends showed that propellant usage is unimodal with respect to flight time. Polar landings were sensitive to asteroid size, while equatorial landings were sensitive to asteroid rotational speed. Number of iterations for the successive solution method did not show definite trends. The number of iterations required was small on the order of two to five for the majority of cases. Overall, the low number of required iterations shows stability in the successive solution method and its convergence the optimal propellant trajectory. The designed thrust magnitude profiles were the bang-bang predicted by Optimal Control Theory.

Since propellant usage is unimodal, a simple one variable optimizer, Brent's method, was wrapped around the optimal propellant trajectory design algorithm in order to optimize the flight time corresponding to the minimum propellant usage over all flight times. A coarse discretization step size of ten seconds was used in the inner loop optimization evaluation in order to determine the optimal flight time. After the optimal flight time was calculated, a smaller time step, the original used in the inner loop analysis (2 sec or 5 sec), was used to design the final trajectory. This allows for decreased computer execution time as compared to running with the smaller time step for the entire optimization process. The time step size is a balance between computational time and necessary accuracy. Seven to eleven executions of the inner loop algorithm were needed to determine this final optimal flight time optimal propellant trajectory.

Inclusion of additional trajectory constraints, solely vertical motion near the landing site and glide slope, were evaluated. The algorithm did successfully incorporate them as demonstrated with the polar landings on the triaxial ellipsoidal asteroids. It was not feasible to apply these constraints to the equatorial and Castalia trajectories as the vehicle did not have enough velocity to match the landing site speed when forced to remain directly over the landing site at low altitude. There is an option to apply the glide slope constraint for the majority of the trajectory to keep the vehicle in the landing site cone for most of flight and allow small deviations near the landing site.

The algorithm was not programmed for speed and efficiency nor was an efficient programming language used (such as C); however, the algorithm finished in a matter of minutes. For example, the inner loop optimization for a 600 second case with 3 iterations, over 3300 equations per iteration, took 3.5 minutes to run. The NP trajectory took 7 minutes to design the optimal flight time trajectory (inner and outer loops combined). These were not executed on a computer optimized for speed. It is expected that by changing to a different language, efficient programming, and a moderate to fast computer the computation time of this algorithm will drop significantly and be fast enough to operate during the mission using the onboard the flight computer. This algorithm runs autonomously once the inputs, such as gravitational coefficients, are determined.

This algorithm designs the optimal propellant trajectory as dictated by Optimal Control Theory. It optimizes the flight time for minimum propellant usage over all flight times. It is reliable and viable for use on the flight computer.

BIBLIOGRAPHY

Acikmese, B., Blackmore, L., and Scharf, D. (2008). Enhancements on the convex programming based powered descent guidance algorithm for Mars landing. *AIAA/AAS Astrodynamics Specialist Conference.* 19

Acikmese, B., Carson, J., and Blackmore, L. (2013). Lossless convexification of nonconvex control bound and pointing constraints of the soft landing optimal control problem. *IEEE Transaction on Control System Technology*, 21(6):2104–2113. 19, 46, 143

Acikmese, B. and Ploen, S. (2007). Convex programming approach to powered descent guidance for Mars landing. *Journal of Guidance, Control, and Dynamics*, 30(5):1353–1366. 18, 19

Bernard, J., Dufour, F., Gaudon, P., Ceolin, T., and Kerambrun, S. (2002). Rosetta mission analysis of the landing phase on a comet. *AIAA/AAS Astrodynamics Specialist Conference.* 12

Berry, K., Sutter, B., May, A., Williams, K., Barbee, B. W., Beckman, M., and Williams, B. (2013). OSIRIS-REx touch-and-go (TAG) mission design and analysis. *Advances in Astronautical Sciences*, 149:667–678. 13

Blackmore, L., Acikmese, B., and Scharf, D. (2010). Minimum-landing-error powered-descent guidance for Mars landing using convex optimization. *Journal of Guidance, Control, and Dynamics*, 33(4):1161–1171. 20

Brent, R. P. (1973). *Algorithms for Minimization Without Derivatives*, chapter 4-5. Prentice-Hall, NJ. 133

Carson, J. and Acikmese, B. (2006). A model predictive control technique with guaranteed resolvability and required thruster silent times for small-body proximity operations. *A collection of technical papers: AIAA Guidance, Navigation, and Control Conference*, 8:5205–5221. 14

Cheng, A. (2002). Near Earth Asteroid Rendezvous: mission summary. In Jr, W. B., Cellino, A., Paolicchi, P., and Binzel, R., editors, *Asteroids III*, pages 351–366. University of Arizona Press. 10

Dietze, C., Herrmann, F., Kub, S., Lange, C., Scharringhausen, M., Witte, L., Van Zoest, T., and Yano, H. (2010). Landing and mobility concept for the small asteroid lander MASCOT on asteroid 1999 JU3. *61st International Astronautical Congress*, 11:9266–9278. 12

Dunham, D., Farquhar, R., McAdams, J., Holdridge, M., Nelson, R., Whittenburg, K., Antreasian, P., Chesley, S., Helfrich, C., Owen, W., Williams, B., Veverka, J., and Harch, A. (2002). Implementation of the first asteroid landing. *Icarus*, 159:433–438. 10

Furfaro, R., Cersosimo, D., and Wibben, D. (2013). Asteroid precision landing via multiple sliding surfaces guidance techniques. *Journal of Guidance, Control and Dynamics*, 36(4):1075–1092. 15

Gaudet, B. and Furfaro, R. (2013). ZEM/ZEV guidance approach for asteroid touch-and-go sample collection maneuvers. *Advances in the Astronautical Sciences*, 148:897–914. 17

Gherardi, D., Agnolon, D., Rebuffat, D., Chapuy, M., Cometto, F., Peacocke, L., Amata, G. B., Cacciatore, F., and Deslous, S. (2013). GNC for Marco Polo-R and moons of Mars sample return missions: System design, critical technologies and synergy. *Advances in Astronautical Sciences*, 149:637–650. 13

Gil-Fernadez, J. and Graziano, M. (2010). Autonomous GNC for descent and landing on small, irregular bodies. *Advances in the Astronautical Sciences*, 136:2307–2316. 17

Grant, M. and Boyd, S. (2011). CVX: Matlab software for disciplined convex programming, version 2.0. http://cvxr.com/cvx. 71

Kaidy, J., McGee, T., Criss, T., Heyler, G., Shyong, W.-J., and Guzman, J. (2010). Spacecraft precision landing system for low gravity bodies. *Advances in the Astronautical Sciences*, 137:221–237. 15

Kawaguchi, J., Hashimoto, T., Kubota, T., , Sawai, S., and Fujii, G. (1997). Autonomous optical guidance and navigation strategy around a small body. *Journal of Guidance, Control, and Dynamics*, 20(5):1010–1017. 17

Kubota, T., Hashimoto, T., Sawaib, S., Jun'ichiro Kawaguchi, K. N., Uo, M., and Baba, K. (2003). An autonomous navigation and guidance system for MUSES-C asteroid landing. *Acta Astronautica*, 52:125–131. 11

Lan, Q., Li, S., Yang, J., and Guo, L. (2014). Finite-time soft landing on asteroids using nonsingular terminal sliding mode control. *Transactions of the Institute of Measurement and Control*, 36(2):216–223. 16

Lantoine, G. and Braun, R. D. (2007). Optimal trajectories for soft landing on asteroids. *Advances in the Astronautical Sciences*, 129:447–468. 15

Liu, X. and Lu, P. (2014). Solving nonconvex optimal control problems by convex optimization. *Journal of Guidance, Control, and Dynamics*, 37(3):750–765. 22

Lu, P. and Liu, X. (2013). Autonomous trajectory planning for rendezvous and proximity operations by conic optimization. *Journal of Guidance, Control, and Dynamics*, 36(2):375–389. 21

Lunghi, P., Lavagna, M., and Armellin, R. (2015). A semi-analytical guidance algorithm for autonomous landing. *Advances in Space Research*, 55:2719–2738. 14

May, A., Sutter, B., Linn, T., Bierhaus, B., Berry, K., and Mink, R. (2014). OSIRIS-REx touch-and-go (TAG) mission design and analysis. *65th International Astronautical Congress*. 13

Neese, C. (2004). Small body radar shape models V2.0 EAR-A-5-DDR-RADARSHAPE-MODELS-V2.0, NASA planetary data system. 73

Ploen, S., Acikmese, B., and Wolf, A. (2006). A comparison of powered descent guidance laws for Mars pinpoint landing. *AIAA/AAS Astrodynamics Specialist Conference.* 20

Pontryagin, L. S., Boltyanskii, V. G., Gramkreledze, Q. V., and Mishchenko, E. F. (1962). *The Mathematical Theory of Optimal Processes.* Intersciences, New York. 46

Rade, L. and Westergren, B. (1999). *Mathematics Handbook for Science and Engineering.* Springer, 4th edition. 35

Richter, L., Dietze, C.and Hallmann, M., Ho, T.-M., Krueger, H., Lange, C., Sproewitz, T., Wagenbach, S., Witte, L., Barucci, A., Bellerose, J., Okada, T., Yano, H., Bibring, J.-P., Biele, J., Ulamec, S., Block, J., Boehnhardt, H., Bousquet, P., Koschny, D., and Nadalini, R. (2009). Marco Polo Surface Scout (MASCOT) - study of an asteroid lander for the Marco Polo mission. *60th International Astronautical Congress*, pages 1331–1344. 12

Scheeres, D. J. (2012). *Orbital Motion in Strongly Perturbed Environments: Applications to Asteroid, Comet and Planetary Satellite Orbiters.* Springer. Ch. 2. 23, 26, 27, 28

Scheeres, D. J., Gaskell, R., Abe, S., Barnouin-Jha, O., Hashimoto, T., Kawaguchi, J., Kubota, T., Saito, J., Yoshikawa, M., Hirata, N., Mukai, T., Ishiguro, M., Kominato, T., Shirakawa, K., and Uo, M. (2006). The actual dynamical environment about Itokawa. *AIAA/AAS Astrodynamics Specialist Conference*, pages 1553–1574. 11

Scheeres, D. J., Ostro, S. J., Hudson, R. S., and Werner, R. A. (1996). Orbits close to asteroid 4769 Castalia. *Icarus*, 121:67–87. 74

Shuang, L., Pingyuan, C., and Hutao, C. (2006). Autonomous navigation and guidance for landing on asteroids. *Aerospace Science and Technology*, 10:239–247. 16

Takahashi, Y. and Scheeres, D. J. (2014). Small body surface gravity fields via spherical harmonic expansions. *Celestial Mechanics and Dynamical Astronomy*, 119(2):169–206. 28, 29, 32, 34, 74, 77

Takahashi, Y., Scheeres, D. J., and Werner, R. A. (2013). Surface gravity fields for asteroids and comets. *Journal of Guidance, Control and Dynamics*, 36(2):362–374. 27, 28, 29

Tutuncu, R. H., Toh, K. C., and Todd, M. J. (2003). Solving semidefinite-quadratic-linear programs using SDPT3. *Mathematical Programming*, 95:189–217. 72

Ulamec, S. and Biele, J. (2009). Surface elements and landing strategies for small bodies mission - Philae and beyond. *Advances in Space Research*, 44:847–858. 12

Ulamec, S., Biele, J., Blazquez, A., Cozzoni, B., Delmas, C., Fantinati, C., Gaudon, P., Geurts, K., Jurado, E., Küchemann, O., Lommatsch, V., Maibaum, M., Sierks, H., and LarsWitte (2015). Rosetta lander - Philae: landing preparations. *Acta Astronautica*, 107:79–86. 12

Ulamec, S., Biele, J., Espinasse, S., Feuerbacher, B., Moura, D., H. Rosenbauer, H. S., and Willnecker, R. (2004). PHILAE, the lander of the ROSETTA mission on its way to Comet 67P/Churyumov-Gerasimenko. *55th International Astronautical Congress*, 10:6348–6357. 12

Vallado, D. (2013). *Fundamentals of Astrodynamics and Applications*. Microcism Press, California. 24

Werner, R. A. (1994). The gravitational potential of a homogeneous polyhedron or don't cut corners. *Celestial Mechanics and Dynamical Astronomy*, 59:253–278. 28, 29

Werner, R. A. (2010). Evaluating descent and ascent trajectories near non-spherical bodies. Technical Report NPO-46697, NASA Tech Brief. 28, 29

Werner, R. A. and Scheeres, D. J. (1997). Exterior gravitation of a polyhedron derived and compared with harmonic and mascon gravitation representations of asteroid 4769 Castalia. *Celestial Mechanics and Dynamical Astronomy*, 65:313–344. 28, 29

Yang, H., Chen, Y., and Baoyin, H. (2013). Fuel optimal guidance for soft landing on irregular asteroids using sliding mode control. *64th International Astronautical Congress*, pages 4949–4960. 16

Yoshimitsua, T., Kawaguchia, J., Hashimotoa, T., Kubotaa, T., Uob, M., Moritab, H., and Shirakawab, K. (2009). Hayabusa - final autonomous descent and landing based on target marker tracking. *Acta Astronautica*, 65:657–665. 11